Pressurized Melt Ejection Into Scaled Reactor Cavities

W. W. Tarbell, M. Pilch, J. E. Brockmann,
J. W. Ross, D. W. Gilbert

Prepared for
U. S. NUCLEAR REGULATORY COMMISSION

PRESSURIZED MELT EJECTION INTO
SCALED REACTOR CAVITIES

WILLIAM W. TARBELL
MARTY PILCH
JOHN E. BROCKMANN
JAMES W. ROSS*
DON W. GILBERT*

August 1986

---

* An employee of Ktech Corp. working under contract to Sandia
National Laboratories

ABSTRACT

This report describes four tests performed in the High-Pressure Melt Streaming Program (HIPS) using linear-scaled cavities of the Zion Nuclear Power Plant. These experiments were conducted to study the phenomena involved in high-pressure ejection of core debris into the cavity beneath the reactor pressure vessel. One-tenth and one-twentieth linear scale models of reactor cavities were constructed and instrumented. The first test used an apparatus constructed of alumina firebrick to minimize the potential interaction between the ejected melt and cavity material. The remaining three experiments used scaled representations of the Zion nuclear plant geometry, constructed of prototypic concrete composition.

A metallothermitic reaction produced molten iron (55 w/o) and alumina (45 w/o) to form the core debris simulant. The reaction was caused to occur within a steel vessel initially pressurized with either nitrogen or carbon dioxide. The two gases were used to determine the influence of gas solubility on the dispersal process. The pressure level was also varied to study the influence of driving pressure on the extent of debris dispersal. Melt was ejected into the cavity when the reaction front contacted and failed a fusible plug in the base of the pressure vessel. The two smaller-scale experiments were placed in a $45-m^3$ steel interaction chamber to collect debris and aerosol generated during the melt ejection and debris dispersal processes.

The instrumentation employed to study the phenomena included pressure and temperature transducers, aerosol and debris collectors, high-speed cameras, and X-ray imagining equipment. Techniques were utilized following the tests to analyze the size, shape, and chemical composition of the aerosol and debris.

Calculations were performed to compare with experimental data and to provide information regarding the relevant physical processes. Estimates of the pressure vessel blowdown history, breach aperture growth, melt entrainment and particle size, debris discharge history, and energy transfer from the debris to the atmosphere were completed and presented along with the experimental data.

CONTENTS

CONTENTS (Continued)

LIST OF ILLUSTRATIONS

LIST OF ILLUSTRATIONS (Continued)

LIST OF ILLUSTRATIONS (Continued)

LIST OF ILLUSTRATIONS (Continued)

LIST OF TABLES

I. INTRODUCTION

The use of probabilistic risk assessments (PRAs) to identify the risk associated with operating commercial nuclear power plants has become increasingly common. One objective of the PRA methodology is to provide a cost-effective means for evaluating plant performance during severe accident situations. Until recently, the Reactor Safety Study[1] (WASH-1400) was considered to be applicable to a wide range of facilities. New PRAs[2,3] have subsequently been produced to consider the operational risk associated with specific plants. These recent studies have extended the WASH-1400 analysis techniques in order to refine the calculations and reduce the uncertainty of the results.

The Zion Probabilistic Safety Study[2] (ZPSS) was an attempt to improve the WASH-1400 results for large, dry containment pressurized water reactors by recognizing differences in the core meltdown processes. A significant conclusion from this study was that in over 75% of the accident sequences considered, failure of the reactor pressure vessel (RPV) occurred while the primary system remained at some elevated pressure. The point of failure was predicted to occur at one or more of the RPV instrument tube penetrations, resulting in a small orifice through which the molten core material was ejected. As the molten material entered the cavity region beneath the RPV, it formed a pool of core debris that flowed radially outward and into the tunnel region. The analysis suggested that this initial movement of debris or the subsequent blowdown of the primary system caused virtually all of the expelled core material to be dispersed into the containment regions.

The ZPSS predicted that debris dispersal will result in the formation of a relatively shallow debris bed on the containment floor that could be cooled by the addition of water from spray activation. This scenario eliminated the possibility of an extended interaction between the core debris and concrete basemat with the resulting gas and aerosol production. Steam generated by quenching the debris bed was not sufficient to cause containment failure by overpressurization. The ZPSS methodology has also been used for other plants with essentially the same benign termination to the accident.[3,4]

Reactor accidents of this type were identified with either transient (T) or small-break loss-of-coolant (S) initiating events accompanied with failure of recirculation or injection, loss of feedwater, or station blackout. Based upon a number of probabilistic risk assessments, these accident initiators dominated the core damage frequency.[5] For an accumulation of fourteen reference plants, the estimated core melt frequency for

S and T events was over 80% for pressurized water reactors (PWR) and over 90% for boiling water reactors (BWR).

Researcher were not universally in agreement that these accident sequences resulted in the mode of failure described. Arguments have been presented that natural circulation within the primary system may cause failure of the RPV head seal or the recirculation pump seals in the cold legs to leak, allowing depressurization before vessel failure.[6] Others argue that the lower head may fail globally at a point above the pool surface, resulting in a sudden circumferential tear.[7] The resulting large aperture will greatly reduce the time interval for blowdown and mitigated the dispersal of debris from the cavity.

The phenomena associated with RPV failure while the primary system was pressurized represented a considerable departure from the assumptions made in the RSS. Experimental data and verified analytical results for these processes were incomplete. Because of this, research was initiated at Sandia National Laboratories (SNL) to perform an experimental and analytical investigation of the phenomena associated with this type of accident scenario, particularly the dispersal of debris from the reactor cavity. The ensuing effort was termed the High-Pressure Melt Streaming Program (HIPS).[8] The objective of program was to determine the character and magnitude of debris dispersal for the Zion cavity configuration over a range of accident conditions.

To accomplish the objective of the HIPS program, a unique experimental technique was developed to simulate small-break loss-of-coolant and transient accident sequences. This allowed conducting linear-scaled experiments using models of reactor cavities to aid in determining the extent of debris dispersal. Accompanying analyses were used to explain the observations and extrapolate the results to large scale.

This report describes four tests performed in the HIPS program using linear-scaled cavities of the Zion nuclear plant. Table 1 gives an overview description of the four experiments. The specific purpose of these experiments was to quantify debris dispersal at two scales for a range of operating conditions. The first two tests are nominally 1:20 linear-scaled models of cavities, one constructed of a nonreacting firebrick material and the second of prototypic concrete composition. Each experiment was placed inside a 45-m^3 steel enclosure to retain the debris and aerosol produced during the event. The results indicated that significant debris dispersal occurred for these conditions, over 50% of the available debris in the first test and greater than 90% in the second event. In both experiments, energy liberated from the airborne debris heated the atmosphere in the steel enclosure, causing a sharp increase in pressure. The potential for direct heating and pressurizing of the atmosphere

represented a new and significant threat to the integrity of the containment building.

Table 1
Description of Experiments

TEST	SCALE	MELT MASS	CAVITY CONSTRUCTION
SPIT-18	1:20	10.3 kg	Alumina Brick
SPIT-19	1:20	10.3 kg	Concrete
HIPS-2C	1:10	80.0 kg	Concrete
HIPS-5C	1:10	80.0 kg	Concrete

The two additional tests described in this report were done at 1:10 linear scale using a prototypic cavity geometry and concrete composition. These tests represented an eightfold increase in mass over the initial, smaller experiments. Because the steel enclosure was heavily damaged in the previous tests, it was not used for these larger experiments; the debris being allowed to freely expand from the exit of the apparatus. The observations from these tests gave insight into the nature and behavior of the debris as it escaped the confines of the reactor cavity.

The results from these experiments suggested that the accident may not proceed as depicted in the safety analyses. The highly fragmented nature of the debris expelled from the cavity was unlike the film flow suggested in the ZPSS, causing the material to be susceptible to dispersal by the influence of the high-speed gas blowdown of the primary system. Accelerating the drops within the cavity region caused them to exit the cavity. This behavior may allow the particles to penetrate into the

containment. The small size of the particles enhanced the exchange of thermal and chemical energy to the containment atmosphere. In an accident, if the amount of energy transmitted to the atmosphere is large, the resulting pressure and temperature increase could potentially fail even the strongest containment structure. The aerosol that accompanied the melt dispersal represented a potentially new radionuclide source term, not previously considered in accident analyses.[9]

Section II describes the experimental equipment and procedures, including both instrumentation and initial conditions for each of the four experiments. The experimental results and analyses with discussion are given in Section III, followed by the conclusions in Section IV.

II. DESCRIPTION OF EXPERIMENTAL APPARATUS

The apparatus for the experiments discussed in this report consisted of a melt generator, a scaled reactor cavity, and a steel enclosure. The generator produced a melt at temperatures and pressures that simulated the predicted condition of the molten core debris within the RPV during S and T accident sequences. The melt was expelled from the generator into a scale model of the reactor cavity. Two of the four tests described used a steel enclosure to collect aerosol and debris produced during the event. The following paragraphs describe the equipment, instrumentation, and initial conditions for each of the experiments. Some items were common to more than one test, but the experiments were unique enough that a separate discussion is given for each.

A. SPIT-18

The SPIT-18 experiment was the second test in the HIPS program to use a realistically scaled cavity. (The previous SPIT-17 experiment[5] used a scale model of the Zion cavity constructed of aluminum.) The objective was to demonstrate debris dispersal using a nominally 1:20 linear-scaled model of a reactor cavity. The melt mass (10 kg) was based on the assumption that nominally one-half of the core and internals (estimated to be 80,000 kg) will be molten at the time of vessel failure. To achieve the objective, the design of the experimental apparatus and the selection of initial test conditions were intended to maximize the potential for debris removal.

1. Apparatus

A sketch of the melt generator used for the SPIT series tests is shown in Figure 1. The melt generator was basically a pressure vessel to contain the metallothermic reaction that produced a mixture of molten iron and aluminum oxide. It was constructed of a mild steel pipe, 11.4 centimeter outer diameter by 90 centimeter long, with bolted flanges welded to each end. A second 10 centimeter diameter steel pipe was placed inside the first pipe to act as a crucible shell for the thermite powder. Graphite plates (1.2 centimeter thick) were placed at either end to complete the crucible. The bottom generator flange cover was machined to hold a replaceable insert plate. The insert plate was drilled and tapped to accept a fusible melt plug made from a
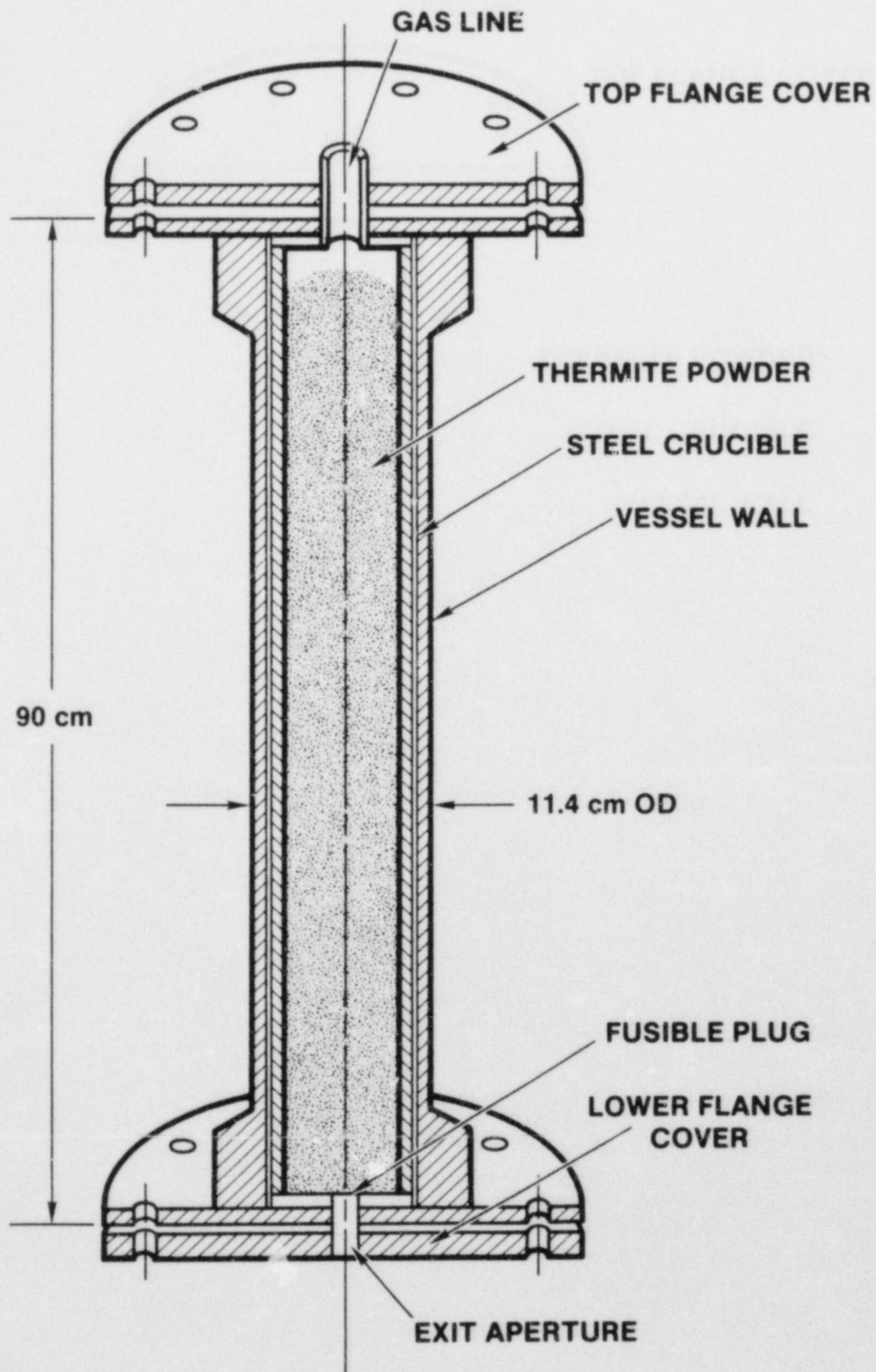
FIGURE 1. SCHEMATIC OF MELT GENERATOR USED ON THE SPIT TESTS

commercially available brass pipe fitting. The plug extends into the melt generator through a hole in the lower graphite plate so that it was exposed to the thermite powder. As the reaction front proceeds downward, the molten material ultimately contacted and melted the fusible plug, allowing the molten material to be ejected into the cavity.

The upper melt generator flange cover was machined to accept a gas feed line (nominal 1/2-in diameter stainless steel tubing) to pressurize the vessel prior to the start of the thermite reaction. The thermite reaction was initiated by an igniter embedded in the upper portion of the powder bed. Gaseous contaminates released during the reaction plus heating of the overlaying gas layer normally contributed additional pressurization of the generator. The gas line was also connected to an accumulator vessel intended to mitigate the pressure increase during the thermite reaction. Even with the accumulator in place during previous tests, the pressure level at the time of ejection was typically 30% to 50% greater than the initial value. Reference 8 contains additional information on the melt generator construction and thermite reaction.

A schematic of the SPIT-18 cavity is given in Figure 2. Although it did not represent any specific reactor geometry, the overall dimensions corresponded to a 1:20 linear scaling of a large PWR cavity. Specifically; the melt generator to floor distance, the length of the tunnel, and the angle of inclination (26 degrees from vertical) were a close simulation of the Zion and Indian Point plants. The apparatus was constructed in the form of a rectangular box of mild steel plate with openings for the melt generator and cavity exit. Commercial firebrick (99.2 w/o alumina) was used as a liner for the bottom and sides of the box. The bricks were in the "as-received" condition except for a short period of oven baking to remove excess water. The small gaps between the bricks were not filled.

The alumina brick selected for the SPIT-18 cavity was intended to eliminate the possible influence of a melt-concrete interaction on the debris dispersal processes. By using a refractory material in the cavity, the potentially disruptive effects of energetic concrete decomposition were reduced. Therefore, debris dispersal observed during this experiment should only be affected in the cavity by thermal and hydrodynamic phenomena. Likewise, using a simple cavity geometry simplified the flow patterns and regions where the debris could be trapped. To this end, the cavity was designed with a continuous cross-sectional area from the generator outlet to the exit of the cavity. The slightly reduced size of the cavity exit provided the only geometric restriction to the flow of gas and debris.

A schematic of the steel enclosure (known as the interaction chamber) is shown in Figure 3, along with the relative size of
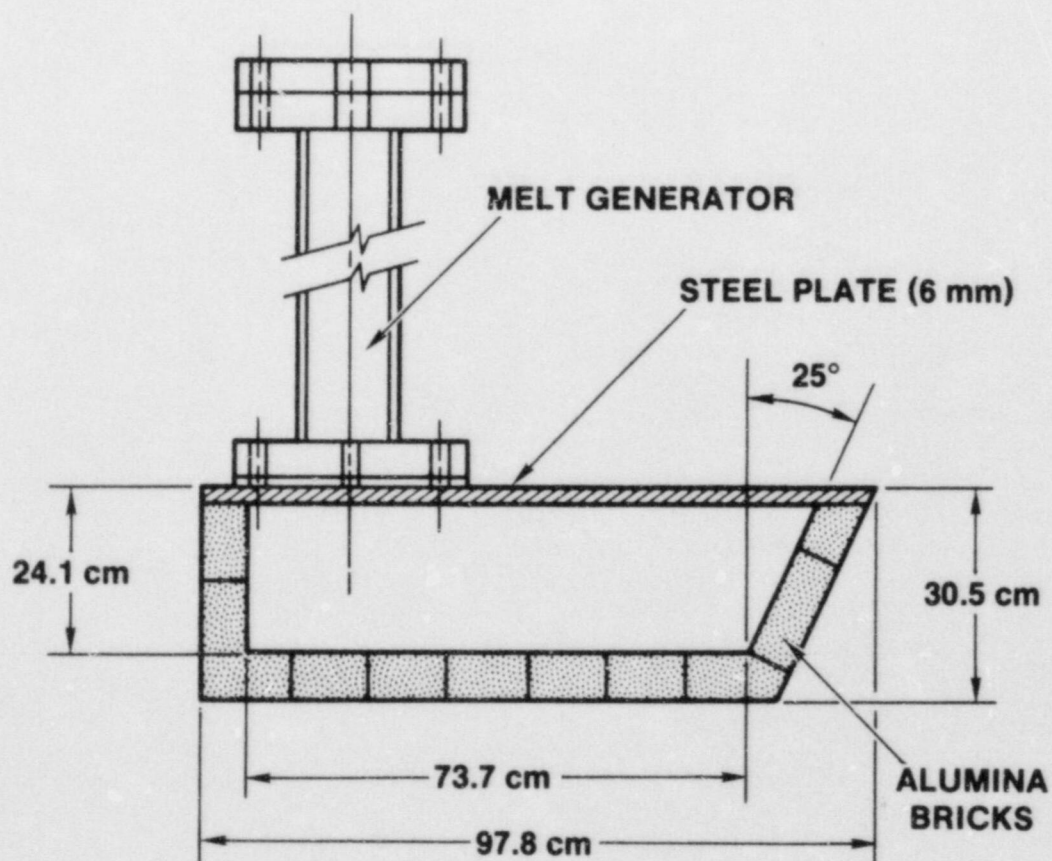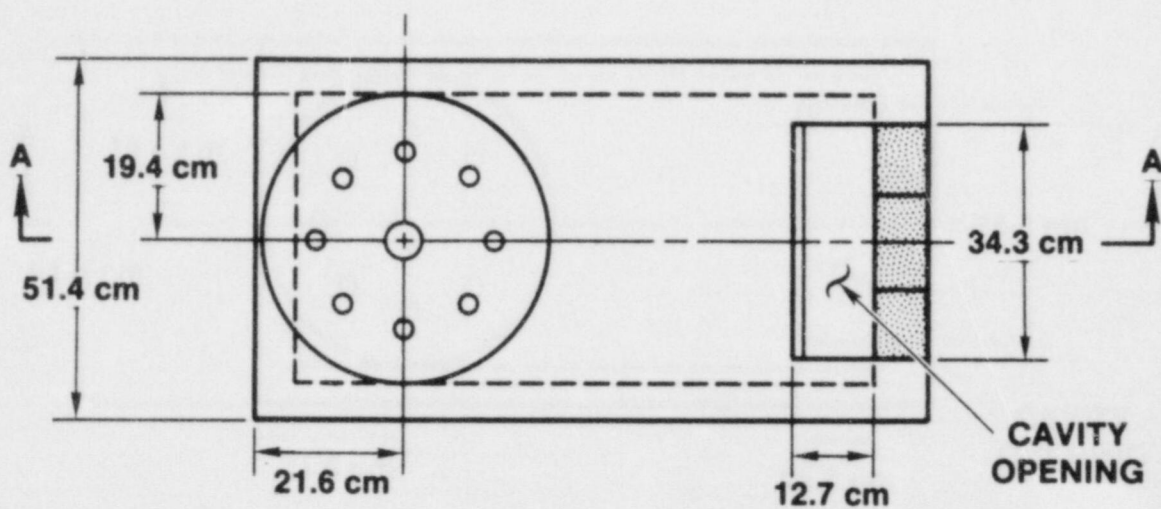
FIGURE 2. SCHEMATIC OF SPIT-18 TEST APPARATUS
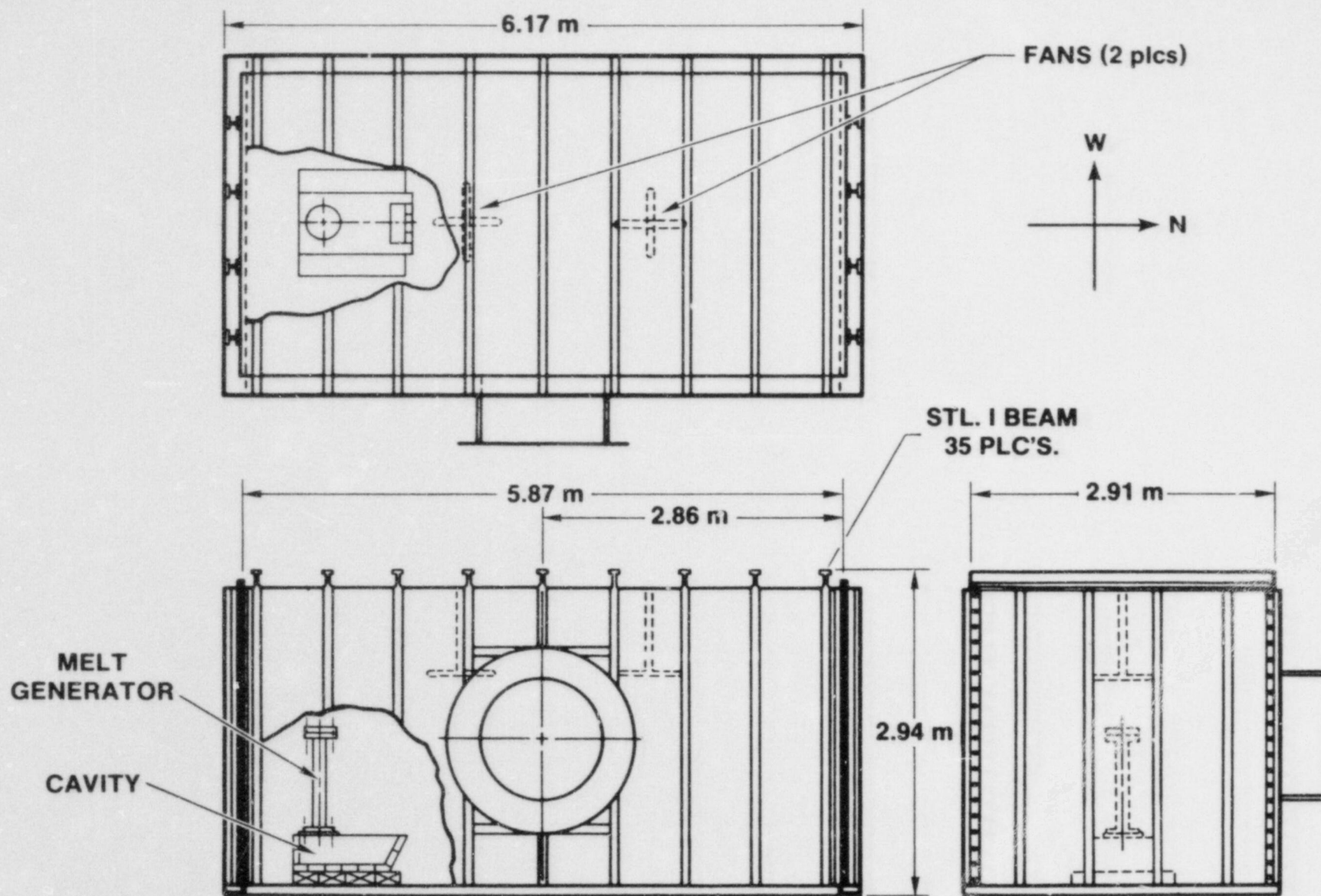
FIGURE 3. SCHEMATIC OF SPIT-18 APPARATUS PLACED IN THE INTERACTION CHAMBER

the melt generator and cavity apparatus. The walls, ceiling, and ends of the chamber were steel plate (8 millimeter thick) reinforced at regular intervals (0.67 meters) by I-beams. The side that faced east included a 1.2 meter diameter port for the instrumentation connections. The removable doors were attached at two sides and the upper edge by 1.2 centimeter diameter bolts spaced 15 centimeters apart. The lower edge of each cover was not bolted into placed but was sealed against the 15 centimeter thick concrete pad that formed the base for the chamber. A one centimeter thick sponge rubber gasket was used to seal the end covers to the chamber. The chamber was attached to the pad at several locations by embedded steel angle-iron pieces welded to the lower perimeter. The chamber was not considered to be a pressure vessel, with an estimated ultimate load capacity of less than 0.07 MPa. The design of the removable end covers prevented an absolute gas tight seal, although the leakage rate was considered small compared to the overall volume. The actual leak rate was not measured.

Internally, the interaction chamber was almost devoid of structures except for a large instrumentation port. Two fans with six blades each driven by air motors were suspended from the ceiling to develop air circulation patterns. The capacity of these units was intended to cause a flow in one minute equivalent to the volume of the chamber. The fans were designed to create a uniform distribution of the material suspended in the atmosphere following melt ejection (aerosols). The objective was to make the aerosol samples representative of the actual generation of material. The chamber also incorporated several transparent ports in the sides and ceiling to allow camera coverage of the test events. A 600 Watt quartz lamp was placed near the ceiling and behind the apparatus to provide illumination before the start of the test sequence.

2. Instrumentation

Because the primary objective of this test was to study the dispersal of debris and aerosol from the cavity, most of the instrumentation was designed to monitor these phenomena. Table 2 summarizes the instrumentation employed on this experiment.

The pressure gauge inserted into the expansion volume of the melt generator measured the gas pressure in the free space above the melt pool. The device (Kulite Model HEM-375) was placed into a cavity machined in the top flange cover and protected by steel turnings (like heavy steel wool) inserted ahead of the exposed gauge surface. The metal turnings allowed gas to pass freely but prevented molten material from directly contacting the sensing element. The location of the gauge allowed it to measure the initial gas pressure, the increase incurred during the thermite reaction, and the blowdown history following melt ejection.

Table 2

Summary of SPIT-18 Instrumentation

DEVICE TYPE	No.	RANGE	LOCATION	PURPOSE
Pressure	1	0–69 MPa	Gas Source	Reference pressure
Pressure	1	0–69 MPa	Gas accumulator	Gas line pressure
Pressure	1	0–69 MPa	Melt generator	Blowdown
TC	1	0–1500°C	Gas line	Gas into accumulator
TC	1	0–1500°C	Melt generator	Expansion chamber
Pitot-tube	1	–	Cavity exit	Gas velocity
Pressure	1	0–0.069 MPa	IC* wall	IC atmosphere
TC	31	0–1500°C	IC volume	IC atmosphere and wall temperatures
Photometer	1	–	NE IC corner	Aerosol concentraion
Filter	12	–	IC volume	Aerosol mass
Cascade Impactor	6	–	NE IC corner	Aerosol size distribution
Cascade Cyclone	1	–	NE corner	Aerosol size distribution

Table 2 (Continued)

Summary of SPIT-18 Instrumentation

DEVICE TYPE	No.	RANGE	LOCATION	PURPOSE
Deposition Surface	10	–	IC walls	Distributed aerosol
Deposition Sample	6	–	IC N wall and ceiling	Time resolved deposition
Catch Pan	41	–	IC floor	Debris dispersal

* Interaction Chamber

A thermocouple (Type-K with stainless steel sheath) inserted approximately six centimeters into the expansion volume measured the temperature of the gas above the melt. The device was shielded with a 6 millimeter diameter stainless steel tube to survive possible direct deposition of molten material. Small holes drilled into the tube allowed hot gases to penetrate to the thermocouple but large melt globules were intercepted. The design represented a compromise between the protection needed for survival and the degradation in frequency response caused by the addition of the shielding material. Consequently, the response of this device was on the order of several seconds or more, which limited its ability to rapidly achieve thermal equilibrium with the temperature changes occurring in the melt generator.

The pitot-static tube at the exit of the cavity was intended to monitor the dynamic pressure ahead of the dispersed melt. A low-range differential pressure transducer (Validyne DP7 ±1 psid) was connected to the stagnation and static pressure ports of the pitot-static tube. The gas initially in the cavity was expected to be heated by the ejected melt, which caused it to rapidly expand and flow out the exit. In addition, gas in solution with the melt may also have effervesced and contributed to the flow ahead of the melt. The small holes inherent in the construction of the pitot-static tube made it susceptible to damage or plugging by the debris that emerged from the cavity.

Wall temperature measurements in the interaction chamber were important to determine the mechanisms related to aerosol deposition on surfaces. Thermocouples (Type-K 0.8 millimeter diameter) were attached to the wall at regular intervals (one meter spacing) within the chamber to monitor the response of the structure. The temperature increase monitored by these devices was expected to be from both direct exposure to the ejected debris and by heat transfer from the chamber atmosphere. Heating by the atmosphere was expected to be of longer duration than from the debris directly as convective currents developed within the chamber.

The temperature of the gas within the chamber was measured by thermocouples extending from the sidewalls and ceiling. Each probe (Type-K with 3.2 millimeter diameter stainless steel sheath) was positioned so that its sensing junction was located one meter from the adjacent chamber surfaces. The large diameter sheath of these devices insured sufficient mechanical rigidity to withstand the air turbulence expected in the chamber following ejection and blowdown. This construction caused the estimated time constant of the devices to be at least 15 seconds in air.[10] This meant that the long-term temperature history within the chamber was accurately determined, while the rapid transients following debris dispersal were probably distorted.

The devices employed to measure the aerosol generated during the test event are listed in Table 2. The purpose of the devices was to obtain data that would determine the aerosol source term associated with pressurized melt ejection and debris dispersal. This determination required knowledge of the aerosol generation rate, size and mass distributions, aerodynamic characteristics such as shape factor, and chemical composition. These characteristics were considered over the time interval of the experiment in order to quantify the source term.

Filter samplers (Millipore LS Type - 47 millimeter) were placed in the chamber at several locations. Figure 4 shows the relative locations of the filters and other devices in the interaction chamber. The instrument rack depicted in the figure housed the majority of filter samplers. The remainder of the filters were placed on one meter tall stands in the locations shown. Aerosol mass concentration was obtained from these devices by weighing the material collected on the teflon filter media using the period of exposure and mass flow rate through the device. Line losses and the amount of material deposited in the sample line were estimated to be insignificant compared to the quantity of material collected by the filter element.

The number of devices allowed staggering the sample time (by means of electrically controlled valves in the vacuum line that lead to the filter housing) to determine the change in the aerosol mass concentration with time. Placement of the filters in several locations permitted evaluation of the uniformity of the aerosol concentration within the chamber.

Cascade impactors and cascade cyclones were used to separate the collected aerosol into sizes based on aerodynamic diameter. Typically, six or seven size ranges were obtained with a single device. Collection efficiencies were lowest for the large (>10 micrometer) particle range. Two impactors were mounted on a rotating framework to cause the tangential velocity of the sampler inlet to be nearly equivalent to the inlet velocity. This method of isokinetic sampling[11] was intended to improve the collection efficiency for the large particles. Four of the impactors were mounted in an instrument rack and were operated simultaneously. Two were run at a nominal flow rate of 14 L/min while the other two were at 5 L/min. Comparison of the size distributions from the various devices showed whether the inlet sampling efficiency varied with flowrate.

The cascade impactors were principally intended to give size distributions of the suspended material. The devices (Andersen Mk-II) were efficient in collecting particles in the size range of less than 10 micrometer aerodynamic diameter, yielding distribution information in the range of approximately one-tenth
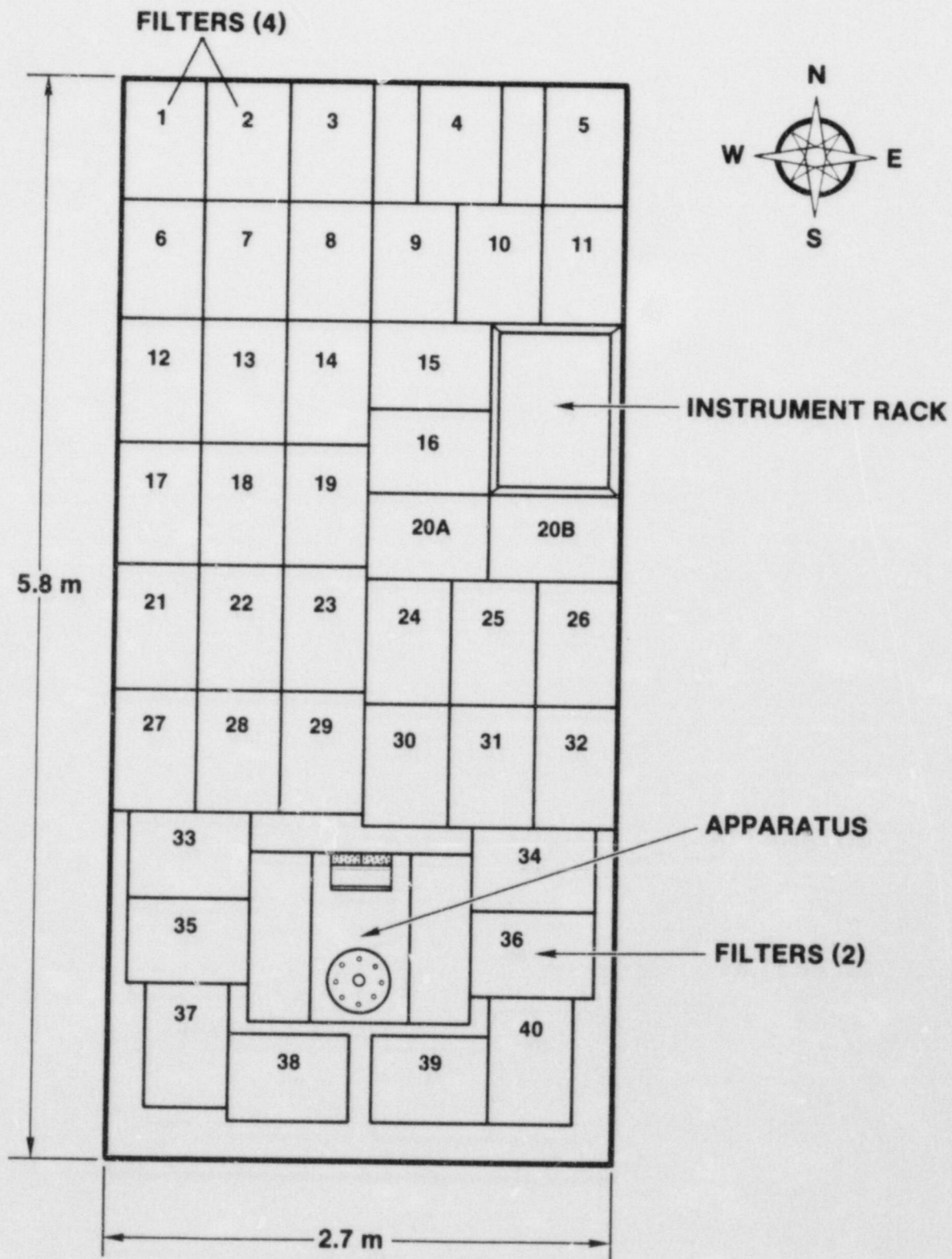
FIGURE 4. CATCH PAN ARRANGEMENT FOR SPIT-18 EXPERIMENT

micrometer diameter to ten micrometer diameter. Each device had eight collection stages followed by a backup filter to retain the smallest particles. A preseparator was also used to remove particles larger than ten micrometer aerodynamic equivalent diameter. Table 3 gives the cut sizes of the preseparator and each stage for the two flow rates used on the tests, the cut sizes for the six stages of the cascade cyclone are also given. The calibration data of Cushing[12] and McFarland[13] were used to determine these cut sizes.

Table 3
Particle Cut Sizes for Cascade Impactors
and Cascade Cyclones

| | Aerodynamic Equivalent Diameter (micrometer) | |
Stage	5 L/min	14 L/min
Impactor		
Preseparator	10.2	10.5
1	*	*
2	*	*
3	*	6.5
4	7.4	4.4
5	4.1	2.5
6	1.92	1.13
7	1.24	0.72
8	0.74	0.42
Backup Filter	0	0
Cyclone		
-10		15.0
-1		8.6
-2		4.6
-3		2.6
-4		1.5
-5		0.9
Backup Filter		0

* Cut size larger than that removed by the preseparator.

The construction of the cascade cyclone (Sierra Series 280) allowed it to obtain a larger sample, nominally hundreds of milligrams per stage compared to less than fifteen milligrams per

stage for the cascade impactor. The cyclones were operated for a much longer period of time (relative to an impactor) before the device became overloaded. Material from the cascade cyclones will be analyzed for chemical composition using PIXE (Photon Induced X-ray Emission) or inductively-coupled atomic absorption (ICP) analysis. Because the material will be consumed when using these techniques, the large sample from the cascade cyclone will be required.

Deposition surfaces were constructed using standard glass microscope slides (Corning Glass Works – 75 x 38 x 1 mm). The slides were mounted on the ceiling and walls of the interaction chamber so that they collected aerosol particles as they settled out of the atmosphere. Deposition samplers were made using glass slides mounted in a fixture that allowed exposure of individual surfaces at specified periods of time. The technique permitted the surface deposition mass concentration to be obtained from each sampler. Comparing the data from all the samplers provided the time-resolved surface mass concentration and deposition rate, and provided an indication of deposition mechanisms.

Large aluminum pans (46 by 66 centimeter) were placed on the floor of the interaction chamber to collect the debris dispersed from the cavity. Figure 4 shows a schematic of the pan placement before the test. Over 85% of the exposed floor area was covered by the pans, with the remainder mostly in the vicinity of the apparatus where complete pans could not be used. The purpose of the pans was to permit segregating the dispersed mass by location to evaluate the propensity for material to congregate.

Cabling from the instrumentation was connected to recording devices placed in a control center located approximately 20 meters from the interaction chamber. Slow responding units such as thermocouples and aerosol devices were monitored by a scanning electronic voltmeter (Hewlett-Packard Model 3497A) controlled by a desk-top computer (Hewlett-Packard Model 9845B). A complete scan of all channels was taken once every six seconds, and then converted to engineering units using calibration specifications. The data were stored on the computer's internal hard-disk drive. The information was subsequently manipulated and plotted using the same device.

A reel-to-reel tape recorder (Honeywell Model 101) with a 10 kilohertz bandwidth was employed to monitor the faster responding sensors such as pressure transducers and the photometer. These data were later played back through a computer interface for presentation as discrete points or plots.

3. Initial Conditions

The experimental technique used on the SPIT-18 test allowed a number of important variables to be established before the start of the thermite reaction. Several of these variables (melt mass, melt composition, gas composition, aperture diameter, and ambient pressure) were significant in determining the results from the experiment. Table 4 summarizes the initial conditions employed for the SPIT-18 experiment.

Table 4
SPIT-18 Initial Conditions

Melt Mass	10.3 kg
Thermite Composition	Iron Oxide (Fe_3O_4) - 7.63 kg plus Aluminum (Al) - 2.37 kg
Melt Composition	Iron (Fe) plus Alumina (Al_2O_3)
Dopants	Barium Molybdate ($BaMoO_4$) - 0.2 kg plus Lanthanum Oxide (La_2O_3) - 0.1 kg
Gas	Dry Bottled Nitrogen (N_2)
Gas Volume	0.032 m^3 (including accumulator)
Initial Pressure	10.6 MPa
Ambient Temperature	13°C
Fusible Plug Diameter	2.5 cm

The iron oxide and aluminum were obtained in powder form and mixed just prior to the experiment. The producer of the iron oxide (Type MS-30 Chemalloy Company, Bryn Mawr, PA) guaranteed that the material had less than 1% impurities and a particle size range of 74 to 600 micrometer (sieve size: 100% minus 60 mesh, 40% max minus 325 mesh). Sieving the as-received material has shown a significant amount (up to 35 w/o) of the particles fall below the minimum size. Batches of the material with more than 10 w/o of sub-size particles were rejected. The iron oxide powder was heated in an oven for four hours at 600°C to drive off absorbed water. This process was designed to minimized hydrogen

gas generation and associated flaring during the thermite reaction. The finely divided aluminum was obtained in a nodular form from Alcoa (Powder #101 Aluminum Company of America, Pittsburgh, PA). The typical batch contained less than 0.3% impurities, mostly in the form of iron and silica. The aluminum powder was used in the as-received condition. The powders were mixed just prior to charging into the melt generator.

The four mechanisms believed responsible for the dispersal of debris (film entrainment, particle levitation, film sweepout, and splashout) from the reactor cavity were considered to be directly dependent on the pressure of the gas in the reactor pressure vessel.[2] The amount of material removed was assumed therefore to be determined by the initial system pressure and the period of time that the blowdown gases were capable of dispersing material. In a reactor accident, the upper bound of system pressure is fixed by the setting of the primary relief valves, approximately 17 MPa for pressurized water reactors (PWR). Because the goal in this test was to study debris dispersal at conditions near the upper end of the operating range, the pressure level in the SPIT-18 test was desired to be at the melt generator vessel's maximum value (14 MPa). The initial pressure level selected allowed for the potential pressure increase caused by heating of the gas during the thermite reaction.

Fission product simulants (dopants) were added to the thermite mixture to aid in determining the aerosol source term. These materials did not contribute exothermally to the thermite reaction, so their presence lowered the ultimate melt temperature achieved. For this reason, only a limited amount of inert material was employed in the composition. In this test, the mass of the dopants was limited to 300 grams (200 grams of $BaMoO_4$ and 100 grams of La_2O_3) to provide information on release of barium, lanthanum, and molybdenum. If the 100 gram brass fusible plug was included, it added about 1.0 w/o of copper and 0.5 w/o of zinc. The extent to which the plug was mixed and dispersed with the ejected melt was unknown.

Studies have indicated that hydrogen and steam may be soluble under high pressure in the molten core debris found in a reactor pressure vessel.[14] Bottled nitrogen was used as the driving gas in this test because it was considered highly soluble in the iron based melt.[15] As the molten material entered the cavity region, the effervescence of the dissolved gas caused disruption of the jet geometry. The gas may then be expected to expand out of the cavity region, causing the removal of melt particles. This mechanism and others responsible for debris dispersal are discussed in more detail in a Section III.E.

B. SPIT-19

The objective of the SPIT-19 test was to determine the extent of debris dispersal from a scaled (1:20) model of the Zion reactor cavity. The design was based on the internal geometry of the Zion cavity,[16] except some equipment details were omitted.

1. Apparatus

The SPIT-19 experiment was virtually identical to SPIT-18 except in the construction of the cavity. The apparatus for this test was designed to be an accurate representation of the geometry of the Zion nuclear power plant. A schematic of the cavity is shown in Figure 5. All of the linear dimensions were a 1:20 reduction of those found in the actual plant. For this test, the lower melt generator flange cover was replaced by a steel plate cast into the concrete that formed the cavity. The position of the plate corresponded to the scaled distance from the bottom of the RPV to the cavity floor in the Zion plant.

The model accurately depicted the major geometric details of the cavity, but mechanical features such as the instrument tubes, ladders and catwalks, and the cavity sump were not included. The annular gap around the RPV was not incorporated into the model. The cavity was constructed of prototypic limestone-common sand concrete,[16,17] that was allowed to air cure for thirteen months. It was constructed in two sections with a horizontal parting line along a plane defined by the tunnel ceiling. Long bolts inserted through tubes embedded in the concrete held the two halves securely together. Separating the two halves permitted access to the cavity following the test. The small vertically-oriented tube inserted into the tunnel near the junction with the upward slanted section was for measuring cavity pressure.

A schematic drawing showing the SPIT-19 apparatus placed in the interaction chamber is given in Figure 6. The chamber arrangement was similar to the SPIT-18 test except that the fans were moved to avoid the debris that emerged from the cavity. Several additional view ports were included (not shown on the drawing) to increase the camera coverage. A 600 Watt quartz lamp was placed near the ceiling of the chamber and behind the apparatus to provide illumination prior to the start of the ejection sequence. The lamp was not expected to survive if impacted by debris. The chamber was also modified to use flash X-ray equipment to monitor the material emerging from the cavity exit.

FIGURE 5. DIMENSIONS AND DETAILS OF SPIT-19 CONCRETE CAVITY
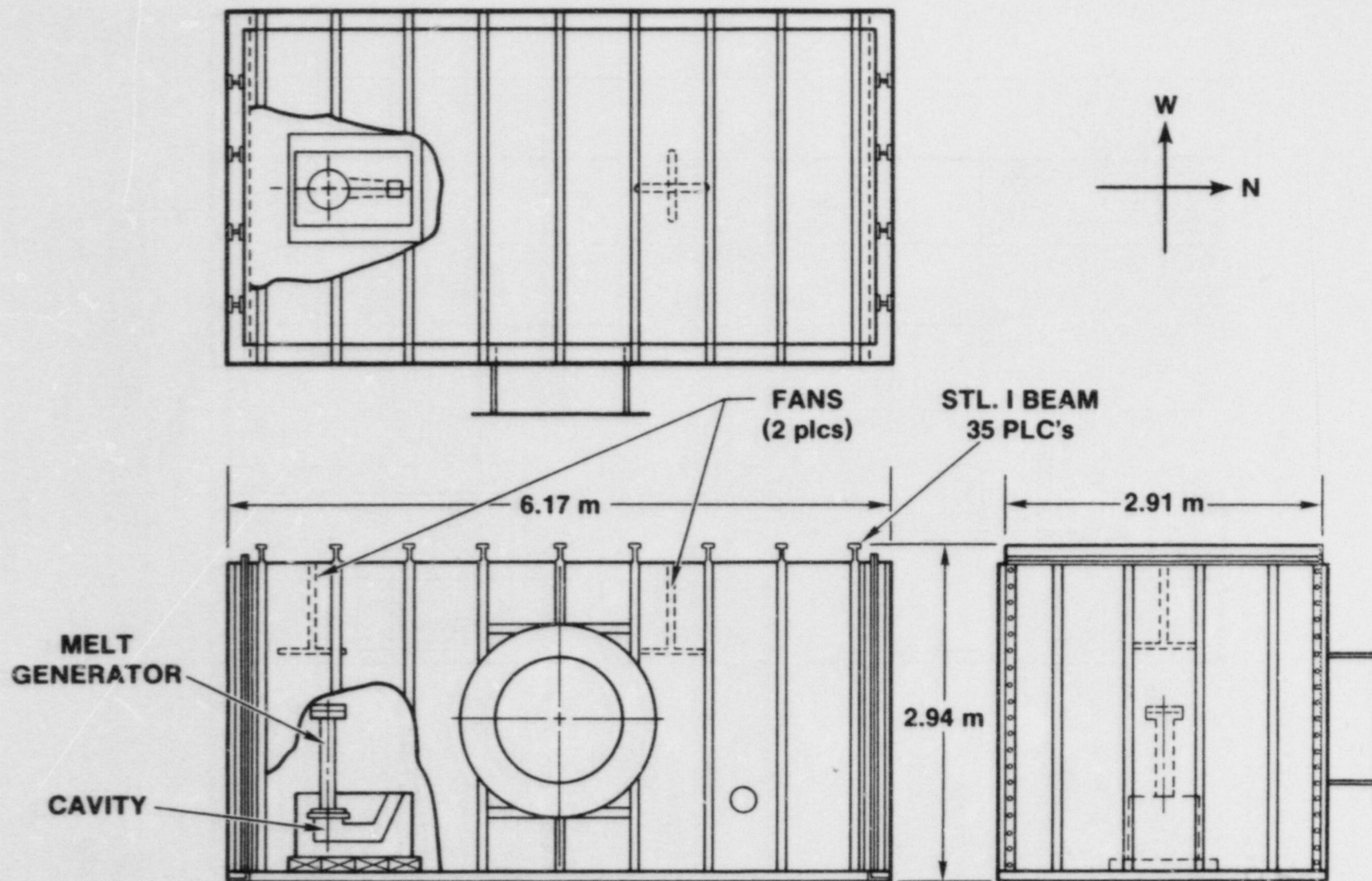
FIGURE 6. SCHEMATIC OF SPIT-19 APPARATUS PLACED IN THE INTERACTION CHAMBER

2. Instrumentation

Like SPIT-18, the instrumentation for this test was directed towards monitoring the extent of debris dispersal and aerosol generation. In addition, thermocouples and pressure gauges were used to study the response of the chamber atmosphere during the debris dispersal. A summary of the SPIT-19 instrumentation is given in Table 5.

The pressure transducer (Precise Sensors Model 111-2) placed in the melt generator expansion volume used water cooling to minimize errors induced by the high temperature of the gas. The device measured the pressure of the gas above the melt and the blowdown history following ejection. The natural frequency of the gauge was listed by its manufacturer as 70 hertz, which was considered more than adequate to resolve the estimated 500 to 1500 millisecond blowdown period. The remaining two pressure transducers (Kulite Model HEM-375) were placed in adjacent locations to provide confirmatory information.

The temperature of the gas above the melt and in the connecting line to the accumulator was monitored by thermocouples (Type-K with stainless steel sheaths) inserted into the melt generator expansion volume and gas line. The melt generator sensor was heavily shielded as in SPIT-18 to withstand direct melt deposition. The time constant of the thermocouple and shield in air was between 1 and 4 seconds based on estimates from a previous applications.

The interaction chamber was instrumented with thermocouples (Type-K with stainless steel sheaths) that measured the temperature change of both the atmosphere and structure. The atmospheric sensors were inserted through the walls and ceiling to a point one meter from adjacent surfaces. Because the overall height and width of the interaction chamber were each approximately three meters, the thermocouple arrays established two horizontal planes, one and two meters from the floor, respectively. The diameter of the thermocouple sheath (3.2 millimeters) provided mechanical rigidity to the unsupported devices. The response of these devices in air was estimated to be on the order of 1 to 4 seconds.[10]

The interaction chamber sidewalls were fitted with small sheathed thermocouples (Type-K with 1.6 millimeter diameter stainless steel sheath) placed in tube-compression fittings mounted flush with the inside surface. The good mechanical contact between the sheath, fitting, and wall insured that the devices accurately measured the induced surface temperature. The locations of these sensors corresponded to the junction of the atmospheric thermocouples projected into the three coordinate directions, except in the vicinity of the instrumentation port where sensors could not be mounted.

Table 5

Summary of SPIT-19 Instrumentation

TYPE	DEVICE NO.	RANGE	LOCATION	PURPOSE
Pressure	1	0-69 MPa	Gas source	Reference pressure
Pressure	1	0-41 MPa	Melt generator	Blowdown
Pressure	1	0-69 MPa	Accumulator	Gas line
Pressure	4	0-0.069 MPa	IC* walls and ceiling	IC Pressure
TC	1	0-1500°C	Melt generator	Gas temp above melt
TC	1	0-1500°C	Gas line	Reference
TC	24	0-1500°C	Cavity	Concrete temp
TC	29	0-1500°C	IC walls and ceiling	Chamber wall temp
TC	11	0-1500°C	IC atmosphere	Gas temperature
TC	1	0-1500°C	Melt plug	Event timing
Pitot tube	1	–	Cavity	Gas velocity
Flash X-ray	3	–	Cavity exit	Debris character
Pyrometer	1	1500°C-3500°C	Cavity exit	Debris temperature
Photometer	1	–	NE corner IC	Aerosol concentration

Table 5 (continued)

Summary of SPIT-19 Instrumentation

DEVICE TYPE	NO.	RANGE	LOCATION	PURPOSE
Filter	18	–	IC volume	Mass distribution
Cascade Cyclone	1	–	IC volume	Size distribution
Impactor	6	–	IC volume	Size distribution
Deposition	6	–	North-end IC	Time resolved deposition sample
Deposition	12	–	IC walls and ceiling	Total deposition surface
Catch Pan	40	–	IC floor	Debris collection

* Interaction chamber

Thermocouples placed at various depths in the concrete cavity were designed to measure the response to melt impinging on or flowing over the exposed surfaces. By correlating the temperature of the concrete versus depth, the incident heat flux was estimated.[18] Small diameter sheathed thermocouples (Type-K with 1.6 millimeter diameter stainless steel sheaths) were embedded in the concrete in arrays at several locations as depicted in Figure 7. The right-angle curvature of the thermocouples was used to minimize the potential error induced by heat conducted away from the sensing junction by the relatively high thermal conductivity (compared to the surrounding concrete) of the metallic sheath. Locational accuracy of the sensing junctions was estimated to be 1 millimeter.

A pitot-static tube sensor was located in the tunnel portion of the cavity measured the dynamic pressure exerted by the gas flow. It was primarily intended to measure the gas ahead of the melt caused by heating of the cavity atmosphere and the effervescence of dissolved gas. The device was placed along the centerline of the tunnel, approximately 2.5 centimeters from the ceiling. The connecting tubing was routed between the two cavity sections to a differential pressure transducer (Validyne DP7 ±5 psid). The response of this system to a step change in flow velocity was estimated to be on the order of 50 milliseconds. The relatively fragile construction and small openings of the device limited its usefulness after melt arrival.

The brightness of the material emerging from the cavity reduced the value of photographic film as a diagnostic for determining the character of the dispersed debris. Radiographs of the molten material were valuable because the resulting records were not obscured by the enveloping aerosol cloud or blinded by the radiated light. The flash X-ray (Hewlett Packard Model KC-150, 150 keV) technique was particularly useful because the inherent short exposure times (70 nanoseconds) essentially "froze" the motion of even the fastest particles.

Figure 8 is a photograph of the SPIT-19 apparatus showing the position of the X-ray film cassettes near the cavity exit. The aluminum cassettes were insulated with a refractory blanket material to protect the film from the hot debris. The X-ray generators corresponding to each cassette were located just outside the interaction chamber (source to target distance- ~2 m, target to cassette distance- ~0.8 m), directed through windows made of relatively low X-ray adsorbing material. The center cassette was placed to give a view orthogonal to the direction of the flowing debris. The remaining two cassettes on either side of the center unit yielded somewhat oblique views of the emerging stream. The X-ray units were triggered by a breakwire placed across the exit opening. Each generator head

DETAIL "A"
(6 PLC's)
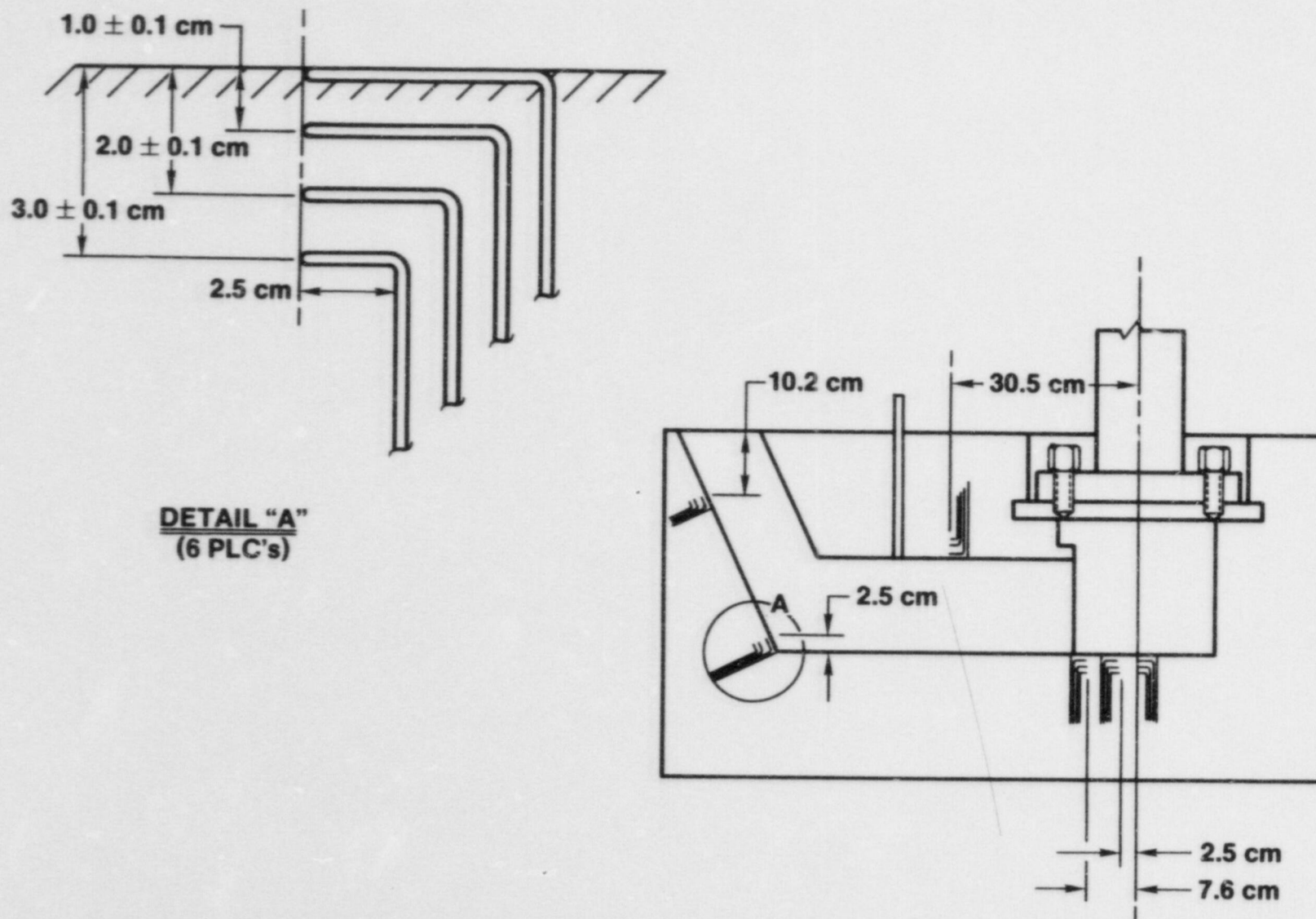
FIGURE 7. THERMOCOUPLE ARRANGEMENT IN SPIT-19 CAVITY
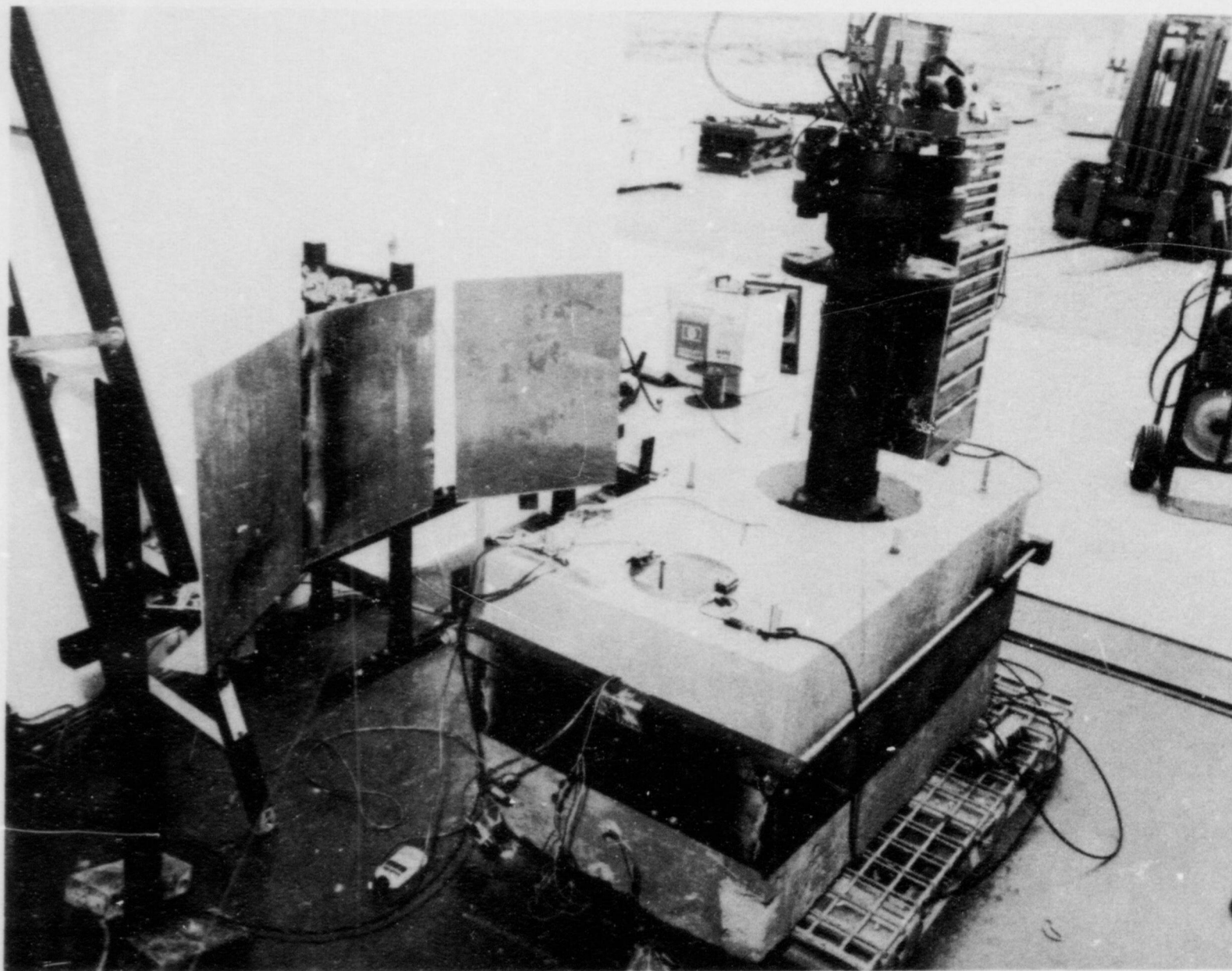
FIGURE 8. PRE-TEST PHOTOGRAPH OF SPIT-19 APPARATUS SHOWING PLACEMENT OF X-RAY CASSETTES

was then fired at a predetermined delay interval (15, 45, and 99 milliseconds) after receipt of the signal from the breakwire. It was estimated that film and geometric unsharpness combined limited the resolution to no better than 0.3 millimeters.

A two-color pyrometer was directed at the cavity opening to measure the temperature of the debris as it emerged. The manufacturer of the device (Ircon Model R-35C10) claimed a useful range of 1500°C to 3500°C and a time constant of 10 milliseconds. The device assumed that the target material behaved as a gray body, so that the ratio of transmitted energies yielded temperature directly without the need for emissivity corrections. This feature also reduced the influence of intervening, semi-transparent materials such as dust or smoke. The pyrometer was placed outside the interaction chamber, aimed alongside the melt generator at an angle of 30° from horizontal. The circular target area at this distance was on the order of 2.5 centimeters, or well within the characteristic length of the cavity opening.

Two photometers designed by the experimeters were used to measure the aerosol mass concentration by monitoring the attenuation of a light beam by airborne particles. The attenuation measurement was also correlated to the aerosol mass concentration as measured by the filter samples. Both photometer devices on this test withdrew samples from the chamber atmosphere through a channel (nominally 2 or 5 centimeters in diameter) at a known flow rate. The aerosol laden stream was caused to pass between a white-light source and a photodetector to obtain the amount of attenuation caused by the particles. Filter samples were taken at discrete times to obtain other mass concentration measurements and provide in-situ calibration of the photometers.

The catch pan arrangement for this test is shown in Figure 9, along with the locations of the aerosol detection devices. The pans were intended to collect the debris that was dispersed from the cavity during the experiment. The forty pans covered an estimated 60% of the total floor area, or 84 percent of the available area excluding the apparatus and instrumentation rack. The majority of the aerosol devices were placed in the instrument rack. Only the two rotating impactors and six filters were in the other locations (Figure 9).

3. Initial Conditions

The initial conditions of the SPIT-19 test were intended to duplicate those employed during the SPIT-18 experiment. Other than the cavity design, the principle difference in the SPIT-19 test was a modification to the gas supply system to prevent flow reversal from the accumulator into the melt generator. In the previous test, the pressure increase during the thermite reaction
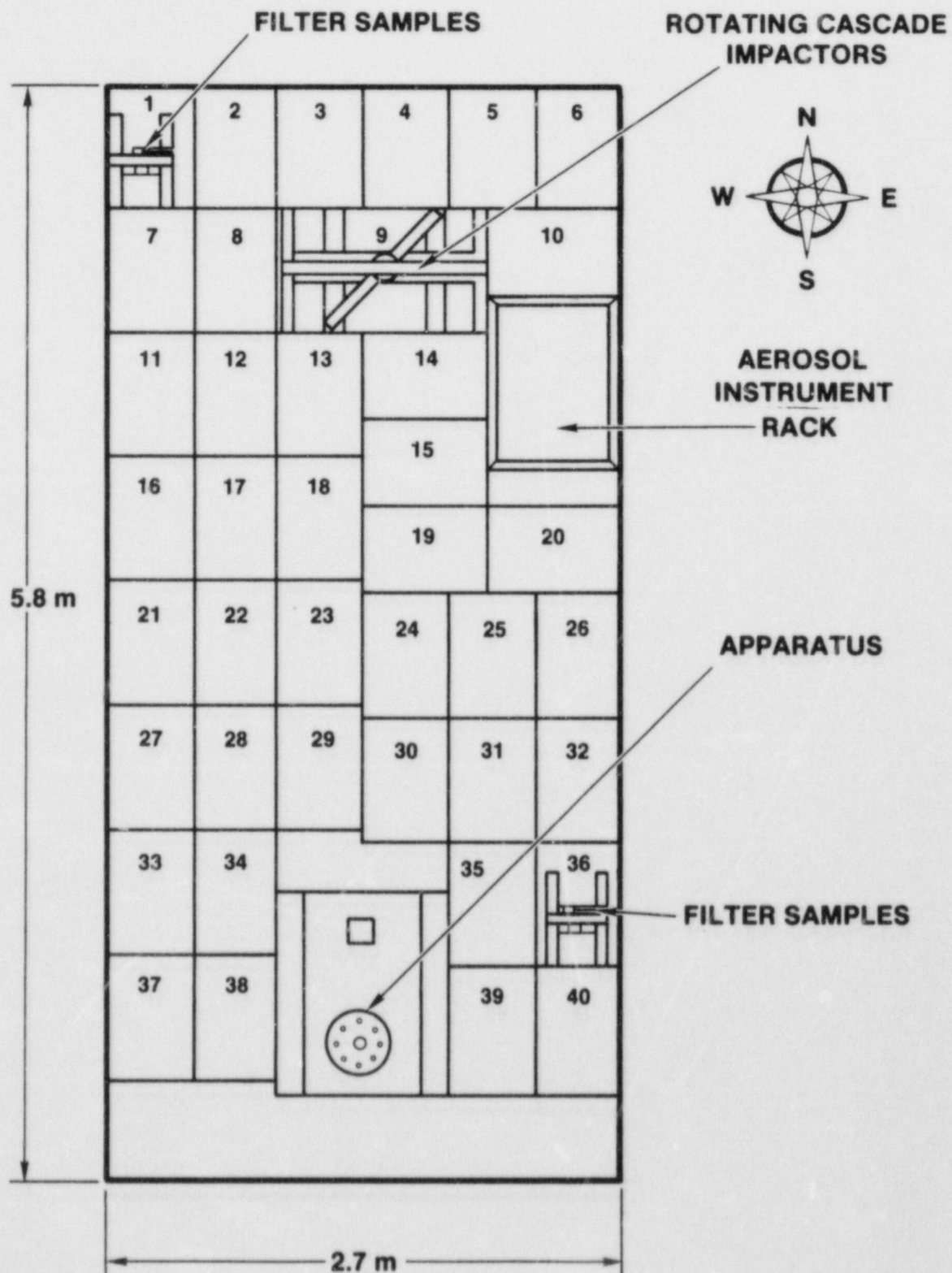
FIGURE 9. PLACEMENT OF CATCH PANS FOR THE SPIT-19 TEST

was partially absorbed by the large volume of the accumulator, but the gas then discharged back into the melt generator after melt ejection, potentially contributing to debris dispersal late in the sequence. For the SPIT-19 test, a check valve was placed between the melt generator and the accumulator to close when the flow direction changed. In this manner, the volume of gas involved in the blowdown process was effectively only that within the melt generator itself. Table 6 lists the initial conditions for the SPIT-19 test.

Table 6
SPIT-19 Initial Conditions

Melt Mass	10.3 kg
Thermite Composition	Iron Oxide (Fe_3O_4) - 7.63 kg plus Aluminum (Al) - 2.37 kg
Melt Composition	Iron (Fe) plus Alumina (Al_2O_3)
Dopants	Barium Molybdate ($BaMoO_4$) - 0.2 kg Lanthanum Oxide (La_2O_3) - 0.1 kg
Gas	Dry Bottled Nitrogen (N_2)
Gas Volume	0.0027 m^3 (not including accumulator)
Initial Pressure	10.8 MPa
Ambient Temperature	9°C
Melt Plug Diameter	2.5 cm

C. HIPS-2C

The objective of the two HIPS experiments was to study debris dispersal at a larger scale than the previous SPIT tests. The HIPS experiments were similar to the SPIT tests except that the cavity was based on a 1:10 scale of the Zion plant. The HIPS melt generator was designed to create 80 kg of material with a gas volume roughly scaled to the actual primary system. Several refinements were also incorporated in the design of the HIPS equipment as a result of the experience gained during the SPIT experiments.

1. Apparatus

The HIPS experimental apparatus consisted of a melt generator and concrete cavity. The interaction chamber described in the previous sections was not used because it sustained considerable damage during the SPIT-19 experiment and it was too small to contain the expected overpressure from direct atmospheric heating. The larger melt mass of the HIPS experiments necessitated a new melt generator with the resulting design shown schematically in Figure 10.

One difficulty with the SPIT melt generator was that the available volume for gas underscaled the reactor coolant system. This problem was eliminated in the HIPS generator as the dimensions of the new device represented a factor of eighteen increase in the gas volume. This allowed eliminating the accumulator and associated plumbing required on the two previous SPIT tests. As seen in Figure 10, the HIPS melt generator was constructed of a mild steel pipe casing (41.1 centimeter diameter by 156.7 centimeter long) with bolted flanges welded to each end. The lower flange cover was machined to accept a replaceable insert that retained the fusible melt plug.

The thermite melt crucible was made from a 76 centimeter long by 25.4 centimeter diameter steel pipe section (6 millimeter wall thickness). Graphite plates, 1.2 centimeters thick, were placed at each end of the crucible pipe section to protect the other parts of the melt generator. The annular gap between the inner and outer pipe sections was filled with an alumina refractory dry ram (Inductogrog No. 150 Inductotherm Corp. Rancocas, NJ) material to a height above the initial level of the thermite.

The dimensions of the HIPS concrete cavity were based on a 1:10 linear scaling of the Zion nuclear plant. The major geometric details were accurately reproduced to insure correct gas and debris flow patterns. Some details, such as instrument tubes, catwalks and ladders, and the cavity sump were not considered significant contributors to the debris dispersal processes and were not included in the model. A schematic drawing showing details and dimensions of the HIPS cavity is given in Figure 11. The upward slanted section (26 degrees from vertical) terminated at a level that corresponded to the floor of the containment building.

The external dimensions of the cavity provided an adequate concrete thickness in all areas that could potentially be eroded by the impinging melt. The cavity was formed in two sections with a parting surface along the plane of the upper tunnel
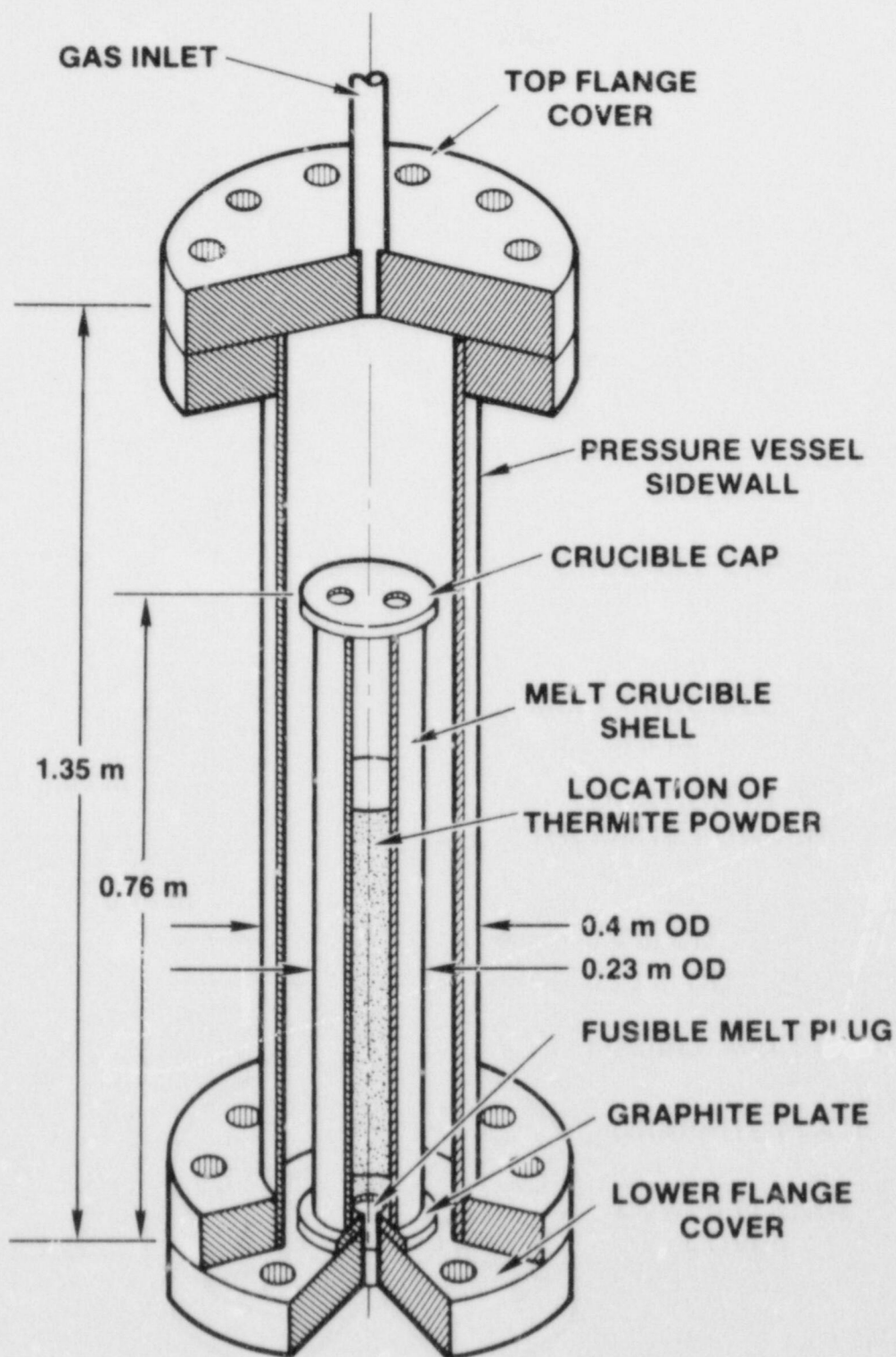
FIGURE 10. SCHEMATIC OF MELT GENERATOR USED FOR THE HIPS EXPERIMENTS
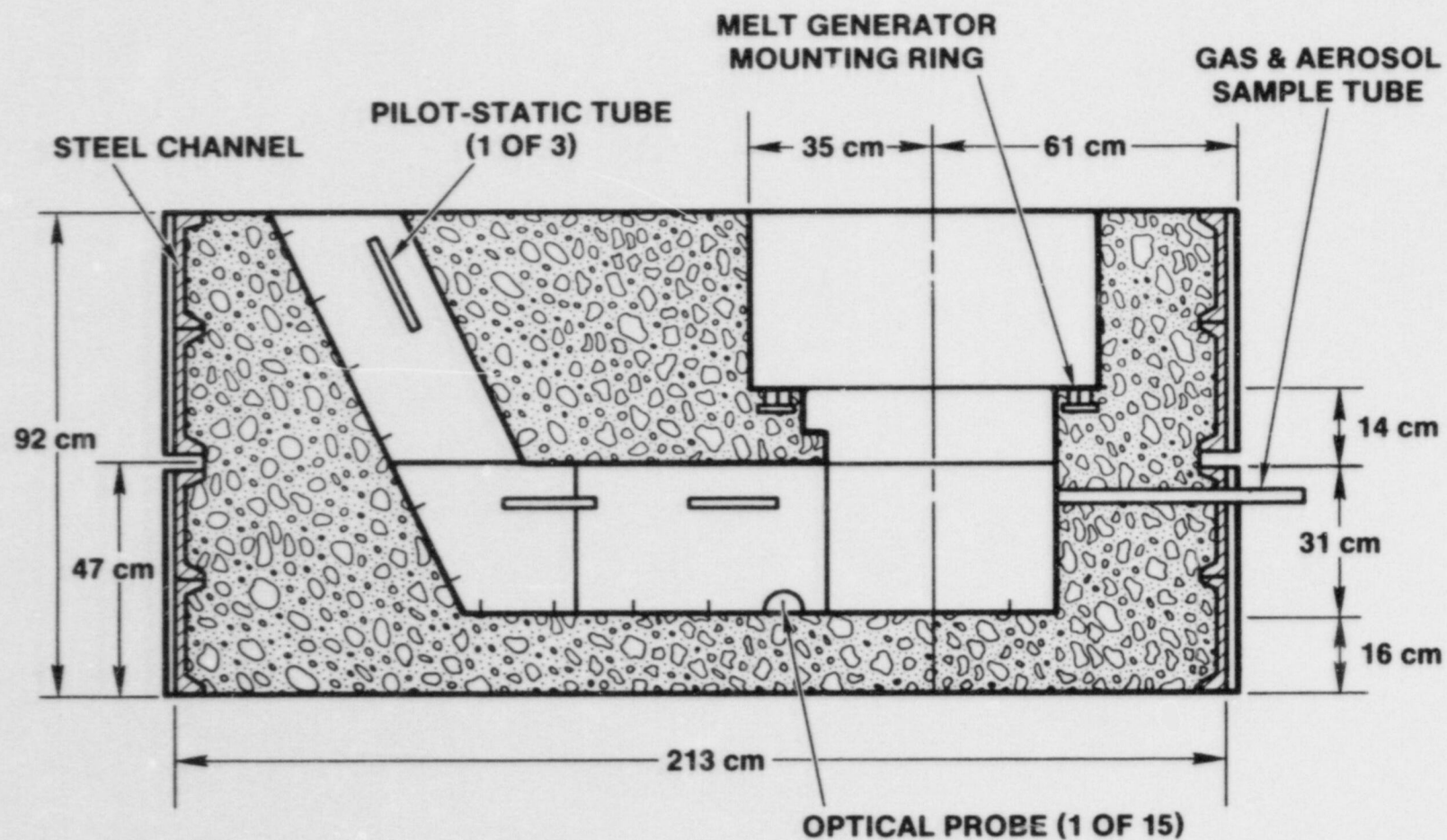
FIGURE 11. DETAILS OF THE HIPS CONCRETE CAVITY

surface. Each section was made using large steel channel members welded together to form the outer periphery. The steel provided additional strength and a convenient form for the concrete placing operation. The cavity was made with a limestone/common sand concrete similar to that used at the Zion plant.[16,17] Several reinforcing steel members were placed in the base of the cavity (approximately 8 centimeters from the floor surface), primarily to strengthen the structure for handling.

The cavity incorporated an embedded steel ring with attached nuts to mount the melt generator. The distance from the melt plug to the cavity floor was scaled based on the RPV to floor dimension. When the melt generator was in place, the lower flange cover effectively sealed the cavity opening. The cavity sections were connected together with a total of sixteen 12.5 millimeter diameter bolts inserted through tubular sleeves welded to the steel channel members.

2. Instrumentation

A summary of the HIPS-2C instrumentation is given in Table 7. Pressure gauges were placed in the top flange cover of the melt generator to obtain the pressurization and blowdown histories. The primary device was a water cooled gauge (Precise Sensors Model 111-2) placed in a machined recess filled with steel turnings to protect the sensing element. Another gauge (Kulite Model XT-190) was located in a less hostile position in the gas line near the melt generator. The second device provided a backup in the event that the primary device was affected by the heat flux from the molten pool formed during the thermite reaction. Two thermocouples were inserted through the flange cover to a depth of approximately 30 centimeters to monitor the temperature of the gas above the melt. One sensor had a 3.2 millimeter diameter stainless steel sheath while the other was a 1.7 millimeter diameter sheath unit inserted into a 6 millimeter diameter stainless steel tube. Small diameter holes (0.5 millimeter diameter) in the steel tube allowed the hot gases to reach the sensor while protecting against possible contact with debris.

The results of the previous SPIT tests indicated that very few conventional diagnostic devices were capable of surviving the hostile cavity environment during the melt ejection process. Consequently, many of the instruments employed in the HIPS-2C test were developmental or were intended to function only a short time. Thermocouples (1.7 millimeter diameter stainless steel sheath) were installed in the cavity at the fusible plug, on the floor directly beneath the aperture, and at the cavity exit. The intent of these devices was to provide an indication of the position of the debris within the cavity. The time interval

between the response of each device was used to determine debris velocity. Aerosol instrumentation was not used because the lack of a confining volume prevented making definitive measurements.

Table 7
Summary of HIPS-2C Instrumentation

DEVICE TYPE	NO.	RANGE	LOCATION	PURPOSE
Pressure	1	0-34.5 MPa	Gas line	Reference
Pressure	1	0-41.4 MPa	Melt generator	Blowdown
TC	2	0-1500°C	Melt generator	Gas temperature
TC	1	0-1500°C	Melt plug	Timing
TC	24	0-1500°C	Cavity	Concrete temp
TC	1	0-1500°C	Cavity exit	Event timing
Pitot Tube	3	±30 psid	Tunnel	Gas velocity
Pyrometer	1	1500°C-3500°C	Cavity exit	Debris temp
Pyrometer	1	1700°C-4000°C	Cavity Exit	Debris temp
Flash X-ray	6	-	Cavity exit	Debris character
Catch Pan	18	-	Downrange	Debris collection
Cameras	12	30-400 fps*	-	Observation

* fps - frames per second

Two pyrometers were used to measure the temperature of the debris as it emerged from the cavity exit. The first of these devices was the same as described for the SPIT-19 experiment, a two-color unit with a 10 millisecond response time (Ircon R-35C10). The second pyrometer was a single-wavelength device using a photomultiplier tube for the sensing element (Thermogage

Inc.- Serial Number 2589). The response of this unit was significantly faster, on the order of one microsecond. The device was incorporated into the test to determine if rapid variations in the debris temperature occurred during propagation of the debris. Because the emissivity of the molten material was uncertain, the data from this device were somewhat uncertain in magnitude.

Three pitot-static tubes were employed on this test in the tunnel region and inclined portion of the cavity. Each device was connected to a differential pressure transducer (Validyne DP 7±30 psid) to record the velocity of the gas through the tunnel. As previously indicated, these units were expected to be damaged or destroyed during the period of melt discharge.

Catch pan arrays were placed at 15 meter intervals from the cavity to collect debris that was dispersed and subsequently settled to the ground. Six pans were placed at each of four locations along the expected flightpath of the debris stream.

The larger geometry of the HIPS cavity compared to the SPIT apparatus and the absence of the confining chamber allowed more flexibility in the use of X-ray equipment. For this test, six cassettes in two rows were used at the exit region of the cavity. The upper row was above and slightly downrange from the bottom row to account for the angle of flight of the debris stream. The two X-ray systems (150 keV and 300 keV) were triggered by a breakwire across the exit opening that gave a predetermined time delay for each unit (15, 30, 60, 100, 150, and 250 milliseconds). Because the mean dimension of the debris stream in the HIPS geometry was larger than in the SPIT tests, the resolution of the radiographs was affected somewhat by the larger distance between the film cassette and the respective X-ray generator. The combined lack of definition and focus was estimated to be on the order of 0.5 millimeter.

The thermocouples placed in the SPIT-19 cavity showed that very little heat propagated into the concrete from the exposed surface. The limited time the debris remained in the cavity before being expelled prevented extensive propagation into the concrete. Similar sensor arrays were used in the HIPS-2C cavity in the event that debris might be held up in the cavity and not completely dispersed.

The signals from the sensors were recorded on a reel-to-reel tape recorder (Honeywell Model 101) for the faster response devices (pressure gauges and pyrometers) while the voltage scanner (Hewlett Packard 3497A) was used for the thermocouples and backup transducers. A total of eleven high-speed and video cameras were employed to record the test event. Camera speeds

were established in a range from 30 (video) to 2000 frames per second (framing camera) to optimize the resolution of the data. The position and view (close-up or wide-angle) were also different to optimize the return of useful information.

3. Initial Conditions

The initial conditions for the HIPS-2C experiment were similar to those used in the SPIT-18 and SPIT-19 tests. The initial pressure level prior to ignition was set lower; however, because the pressure increase induced by the larger quantity of melt was not known. A summary of the HIPS-2C initial conditions is given in Table 8.

Table 8
HIPS-2C Initial Conditions

Melt Mass	80.0 kg
Thermite Composition	Iron Oxide (Fe_3O_4) - 61.04 kg plus Aluminum (Al) - 18.96 kg
Melt Composition	Iron (Fe) plus Alumina (Al_2O_3)
Dopants	None
Gas	Dry Bottled Nitrogen (N_2)
Gas Volume	0.0815 m^3
Initial Pressure	7.4 MPa
Ambient Temperature	11°C
Melt Plug Diameter	2.5 cm

D. HIPS-5C

The objective of the HIPS-5C experiment was to investigate the lower bounding condition for debris dispersal. It differed from the HIPS-2C in that low pressure carbon dioxide gas was used to pressurize the melt generator. Carbon dioxide was known to

-38-

have a much lower solubility than nitrogen in the reacted thermite composition.[15] By reducing the amount of gas in solution, the extent of debris fragmentation and the potential for dispersal by gas effervescence was minimized. Consequently, debris dispersal in this test was anticipated to be principally caused by the influence of the blowdown gas from the melt generator.

1. Apparatus

The HIPS-5C apparatus was virtually identical to that used in the HIPS-2C experiment except that the HIPS-5C cavity had a magnesium oxide brick lining on the upper tunnel surface. This was a result of modifying a cavity previously intended to have a brick lining on all of the exposed surfaces. The bricks were removed and replaced (except where noted) with limestone-common sand concrete. The small sections of magnesium oxide remaining in the tunnel were not considered to significantly alter the phenomena taking place during the melt ejection process.

For this test, the fusible brass plug in the melt generator lower flange was larger than that used in HIPS-2C (4.8 versus 2.5 centimeter diameter). In addition, a graphite plate placed around the plug was designed to minimize additional ablation of the hole during the melt ejection process. These modifications were intended to reduce the influence of aperture initial size and growth on the debris dispersal processes. Limiting the hole ablation permitted the assumption that the mass flow rate was nearly constant with time, simplifying the analysis of the experiment. The insert plate was also made larger in diameter, 30.5 versus 14.0 centimeters, to avoid ablation of the flange cover during melt ejection. The larger diameter required that the plate be made of thicker stock (5.1 centimeter) to provide the necessary strength at high vessel pressure.

It was observed during the HIPS-2C experiment that a large quantity of insulating powder from the melt generator was carried into the cavity by the blowdown gas. While this did not jeopardize the results of the test, it was undesirable. For this test, a two-centimeter thick magnesium oxide refractory coating (K/R-Cast 98 Kaiser Refractories Oakland, CA) was placed inside the steel melt crucible. The coating was formed within the existing pipe section using a smaller diameter steel shell made from 20-gauge metal sheet. The resulting annular gap was filled with a water-based magnesium oxide insulating composition which was cured with heating units. The modification caused the diameter of the thermite powder bed to be slightly less than before, but the corresponding increase in height was easily accommodated. Melting of the thin steel inner shell was not considered detrimental to the melt composition, so it was left in place for the test.

2. Instrumentation

Much of the in-cavity instrumentation used on the HIPS-2C experiment proved to be ineffective in resolving the position of the melt. The intense heat flux from the melt caused most of the devices to fail, before useful data could be obtained. All of the in-cavity devices were omitted in the construction of the HIPS-5C cavity. A summary of the instrumentation is given in Table 9.

Table 9
Summary of HIPS-5C Instrumentation

DEVICE TYPE	NO.	RANGE	LOCATION	PURPOSE
Pressure	1	0-34.4 MPa	Gas line	Reference
Pressure	1	0-34.4 MPa	Melt generator	Blowdown
Pressure	1	0-3.4 MPa	Cavity	Cavity pressure
Pressure	2	0-34.4 MPa	Cavity	Cavity pressure
TC	2	0-1500°C	Melt generator	Gas temperature
Photodiodes	3	–	Cavity	Debris velocity
Pyrometer	2	1500°C-3500°C	Cavity exit	Debris temp
Real Time X-ray	6	1000 fps*	Cavity exit	Debris character
Catch Pan	12	–	Downrange	Debris collection
Cameras	10	10-400 fps	–	Observation

* fps - frames per second

The three light sensitive photodiodes in the cavity were designed to determine the transit time for the melt from the

generator exit to the cavity floor or to the cavity exit. These devices were optically filtered and used a small aperture to limit the field of view to the immediate vicinity. By orienting the devices orthogonal to the path of the melt, they were sensitive only to the melt as it arrived at the sensor and not to the bright flash accompanying the molten material. Monitoring the time interval between the response of two of these devices and knowing the distance traveled gave an average velocity of the melt as it moved through the cavity.

Flash X-ray imagining of the debris stream in the HIPS-2C test showed the size and distribution of the melt particles in the gas that emerged from the cavity exit. Unfortunately, this technique did not give the velocity of the particles nor their direction of flight. High speed photographic techniques were hampered by their inability to penetrate the surrounding aerosol cloud or luminous melt vapor. To overcome these problems, a real-time X-ray diagnostic technique was used on the HIPS-5C experiment. The technique used a continuous 150-KeV X-ray source (Norelco Model CK-150) to provide a high flux of photons in conjunction with an image intensifier that converted the incident photons to electrons that were subsequently focused onto a screen.

Because a normal video camera is limited to 30 frames per second, it would be inadequate to monitor the motion of high-speed particles detected by the image intensifier. For the HIPS-5C test, a specialized high speed video system (Spin-Physics Model 2000 camera and digitizing recorder) was used to view the image intensifier screen. This device allowed up to 2000 frames per second in full image, and up to 12,000 frames per second for split-screen applications.

For this test, the image intensifier was installed with its field of view (approximately 15 centimeters in diameter) across the exit of the cavity, perpendicular to the expected flow of debris. Insulating ceramic board was used to form box-like structures around the X-ray head and image intensifier for protection from the hot melt particles and heat flux. Thin plexiglass windows were placed directly in front of the X-ray source and image intensifier screen that insured minimum attenuation of the emitted and incident energy. The image intensifier was placed approximately 10 centimeters laterally from the lip of the cavity exit while the X-ray head was about 50 centimeters from the opposite edge. These short distances were necessary because the photon flux varied inversely with the square of the propagation distance.

The maximum framing speed of the camera system was established based on the constraints of the experiment. As the camera speed increased, the amount of light available from the

screen of the image intensifier for each frame (electron flux multiplied by the time of exposure) was reduced. On this test, the camera speed was set to 1000 fps because at the higher framing rates the contrast between the melt particles and surrounding background was insufficient to accurately resolve useful data. The total recording time available was approximately 45 seconds.

The two pressure gauges installed in the cavity were intended to measure the pressure increase as the melt emerged and heated the gas trapped in the cavity. One gauge was placed in the circular cavity region while the other was installed in the inclined shaft near the exit. The thickness of the cavity required the sensors to be connected to the cavity by 7.7 millimeter diameter steel tubes inserted through the concrete wall. The total length of the tube was approximately 30 centimeters. This length, combined with the small diameter of the tube, effectively caused it to function as a low-pass acoustic filter. It was estimated that pressure pulses with frequencies above 500 hertz were attenuated by the connecting tubing. The exposed gauge faces were protected with a 2 millimeter thick layer of porous stainless steel metal, which permitted pressure equalization to the gauge while reducing the incident heat flux.

3. Initial Conditions

The initial conditions for the HIPS-5C test are summarized in Table 10. The initial pressure level was selected to study debris dispersal at conditions approximating those predicted at the lower range of the accident sequences.

E. Scaling Analyses

Because all the experiments discussed here represent scale models of actual reactor cavities, it was important that the scale of the experiments and its influence on the results be understood. Section IV of Reference 8 gives an extensive analysis of the scaling involved in these experiments.

The critical mechanisms for debris removal from the reactor cavity have been identified as particle levitation, film sweepout, film entrainment, and splashout. References 2 and 8 give the equations describing each of these mechanisms and the cutoff criteria for debris dispersal. The Kutateladze number[19] is used to describe the potential for debris removal by the action of a high-velocity gas moving over the surface of the

melt. It is shown in the next section that both the HIPS and SPIT experiments demonstrate Kutateladze numbers similar to the reactor accident situation.

Table 10
HIPS-5C Initial Conditions

Melt Mass	80.0 kg
Thermite Composition	Iron Oxide (Fe_3O_4) - 61.04 kg plus Aluminum (Al) - 18.96 kg
Melt Composition	Iron (Fe) plus Alumina (Al_2O_3)
Dopants	None
Gas	Carbon Dioxide (CO_2)
Gas Volume	0.118 m^3
Initial Pressure	5.8 MPa
Ambient Temperature	15°C
Melt Plug Diameter	4.8 cm (growth limited by graphite plate)

Evaluating the cutoff criteria for each experiment did not establish the quantity of material that can be potentially removed. The total predicted dispersal was proportional to the length of time the cutoff criteria were exceeded. This required that the time-scale of the experiment be known in relation to that of the accident. Because the debris dispersal was directly related to the blowdown of the primary system or the melt generator, the time scale of the experiment was found by considering the mass flowrates for the respective systems. This was done in Reference 8 with the result that experiment time was related to actual time in the same manner as the length, i.e., 1:10 for HIPS tests; 1:10 and 1:20 for the SPIT experiments.

The experiments were designed in a direct linear relationship to the reactor and used prototypic pressure levels in the melt generator so that the gas flow patterns established

-43-

in the test cavity were representative of the accident situation. This was an important consideration in accurately modeling the mechanisms assumed to be responsible for debris dispersal from the cavity. Because the gas velocities and melt properties were similar in the reactor accident and experiment, the dispersal mechanisms produced debris particle sizes estimated to be the same in both situations.

III. EXPERIMENTAL RESULTS AND ANALYSES

This section presents the results obtained from the four experiments, organized to group together the results for a specific phenomenon from all tests. In this manner, subsections are presented for melt generator pressure history, debris size characterization, interaction chamber pressure and temperature response, etc. Theoretical results are also presented to aid in understanding and interpreting the experimental observations.

A. Test Observations

This section presents qualitative observations made during and following each experiment. The intent is to give an overall impression of the tests and to aid in the interpretation of the more quantitative results that follow. Each test is discussed separately.

1. SPIT-18

For this test, a video camera was positioned at one of the transparent ports in the side of the interaction chamber, principally to provide remote observation of the apparatus during the test. The ejection of the melt was seen on the video monitor and coincided with a "thump" that was heard and felt by the experimenters in the control center. The melt caused a brilliant illumination in the chamber that lasted for several seconds. The brightness of the flash prevented any usable information to be obtained by the video camera during this period. As the glow from the debris subsided, the visibility within the chamber was initially adequate but became progressively more limited as material suspended in the atmosphere moved downward. The airborne material was suspended near the ceiling of the chamber at first, but gradually dispersed throughout as the fans circulated the atmosphere. Within a few minutes, the illumination of the quartz lamp placed in the chamber was inadequate to be seen by the camera.

The initial inspection of the interaction chamber immediately following the test showed that aerosols were escaping from a number of leakage points developed during the experiment. The most obvious of the leaks was at the unbolted lower horizontal seal of both removable doors. Closer inspection showed a 2 to 3 centimeter separation between the cover and concrete pad in these regions, attributed to an internal pressure

load that caused the structural members to yield. The steel plate between the I-beam reinforcements on the north cover was obviously distorted. Less significant leaks were also found on the long side of the chamber opposite the instrumentation port. A number of bricks used to support the chamber during the pouring of the concrete floor were displaced away from the structure.

The dense aerosol cloud within the chamber persisted for about one hour before details within the chamber were seen. Debris was observed scattered about the catch pans and exposed floor area, with the appearance of either small spherical shapes or splashes. The splashes appeared to have been molten when they impacted the floor, forming relatively thin patterns of large cross section. The quantity of debris was more extensive near the base of the wall away from the apparatus (north wall in Figure 4) than in the other regions. Much of the material appeared to have struck the north wall and dropped to the floor. All exposed surfaces in the chamber were covered by a fine dusty layer of tan colored aerosol.

When the chamber was entered, it was noted that the lower edges of the long sides were separated from the concrete base. A gap, approximately one centimeter wide, was formed along the entire length of the west wall. The gap was created when the internal pressure moved the wall outward and upward from the base. Three anchors in the concrete base were dislodged when the wall was displaced. The separation on the opposite side was not as pronounced because the instrumentation port was abutted against a block wall that limited the available displacement. Figure 12 shows the appearance of the apparatus and interaction chamber after the south wall was removed. The gap between the west wall and concrete pad can be seen at the lower left of the photograph.

Figure 12 also shows some of the debris that was found distributed throughout the chamber. The concentration of material was much greater along the back (north) wall than any other region of the chamber. The layer of fine dust noted through the optical ports covered all of the exposed surfaces, including the ceiling of the chamber. The distribution of this aerosol material was not preferential, but was uniform throughout the chamber.

After the cavity apparatus was removed from the chamber, inspection showed several large irregularly shaped globules near the cavity exit (Figure 13). All other debris in the chamber was splash-like or in the form of small spheres. The relatively smooth exterior of these large globules near the exit suggested that they were not traveling at high velocity upon impact and were close to freezing. They were probably removed from the cavity late in the blowdown cycle when the gas velocities were much diminished.
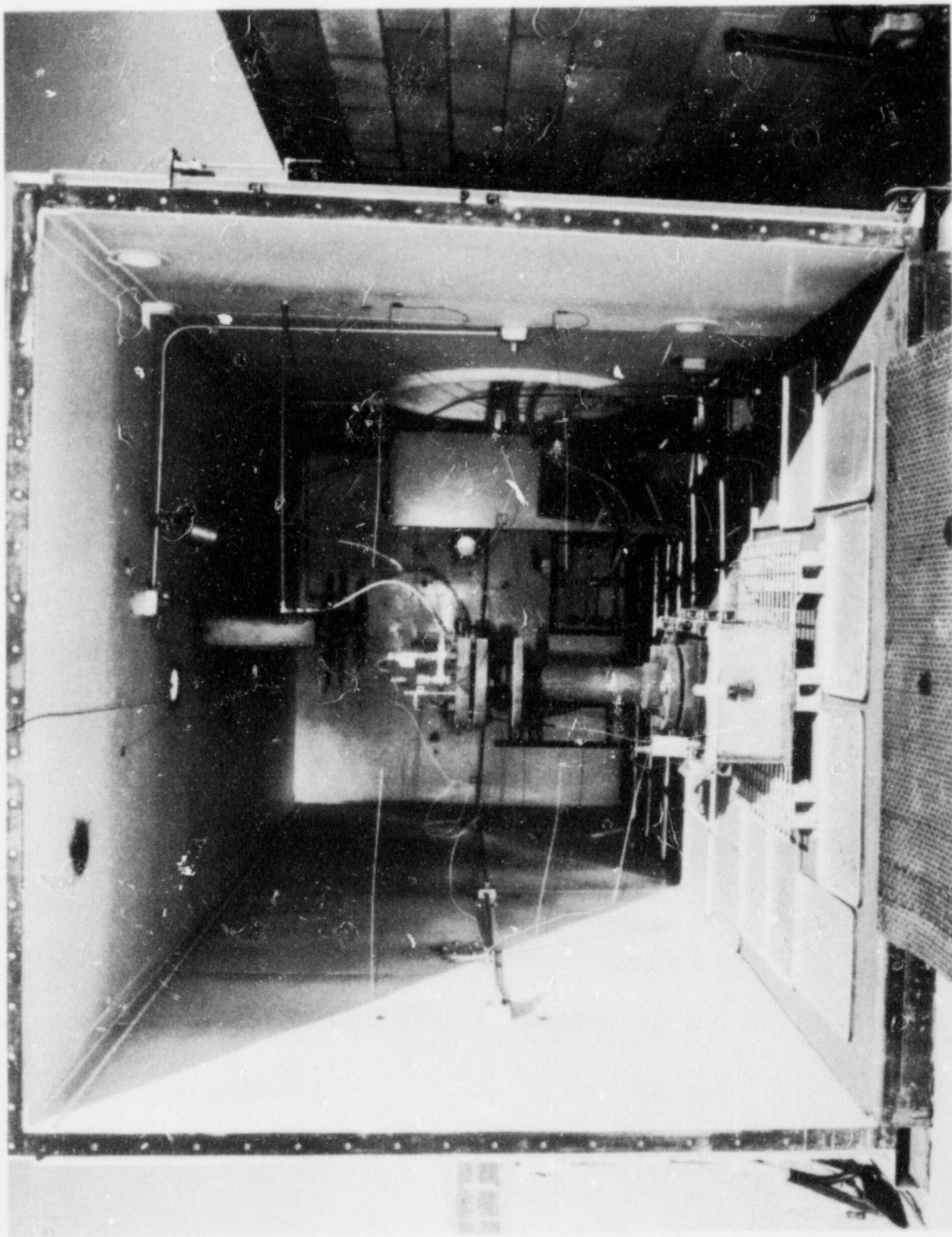
FIGURE 12. APPEARANCE OF INTERACTION CHAMBER FOLLOWING SPIT-18 TEST

47
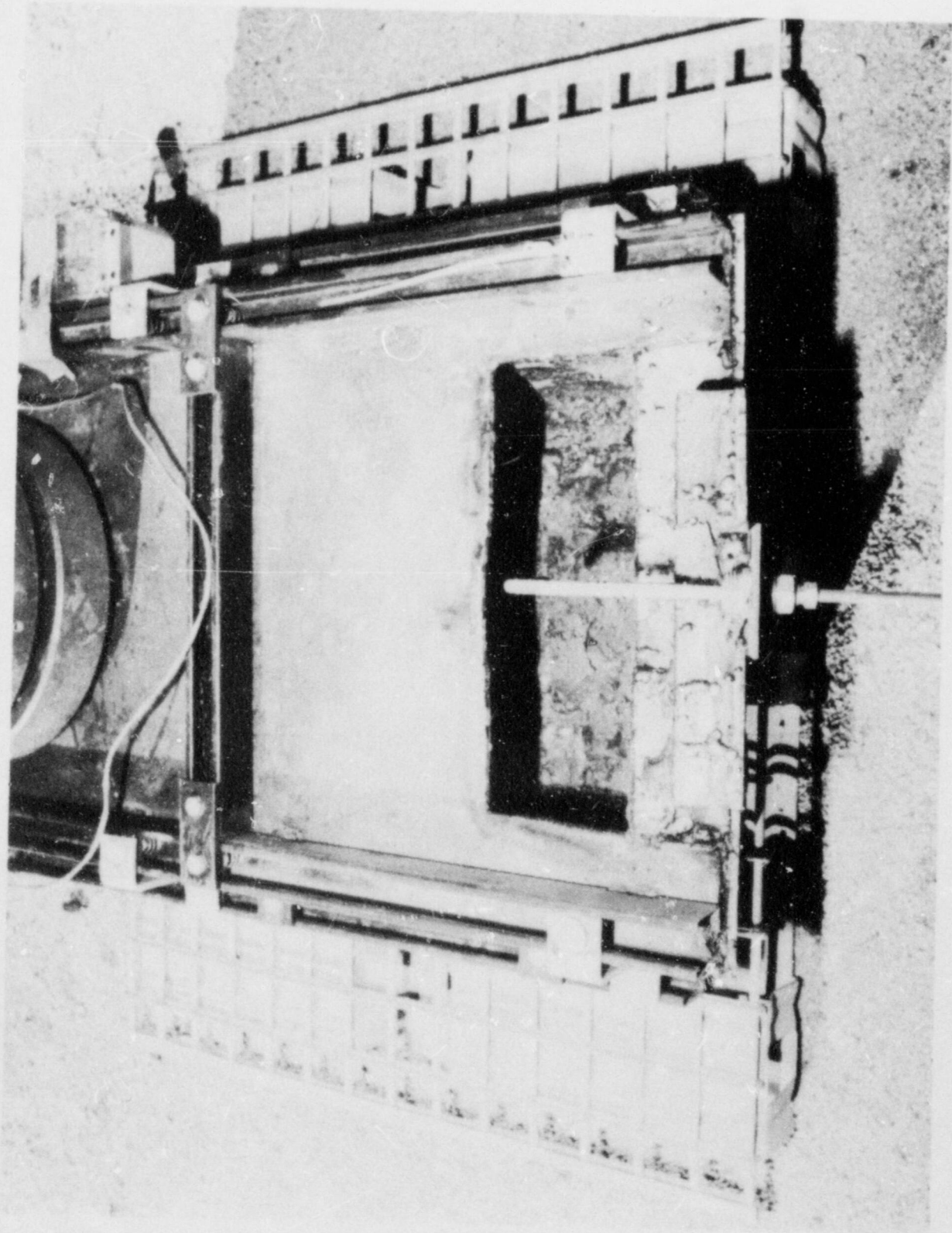
FIGURE 13. PHOTOGRAPH OF CAVITY EXIT OPENING

48

When the top cover of the cavity was removed, it was observed that all the exposed brick surfaces were covered with a layer of frozen melt. As shown in Figure 14, the crust layer in the cavity was uniform with no obvious discontinuities. The light colored area towards the rear of the cavity was dry-ram material used in the melt generator. The crust material adhered very lightly to the brick surface and was easily removed. Ten random samples, two from each of the exposed brick surfaces, were taken and measured with a vernier micrometer to determine mean thickness. The values are given in Table 11. This technique yielded an average thickness of 0.325 (±0.089) centimeters. The rough texture was the largest contributor to the variation from the mean value. There was not a consistent relationship between crust thickness and its position within the cavity.

Table 11
Samples Removed from the SPIT-18 Cavity

Sample Number	Thickness (cm)	Mass (g)	Volume (cm^3)	Calculated Density (g/cm^3)	Magnetic Attraction
1	*				Yes
2	0.356	3.52	2.0	1.76	Yes
3	0.254	2.26	0.75	3.01	No
4	0.483	3.18	1.0	3.18	Yes
5	0.305	2.55	1.0	2.55	Yes
6	0.305	2.47	1.0	2.47	Yes
7	0.254	1.97	1.5	1.31	No
8	0.191	2.61	0.5	5.22	Yes
9	0.254	1.64	0.25	6.56	No
10	0.432	3.52	1.0	3.52	No

* Sample too large to be measured using this method.

FIGURE 14. POST-TEST APPEARANCE OF CAVITY INTERIOR

Bulk density was obtained from the mass and volume of each sample (see Table 11). The volume was found by immersing each sample in a water filled graduated cylinder. This method gave a mean density value of 3.30 g/cm^3 and a standard deviation of 1.56 $g/cm.^3$ The low density value of the specimens relative to iron or alumina indicated that the crust layer 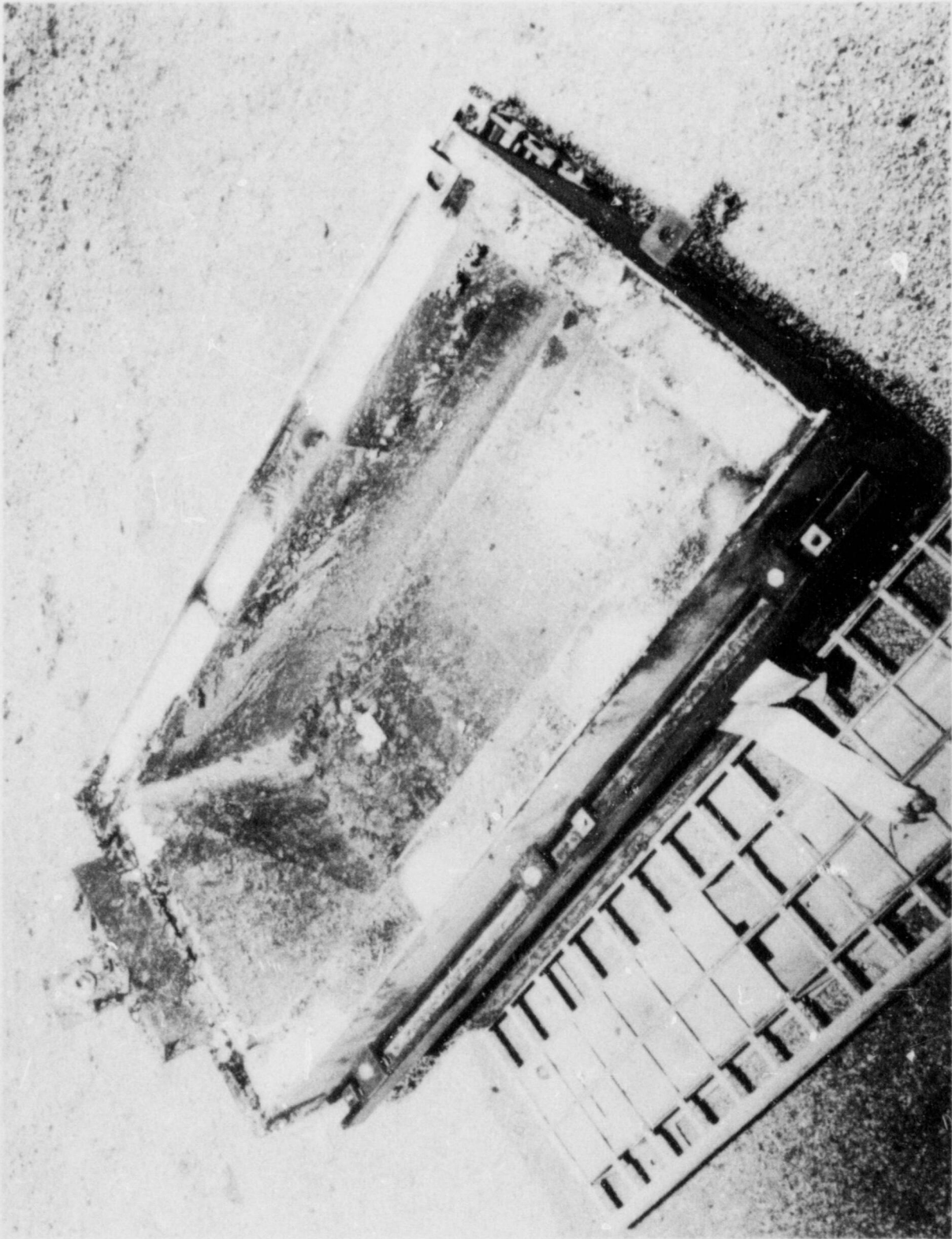was highly porous. If the water failed to enter the pores (prevented by surface tension or closure of the pores), a larger effective volume would be calculated than in reality. Voids may have formed by trapped gas within the melt during a rapid quench on the cold brick surface. The porosity may have been caused by outgassing from the exposed cavity surface, or by moisture contained in the pores of the bricks. It was considered unlikely that gas effervescence occurred over a time interval sufficiently long enough to be responsible for the observed pore structure.

2. SPIT-19

The two video cameras used on this test provided views of the inside and outside of the interaction chamber. The latter device was intended to provide an indication of the aerosol and gas that might escape from the interaction chamber after the test. Similar to the SPIT-18 test, the ejection of material coincided with a ground shock that was detected by experimenters within the control center.

The time from ignition to ejection was unexpectedly short (4.9 seconds), compared to the 20 to 30 seconds typical of previous tests. The cause of the rapid reaction rate in the SPIT-19 experiment has not been specifically determined. It has been assumed that the reaction rate was enhanced by gases propagating ahead of the reaction front. This was caused when the pressure was released from the melt generator during troubleshooting of a misfire (the thermite reaction was not initiated on command from the control center). The venting probably caused the compacted thermite to loosen, increasing the void fraction in the powder. During the reaction, gases were then able to penetrate ahead of the reaction front to preheat the thermite powder and enhance the burn rate.

The time for the thermite reaction to complete and fail the fusible plug was considerably shorter than any previous test. The shortest time interval on all prior experiments was 13 seconds. The average reaction time for the 18 SPIT experiments was roughly 25 seconds. Based on this experience, the fast framing cameras on the interaction chamber were set to start at ten seconds after ignition. The cameras did not come to speed until well after the debris dispersal was complete. Thus, high resolution camera data were not obtained for comparison to other recorded data.

The ejection of the melt appeared as a brilliant flash on the video monitor that lasted for several seconds. As the material cooled and the illumination subsided, the atmosphere within the chamber gradually became very dark. As in the SPIT-18 experiment, the extent of airborne material was sufficient to obscure the light given by a quartz lamp mounted inside the structure. The dark cloudy appearance of the atmosphere continued for nearly one hour.

The record from the external video camera was not available at the time of the test. Subsequent review of the camera record clearly showed the emergence of melt from the cavity as a bright flash visible in all the camera ports. The flash was followed shortly by an upward movement of the steel interaction chamber, separated away from the concrete slab. As the structure moved it pivoted along the east wall where the instrumentation panel was tied to an adjacent concrete block wall. At the peak of the upward movement, the southeast corner of the chamber was nearly one meter above its initial position. The total time from initial movement of the chamber until it returned to the pad (not in its original position) was estimated from the video record to be approximately 0.3 seconds. During the elevation of the chamber, substantial aerosol and debris escaped from the opening.

Inspection of the chamber after the test revealed that it was displaced laterally approximately 6 centimeters from its original position. The displacement caused the south end of the structure to settle atop the concrete pad, so that the edge of the structure was elevated approximately 10 centimeters. Figure 15 is a photograph taken following the test of the lower southwest corner of the interaction chamber. In this view, the south door was removed to show the structure above and to the north of its original position. Some damage to the concrete pad was also recorded in this photograph.

The inspection also showed that both removable doors on the chamber were extensively damaged. The internal loading on the door surface was sufficient to cause large strain in the region near the lower edge where bolts could not be used. The load resulted in permanent deformation of the steel plate in this area, particularly between the vertical I-beam reinforcements. The lower 3 to 6 bolts on each side of the door were "pulled" through the 5 millimeter steel plate of the doors. This action resulted in gaps of 4 to 8 centimeters between the deformed steel plate of the door and the sealing surface of the chamber.

The interior appearance of the interaction chamber after removal of the south door is given in Figures 16 and 17. Large pieces of concrete from the interaction chamber pad were found
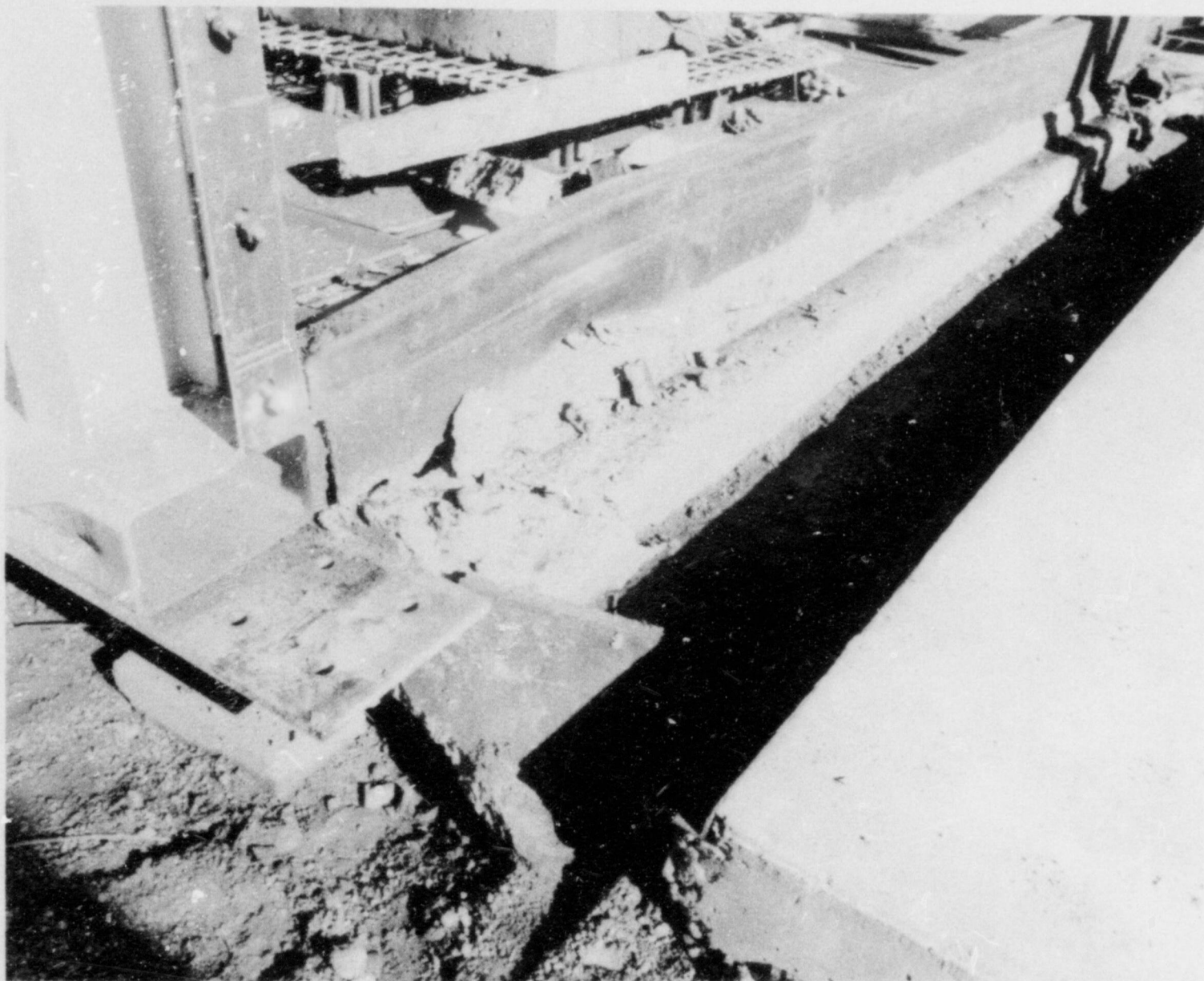
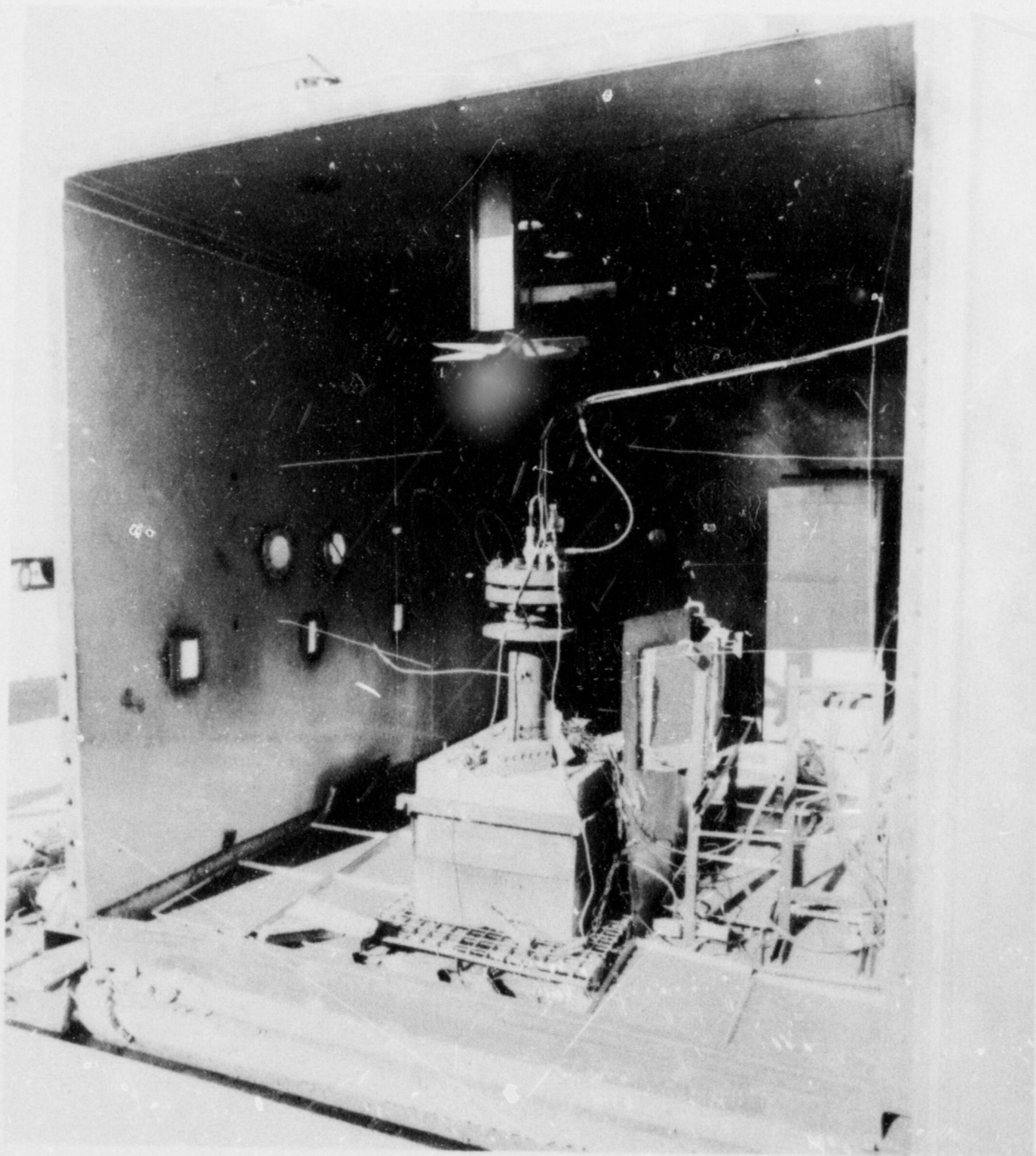FIGURE 15. SOUTHWEST CORNER OF INTERACTION CHAMBER FOLLOWING SPIT-19 EXPERIMENT

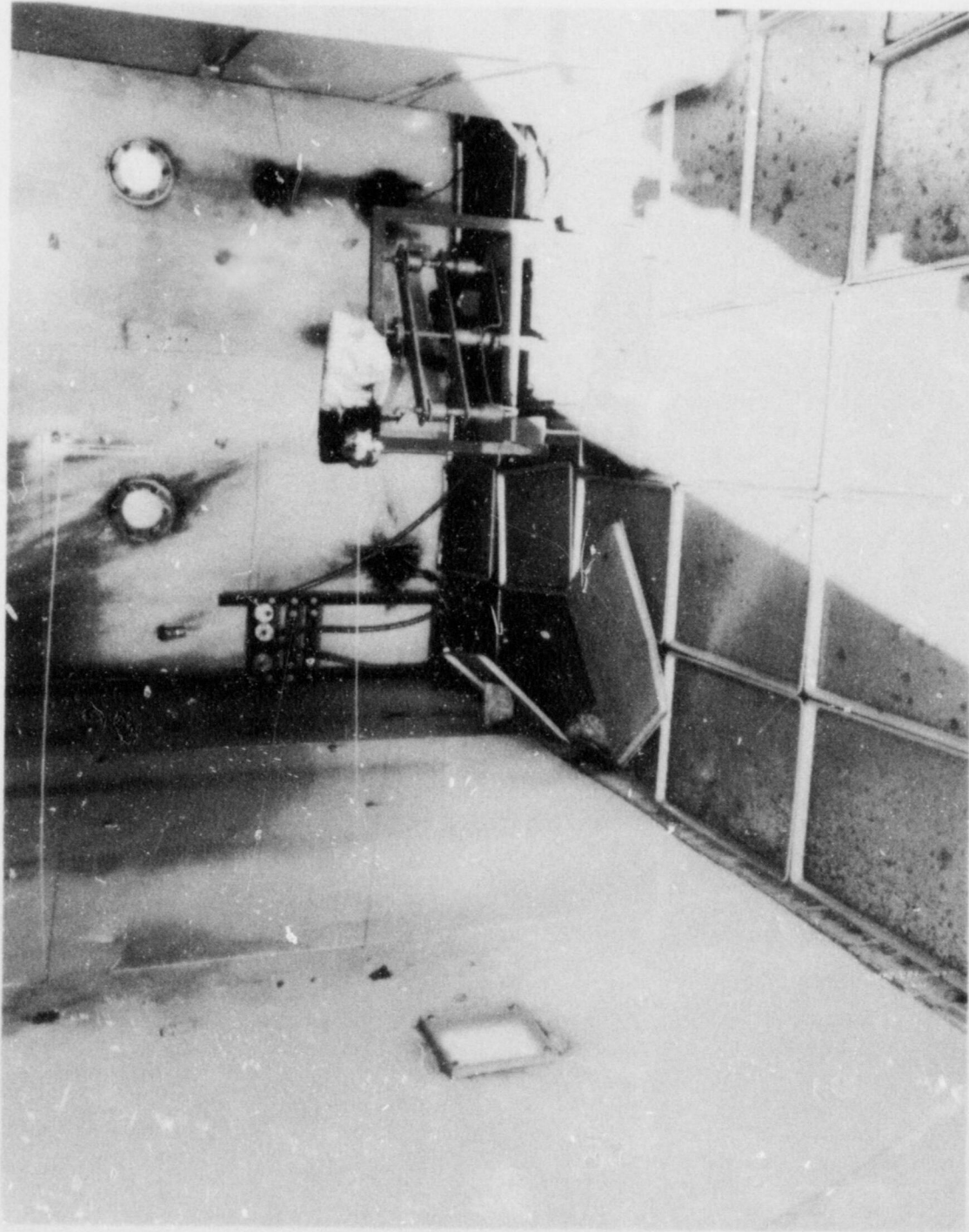FIGURE 16. INTERIOR OF INTERACTION CHAMBER FOLLOWING SPIT-19 EXPERIMENT

FIGURE 17. POST–TEST CATCH PAN APPEARANCE

scattered about the chamber. These pieces were created when the anchors attached to the sides of the chamber were pulled up through the surrounding pad. Some pieces weighed as much as 15 kilograms. The movement of the structure broke several welds around the periphery of the chamber resulting in a large gap (2 to 4 centimeters) between the chamber wall and concrete pad. Figure 17 illustrates more of the chamber damage, and the final position of the catch pans. Some debris was apparent in the pans.

All of the exposed surfaces within the chamber were covered with a fine layer of deposited aerosol. The concentration was greater on the ceiling and the upper edges of the walls than on the floor and lower wall surfaces. A substantial portion of the material could be removed by contact, but the remaining residue was tightly bound to the wall surfaces.

Debris was found in every one of the undisturbed catch pans. The greatest concentration of material was at the bottom edge of the north wall. Unlike the even distribution seen along the north end of the chamber following the SPIT-18 test, the particles were concentrated in the corners. Figure 18 is a photograph of the northeast corner of the interaction chamber, that shows the accumulation of debris in this region. The congregation of material near the larger gap locations indicated that the debris was influenced by the gas flow out of the chamber. The relative size of the gaps is illustrated in Figure 18.

Inspection of the cavity apparatus showed that melt escaped along the parting line separating the two halves. Some residual melt was found on the metal plates placed over the parting line, in the form of small spherical beads adhered to the surface. The discolored concrete above and below the metal plates evidenced that the debris was deflected at right angles after it emerged from the cavity. The velocity and temperature of the escaping material were great enough to prevent "sticking" of the melt to the exposed metal. Inside the apparatus, the exposed portions of the inclined tunnel were covered by a thin layer of frozen melt (Figure 19). The solidified material formed a uniform, thin layer with scattered large globules. Some large pieces of melt were also found on the top surface of the apparatus, in the vicinity of the exit opening.

After the two halves of the cavity were separated, portions of the parting surfaces were covered by a thin, irregular layer of frozen melt. A photograph of the lower cavity half is given in Figure 20. The rough appearance of the mating surfaces was caused by the grout used between the two halves. The dark area near the circular cavity was created by melt that penetrated into the gap between the two cavity halves. The thickness of the material in this region was less than one millimeter.

-56-

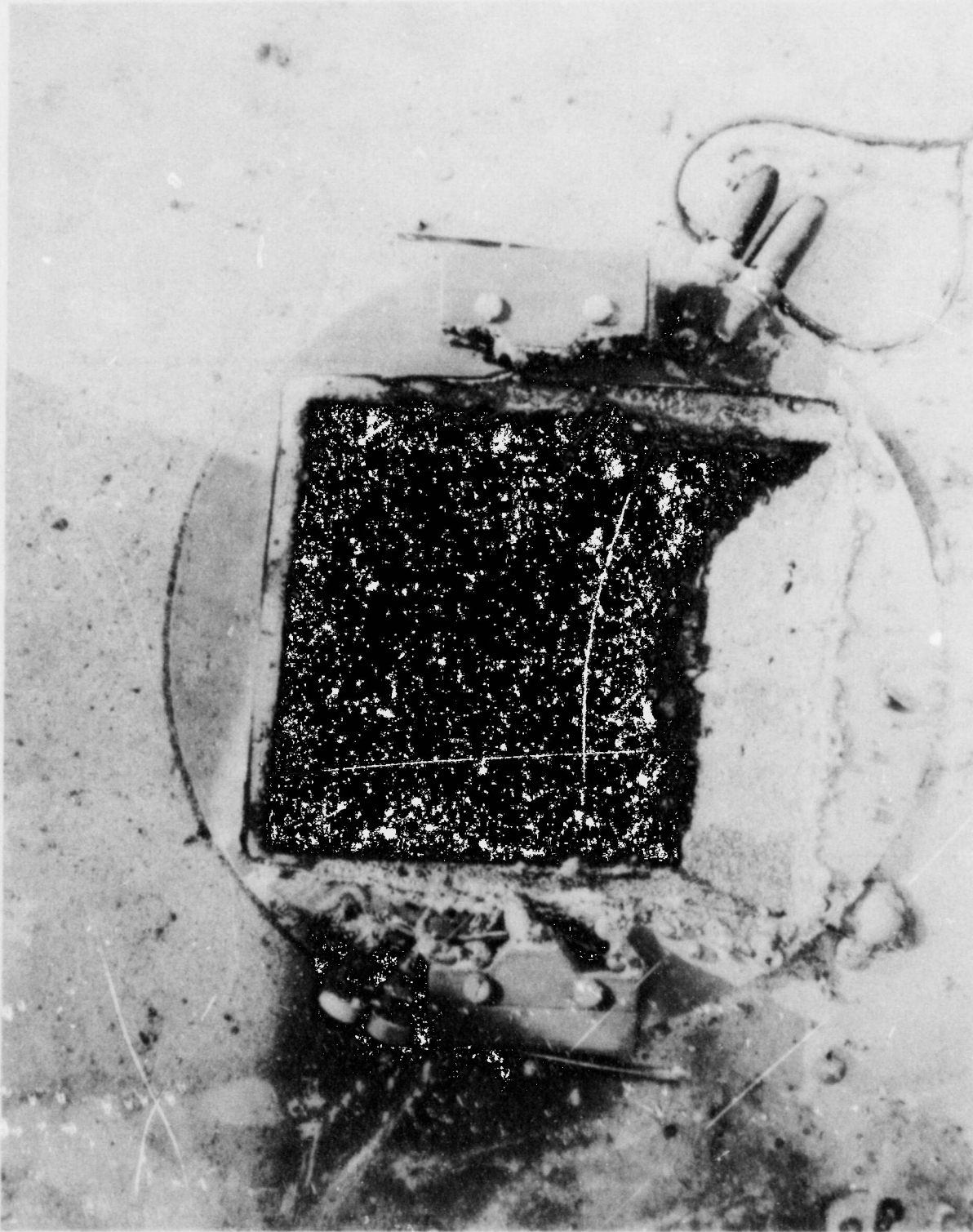FIGURE 18. INTERIOR OF INTERACTION CHAMBER AT NORTHEAST CORNER
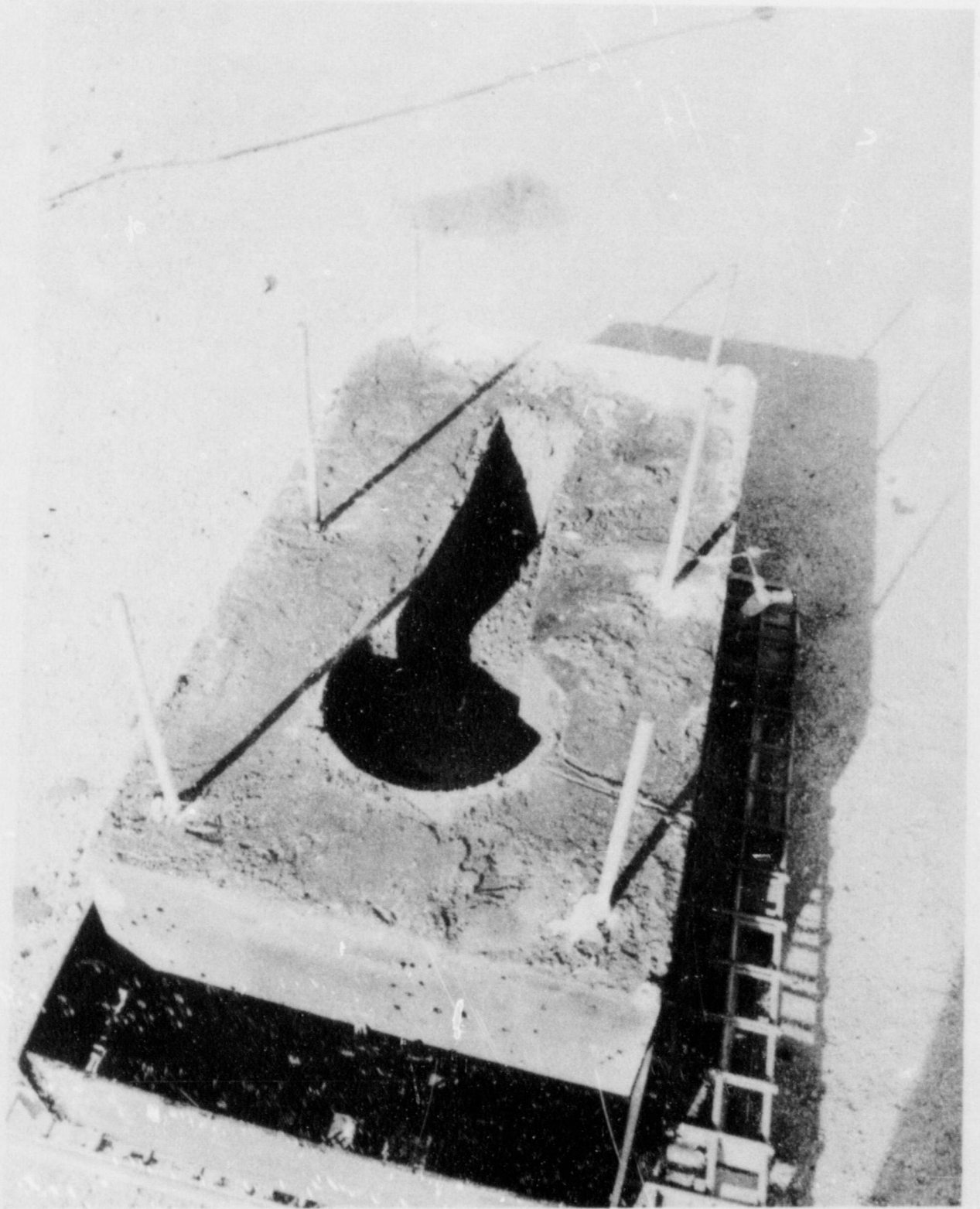
57

FIGURE 19. EXIT OPENING OF SPIT-19 CAVITY

FIGURE 20. LOWER HALF OF SPIT-19 CAVITY

The cavity and tunnel regions showed that all exposed surfaces were covered with a layer of solidified melt estimated to be 1-2 millimeters thick. Numerous large globules were found on the floor of the cavity and tunnel. The dimensions of these globules were on the order of several times the thickness of the melt in the same region. The distribution of the globules was fairly uniform along the tunnel except for a larger mass at the base of the inclined keyway. Unlike the bright grey color of the material in other areas, the large mass was distinctly reddish in appearance.

Measurement of the cavity internal dimensions showed that concrete erosion was slight. Only the area directly under the melt generator appeared decomposed. A sharp probe was used to penetrate this region to a depth of slightly greater than one centimeter. The absence of a solidified melt layer as found in other regions of the cavity caused the white area seen in the photograph.

The exposed surfaces of the upper half of the cavity also exhibited a thin layer of frozen material. Unlike the lower half, no large globules were found. Measurement of the thickness of the melt layer in this region and the lower cavity was unsuccessful because the material was tightly adhered to the concrete. When a portion of the crust was removed, the sample had concrete residue adhered to it. The lower melt generator flange that served as the ceiling of the circular cavity was covered by a layer of soot-like material. The material was generated by the products of the thermite reaction, released after blowdown of the vessel.

3. HIPS-2C

High speed cameras were used on the HIPS-2C test to provide high-resolution film records of the events. The cameras were placed at distances of 20 to 80 meters from the apparatus with lines of sight perpendicular to the flight direction of the debris. The field of view on the closer units typically spanned the region within a few meters of the cavity exit opening. These devices provided detailed information about the material that escaped the cavity and the behavior of the apparatus. The remaining cameras farther from the apparatus were used to monitor the trajectory of the debris and had correspondingly larger fields of view, up to 50 meters downrange from the cavity.

The start of melt ejection into the cavity was indicated on the film records by the signal from a photodetector placed just below the fusible plug in the bottom flange of the melt generator. The output from the photodetector was transmitted to

a strobe light unit on the apparatus and to the high speed tape recorder. This technique allowed the recorded signals from transducers to be correlated to the film records. The first indication of light from the strobe unit was designated as zero time on the film records. The uncertainty in timing for this method was on the order of 10 milliseconds, based on the framing rate of the slowest camera units (100 frames per second). A summary of the sequence of major observations is given in Table 12.

Table 12
HIPS-2C Event Timing

TIME (Seconds)	EVENT
0.00	Strobe light turn-on
0.05	First appearance of debris at cavity exit
0.11	Aerosol cloud forms
0.33	Cavity opens along parting line
0.73	Debris ejection complete
1.23	Top cavity half returns to original position
2.09	Separation of debris and aerosol complete
2.52	Debris reaches apex of trajectory
4.09	First debris impacts ground
5.08	Debris impact complete

The photographs shown in Figure 21 were taken with a high-speed camera from a distance of approximately 75 meters from the apparatus. The photographs indicate that the debris exited the cavity at the angle of inclination defined by the cavity geometry (26 degrees from vertical). The debris began to expand radially outward as it propagated upward from the apparatus, from an initial 0.25 meter lateral dimension to approximately 15 meters
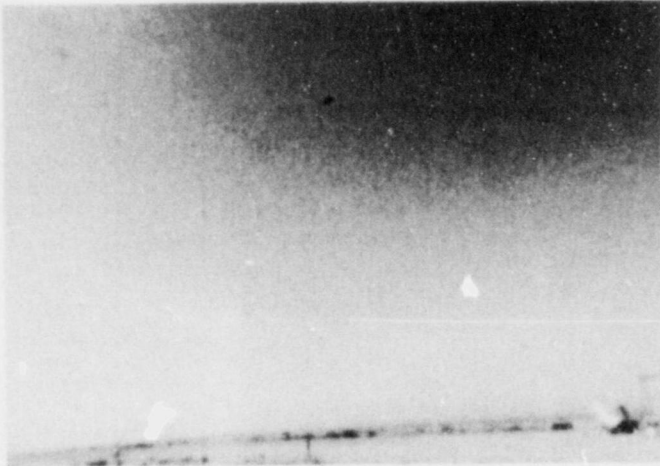
t = 0.1 sec.
MELT JUST EMERGING FROM CAVITY EXIT.
VELOCITY = 30 m/sec.
VERTICAL SCALE IS 38 METERS.

t = 0.5 sec.
MELT EJECTION FROM CAVITY COMPLETE.
AEROSOL CLOUD BEGINS TO FORM.

t = 1.0 sec.
EJECTED MELT REACHES MAXIMUM HEIGHT.
PARTICLES BEGIN SEPARATION FROM AEROSOL.

t = 1.5 sec.
SEPARATION COMPLETE.
PARTICLES FOLLOWING PARABOLIC TRAJECTORIES.

FIGURE 21. DEBRIS DISPERSAL SEQUENCE DURING HIPS-2C TEST

at its greatest point. As shown in all the photos, the leading edge of the debris remained very luminous throughout the duration of flight. The dark cloud of aerosol formed shortly after the melt emerged from the cavity. The aerosol cloud continued to grow and expand throughout the course of the experiment. In the third photograph, the initial separation of the aerosol and debris was obvious, while the last photo indicated that the separation was complete. Subsequent film records demonstrated that the aerosol continued to propagate upward as influenced by buoyancy and the prevailing wind.

The camera records at later times showed that the debris was still molten when the particles eventually impacted the ground. Debris was recovered from the ground at distances up to 50 meters from the apparatus. The maximum height of the debris was estimated to be approximately 35 meters. Material may have reached a higher elevation, but no distinct image was detected on the camera records.

As indicated in Table 12, the melt emerged from the cavity exit approximately 50 milliseconds after the it first entered the cavity. The mean debris velocity through the cavity was calculated to be 40 m/sec (based on an average pathlength from the melt generator to the cavity exit of 2 meters). Based on the error in film timing, the uncertainty in the estimated velocity was ±2 m/sec.

Outside the cavity, high speed camera records were used to determine the velocity of the escaping material. Data were obtained from the movement of the leading edge of the debris cloud as it expanded away from the apparatus. Only the leading edge of the debris cloud was clearly distinguished throughout the duration of the flight. The rapid evolution of the debris cloud prevented clear distinction of other portions. Figure 22 is a plot of debris displacement versus time from the first appearance of the melt from the cavity. The debris propagated away from the apparatus at a relatively constant velocity, as suggested by the slope of the plot given in the figure. After the initial rapid displacement for the first 5 meters, the debris indicated a relatively constant velocity on the order of 25 m/sec. For distances beyond that indicated in Figure 22, the irregular expansion of the debris cloud prevented clearly distinguishable data.

The cameras near to the apparatus showed that the cavity failed along the parting line at approximately 330 milliseconds. The first indication of the failure was the appearance of melt escaping along the parting line between the upper and lower halves of the apparatus. The debris that emerged from the aperture in the cavity moved somewhat more slowly than the material from the exit. Comparison of the records from all
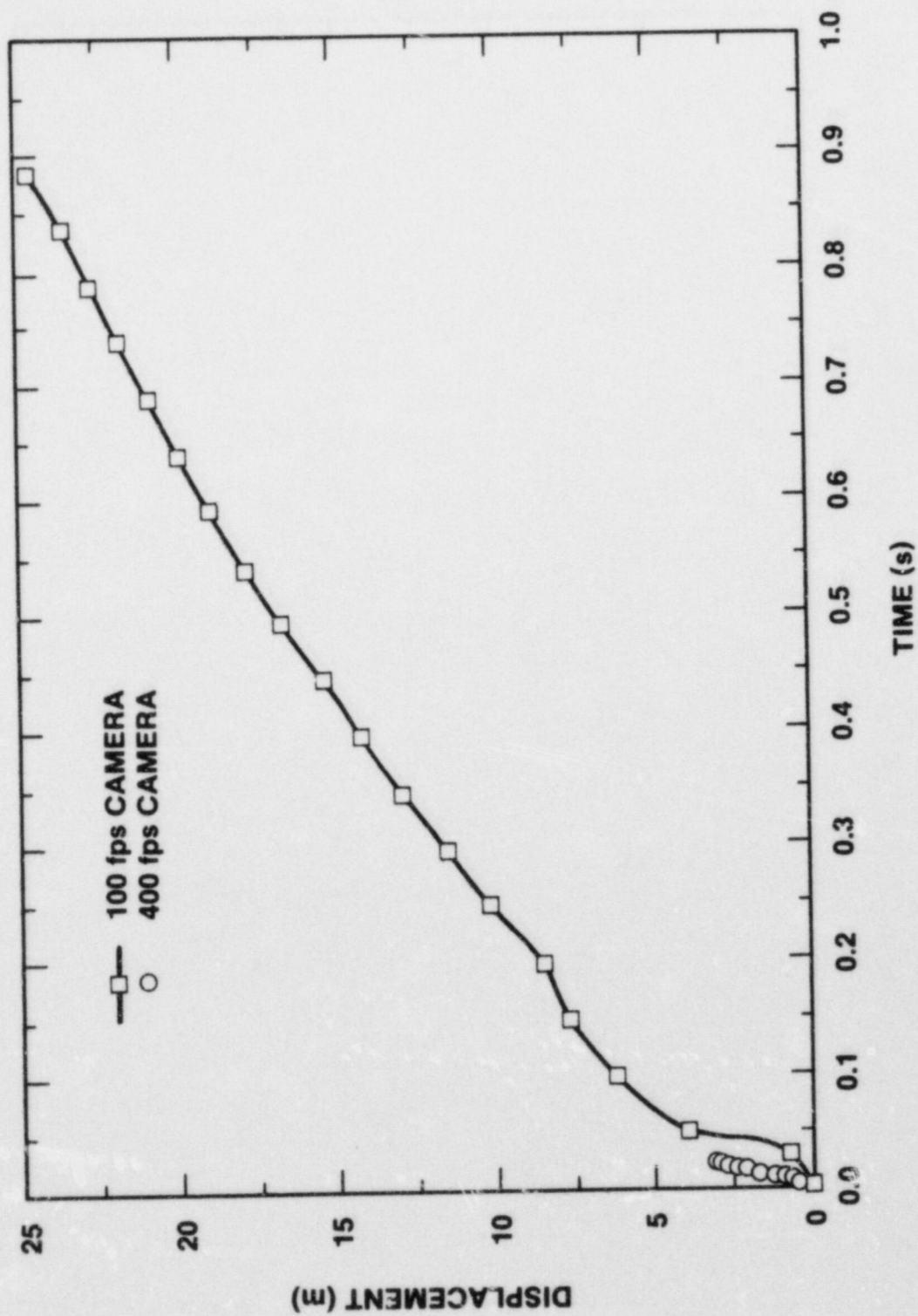
FIGURE 22. HIPS-2C LEADING EDGE OF DEBRIS DISPLACEMENT VERSUS TIME

cameras showed the gap along one edge (facing east) was significantly larger than the opposite side. The gap width at its maximum was estimated to be on the order of 20 centimeters. After approximately 900 milliseconds, the top cavity half returned to its original position.

At approximately 700 milliseconds, the amount of debris leaving the cavity diminished considerably with the last distinguishable material observed at 730 milliseconds. The debris discharge was followed by ejection of a portion of the dry ram powder used in the melt generator. The powder formed a cloud at the exit similar in appearance to the aerosol formed by the melt. The two clouds were clearly discerned, however, by differences in color.

The buoyancy forces on the aerosol cloud caused it to propagate in a more upward direction than the debris. Drag on the particles may also have reduced their horizontal velocity, particularly the larger size material. At 2.1 seconds, the separation between the aerosol cloud and debris was complete. At 2.5 seconds, the debris reached its highest elevation of 35 meters above the ground with the cloud approximately 15 meters wide and about 20 to 25 meters in length along its longitudinal axis. As the material began to fall towards the ground, large particles were distinguished at the lower edge of the cloud nearest to the apparatus. When these debris impacted the ground, many particles fragmented into smaller pieces. Debris continued to strike the ground for the period from 4.1 to 5.1 seconds. During this interval, all of the material appeared molten, based upon the splashing or fragmenting that occurred on impact. The material observed splashing was very luminous indicating that it was not dust levitated from the ground.

The splash pans placed along the flightpath of the debris collected only a limited amount of material. The pan locations were intended to obtain representative samples of the debris at various distances from the apparatus. In this test, the debris was in the form of small spheres and splashes similar to what was seen in the SPIT-18 and SPIT-19 experiments. The mean flightpath length in the HIPS-2C test was on the order of 100 meters, versus 2 to 3 meters in the SPIT experiments, which resulted in more spherical shapes that were characteristic of droplets quenched in an atmosphere. A more extensive description of the recovered debris is given in a subsequent section.

4. HIPS-5C

The HIPS-2C and HIPS-5C experiments were similar except for the type and pressure level of the gas in the melt generator. The HIPS-5C cavity was also modified to insure that the failure

along the parting surface in the HIPS-2C was not repeated. The two cavity halves were joined together with a metal plate welded across the parting surface.

The high-speed motion picture cameras were used to monitor the behavior of the debris and aerosol ejected from the cavity. Figure 23 shows a series of photographs from a fast-framing camera record, while Table 13 lists the timing of the major events. The initial behavior was similar to that seen in the HIPS-2C test: The debris emerged from the cavity at high velocity, an aerosol cloud formed behind the leading edge of the debris, the debris continued to ascend along the path defined by the angle of the cavity keyway (26 degrees from vertical), and the aerosol separated before the debris reached its apex. The last photo shows the debris expanded over a vertical distance that approached 30 meters. This behavior was unlike the HIPS-2C test where most of the expansion occurred in the horizontal plane.

Table 13
HIPS-5C Event Timing

| TIME (Seconds)	EVENT
-0.76	Smoke emerges from cavity exit
0.00	First debris from cavity
0.45	High-velocity debris emerges
0.55	First aerosol appears
0.63	High-velocity debris reaches leading edge of cloud
1.37	Debris ejection ends
2.59	Complete separation of debris and aerosol
2.72	Apex of debris trajectory
3.5	Debris no longer luminous

t = 0.075 sec
DEBRIS BEGINS TO EXIT CAVITY

t = 0.575 sec
DEBRIS HEIGHT 10 meters, AEROSOL CLOUD BEGINS
TO FORM

t = 1.325 sec
EJECTION COMPLETE
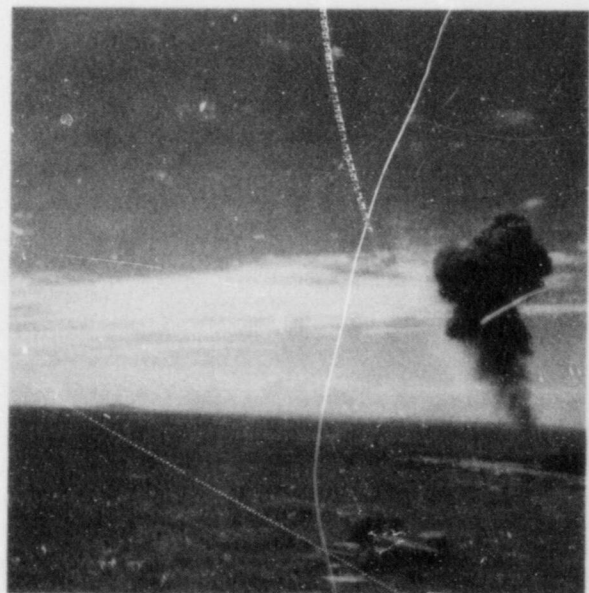
t = 2.375 sec
SEPARATION OF DEBRIS AND AEROSOL COMPLETE,
MAXIMUM DEBRIS HEIGHT 46 meters

FIGURE 23. DEBRIS DISPERSAL SEQUENCE DURING THE HIPS-5C TEST

67

A unique aspect of the HIPS-5C debris behavior was not obvious in the photos of Figure 23. The movement of the debris occurred in two distinct stages, an initial slow velocity propagation followed by an excursion at much greater velocity. At approximately 600 milliseconds after the start of debris dispersal, the material that first emerged from the cavity was overtaken by a large quantity of debris traveling at high velocity. This second mass of material emerged as the leading edge of the debris cloud at approximately 8 meters from the cavity exit. The behavior was quantified by the debris displacement history given in Figure 24. Data were available from two cameras, a 100 fps unit at approximately 100 meters from the apparatus and a 1000 fps camera at nominally 20 meters distance. The latter device gave much higher resolution results, although limited in duration. As before, the displacement history represented the movement of the leading edge of the debris cloud as it propagated away from the apparatus.

Based on the slope defined by the data points, the debris velocity was fairly constant at nominally 12 m/sec for the first 600 milliseconds. The abrupt change in slope at the end of this interval indicated the emergence of the faster moving material. The estimated velocity over the next 250 milliseconds (54 m/sec) was nearly five times larger than that just prior to this interval. The slope again changed at 850 milliseconds to a somewhat slower rate for the duration of the record. The data after 1.25 seconds were considered uncertain because of the difficulty in defining the leading edge of the highly expanded debris cloud.

The debris displacement data from the two tests (HIPS-2C and HIPS-5C) are compared in Figure 25. The uncertain data points at late times have not been included on this plot. The behavior in the two tests differed dramatically throughout the period of the available data. Only near the end of the two records did the displacement histories converge to nearly the same value. This behavior supported the assumption that the debris near the apex of flight followed relatively similar ballistic trajectories despite the significant difference in initial velocities.

Two other aspects of the HIPS-5C experiment differed from the HIPS-2C observations. First, the HIPS-5C cavity remained intact throughout the experiment so that all of the debris exited from the cavity opening. Second, the HIPS-5C debris may not have been molten when it impacted the ground. Shortly after the debris reached the apex of the trajectory, the luminosity of the material decreased to a point where it could not be seen in the camera records. Furthermore, the debris did not splash on impact as seen in the HIPS-2C test.
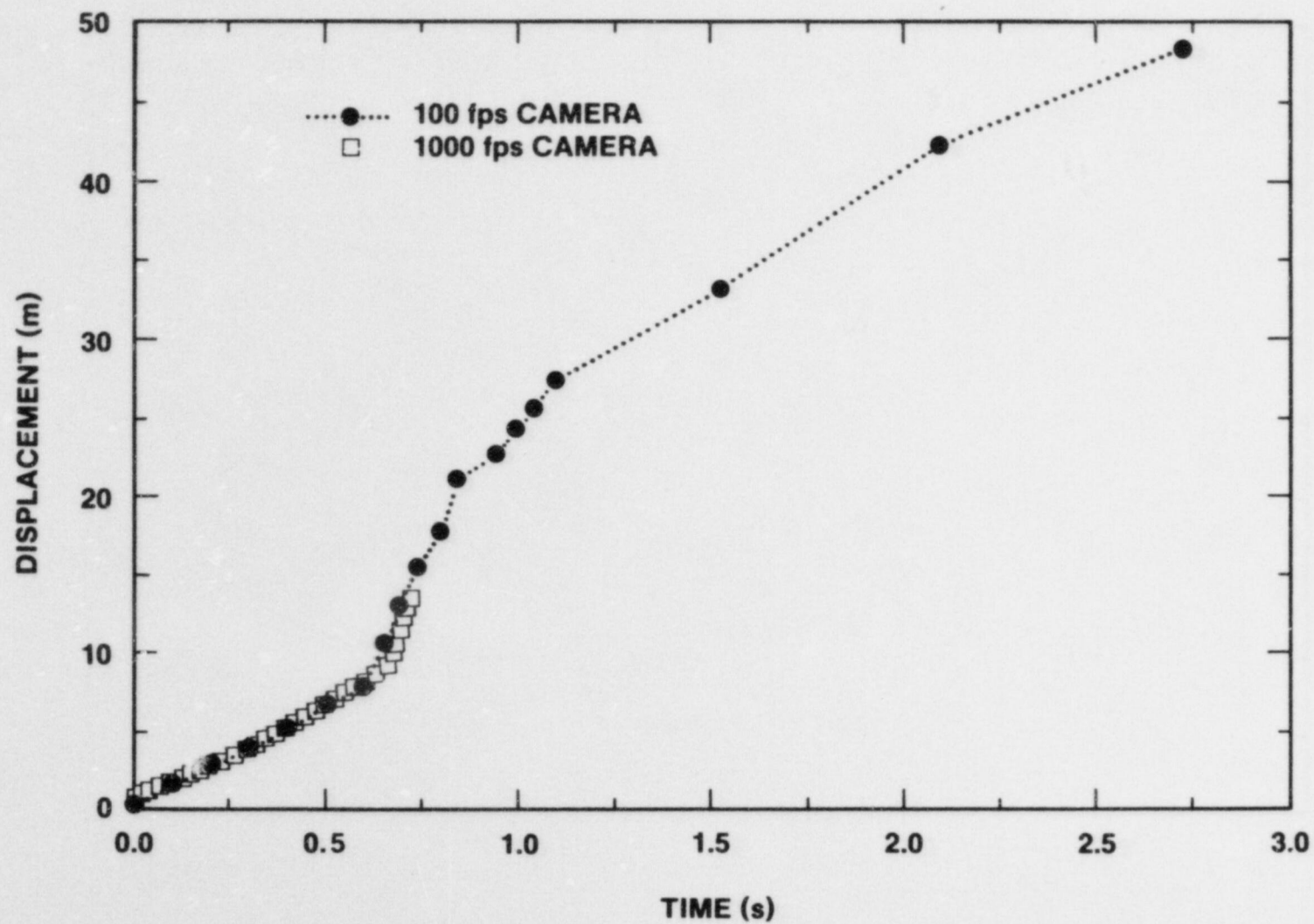
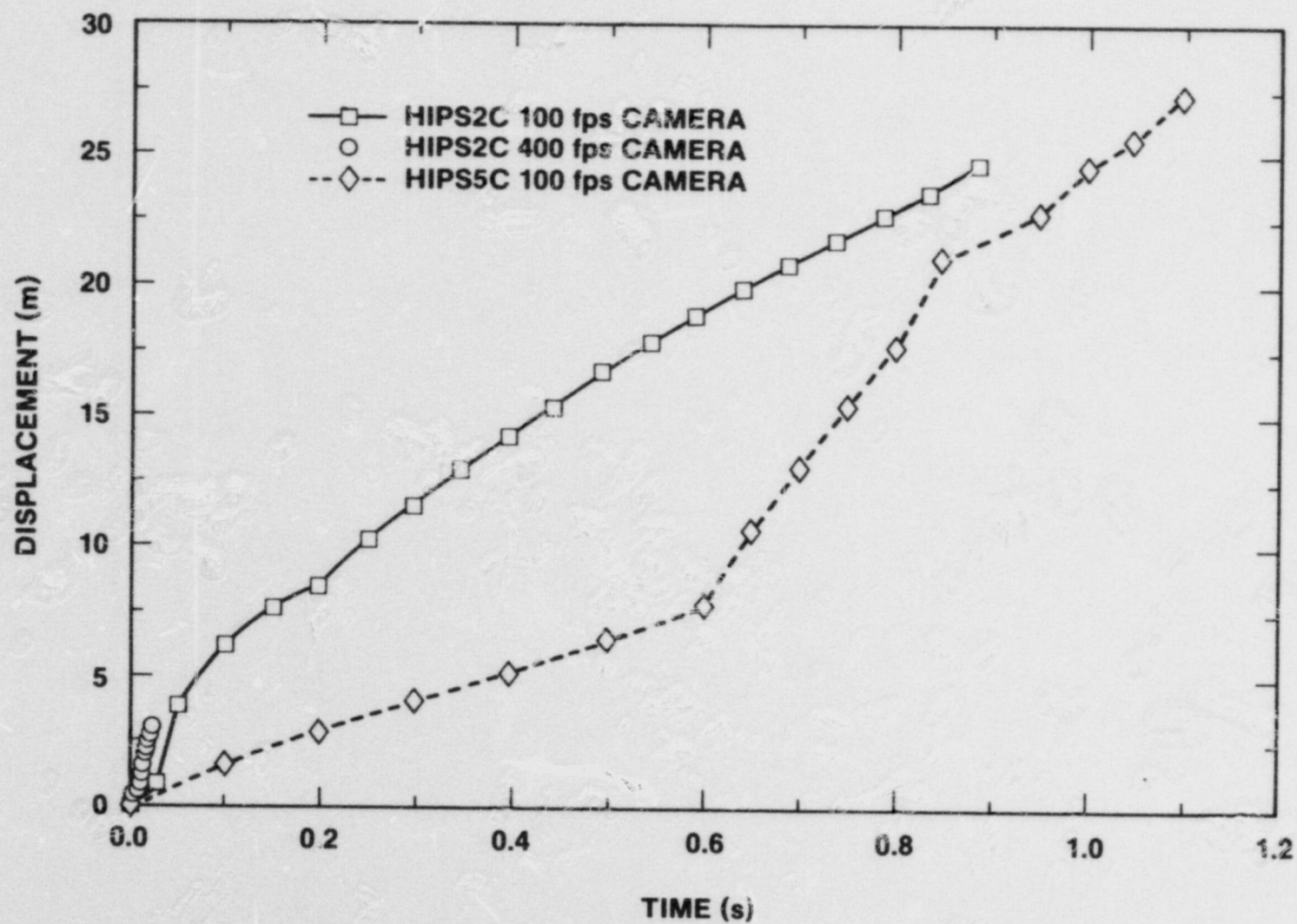FIGURE 24. HIPS-5C DEBRIS DISPLACEMENT VERSUS TIME

FIGURE 25. COMPARISON OF HIPS-2C AND HIPS-5C DEBRIS DISPLACEMENT

Comparison of the major events for the two tests (Tables 12 and 13) indicated a significant difference in the time interval for debris ejection. The interval in the HIPS-5C test was nearly 50 percent longer than that seen in the prior experiment. This longer interval was a consequence of the initially lower driving pressure which caused a longer blowdown period and diminished material velocity. The time corresponding to the apex of the debris trajectory was similar for both tests. The total time of flight for both tests may also have been the same, even though it could not be confirmed by the HIPS-5C film records.

The real-time X-ray record on the HIPS-5C test provided an indication of the debris behavior. The device was mounted to provide a view of the emerging material along the back edge of the cavity opening. This placement was not preferred because material that flowed along the forward surface of the inclined tunnel would not appear in the X-ray image. Other constraints prevented placement of the equipment in the preferred location. The highest film speed that could be used without significant loss of contrast was 1000 fps.

The X-ray record showed that instrumentation cables emerged from the cavity at least 100 milliseconds before the debris. The cables were not seen in the motion picture camera records because they were too small to detect in the large field of view. Debris was particles. The estimated size ranged from submillimeter to several centimeters in mean dimension. The image provided only a two-dimensional view of the objects, and therefore the actual shape was not clearly discerned. The average velocity of the particles was greater than could be accurately resolved at the film speed used. Velocity was estimated by comparison of particle displacements from one frame to the next. Average displacements of 6 to 10 centimeters were obtained in this manner. These values yielded velocities on the order of 60 to 100 meters per second.

The X-ray technique indicated higher particle velocity than that given by the high-speed camera data. Some error occurred in the process of converting the recorded high-speed camera images into usable results because they were not digitized directly. The overall error was estimated to be less than 20 percent.

The measured debris velocity was not significantly less than the estimated gas velocity out of the cavity. Gas that emerged from the cavity expanded both outward along the path defined by the tunnel inclination and in the radial direction as well. If the gas provided the driving force for the debris motion, then it would be expected that the debris would slow continually upward as the gas expanded. Based on the film camera records, the debris did not slow continually, but achieved a relatively

constant velocity that suggested the source was from initial momentum.

The X-ray record indicated that debris was dispersed from the cavity for a total of 563 milliseconds. This was considerably different than the 1.37 seconds given by the high-speed camera data. Two possible causes of the discrepancy were identified. First, the contrast of the X-ray image was proportional to the areal density of the material exposed. Thus, higher density materials and large size objects were more obvious than lighter or smaller items. Aerosol particles and heated gases would not appear in the X-ray image but would look like luminous debris in the high-speed camera records. Second, the location of the X-ray equipment prevented observation of material that escaped along the front edge of the cavity opening as might have occurred early in the sequence before melt entrainment caused by the blowdown of the melt generator. The X-ray record would then show the latter stages of the dispersal process when the high-velocity gas caused the entire cavity opening to be filled with small debris particles.

B. Melt Generator Pressure History

The pressure transducers placed in the upper flange cover of the melt generators allowed recording the pressurization and depressurization history for each experiment. The data were then used in calculations of jet velocity, debris dispersal, and gas blowdown. A simple model of the blowdown process was developed that considered the initial properties of the melt and gas, the dimensions of the system, and the physics of the ejection process including ablation of the aperture and gas coming out of solution. Details of the model are given in Reference 19.

The data from the SPIT tests differed significantly from the HIPS experiments because of the quantity of melt and gas involved. In addition, the SPIT-18 gas system incorporated an accumulator reservoir separated from the melt generator by a small diameter gas line. The accumulator was also used in the SPIT-19 test, but a check valve placed in the connecting gas prevented its contents from discharging after melt ejection. The HIPS melt generator did not incorporate any additional gas volume.

The pressure history for the SPIT-18 test is given in Figure 26. This record was characteristic of the behavior seen in most previous tests of this type with an initial slow increase in pressure to a stable value that subsequently increased upon the start of the thermite reaction. The influence of the
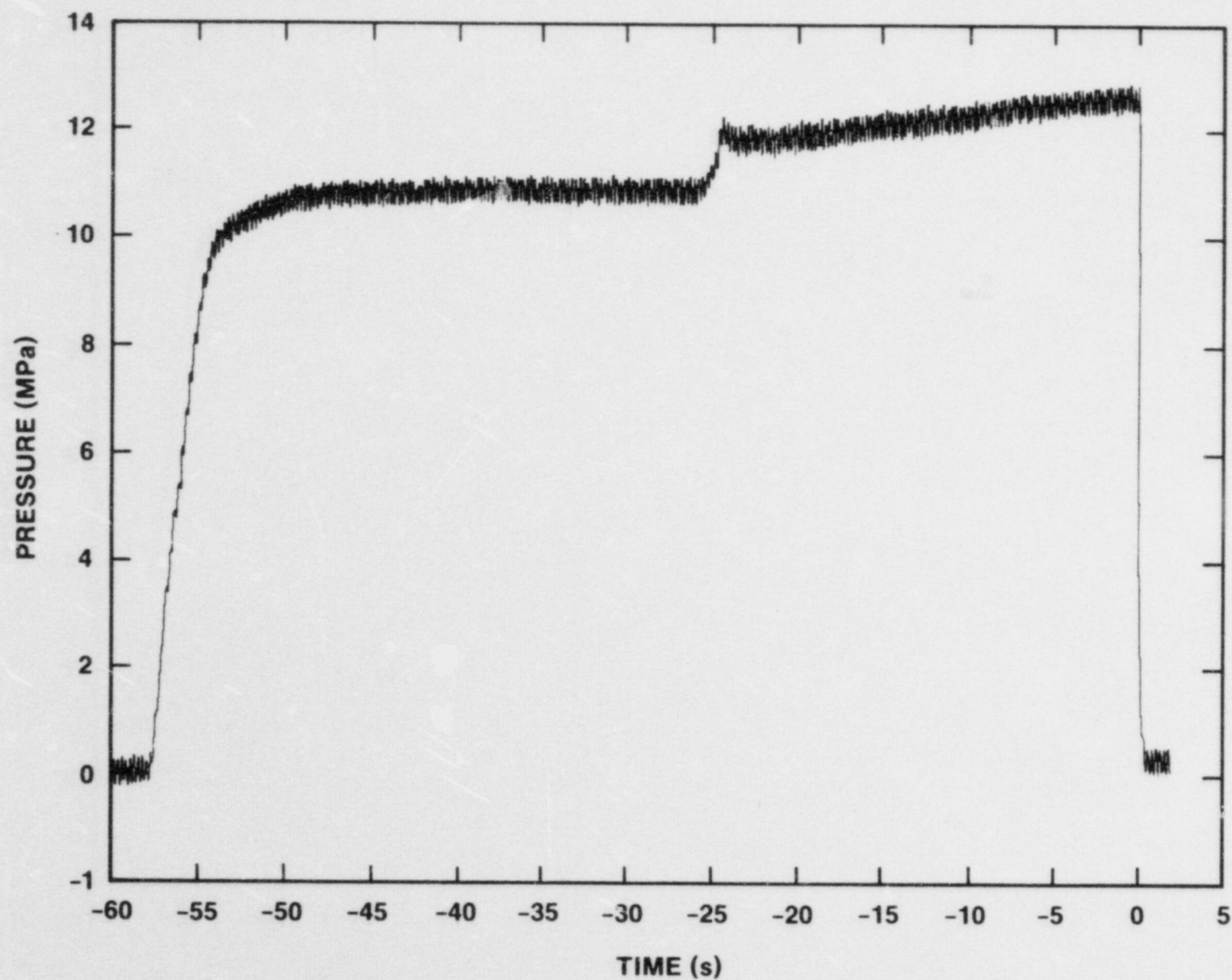
FIGURE 26. SPIT-18 PRESSURIZATION HISTORY

accumulator was observed by the relatively small overall increase in the pressure level prior to ejection. The large amount of noise on the trace was caused by interference from a 60-cycle source of unknown origin. This interference was removed by filtering during the reduction of the higher frequency data records.

Figure 26 shows that approximately 25.4 seconds after ignition, the fusible plug failed and the pressure level decreased rapidly as the melt and gas were discharged. The noise on the gauge trace made the actual pressure levels somewhat uncertain. It was estimated that the pressure was 11.3 MPa at the time of melt ejection. The discharge process was considered to occur in two stages: the first, before gas was discharged and the second, when the gas was expelled. Because the melt was discharged in less than 100 milliseconds, the pressure on this time scale appeared to decrease immediately.

The gas blowdown behavior on an expanded time scale can be seen in Figure 27. The pressure decreased relatively slowly in the first stage as little gas was expelled while the melt drained out of the vessel. When the melt depth decreased to some critical value, instabilities in the pool allowed the overlaying gas to penetrate the surface and be discharged. During this latter stage, the material leaving the vessel was assumed to be principally a gas stream laden with small drops of entrained melt. The transition between stages cannot be clearly seen in the Figure 27. Interference from an unknown electrical source distorted the pressure record at times greater than 520 milliseconds.

Film records indicated that melt was discharged from the cavity for a total of 560 milliseconds. The pressure record suggests that the blowdown occurred over a time interval of roughly the same duration.

The SPIT-19 pressurization history is given in Figure 28. It differed from the SPIT-18 record in that the period of elevated pressure prior to ignition was much longer as final adjustments in instrumentation were made. The blowdown of the melt generator on an expanded time scale is given in Figure 29. The pressure decrease was distinguished by the transition from melt to gaseous discharge (at ~250 milliseconds) as discussed above. The total time for blowdown was on the same order, but shorter, than seen in SPIT-18. The shorter interval was expected, because the accumulator volume was not allowed to discharge in the SPIT-19 experiment.

The pressurization record for the HIPS-2C and HIPS-5C experiments are given in Figures 30 and 31, respectively. In both cases the time required to achieve the initial pressure level was long, on the order of 100 seconds or more. This was
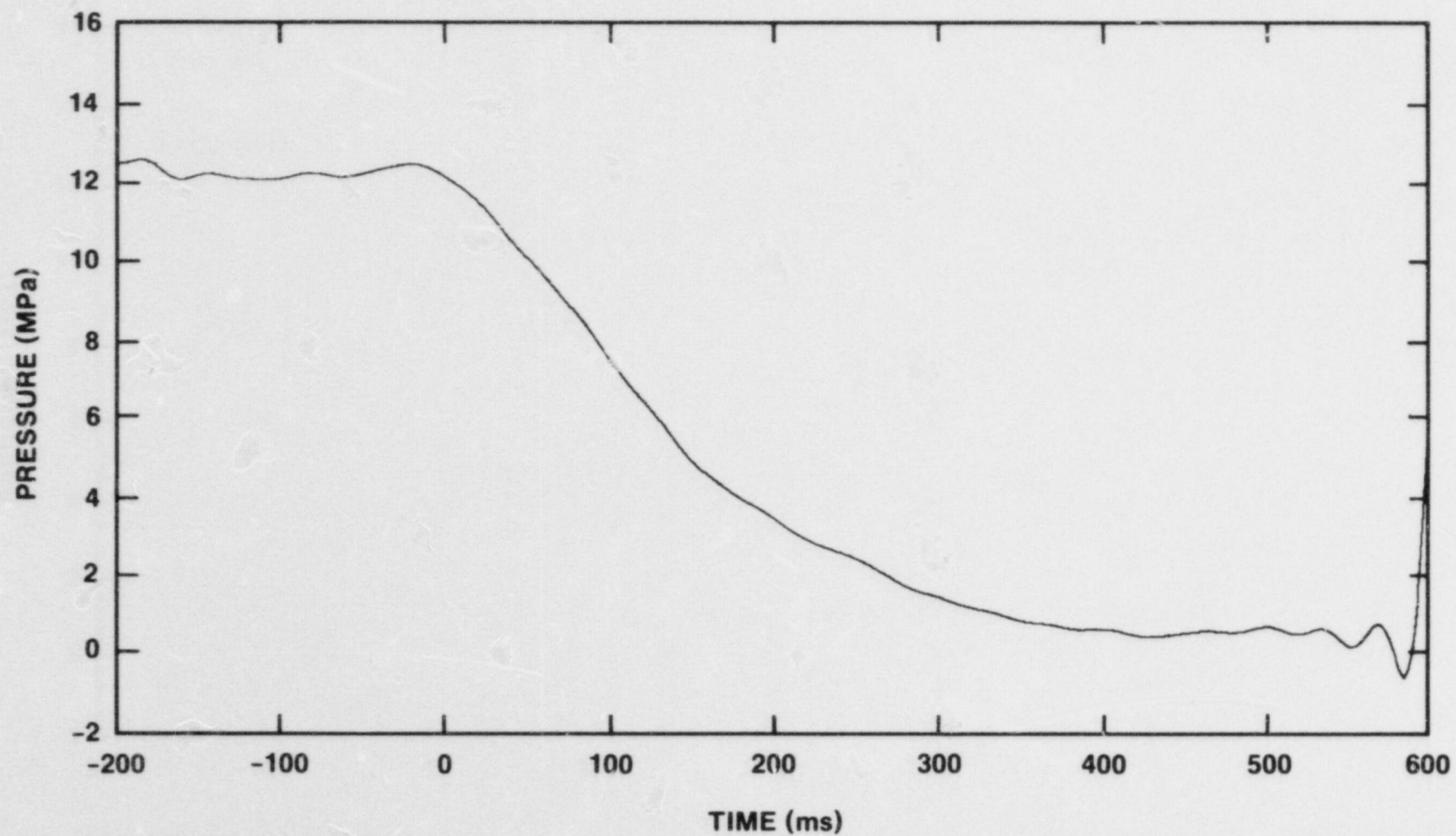
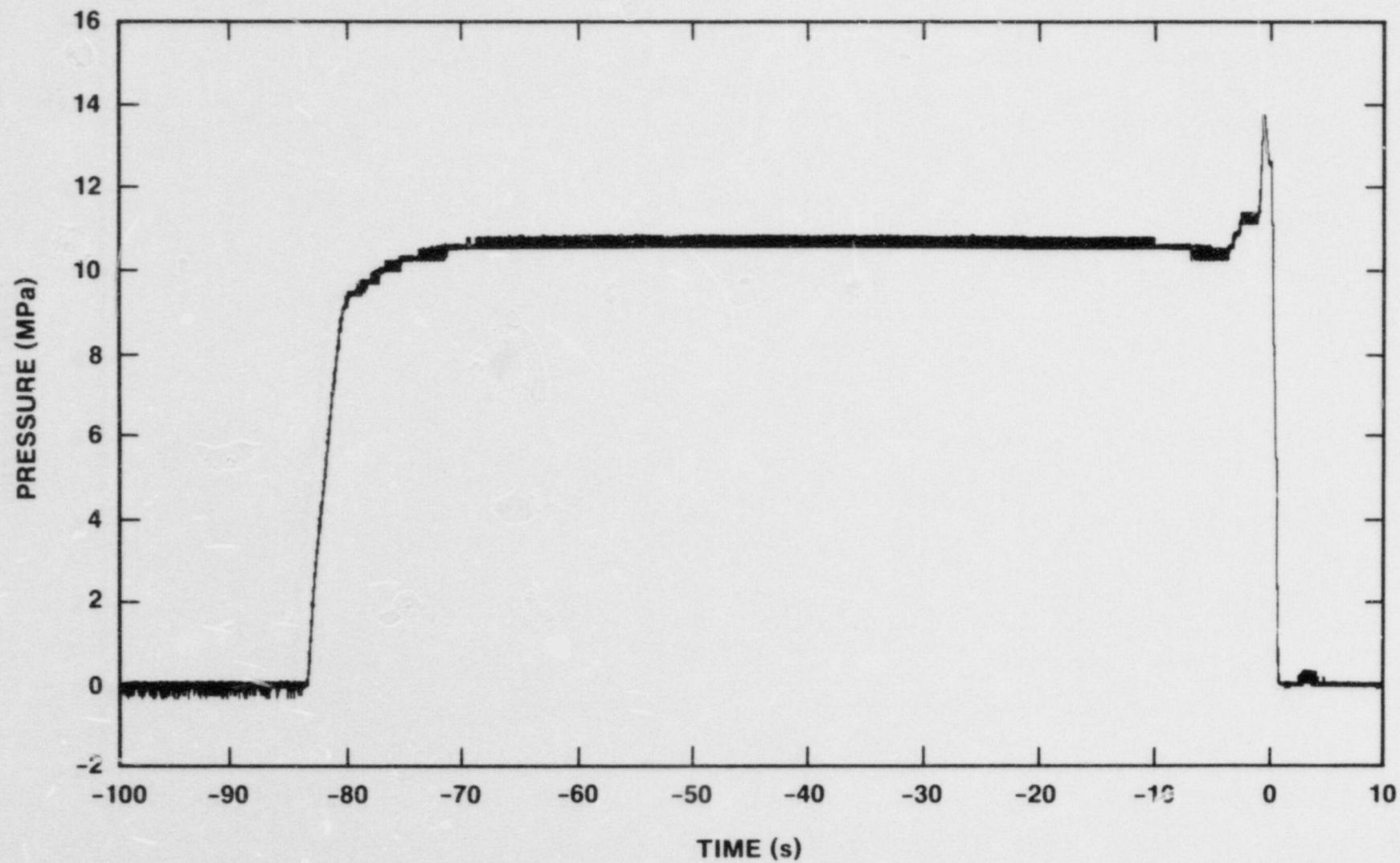FIGURE 27. BLOWDOWN RECORD OF SPIT-18 MELT GENERATOR
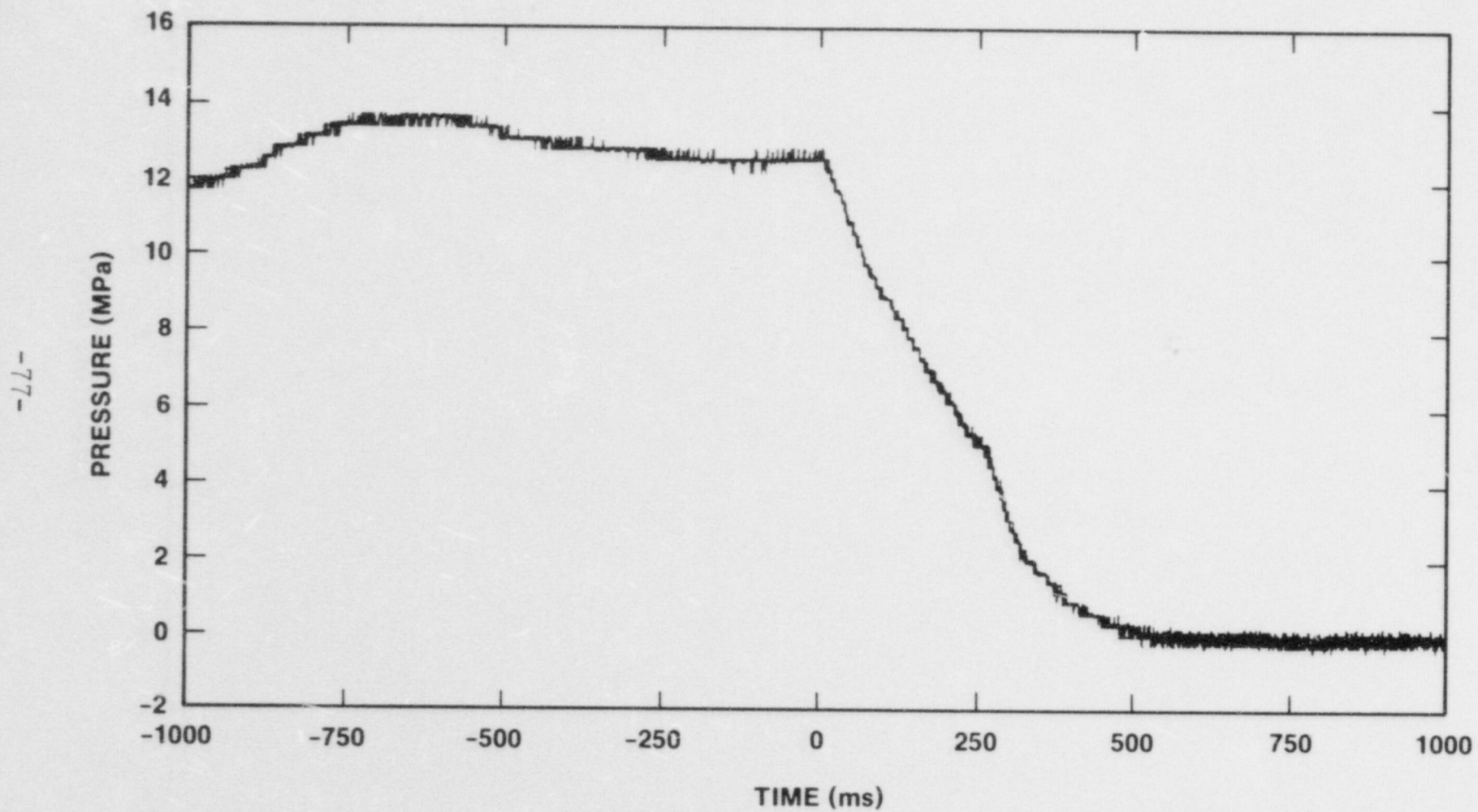
FIGURE 28. SPIT-19 PRESSURIZATION HISTORY

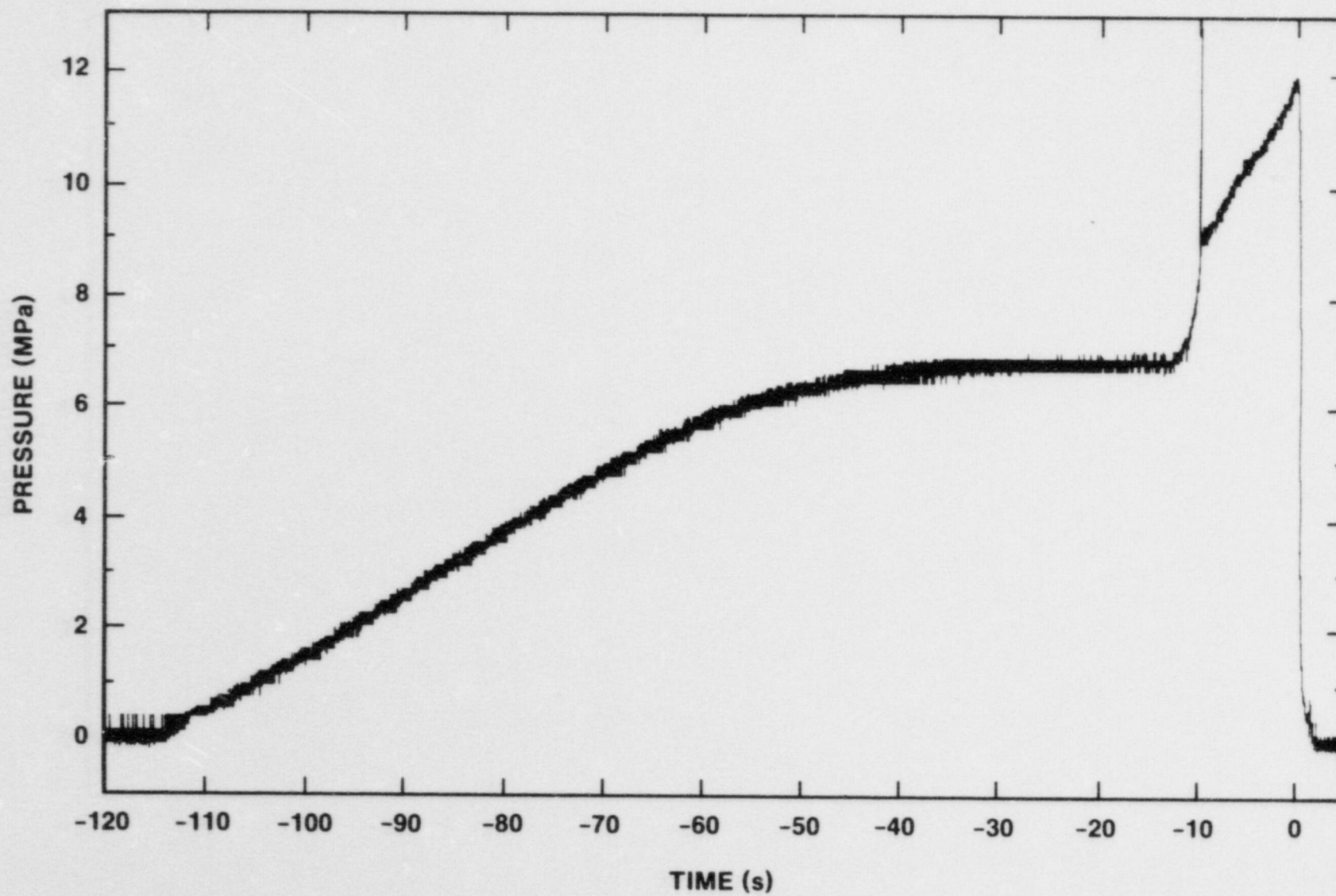FIGURE 29. BLOWDOWN RECORD OF SPIT-19 MELT GENERATOR
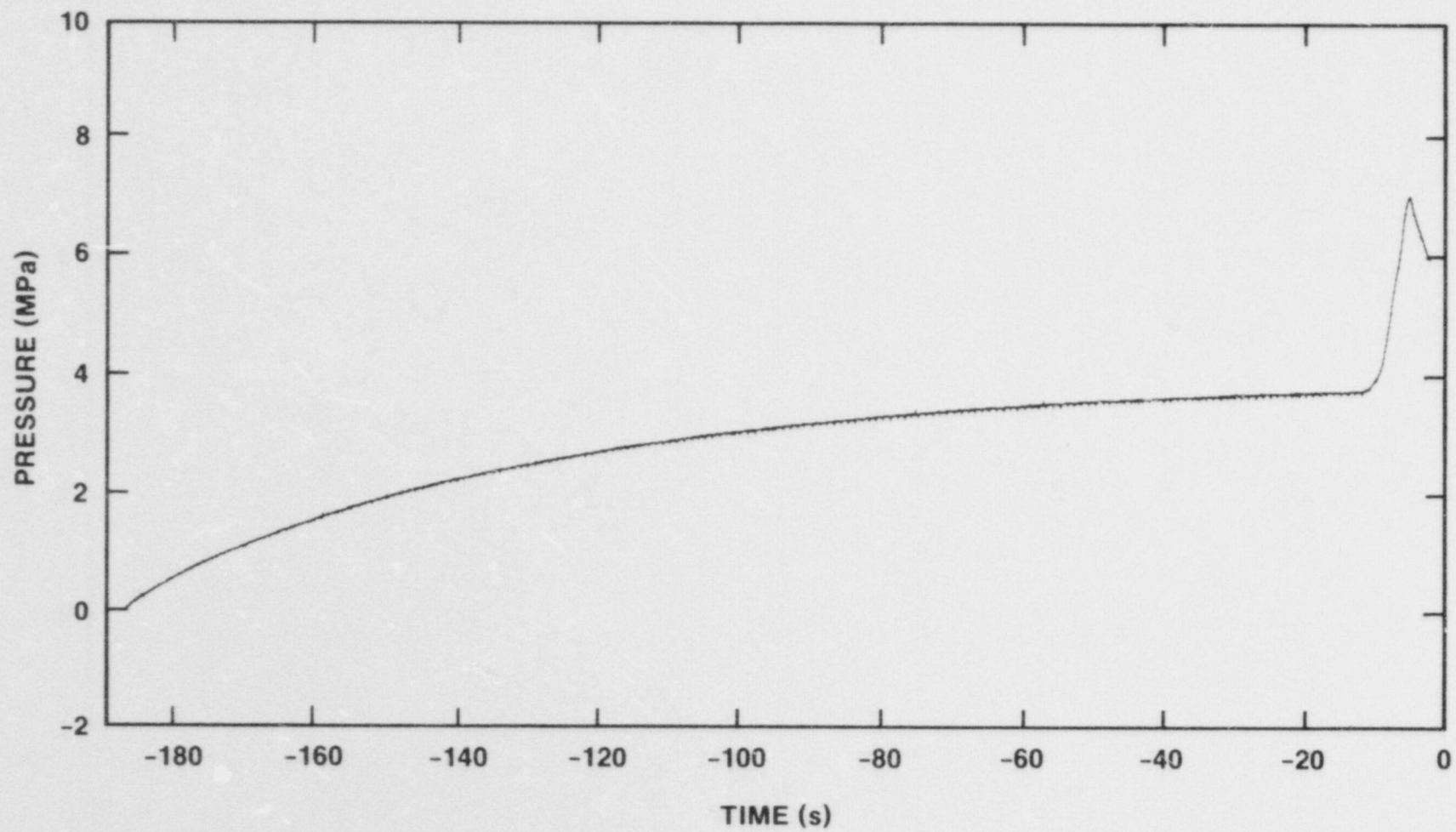
FIGURE 30. HIPS-2C PRESSURIZATION HISTORY

FIGURE 31. HIPS-5C PRESSURIZATION HISTORY

caused by the large free volume of gas in the melt generator, the high pressure level of the HIPS-2C experiment, and the slower fill rate using carbon dioxide gas. In this case, the gas was formed by the expansion of liquid carbon dioxide from a standard bottle.

The blowdown histories are given for HIPS-2C and HIPS-5C in Figures 32 and 33, respectively. For time prior to the inflection point, the curvature in each plot was different, i.e., concave up or down depending on the behavior of the metal insert piece that contained the fusible plug. In the HIPS-2C experiment, however, the initial size of the exit aperture increased by the ablative action of the flowing melt. Thus, the mass flow rate continually increased with time during the HIPS-2C melt discharge. This behavior resulted in the observed increase in slope of the pressure-time curve. In contrast, a graphite insert was used in the HIPS-5C test to minimize the ablation of the plate. The diameter of the aperture was thus prevented from significant expansion beyond the original size. Therefore, the flow rate in the HIPS-5C test followed a characteristic isentropic tank blowdown behavior until the pressure level dropped below the critical value.

An analytical evaluation of the two HIPS tests is given in Figure 34. Here selected data points were obtained from the recorded pressure data to compare to theoretical predictions of the melt discharge and gas blowdown. The close agreement of the calculated and experimental points of inflection showed that the model treated the melt ejection, hole ablation, and gas discharge correctly. The greatest uncertainty in these calculations was the temperature of the melt used as an input condition. In addition, the theoretical and experimental blowdown histories following the onset of gas flow depended on the aperture size. The good agreement of this phase indicated that the calculated hole size was comparable to the observed value.

C. Ablation of the Exit Aperture

Growth of the breach formed in the lower head of the reactor pressure vessel is important in determining the flow of melt and gas into the cavity region. The Zion Safety Study[2] predicted a tenfold increase in the initial 4.7 centimeter diameter hole during the interval of melt discharge. The aperture size at the end of melt ejection determined the gas flow rate during system blowdown and hence the dispersal of core debris from the cavity. The code mentioned in the previous section incorporated a model to describe ablation of the exit aperture.[20] Failure of the brass fusible plug caused the surface of the machined hole to be exposed to the melt exiting the vessel.
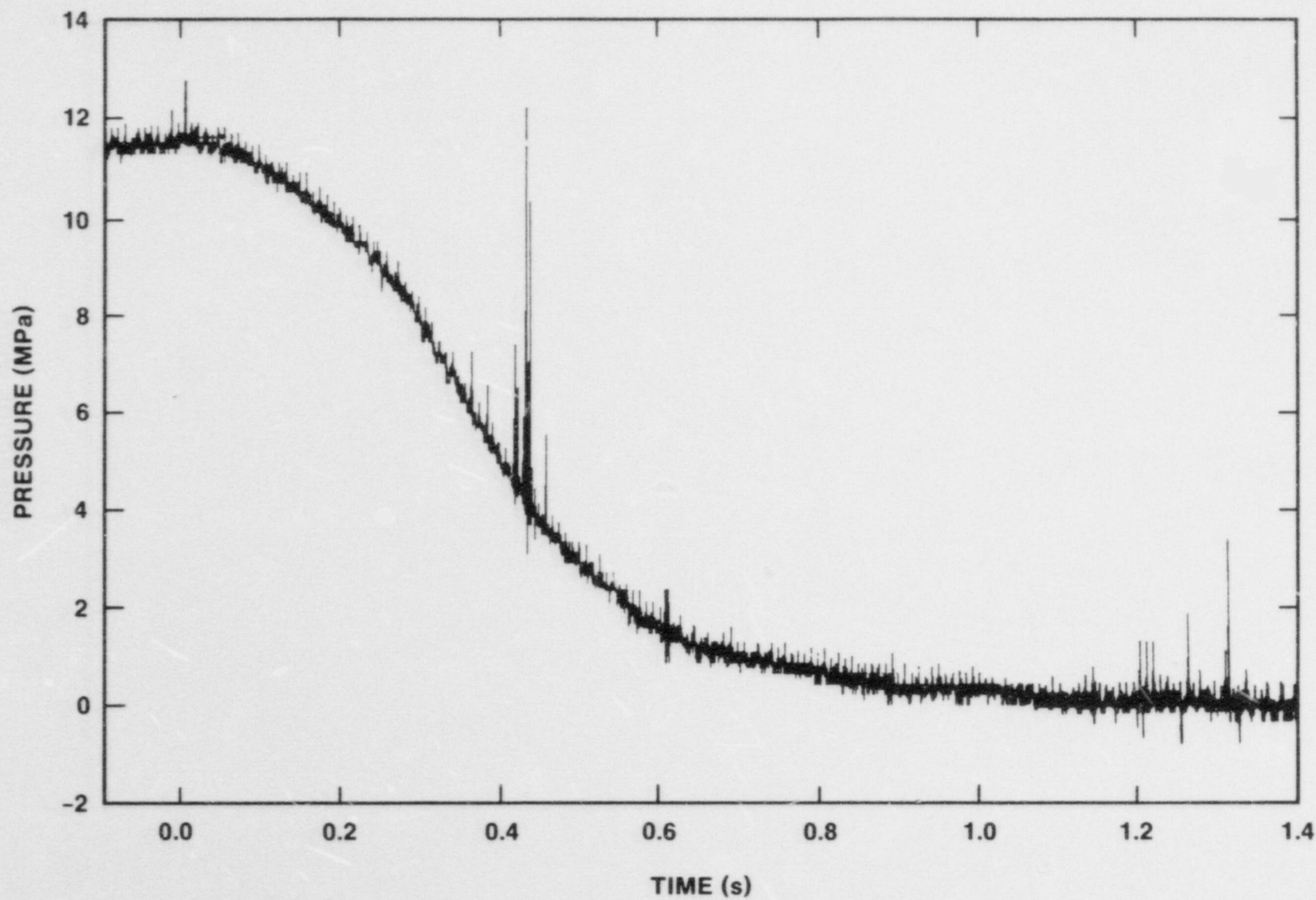
-80-

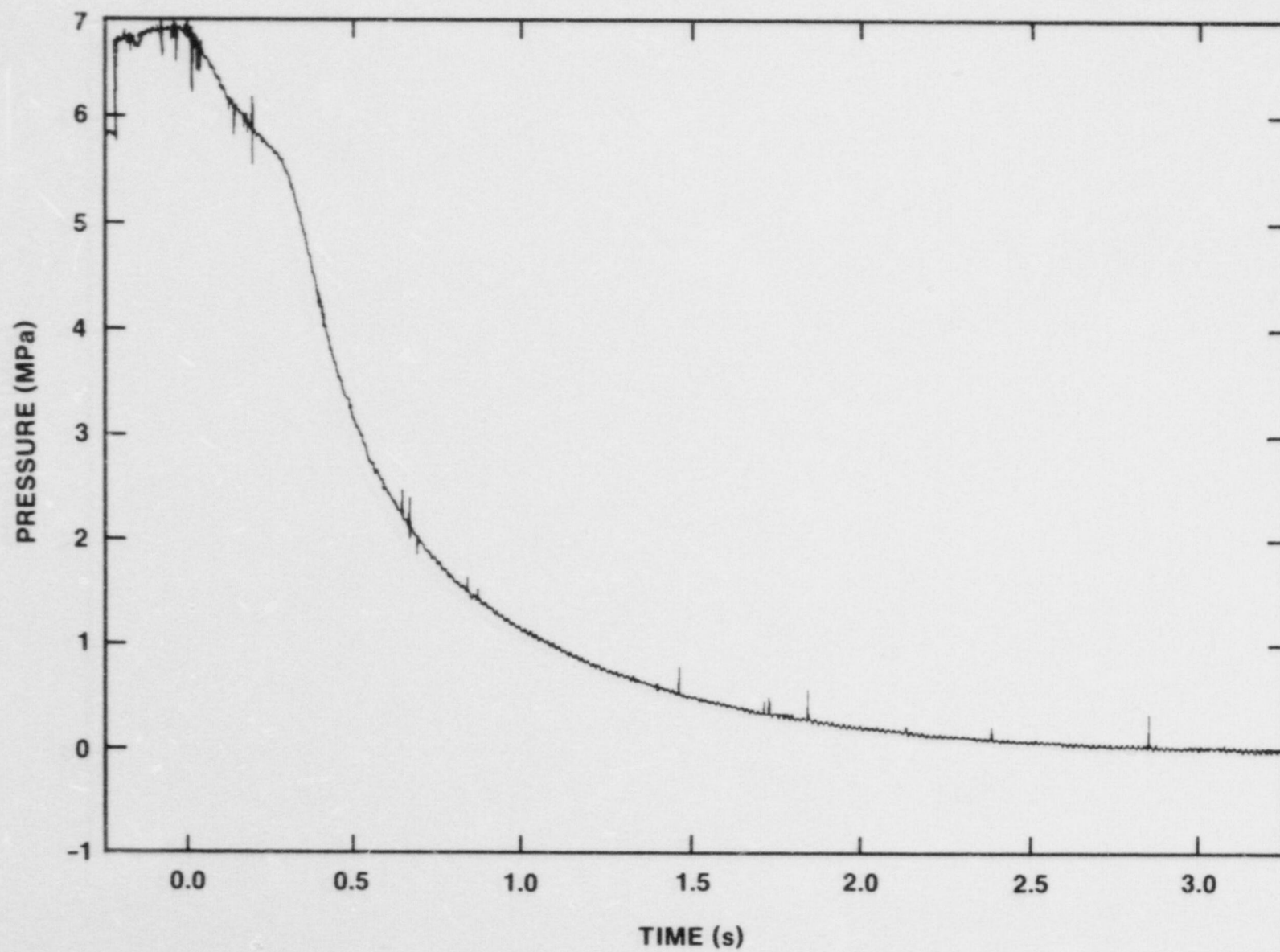FIGURE 32. BLOWDOWN RECORD OF HIPS-2C MELT GENERATOR

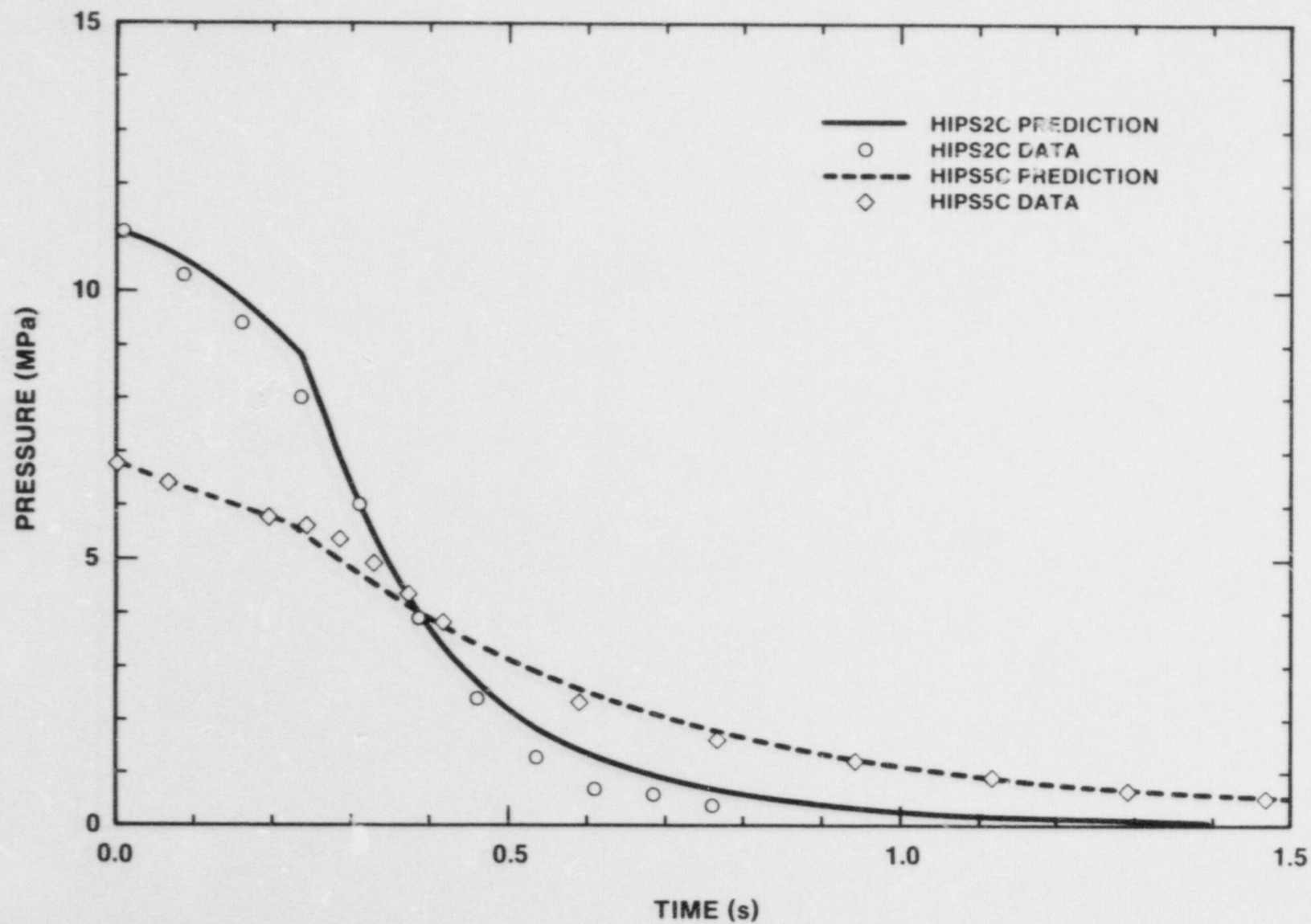FIGURE 33. BLOWDOWN RECORD OF HIPS-5C MELT GENERATOR

FIGURE 34. ANALYTICAL CORRELATION OF HIPS BLOWDOWN

The HIPS-5C plate was nominally 5.08 centimeters thick while all of the other experiments used 2.54 centimeter thick material. Figure 35 is a photographic comparison of an unused aperture plate and one removed from the HIPS-2C test apparatus. The amount of material removed was extensive, considering the relatively small melt mass of the one-tenth scale tests. The formed hole was somewhat irregular in shape, tapering to a larger diameter towards the outside of the vessel. The inner surface (shown) exhibited a small raised ridge at the perimeter of the eroded material. The exposed surface in the hole was not a frozen layer of melt as predicted by several analytical studies, but was the material of the plate with a somewhat roughened texture. The lighter color of the exposed surface was a thin layer of the refractory dry ram from the melt crucible. The outside surface of the plate (not shown) was similar in appearance except that a few drops of melt were adhered to the plate.

The results of the analytical prediction for the HIPS-2C aperture ablation are shown in Figure 36, in terms of hole size as a function of time from start of melt discharge. The results indicate that the calculated aperture dimension expanded from the initial 2.54 centimeter diameter to about 6.3 centimeters in 230 milliseconds. The average dimensions of the actual hole in the plate illustrated in Figure 35 was in the range of 6 to 7 centimeters.

D. Incident Heat Flux from Melt Ejection

In both the hypothesized accident and in the experiment, the jet emerging from the exit aperture was directed at the floor of the cavity. Energy imparted to a concrete surface can potentially cause degradation of the material such as spallation, decomposition, and melting. Measurement of the jet heat flux in the experiment provided an estimate of that expected in a reactor accident. Such information was not acquired in any of the tests reported here, but was accomplished in several previous SPIT experiments where the jet was allowed to freely expand from the melt generator.[8] In these tests, the incident heat flux was inferred from thermocouples embedded in a graphite slug calorimeter. The temperature records were digitized and employed in an inverse heat conduction analysis.[18] The technique was inherently handicapped because of the long thermal response time of the graphite block compared to the duration of jet impingement, but the hostile nature of the environment during melt ejection eliminated other techniques from consideration. The uncertainty in the measurement depended on the accuracy of
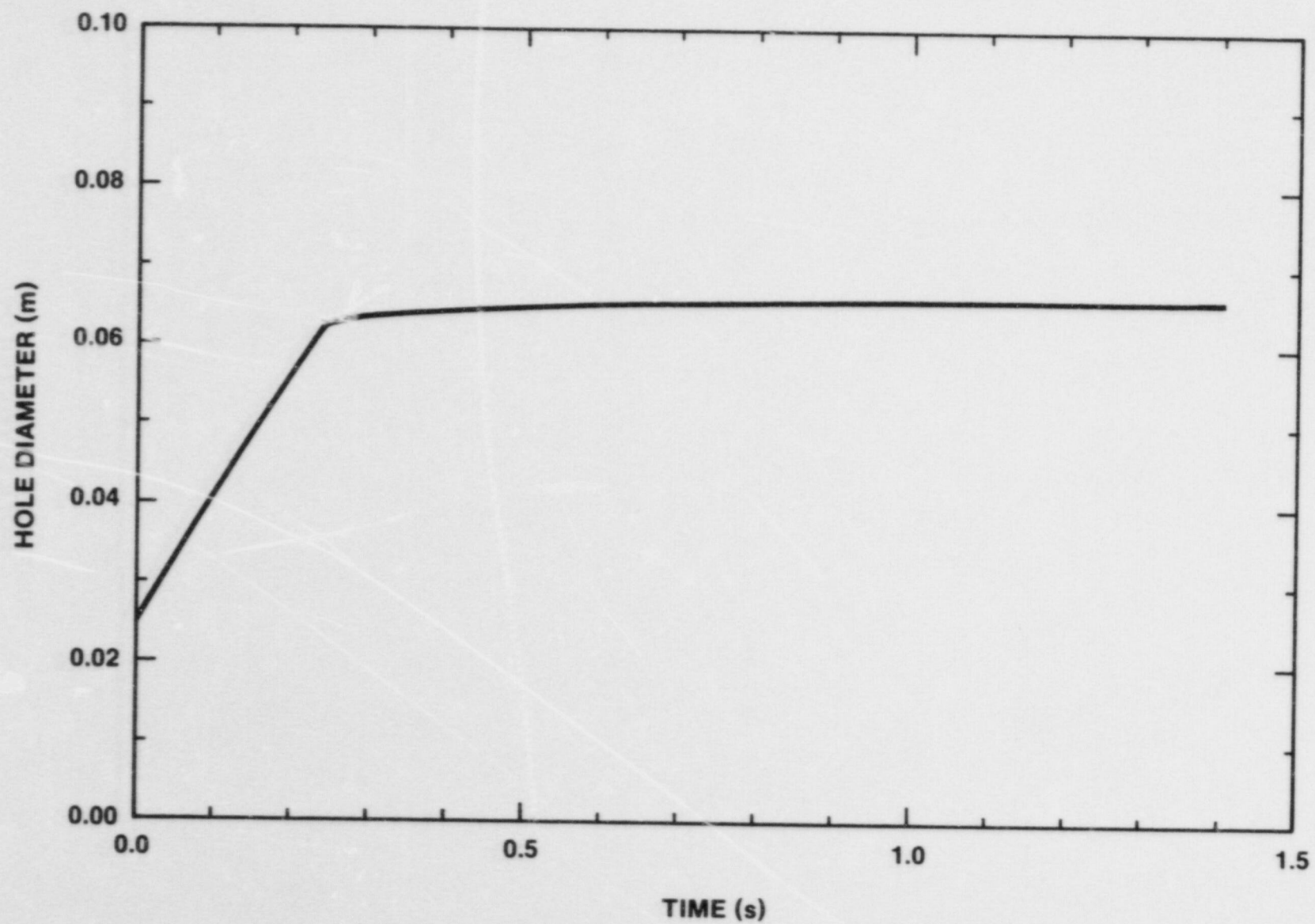
FIGURE 36. PREDICTED APERTURE GROWTH FOR THE HIPS-2C TEST

the thermocouple placement and the precision of the temperature readings.

The heat flux results are given in Table 14 for three SPIT tests that represent a wide range of initial conditions. The results are in terms of the calculated peak heat flux at the front surface of the calorimeter. These values were compared to an empirical correlation for the incident heat flux from a stagnating jet onto an ablating surface.[21] The agreement between the two sets of results is good considering the wide range of initial conditions. The heat fluxes shown were considered high enough to cause ablation of reactor grade concrete surfaces. Concrete ablation, however, will be accompanied by vigorous gas generation that may inhibit the heat transfer from the jet to the surface. If outgassing occurs, the empirical correlation and graphite calorimeter results overpredict the heat flux incident on the concrete and hence the extent of material attack.

Table 14
Peak Incident Heat Flux

| | | | HEAT FLUX | |
| TEST | PRESSURE (MPa) | ESTIMATED VELOCITY* (m/sec) | Calculated from TC Data | Theoretical[21] |
			$(MJ/m^2$-sec)	
SPIT-12	5.4	32	16.3	18.0
SPIT-13	17.0	56	19.7	23.2
SPIT-14	1.7	18	13.4	13.1

$$* \ V = C_d [2 \ \Delta P/\rho]^{.5}$$

C_d = discharge coefficient
ΔP = pressure difference across aperture
ρ = density of melt (3800 kg/m^3)

Only limited concrete ablation (less than one centimeter) was found in the three cavities used in these tests, and only in

the region directly beneath the melt generator aperture. This observation suggested that more extensive attack was prevented by the development of a stable crust on the cavity surfaces in conjunction with the short duration the molten pool was in contact with the concrete surface. The crust formed in the alumina test was significantly thicker than in any of the concrete experiments. The alumina was presumed to lose relatively little gas at the temperatures involved in these tests. Extending these results to reactor scale show that only a small fraction of the core mass will be retained as a crust layer on the cavity walls and floor.

The melt ejection time interval was on the order of 100 milliseconds in the SPIT tests and about 250 milliseconds for the HIPS experiments. Dispersal of the debris in all cases occurred in less than 500 milliseconds. The limited duration of melt residence in the cavity prevented extensive heat transfer to the crust layer covering the exposed surfaces.

E. Debris Dispersal

Debris dispersal (lack of debris retained in the cavity) was obtained by performing a mass balance on the material that remained in the melt generator and cavity following the test. The sum of the two quantities was subtracted from the initial mass to give the amount dispersed from the cavity. Collecting the debris from the interaction chamber would have provided the dispersed mass directly, but some material escaped from the damaged areas. Section III-A describes the overall appearance of the material that emerged from the cavity. This section provides details of the nature of the debris with regard to debris size distribution, temperature, and chemical composition.

Table 15 summarizes the debris dispersal results from the four tests. The results for the amount of material dispersed were based on the quantity of debris in the cavity and melt generator. The values were considered accurate to within 5 percent principally because of the uncertainty in quantifying the mass of the crust layer and the difficult distinction between melt residue and the other materials in the melt generator. In some cases it was difficult to distinguish frozen debris from portions of the apparatus that had melted during the reaction.

Table 15
Debris Dispersal from Scaled Cavities

TEST	SCALE	MASS (kg)	PRESSURE* (MPa)	CAVITY MATERIAL	AMOUNT DISPERSED (%)**
SPIT-18	1:20	10.3	12.6	Alumina	58
SPIT-19	1:20	10.3	12.6	Concrete	95
HIPS-2C	1:10	80.0	11.7	Concrete	99
HIPS-5C	1:10	80.0	6.8	Concrete	99

* Melt generator pressure at ejection
** Percentage of initial mass in melt generator

All three concrete cavity models exhibited debris dispersal greater than 95 percent. The SPIT-19 data were affected significantly by the large globules found at the base of the upward inclined tunnel section. The mass retained in the alumina cavity (SPIT-18) was primarily in the form of a solidified crust on the exposed surface of the brick.

The Kutateladze number (Ku) provides an indicator of the potential for debris dispersal by particle entrainment and other mechanisms. It was predicted that a Kutateladze number greater than ten was needed to disperse material from the cavity. Figures 37 and 38 illustrate the calculated Kutateladze numbers versus time for the reactor case and the four experiments considered here. In Figure 37 the gas in the tunnel region was assumed to be the same temperature as the melt (2800 K) while in Figure 38 the temperature was set at the value measured in the melt generator (300 to 400 K). The time is given on a log scale from just after the start of the melt ejection sequence (t=0.01 seconds).

The plots show that the threshold for dispersal (Ku>10) was not exceeded when only melt was flowing from the vessel, prior to gas blowdown. During this interval, the velocity of the
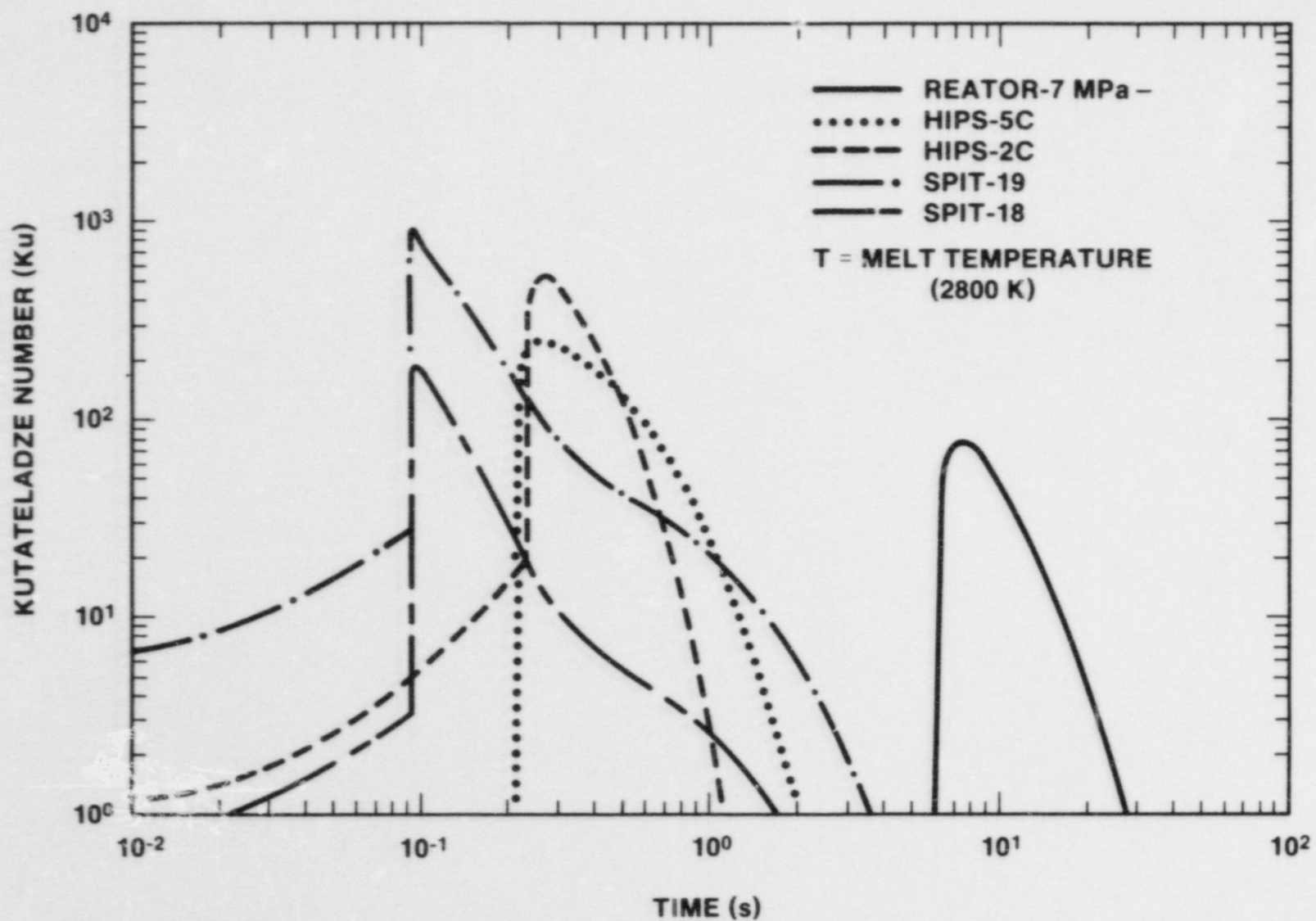
FIGURE 37. CALCULATED KUTATELADZE NUMBERS FOR EXPERIMENTS
AND ACCIDENT (T = Tmelt)

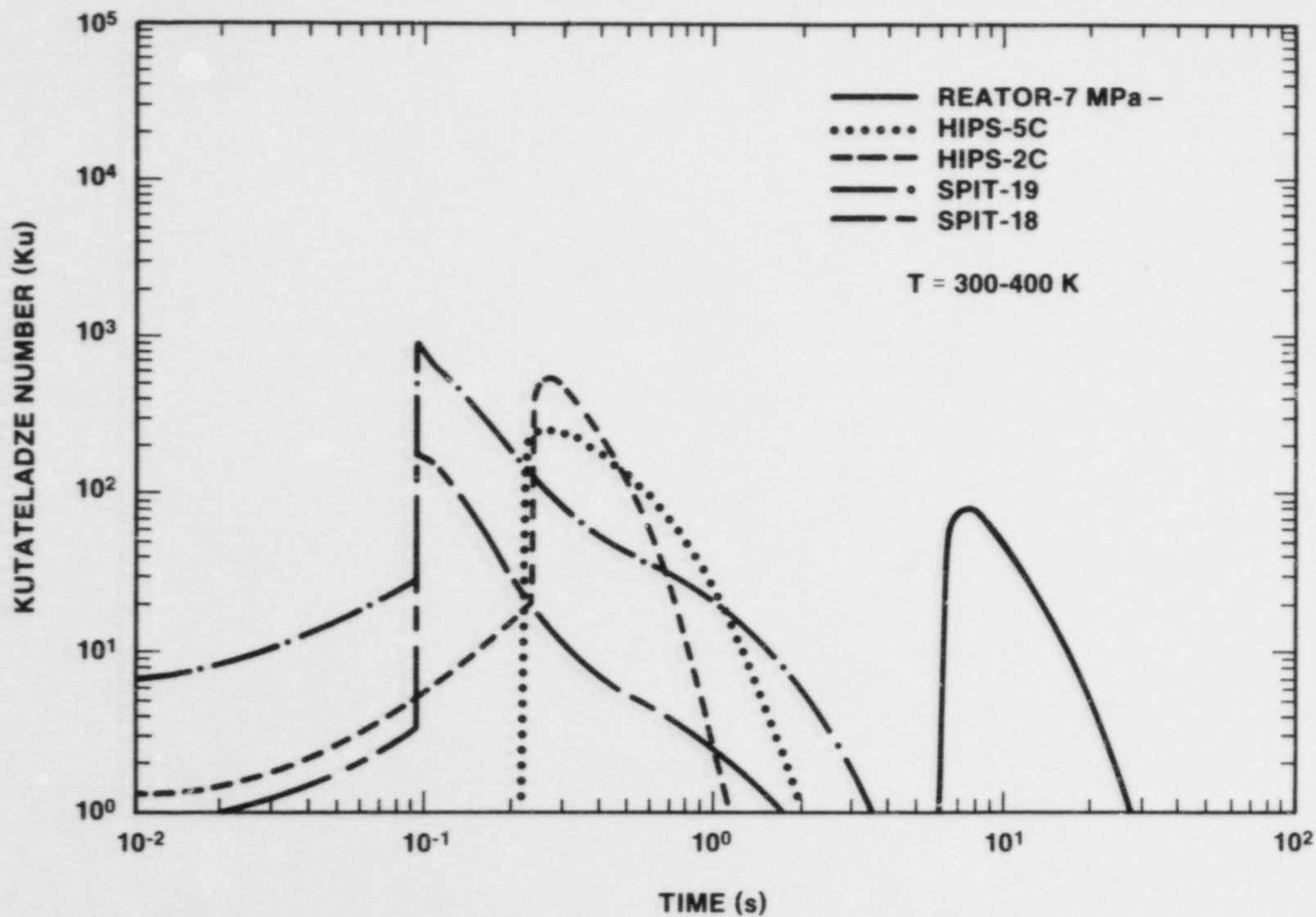FIGURE 38. CALCULATED KUTATELADZE NUMBERS FOR EXPERIMENTS AND ACCIDENT (T = 300–400 K)

effervescing gas was small.   At the onset of gas discharge, the velocity in the cavity region rapidly increased to a level sufficient to exceed Ku=10. Although the threshold for dispersal was exceeded in all tests, the time interval for each was significantly different based on the volume of melt and gas. Because of their relative size, the onset of gas discharge occurred earlier in time for the smaller scale, but the small aperture in the SPIT tests caused the blowdown phase to be more protracted than in the two HIPS experiments.   For the reduced temperature case (Figure 38), the greater gas density caused a reduced velocity through the cavity which produced smaller Kutateladze numbers.

Figures 37 and 38 do not show the extent of material dispersed, but only the threshold for dispersal. The amount of debris dispersed was obtained analytically by calculating the acceleration of a particle induced by the high-velocity gas in the cavity. Figure 39 gives the results of the calculation of the mass ejected from the cavity for each of the four tests and for the reactor case.   The calculations were based on the gas density and velocity, and the debris particle size. The plots show that the bulk of the mass released from the pressure vessel was removed by the action of the gas blowdown. For this example, the reactor pressure vessel was assumed to be initially at a pressure of 7 MPa and discharged a 80,000 kilogram mass of molten core debris.

The X-ray images from these tests indicated that the debris were in the form of highly fragmented particles, with the fragmentation well developed within a short distance of leaving the cavity.   The small size of the particles and their wide spatial distribution in the gas stream indicated a high potential for energy exchange with the surrounding atmosphere. Characterizing the debris size and behavior should determine to a large extent the energy given up as the debris propagates through the atmosphere.

Flash X-ray photographs provided high resolution information of the material exiting the cavity by showing a discrete view isolated in time from other information.   The resulting photographs represented a two-dimensional view of a three-dimensional object, but without the interference of high luminance or obscuring aerosols.   Figure 40 shows radiographic images from the SPIT-19 and HIPS-2C experiments.   In these photographs the contrast level has been reversed so that the debris appeared dark against a light background.   The magnification was the same in both pictures, with the vertical height of the frame being nominally 40 centimeters. The timing of the two photographs was different; 45 milliseconds after the start of ejection for SPIT-19 and 250 milliseconds after ejection for HIPS-2C. These time delays were selected as approximately the midpoint of the debris discharge interval.
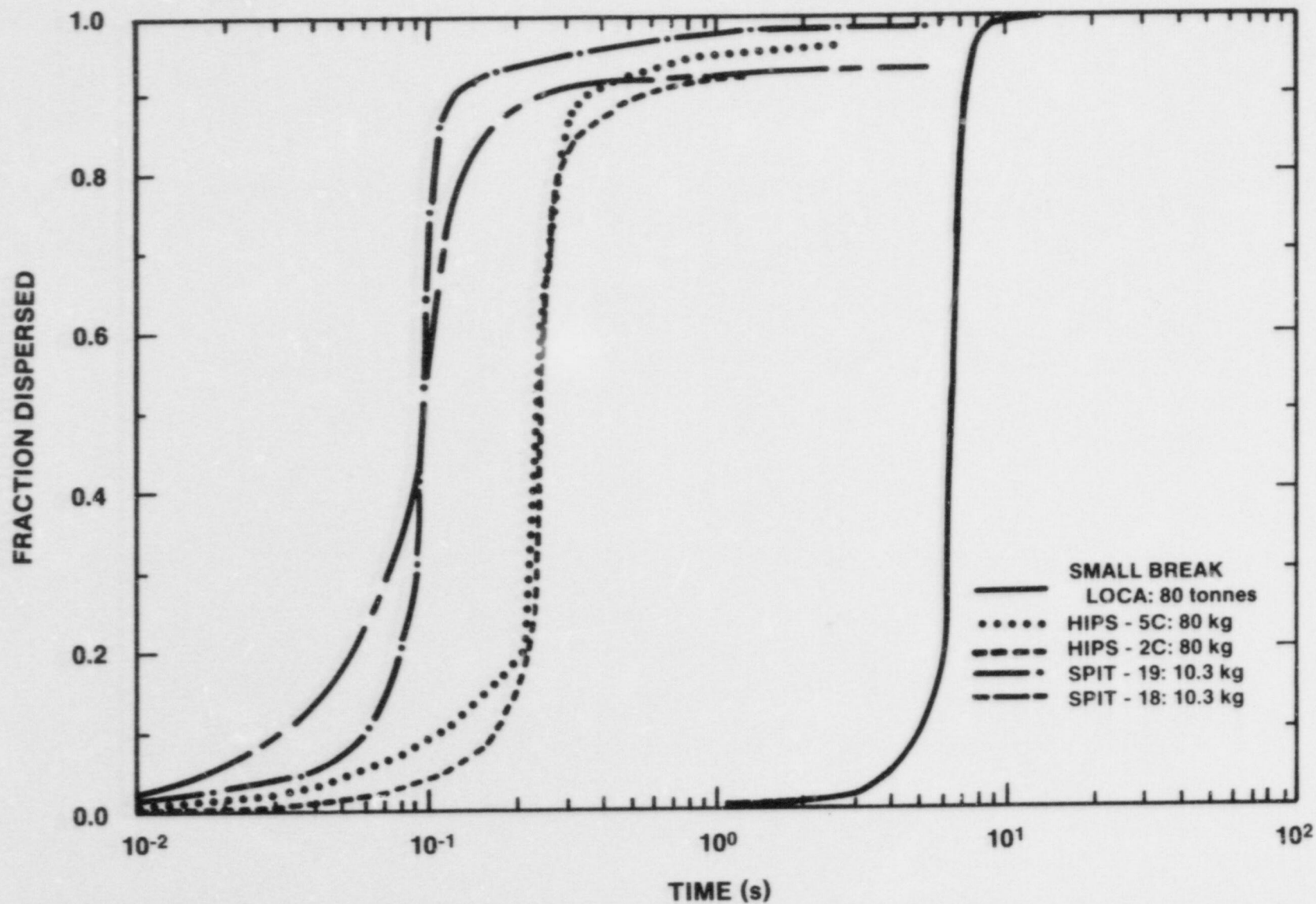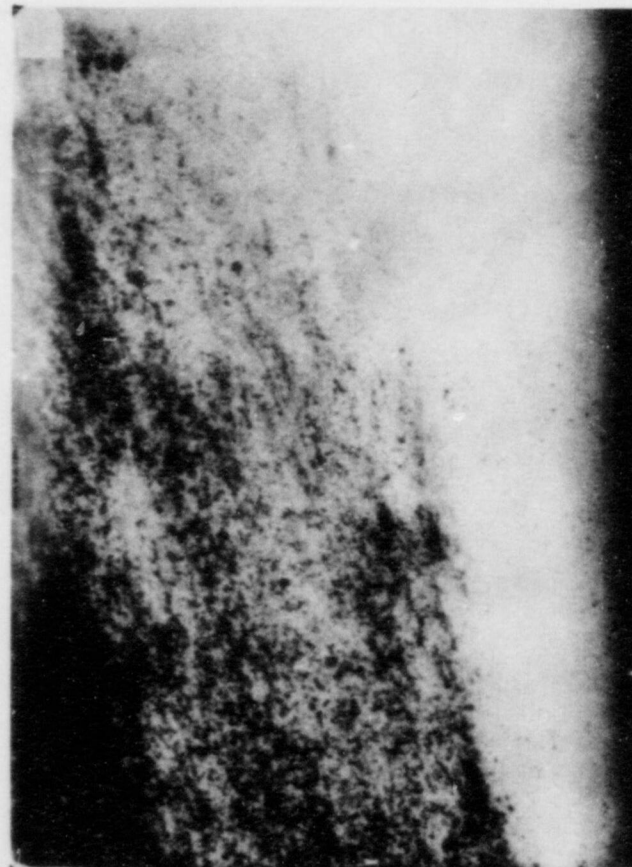
FIGURE 39. CALCULATED MASS EJECTED FROM EXPERIMENT AND REACTOR CAVITIES

SPIT-19
M = 10.3 kg
P = 12.6 MPa

HIPS-2C
M = 80.0 kg
P = 11.6 MPa

FIGURE 40.   X-RAY SHADOWGRAPHS OF DEBRIS EMERGING FROM SCALED REACTOR CAVITIES

The photographs show that the HIPS debris stream was much larger than the SPIT image, as expected from the greater size of the HIPS cavity opening. In both cases, the stream followed the trajectory defined by the angle of the cavity exit. For SPIT-19, the image was taken at an angle of approximately sixty degrees rotated from the longitudinal centerline of the cavity. The resulting image was therefore at an oblique angle from the plane parallel to the direction of debris propagation. The "T" shaped object was a machine bolt placed 2.5 centimeters in front of the edge of the cavity opening, along the longitudinal centerline of the apparatus. The distorted angle of observation caused the bolt to appear as if it were in the debris stream.

The radiograph showed that the material discharged from the SPIT-19 cavity was a highly fragmented stream of particles. The original exposed film was scanned with an optical density device to estimate particle size. Ten measurements taken randomly over the image yielded a particle diameter of 0.9 ±0.5 millimeter. The uncertainty came principally from the lack of edge contrast in the photograph. The long string-like material near the cavity exit was from incomplete fragmentation. These become less common with increased propagation distance indicating that the fragmentation process continued outside of the cavity.

The HIPS-2C radiograph was from one of six attempted on the test, arrayed in two horizontal rows of three cassettes. The position of this cassette was in the upper row viewing the back edge of the melt stream. Thus the photograph did not show the apparatus in its field of view because the lower edge of the cassette was approximately one meter from the cavity opening. At this distance from the cavity, it was apparent that some radial expansion of the debris stream had occurred. The horizontal dimension of the portion of the stream seen in the photograph is approximately 20 centimeters, or nominally double the length of the square cavity opening. The debris particles were more evenly distributed than seen in the SPIT-19 radiographic record, although the areas where the material was concentrated were greater. Many regions contained several particles at different depths that were superimposed upon each other giving the appearance of a single large particle. This was observed near the lower right corner of the photo where the particles formed into a very dense appearing concentration.

Debris temperature measurements were made in each test (except SPIT-18) as the material emerged from the cavity exit. The results are presented in Figure 41, where the time starts with the first appearance of the melt at the cavity exit. The same two-color device was used on the three experiments and was supplemented by a single-color pyrometer on HIPS-2C. The single-color device was also employed on HIPS-5C but it was damaged
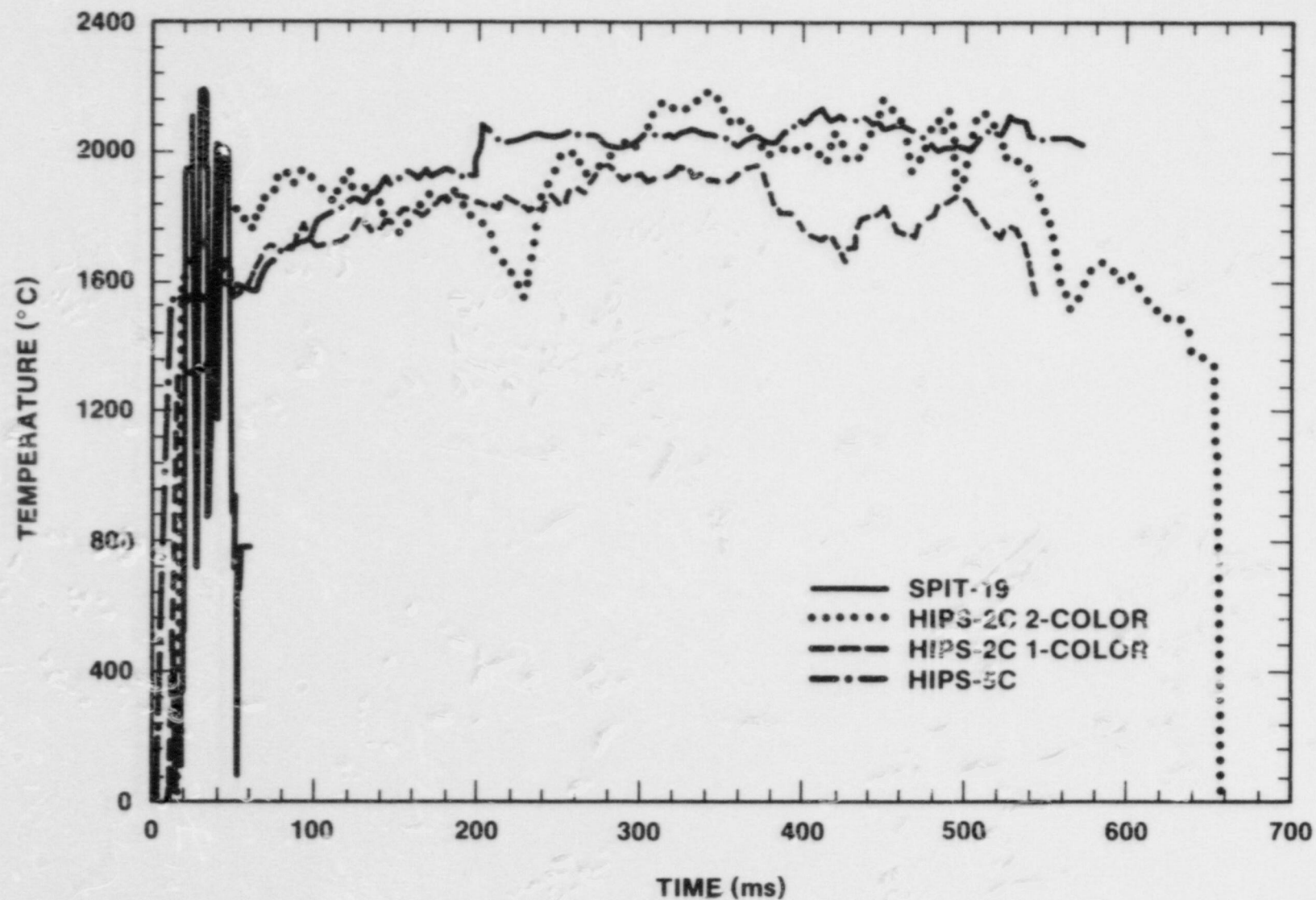
-95-

FIGURE 41. MEASURED DEBRIS TEMPERATURES AT THE CAVITY EXIT

during the event and the data were not usable. The advantage of the two devices was that the two-color pyrometer was less sensitive to emissivity errors while the single-color sensor had a very fast response time. Thus, the results from the two devices could be correlated in both magnitude and transient response.

The results presented in Figure 41 show that the smaller mass used in the SPIT-19 test caused the temperature history to be of shorter duration than either of the HIPS events. Further, the aerosol accumulation within the chamber blocked the line of sight of the instrument soon after ejection of the debris. On an expanded time scale (Figure 42), the SPIT-19 data fluctuated between 2000°C and 2200°C. The rise and fall of the record indicated that this device was responsive to rapid changes in the conditions of the test. It was not determined if the fluctuations were actual changes in the debris temperature or interference from other materials in the view of the pyrometer.

The data from the two HIPS experiments showed close correlation in both temperature and duration. All records indicated that the debris emerged at a temperature on the order of 1600°C, followed by an increase to nominally 2000°C. The cooler initial temperature was attributed to energy lost to the initially cool walls of the cavity. As the walls became coated with melt or heated, the temperature difference decreased and the heat transfer reduced. Considering the differences in the two pyrometric devices, the agreement in the data from the HIPS-5C test was excellent. The results strongly support the assumption that the debris leaving the cavity in these tests was much lower in temperature than suggested by thermodynamic analyses of the thermite reaction.[17] Further, the data from the one-color device were based on an assumed black-body emitter and were not corrected for the actual condition of the melt. The correction would cause the single-color results to be increased slightly, bringing the values closer in agreement with the two-color data.

The pyrometer results indicated that the melt temperatures were lower than predicted for the thermite reaction and that the energy transferred to the concrete cavity was not substantial. The latter point was also evidenced from the slight degree of concrete decomposition seen in these tests. The cause of the lower than expected melt temperature may be from the energy given up to the melt crucible sidewalls and in melting of the aperture plate in the bottom of the melt generator. In addition, chemical analyses of the recovered debris showed unoxidized aluminum, which may have been present because the thermite reaction did not go to completion. Reactions less than 85 percent complete have been shown to directly affect the ultimate temperature.[17]
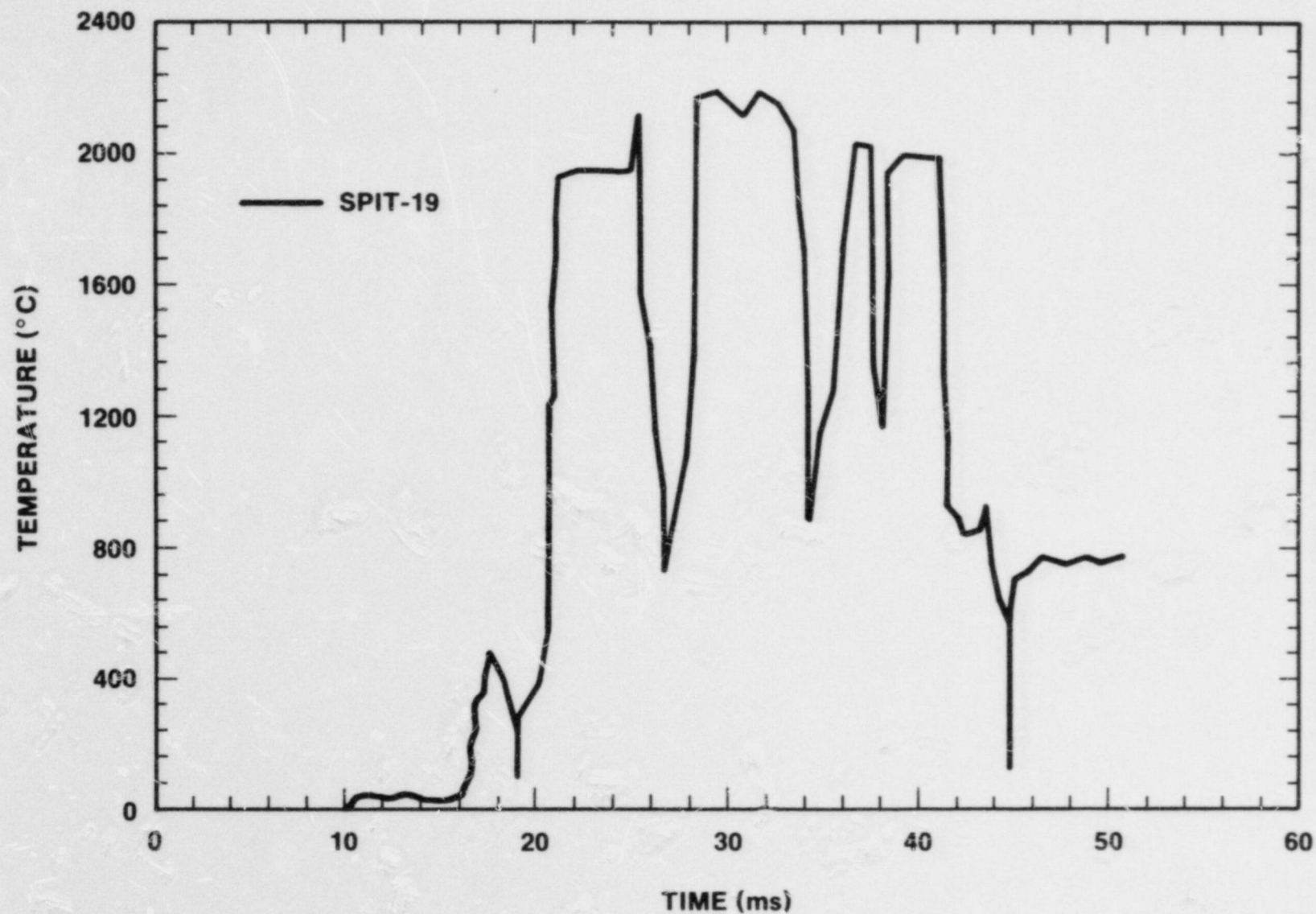
FIGURE 42. MEASURED DEBRIS TEMPERATURES IN THE SPIT-19 TEST

The interaction chamber used for the two SPIT tests allowed collection of much debris expelled from the cavity. The distribution of material with respect to the location of the apparatus was found by weighing the contents of each catch pan placed on the floor of the chamber. The arrangement of the pans can be seen in Figures 4 and 9 for SPIT-18 and SPIT-19, respectively. The pans in the northeast corner were shielded somewhat by the instrument rack, which stood nearly two meters tall.

The debris samples were obtained after each test by individually collecting and weighing the material from the pans. Particles of size less than 40 micrometers were difficult to remove from the pan surface with the soft brush that was employed. The mass of material in this smaller size range was not significant in comparison to the debris of larger size. The quantified results from the collection process for the two SPIT tests are given in Table 16, in terms of collected mass (and percentage of dispersed mass) versus pan number. The results are further illustrated by three-dimensional plots of mass fraction versus pan position as shown in Figures 43 and 44. It was apparent from the results of both tests that the greatest concentration of debris was along the far (north) wall of the interaction chamber, away from the apparatus. The quantity of material in the remaining areas of the chamber was greater along the longitudinal centerline than at the sides of the chamber.

Table 16
Distribution of Displaced Debris

PAN NUMBER	SPIT-18* MASS (g)	SPIT-18* MASS (%)	SPIT-19** MASS (g)	SPIT-19** MASS (%)
1	410.0	6.86	476.4	4.87
2	300.0	5.02	385.2	3.94
3	440.0	7.35	220.0	2.25
4	370.0	6.20	180.0	1.84
5	810.0	13.55	220.0	2.25
6	23.9	0.41	120.0	1.23
7	26.4	0.44	no data	-
8	59.7	1.00	44.1	0.45
9	80.0	1.33	45.0	0.46
10	80.0	1.33	42.9	0.44
11	65.2	1.10	no data	-
12	18.9	0.32	9.4	0.10
13	18.3	0.32	30.4	0.31

Table 16 (continued)

| PAN | SPIT-18* | | SPIT-19** | |
| NUMBER | MASS | | MASS | |
	(g)	(%)	(g)	(%)
14	39.1	0.66	31.4	0.32
15	100.0	1.67	48.8	0.50
16	120.0	2.01	25.0	0.26
17	16.3	0.27	30.0	0.31
18	19.3	0.32	45.0	0.46
19	45.4	0.76	50.0	0.51
20A	170.0	2.84	55.3	0.57
20B	58.1	0.98	-	-
21	18.6	0.30	46.2	0.47
22	18.2	0.30	40.7	0.42
23	50.1	0.84	75.8	0.77
24	170.0	2.84	40.1	0.41
25	62.8	1.05	40.6	0.41
26	50.7	0.84	24.9	0.25
27	13.0	0.22	no data	-
28	11.8	0.19	35.3	0.82
29	74.2	1.23	80.6	0.82
30	140.0	2.35	45.6	0.47
31	39.9	0.66	15.0	0.15
32	43.1	0.73	35.2	0.36
33	8.9	0.15	60.6	0.62
34	16.5	0.27	40.5	0.41
35	7.6	0.14	25.4	0.26
36	11.7	0.20	35.0	0.36
37	10.8	0.19	65.7	0.67
38	25.3	0.42	45.5	0.46
39	32.2	0.54	40.0	0.41
40	13.4	0.22	65.0	0.66
Conduit on north wall	300.0	5.02		
Instrument rack	20.0	0.34		
Total Mass	4409.3	73.8	2916.2	29.8

* Based on 5974 grams dispersed from cavity.
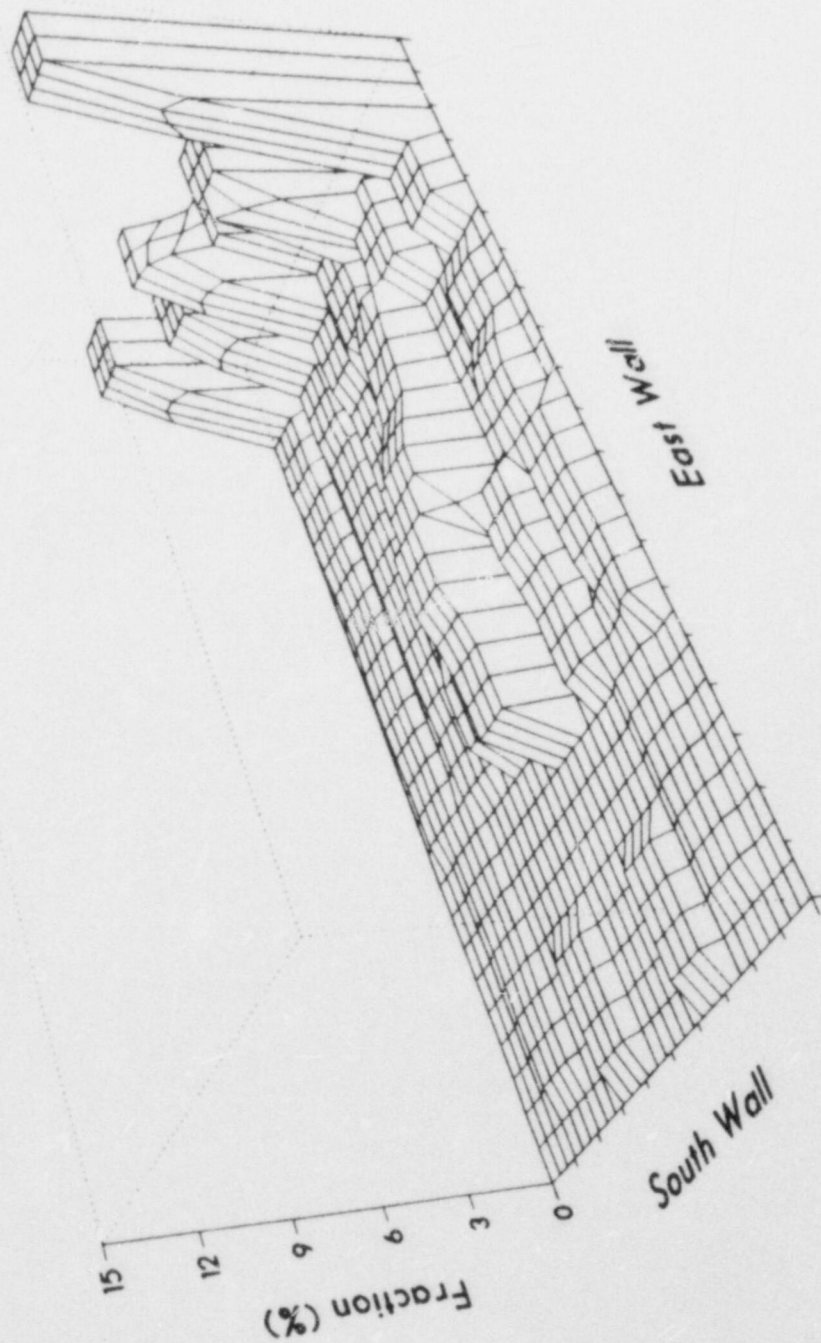** Based on 9785 grams dispersed from cavity.

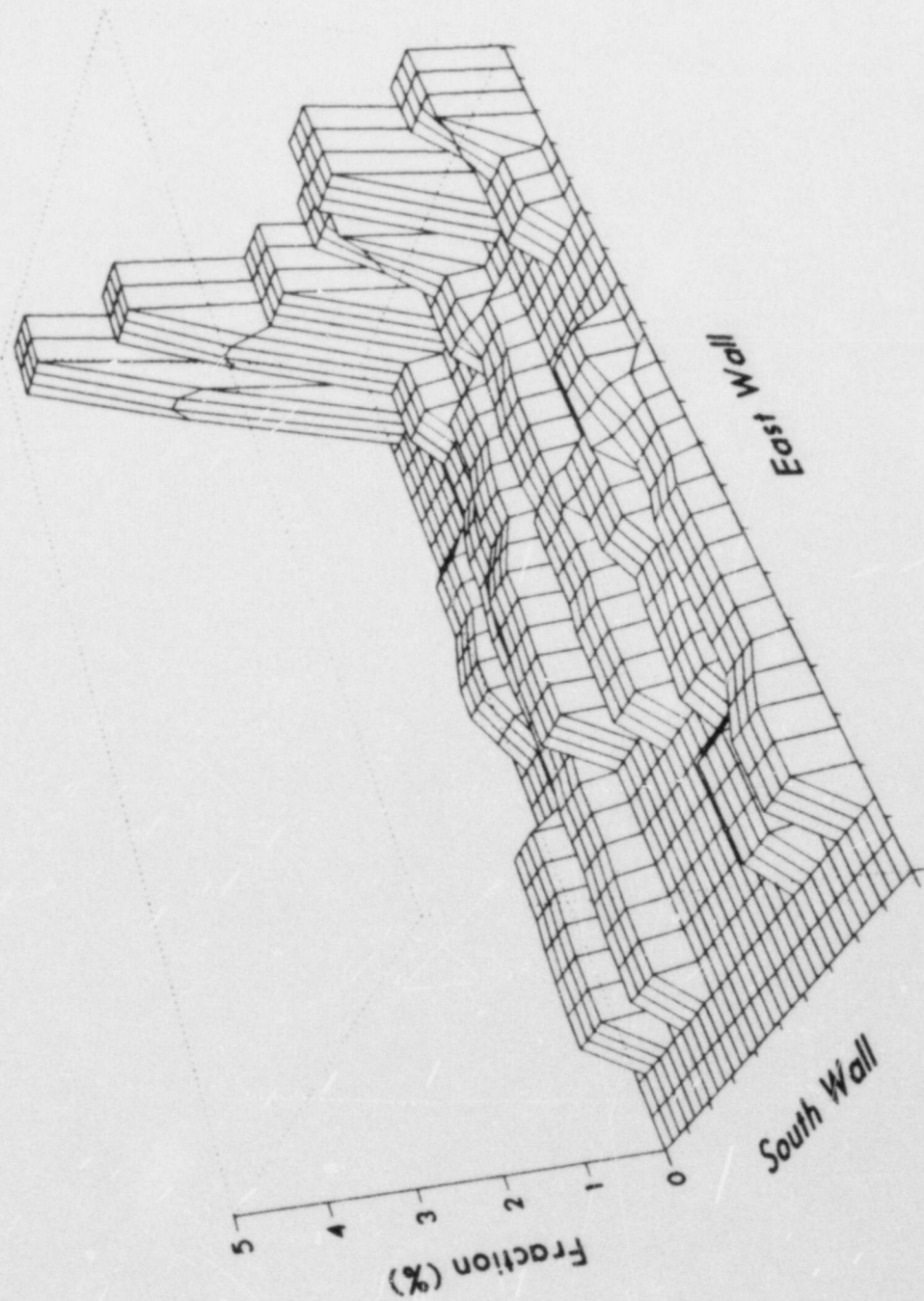FIGURE 43. DISTRIBUTION OF DEBRIS DISPERSED DURING THE SPIT-18 EXPERIMENT

FIGURE 44. DISTRIBUTION OF DEBRIS DISPERSED DURING THE SPIT-19 EXPERIMENT

In comparing the two tests, the fraction of mass along the north wall was significantly larger in the SPIT-18 chamber. The results from the SPIT-19 test show a more uniform distribution of material throughout the chamber, with the mass fractions significantly lower along the north wall than the SPIT-18 experiment. Furthermore, nearly every pan contained a measurable amount of material; only those areas shadowed by equipment did not collect significant quantities. Although the mass fractions in some regions in the SPIT-18 test were substantially higher, the actual mass along the north wall was very comparable in the two tests. This was a consequence of the larger amount of total mass dispersed in the SPIT-19 experiment.

The distribution of debris in the two SPIT tests suggested that the material was ejected from the cavity and then deflected one or more times by the walls and ceiling of the enclosure. Inspection of the chamber ceiling showed an obvious scorched area directly in line with an extension of the tunnel region. A simple particle rebound analysis indicated that particles striking the ceiling and then the north wall would deflect along a line nearly parallel to the north wall. The analytical results were sensitive to the value of the coefficient of restitution, or the amount of energy given up during the interaction of the particle with the surface. In the SPIT-18 test an extensive amount of debris was found on the electrical conduit located on the north wall approximately one meter above the floor, demonstrating that some of the material impacted the wall above this height. Using this height gave a coefficient of restitution of 0.48 with a corresponding energy loss of 77 percent (assuming no frictional loss at impact) on the first impact.

F. Debris Characterization

The interaction chamber used in the SPIT-18 and SPIT-19 experiments retained a large fraction of the expelled material. Only a limited amount of material was obtained during the two HIPS tests using catch pans placed downrange from the apparatus. Debris analyses consisted primarily of identifying the size distribution of the particles, their microscopic structure, and elemental composition.

In the SPIT-18 test, the debris collected from the pans had the general appearance of either spheres, globules, or frozen splashes (Figure 45). Most of the spheres were adhered to each other and were located principally along the lower edge of the North wall. No material was adhered to the chamber ceiling although a discolored area evidenced the impact of material emerging directly from the cavity exit. The splashes were more
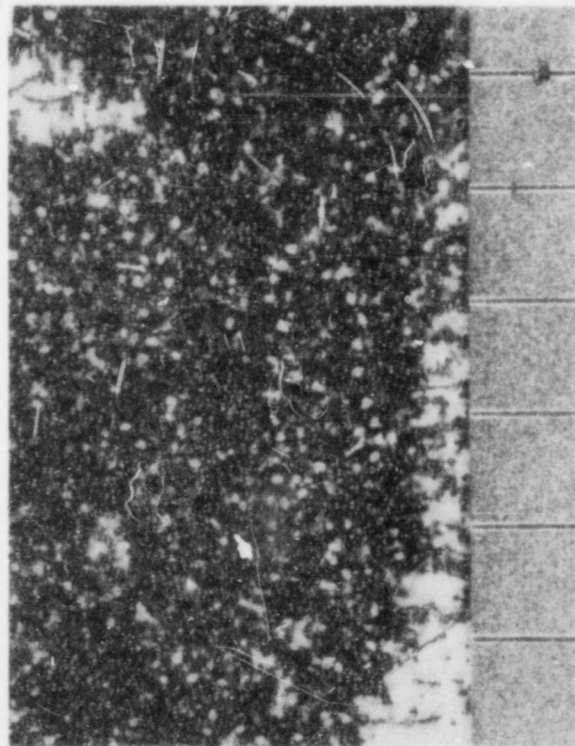
-103-
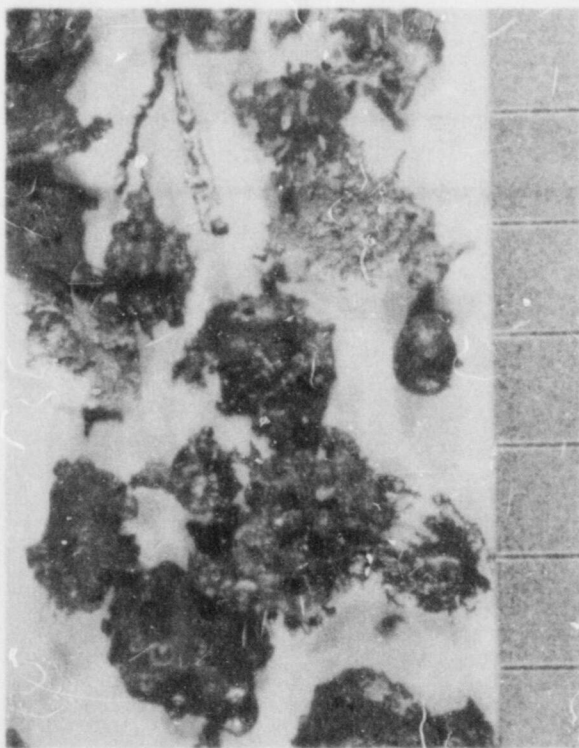
(a) + 1.6 mm
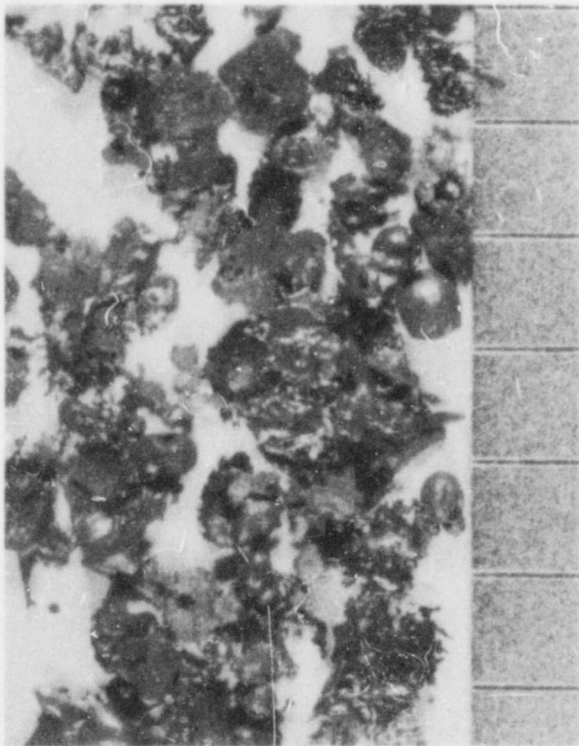
(b) + 0.8 mm
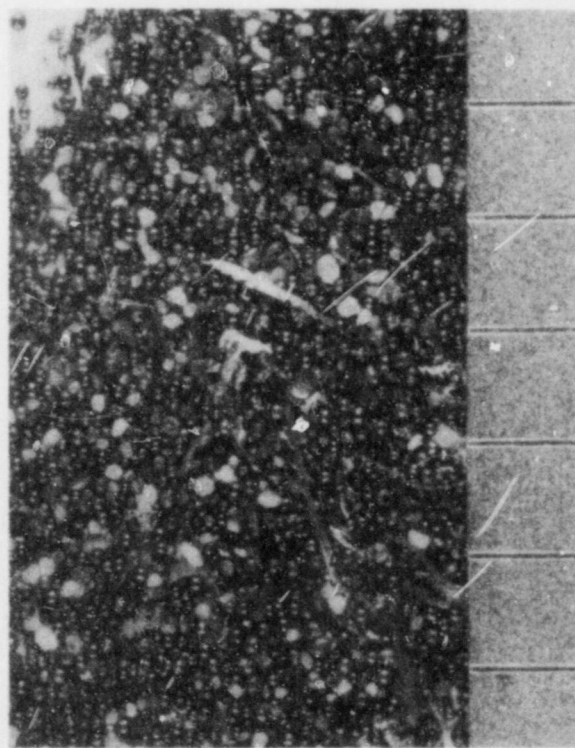
(c) + 20 mesh

(d) + 170 mesh

FIGURE 45. PHOTOGRAPHS OF DEBRIS FROM THE SPIT-18 EXPERIMENT (1mm SCALE MARKS)

predominant on the pans located intermediate between the apparatus and the north wall. Their appearance suggested that the particle was molten upon impact, but subsequently froze in contact with the pan. The center of the splash pattern was nearer to the apparatus than the north wall. The symmetry of the splash pattern indicated that the particle was traveling along a trajectory away from the apparatus. It was not clear if the particle impacted the ceiling or other surfaces prior to coming to rest on the floor. A ballistic trajectory was required to prevent the debris from impacting the ceiling, which required a lower initial velocity than predicted from the experimental conditions. This may have occurred late in the test when the gas velocity in the cavity was reduced, but was not the case during the bulk of the debris dispersal process.

The debris recovered from the SPIT-19 test exhibited spheres, irregular shapes, smooth globules, and splashes (Figure 46). The spheres ranged in size from several millimeters to a few tens of micrometers. These were formed by the influence of surface tension on debris that quenched in the atmosphere. The origin of the irregular shapes was not certain, because they appeared to be the product of some mechanical fracturing of a solidified particle. Almost all of the splashes were found in the size groupings above one millimeter. Many were several centimeters across, produced by drops greater than 1-2 millimeters in diameter. The splashes demonstrated similar characteristics to those described in the SPIT-18 discussion above.

Globules were detected in the size range of several millimeters to less than one millimeter. These were apparently formed by low-momentum molten drops that settled on the pan surface. Virtually all globules were flat on the surface next to the pan and smoothly curved on the side facing the chamber atmosphere. Most were somewhat circular in shape, although several were string-like in appearance. In addition to the material described, a small quantity of debris (approximately 600 grams) was tightly agglomerated together into large masses. Additional material was found in the crevices and openings between the chamber walls and the concrete floor. These materials were not collected because of the large amount of impurities present in the sample.

Very small amounts of material were collected in the HIPS-2C and HIPS-5C experiments. Photographs of the debris from the HIPS-2C and HIPS-5C tests are shown in Figures 47 and 48, respectively. A large number of splashes were apparent in the sample from HIPS-2C. Most of the spheres were large (on the order 1-2 millimeter), probably because smaller particles were driven off course by the prevailing wind. Because the pans were located along a direction of flight in line with the centerline
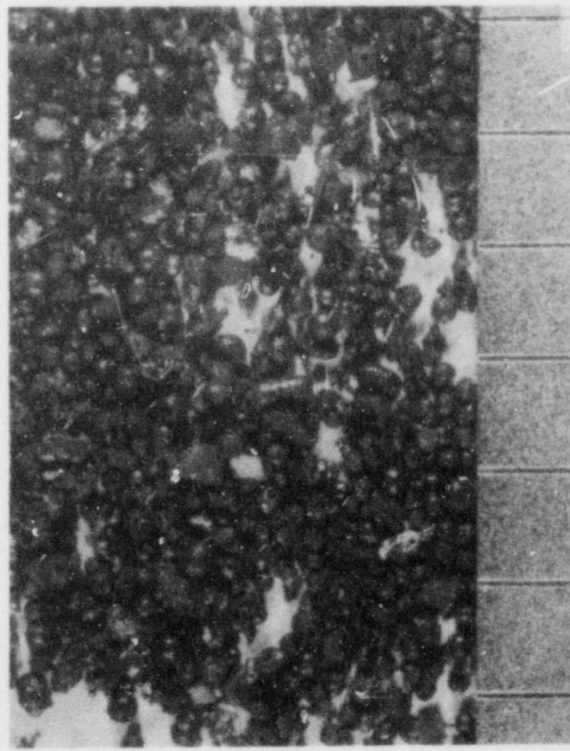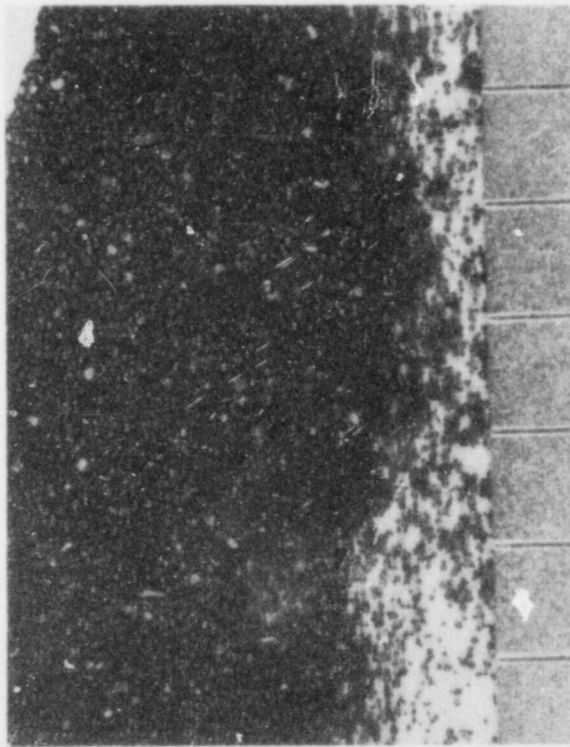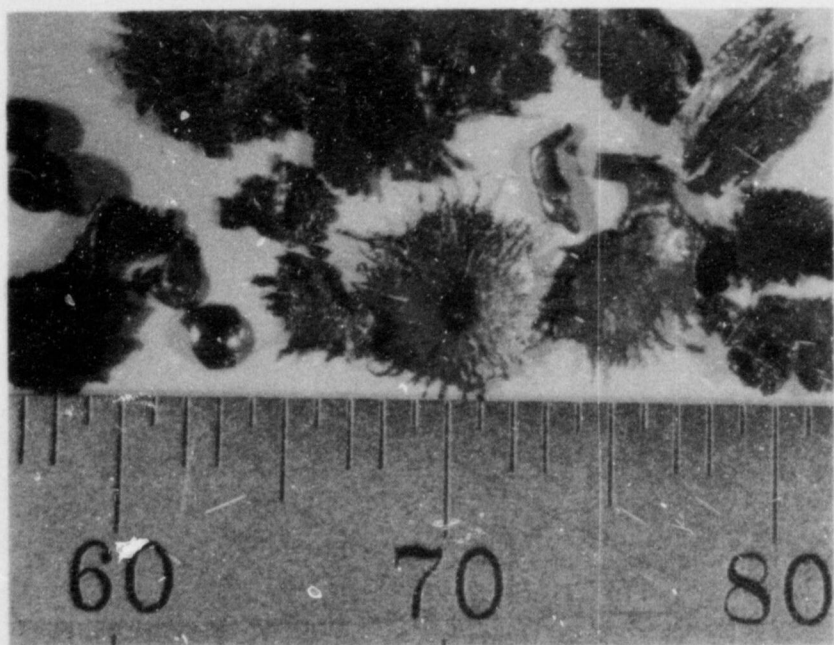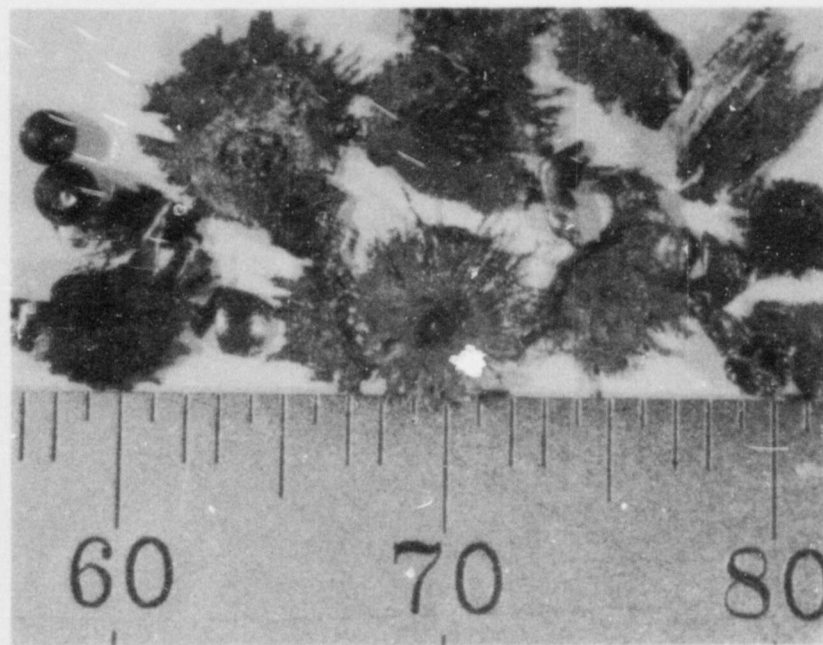
(a) + 1.6 mm
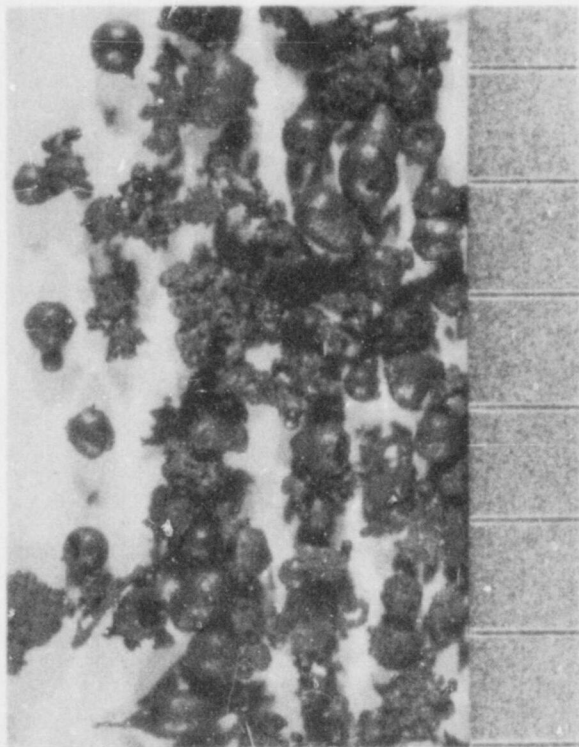
(b) + 0.8 mm

(c) + 40 mesh

(d) + 170 mesh

FIGURE 46. PHOTOGRAPHS OF DEBRIS FROM THE SPIT-19 EXPERIMENT (1mm SCALE MARKS)
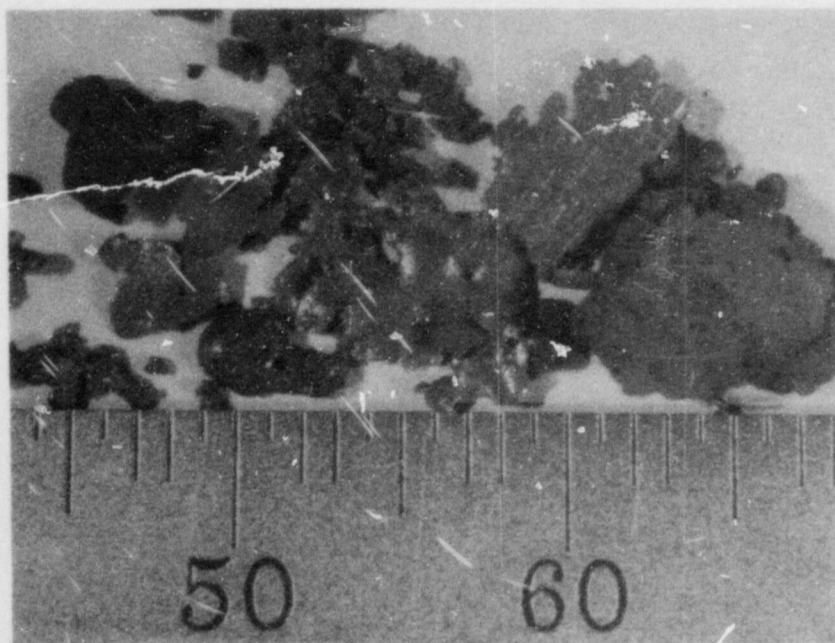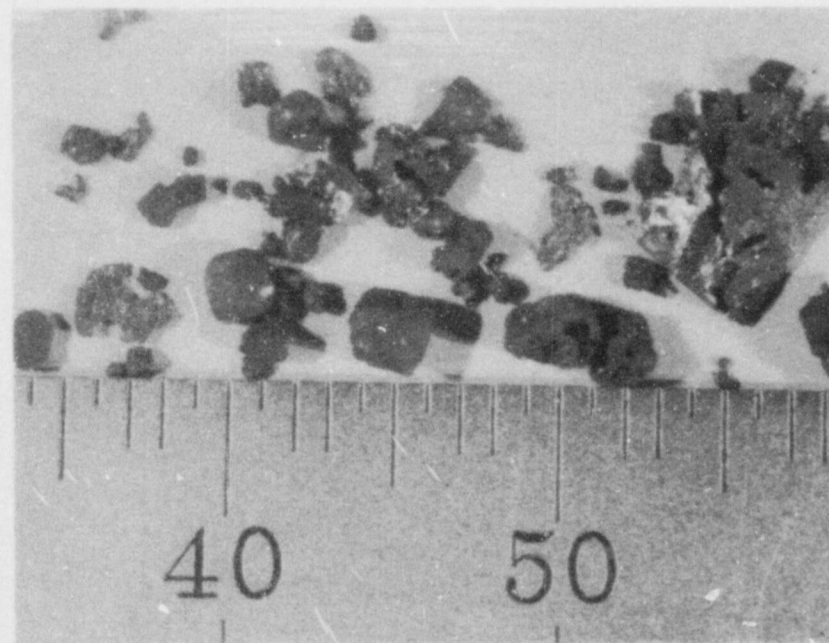
(a) 16 meters   (b) 33 meters

FIGURE 47. PHOTOGRAPHS OF DEBRIS FROM THE HIPS-2C EXPERIMENT (1mm SCALE MARKS)

(a) 16 meters

(b) 33 meters

FIGURE 48. PHOTOGRAPHS OF DEBRIS FROM THE HIPS-5C EXPERIMENT (1mm SCALE MARKS)

of the cavity, only a slight deviation would cause material to not impact on the pans. The spheres demonstrated "sink-holes" in their surface. This was caused by thermal contraction of the inner volume after the outer surface had solidified during atmospheric quench.

The HIPS-5C samples are shown in Figure 48, organized according to collection distance downrange from the apparatus. The sample closest to the apparatus (17 meters) showed small spheres and irregular shapes. The next two collection points (33 and 50 meters) indicated progressively larger spheres and splashes. The amount of material was too sparse to make a qualitative assessment and may have been influenced by aerodynamic effects separating the smaller particles or by bouncing out of the pans. The spheres mostly exhibited sink-holes of the type described above. Many small particles were found on the pans at longer distances. The abundance of spherical shapes suggested that the debris was quenched in the atmosphere before impacting the pan. This was confirmed by the visual observation of very limited luminosity of the debris shortly after the apex of the trajectory.

Size distribution of the debris collected from the SPIT-18 and SPIT-19 tests was obtained by sieve analysis using a Rotap 60 automatic sifter. Only the individual spherical samples were used, the splashes and large agglomerates being separated prior to the sifting process. The debris that remained after separation represented approximately 25 w/o and 40 w/o of the original mass for SPIT-18 and SPIT-19 tests, respectively. The resulting distribution is shown in Figure 49. The error bars represent the uncertainty inherent in the efficiency of the process of removing the extraneous materials from the spherical samples. The uncertainty was somewhat more pronounced at the greater size ranges where the nonspherical fragments were more difficult to remove.

The largest particles from the SPIT tests were less than 10 millimeters in diameter. A mass mean particle size of 0.75 and 0.43 millimeters was determined for SPIT-18 and SPIT-19 samples, respectively. For both tests, well over half of the mass was represented by particles with a diameter less than one millimeter. These sizes closely compared to those estimated from the X-ray shadowgraphs discussed previously. The collected debris was indicative of particles with a small overall size. The size range yielded a large surface area to volume ratio that was very susceptible to energy transfer to the atmosphere. Within the range of uncertainty, both tests appear to follow log-normal distributions.

The lower velocities in the cavity of the SPIT-18 experiment were responsible for the relatively larger size of the debris compared to that from the SPIT-19 experiment. Entrained
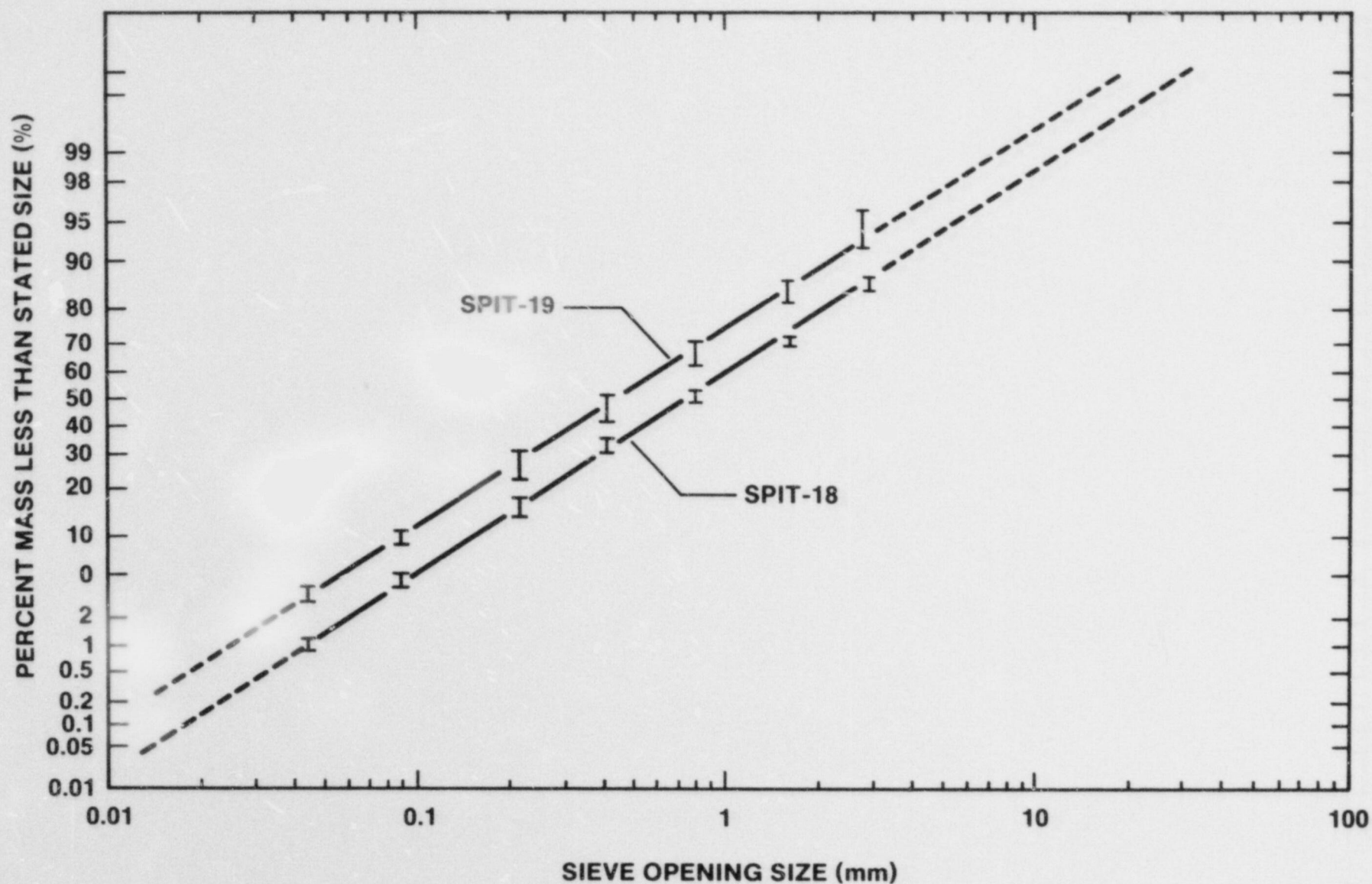
FIGURE 49. PARTICLE SIZE DISTRIBUTION FROM THE DEBRIS COLLECTED DURING THE SPIT-18 AND SPIT-19 TESTS

particles fragment to a maximum stable size defined by the gas velocity and material properties.[22] The conditions in the two SPIT tests were nearly equal except that the cavity cross-sectional area in SPIT-18 was much larger. The larger cavity caused the gas velocity in the region of entrainment to be reduced, resulting in less fragmentation of the particles. The predicted size of the particles leaving the cavity as a function of time[22] is given in Figure 50. The plots show that the calculated debris dispersal was dominated by inertia removal (except early in time). The SPIT-18 particle size was predicted to be approximately one-half an order of magnitude larger than that estimated for SPIT-19. The actual particle size distributions as given in Figure 49 were smaller because the debris in the tests was probably affected by secondary fragmentation caused by interactions within the cavity and in the enclosure.

The predicted particle size results for HIPS-2C and HIPS-5C are also shown on the Figure 50. The calculated maximum particle sizes were somewhat larger than actual because the lower driving pressure in these experiments reduced gas velocities in the cavity region. The velocities were determined by simple isentropic expansion of the gas from the melt generator through the smallest cross-sectional area of the tunnel region. All of the predicted curves shows that the smallest size particles were developed soon after the onset of gas blowdown when the melt generator pressure was highest. Particle sizes in the range of less than ten millimeters formed the bulk of the material ejected from the cavity.

Electron microprobe analysis was performed on randomly selected samples of the collected debris. Figures 51 through 54 are dot-density plots of samples from each test. The characteristic size scale and dot density pattern (in weight percent) are given on each figure. In all the photos, the length of the line at the lower edge of the picture is 100 micrometers, while the density pattern ranges from 5 to 33 percent. A qualitative estimate of the weight percent of an element was made by comparing the density of the dot pattern within the sample region to the characteristic pattern given below the grid. Three elements are shown for each sample: iron, aluminum, and oxygen.

Figure 51 shows the results of the analysis for a particle recovered from the SPIT-18 test. The mean diameter of this particle was determined to be approximately 1.6 millimeter. The first photo shows that iron was found in high concentrations throughout nearly the entire sample. Three large areas had concentrations above the 33 w/o limit defined by the dot density pattern. The second photo shows that the three high iron concentration areas are devoid of significant oxygen, indicating that the iron was not in an oxide form. The aluminum pattern in
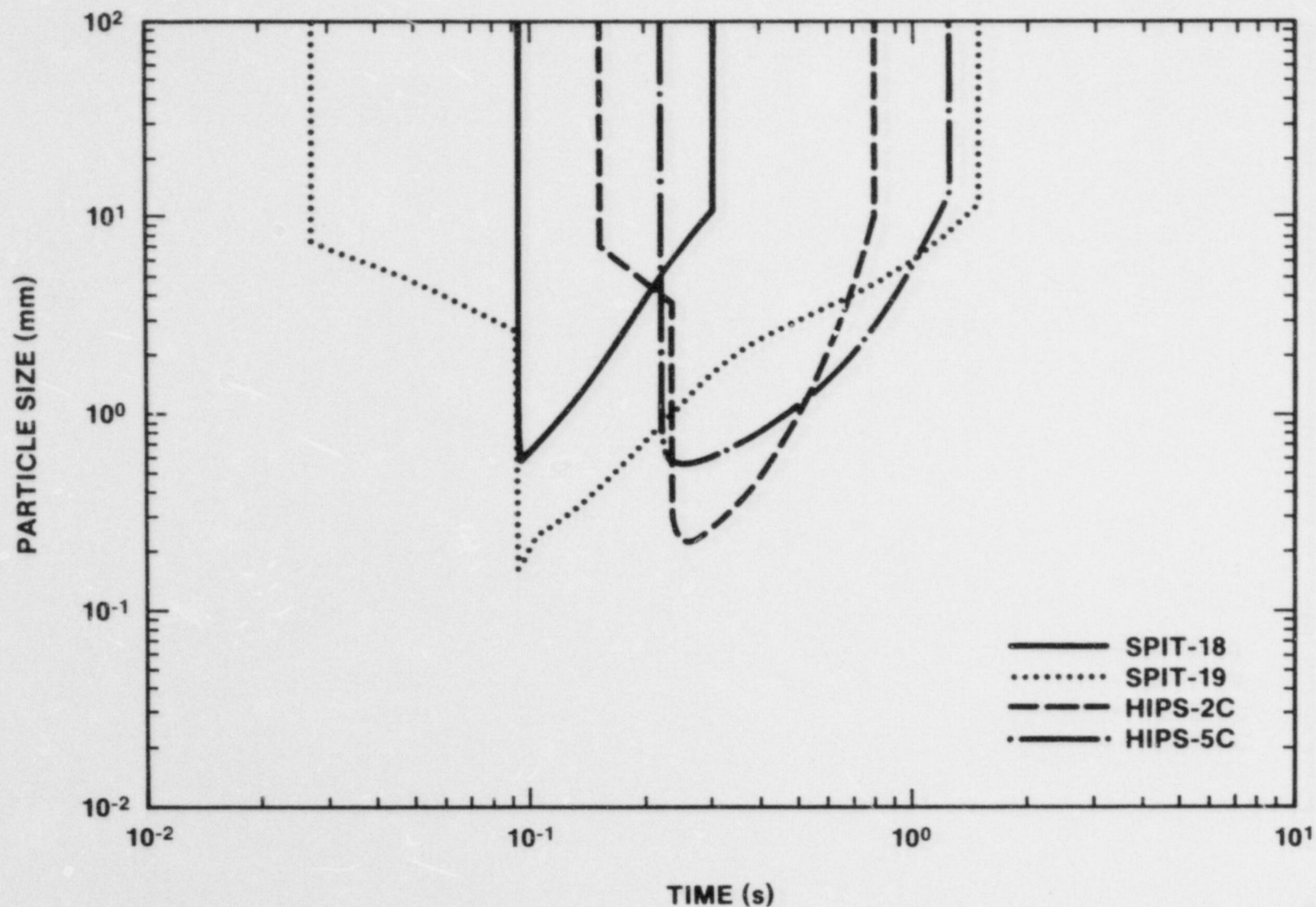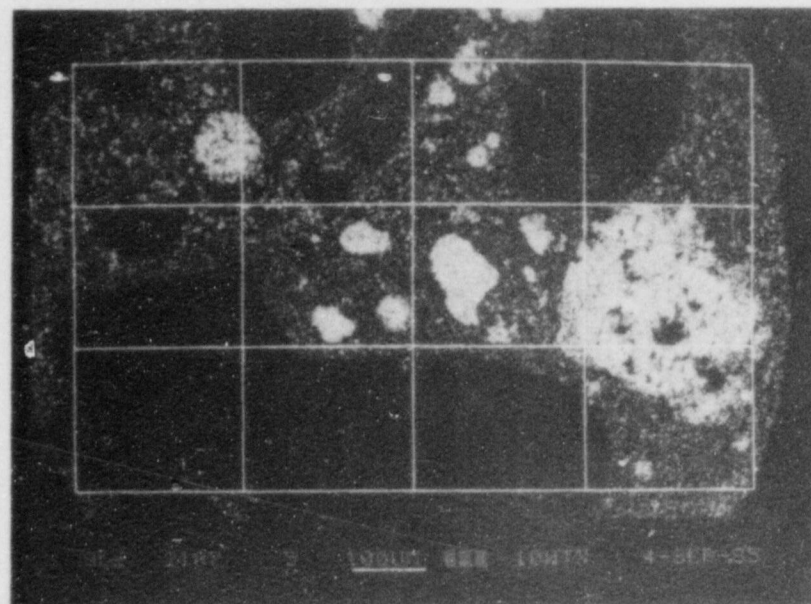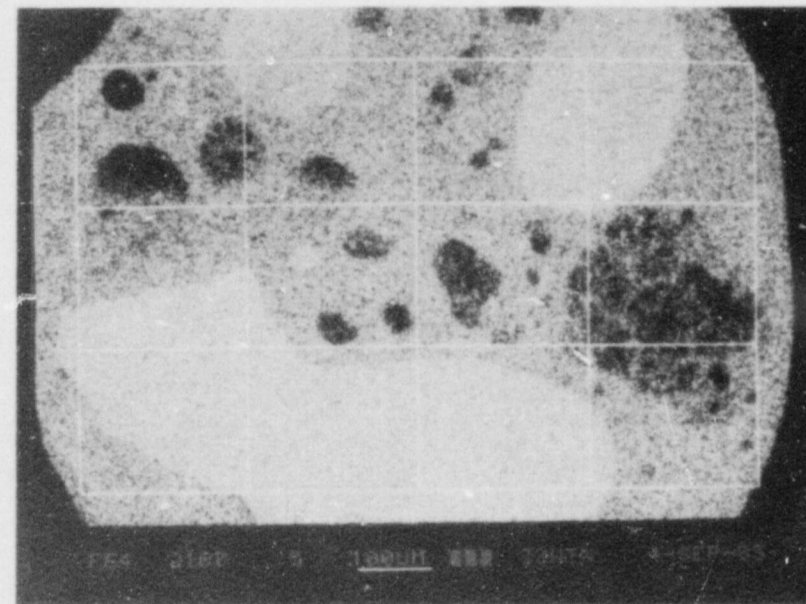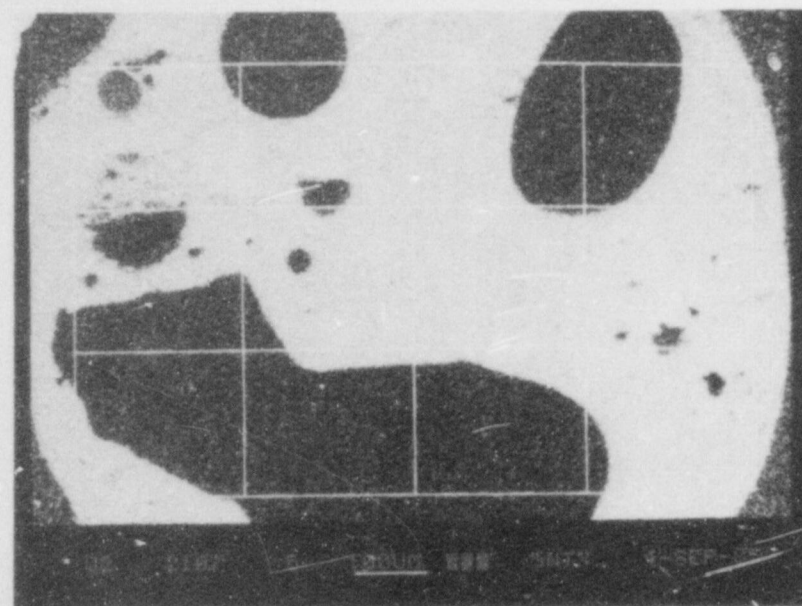
FIGURE 50. CALCULATED MAXIMUM STABLE PARTICLE SIZE
LEAVING THE EXPERIMENTAL CAVITIES

(a) ALUMINA

(b) IRON

(c) OXYGEN

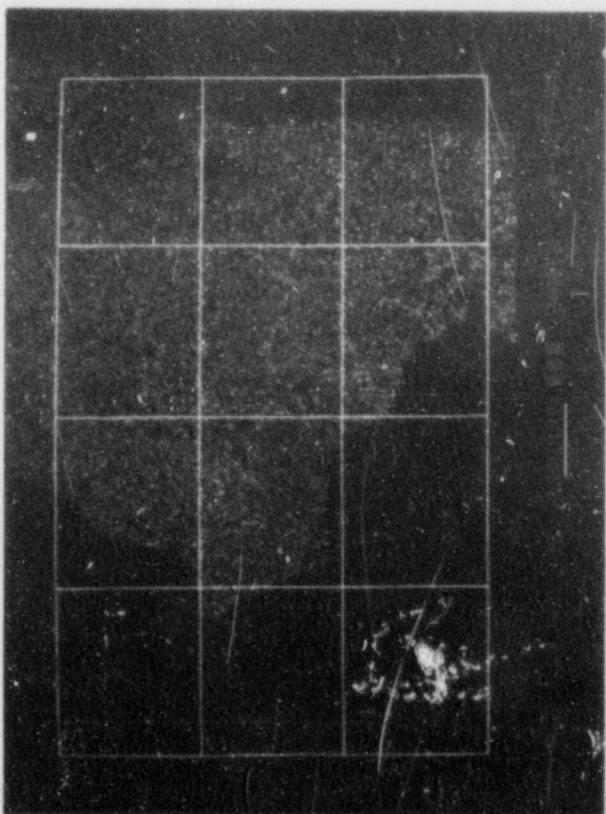FIGURE 51. SEM RESULTS FOR A SPIT-18 DEBRIS SAMPLE
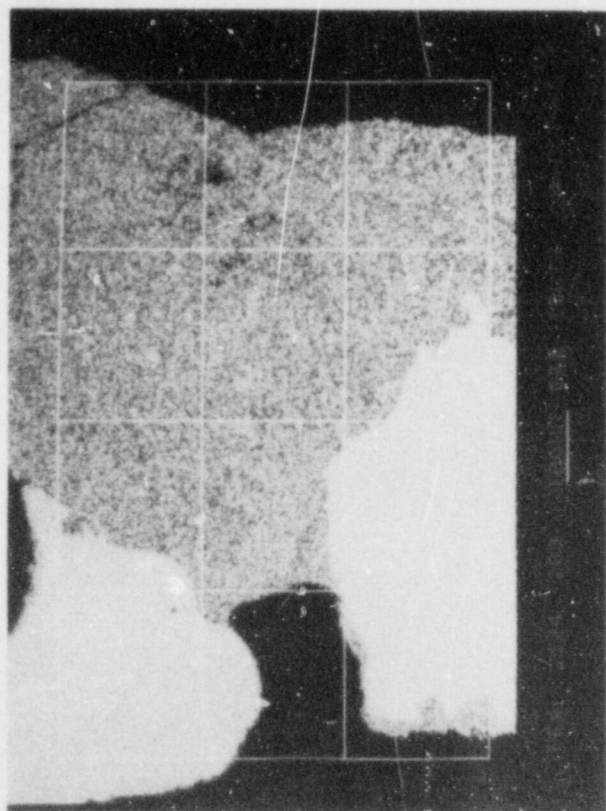
FIGURE 52. SEM RESULTS FOR A SPIT-19 DEBRIS SAMPLE

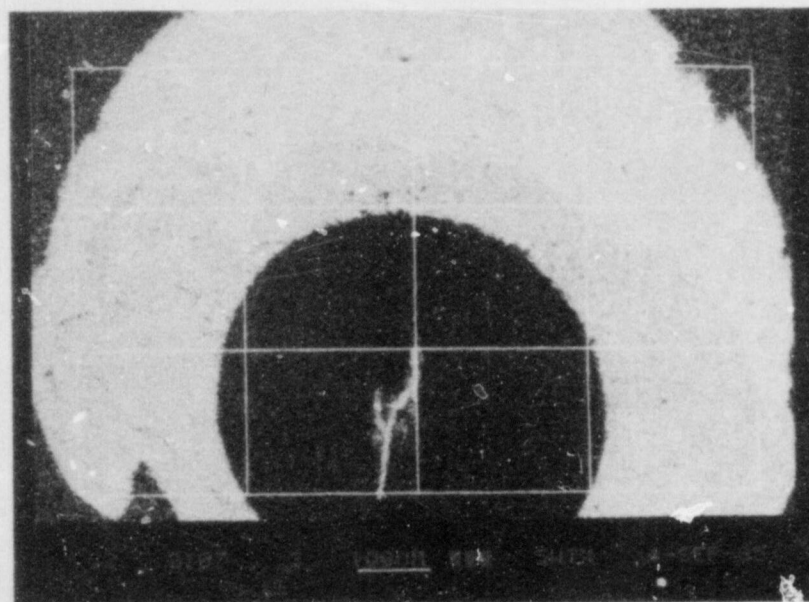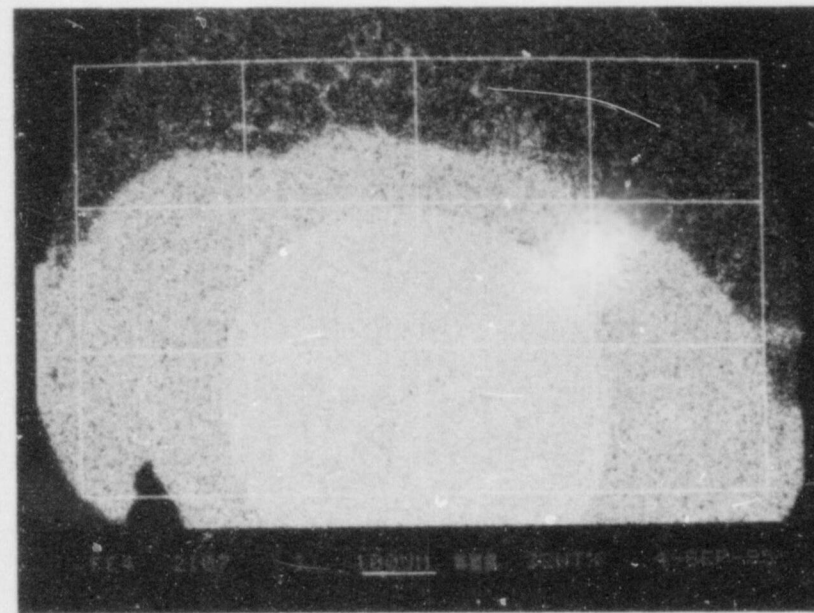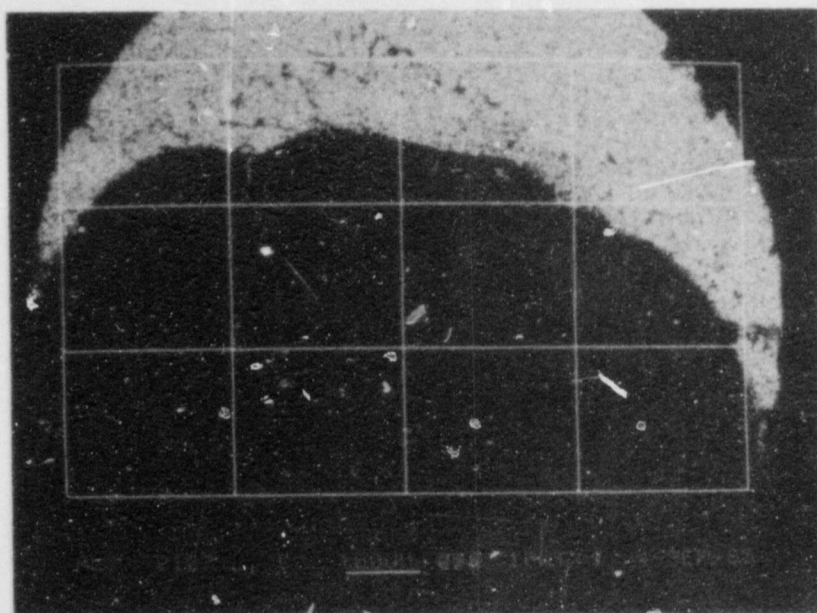FIGURE 53. SEM RESULTS FOR A HIPS-2C DEBRIS SAMPLE

FIGURE 54. SEM RESULTS FOR A HIPS-5C DEBRIS SAMPLE

the third photograph shows areas of high concentration, most of which were in conjunction with oxygen. These areas were attributed to the alumina present in the melt. Aluminum was not present in the iron areas identified above.

The remaining portions of the SPIT-18 sample showed all three constituents. This behavior suggested that complete separation of the iron and alumina did not occur, or that the thermite reaction did not go to completion. If the latter were true, then the original size of the iron oxide and aluminum powders (30 - 600 micrometer diameter) must have been changed significantly, possibly by melting during the reaction process. Significantly more samples need to be studied before the speculation of these observations can be reduced.

A similar set of photographs for a 1.8 millimeter diameter particle from the SPIT-19 test are shown in Figure 52. The size scale (100 micrometer) was the same as shown in Figure 51. Comparing the photographs shows several large dark areas in all three representations. These areas are surface voids that were exposed during the sample sectioning process. The iron representation demonstrates one large and several small areas of very high concentration. As before, these are regions of pure iron. No areas of very high aluminum concentration are seen. The remainder of the sample had the three constituents in relatively equal proportions.

Photographs of particles from the HIPS-2C and HIPS-5C tests are given in Figures 53 and 54, respectively. Both particles were less than one millimeter in diameter, and were recovered on pans placed approximately 30 meters from the exit of the cavity. Portions of the particle boundary can be seen in the specimen from the HIPS-2C test (Figure 53). Two large areas of nearly pure iron are obvious, while the remainder is made up of nearly equal portions of iron, aluminum, and oxygen. The state of the third area was not determined, but it appeared that the metallic constituents were coexisting in the same region. The presence of oxygen in the same area indicated that one or both of the elements were oxidized, although the expected form was aluminum oxide. The area near the left border between the two iron segments is an epoxy filled void developed during the sectioning process.

Nearly all of the boundary of the particle from the HIPS-5C test are seen in the photographs shown in Figure 54. The center of the sample was pure iron, surrounded by a layer of iron oxide. Aluminum oxide was also present but completely separate from the iron-bearing areas. The appearance of the sample suggested that the iron particle oxidized during the time it was propagating through the atmosphere. This was supported by the relatively small thickness of the oxide layer in the vicinity of the alumina

compared to the much greater oxide depth at the free boundary.

The SPIT samples were also studied for the presence of contaminants and fission-product dopants. Within the resolution of the SEM technique, the quantity of the fission-product materials were in the same proportion as they were in the original thermite composition. This behavior suggests that the release of these materials was neither enhanced nor depressed by the melt ejection and debris dispersal processes. The only significant contaminants found in the samples were silica, calcium, and carbon. The former two were from the cavity material while the latter was probably adsorbed from the graphite disk at the bottom of the melt generator.

The elemental analyses of the particles from the four tests suggests that iron and alumina existed as both separate and combined components. Complete separation of these two constituents may have occurred at a smaller size scale, but it could not be detected by the resolution of the technique employed here. Total separation of the two phases was observed in only one sample, although some separation was seen in every specimen. The presence of pure iron and the nearly total absence of pure aluminum indicates that the thermite reaction was nearly complete. The samples collected represent only a very small fraction of the total mass so that extrapolation of the results should be viewed carefully.

G.   Aerosol Characterization

The aerosol data were principally obtained from the two SPIT tests where the material was mostly contained by the interaction chamber. The damage incurred by the chamber during these two events may have allowed some small amount of material to escape the detectors. This would primarily affect the concentration results, rather than the size and mass distributions. Compared to all previous results, the data presented here represent the best estimate of the aerosol generation and behavior available for the high-pressure ejection of core debris.

In the SPIT-18 test, six time-resolved deposition samples were taken, with five of the devices yielding useful information. In addition, ten deposition surfaces were placed on the walls and ceiling of the interaction chamber. The results from both types of devices are given in Table 17. The deposition samples were exposed to the chamber atmosphere for specified time intervals following the debris ejection. In this manner, the mass concentration of the deposited aerosol with respect to time was

-118-

obtained. Not all time intervals were of the same duration, therefore the results are also given in terms of mass concentration per unit time.

Table 17
SPIT-18 Aerosol Deposition Results

DEVICE*	SAMPLING TIME (sec)	MASS CONCENTRATION (mg/cm^2)	TIME-RESOLVED MASS CONCENTRATION (mg/cm^2-sec)
Deposition Sample			
A	0-90	no data	no data
B	90-150	0.048	8.0
C	150-240	0.083	9.2
D	240-420	0.085	4.7
E	420-525	0.092	8.8
F	525-788	0.155	7.3
Deposition Surface			
1-C		no data	
2-C		2.70	
3-C		no data	
4-C		6.88	
5-W		8.49	
6-W		no data	
7-W		0.39	
8-W		1.71	
9-W		1.14	
10-W		0.50	

* Location for deposition surfaces: C-ceiling, W-wall.

The first SPIT-18 deposition sample was not used because a large quantity of the dispersed debris was deposited onto the sample surface. The deposited debris material was adhered to the surface by localized melting so that the debris could not be removed. The remaining samples yielded results that did not vary significantly over the interval from 1.5 to 12.3 minutes following debris dispersal. These data provided an average deposition rate of aerosol to the floor over the first twelve minutes following melt dispersal. The data from the deposition surfaces on the walls and ceiling which were exposed for the duration of the test showed a higher deposition. This was due in part to the presence of debris on some of the samplers caused by the difference in placement within the chamber. The relative locations of the devices allowed some of the surfaces to be more directly exposed to the debris from the cavity.

Deposition surfaces and samples were also used in the SPIT-19 experiment. Many of the glass slides used as the collection surfaces on the ceiling and walls were destroyed during the test. Those surfaces that survived were covered by large quantities (relative to the aerosol mass) of melt tightly adhered to the glass. Furthermore, the intense heat developed in the chamber during the test caused melting of the control wiring for the time-resolved deposition, which permitted only one sample to be exposed. As with the deposition surfaces, the large quantity of melt on the one sampler prevented any useful information from being obtained.

The filter samplers and cascade impactors were mounted to draw samples from the chamber atmosphere. These measurements allowed the mass concentration of the suspended aerosol to be obtained. The collected mass permitted the time-resolved mass concentration (grams per cubic meter) to be calculated, knowing the volumetric flow rate through the sampler and the duration of the sampling period. The SPIT-18 and SPIT-19 filter sample results are given in Table 18.

The filter sample data for SPIT-18 showed the airborne concentration decreased with time. Samplers 13 through 18 were three pairs of identical devices activated over the same time intervals. The error in the results appeared to be on the order of twenty percent for the three directly comparable devices. The SPIT-19 results showed a similar trend with the mass concentration decreasing with time from the initial high value at the time of ejection.

Cascade impactors were also used to determine the mass concentration of the suspended aerosol. In this case, the mass collected from each size range was summed to obtain the total collected mass. The flow rate and sample interval were then used

Table 18
Aerosol Mass Concentration
from Filter Samples

FILTER	LOCATION	SAMPLE INTERVAL (min)	MASS CONCENTRATION (g/m^3)
SPIT-18*			
1	Instrument Rack	0.3 - 0.5	1.29
2	" "	0.5 - 1.0	0.92
3	" "	1.0 - 1.5	0.83
4	" "	1.5 - 2.0	0.75
5	" "	2.0 - 2.5	0.78
6	" "	2.5 - 3.0	0.81
7	" "	3.0 - 3.5	0.73
8	" "	3.5 - 4.0	0.69
9	" "	4.0 - 5.0	0.68
10	" "	8.0 - 10.0	0.38
11	" "	15.0 - 20.0	0.31
12	" "	25.0 - 30.0	0.18
13	NW Corner	0.3 - 0.5	1.89
14	NW Corner	0.3 - 0.5	2.43
15	SE Corner	0.5 - 1.0	1.55
16	SE Corner	0.5 - 1.0	1.64
17	NW Corner	3.0 - 4.0	1.10
18	NW Corner	3.0 - 4.0	0.93
SPIT-19**			
1	Instrument Rack	0.0 - 0.1	4.29
2	" "	0.1 - 0.3	4.64
3	" "	0.3 - 0.5	3.45
4	" "	0.5 - 1.0	2.27
5	" "	1.0 - 1.5	1.94
6	" "	1.5 - 2.0	1.75
7	" "	2.0 - 3.0	1.06
8	" "	3.0 - 4.0	0.79
9	" "	4.0 - 5.0	0.57
10	" "	8.0 - 10.0	0.22
11	" "	15.0 - 20.0	0.03
12	" "	25.0 - 30.0	0.01
13	NW Corner	0.0 - 0.1	5.95
14	SE Corner	0.0 - 0.1	9.47
15	NW Corner	0.1 - 0.3	5.44
16	SE Corner	0.1 - 0.3	12.89
17	NW Corner	0.3 - 0.5	1.84
18	SE Corner	0.3 - 0.5	9.59

*   Flowrate 4.5 L/min.
** Flowrate 5.0 L/min.

to determine the total volume of atmosphere that passed through the device. Table 19 lists the mass concentration results from the cascade impactors on the SPIT-18 and SPIT-19 tests. In both experiments, two different flowrates were employed. The different flow rates provided an indication of how inlet sampling efficiency varied with flow rate. Two other impactors were run at 14 liters per minute and mounted on a rotating framework so that the inlet flow was tangential to the path of the sampler. The speed of the framework was set to match the settling velocity of a characteristic particle, giving isokinetic sampling of the aerosol. This technique was designed to improve collection of larger particles compared to stationary devices.

Table 19
Aerosol Mass Concentration
from Cascade Impactor Data

DEVICE	LOCATION	SAMPLE INTERVAL (min)	FLOWRATE (L/min)	MASS CONCENTRATION (g/m^3)
SPIT-18				
A	Rotating frame	3.0 - 4.0	14	6.17
B	"	3.0 - 4.0	14	2.61
C	Instrument rack	0.0 - 0.7	14	1.24
D	"	0.0 - 0.7	5	1.29
E	"	0.0 - 0.7	14	0.38
F	"	0.0 - 0.7	5	1.10
SPIT-19				
A	Rotating frame	0.0 - 0.5	14	1.71
B	"	0.0 - 0.5	14	0.73
C	Instrument rack	0.0 - 0.5	14	6.39
D	"	0.0 - 0.5	5	2.98
E	"	0.5 - 1.5	14	3.60
F	"	0.5 - 1.5	5	2.55

Comparing the results obtained during the SPIT-19 experiment suggested that the location of the sampler within the chamber may have been important. For example, the devices placed in the southeast corner showed consistently higher mass concentrations than any other location. This region was the closest to the apparatus of all the locations employed. The behavior was influenced to a great extent by the fact that the mixing fans became inoperative shortly after melt ejection. Without the motion induced by the fans, the atmosphere within the chamber was stagnant, preventing the development of a homogenous mixture of suspended particles.

Examining the impactor and filter sample data from the SPIT-18 and SPIT-19 tests yielded a concentration range and confidence level. For SPIT-18, six concentration results were obtained from filter samples 1, 13, and 14 and impactors C, D, E, and F, which gave a concentration range of 0.8 to 1.9 g/m^3 with a 95% confidence. For SPIT-19, filter samples 1, 2, 3, 13, 14, 15, 16, 17, and 18 and impactors A, B, C, and D yielded a concentration range of 1.6 to 7.3 g/m^3 with a 95% confidence.

The results from both the filter samples and the cascade impactors showed that the aerosol mass concentration was higher in SPIT-19 than SPIT-18. This is represented by Figure 55 where the aerosolized fraction of the dispersed debris mass is plotted as a function of time. The aerosolized fraction was found by multiplying the calculated mass concentration by the volume of the interaction chamber, and then the result was normalized by dividing by the dispersed mass of debris. The time was determined as the average of the sample interval. The resulting representation allowed comparing the extent of material in the form of aerosol, outside the cavity apparatus. The figure showed that the mass concentration decreased significantly (i.e., nominally an order of magnitude) with time from the high value at the time of melt ejection. The data of SPIT-18 demonstrated consistently lower concentrations than SPIT-19, except for the rotating impactors that were capable of sampling larger particles. The scatter in the data was considered large for both tests, as estimated from the spread in the results from the paired devices. This was not unexpected, considering the variation in aerosol cloud density within the chamber.

Cascade cyclones were also used on both SPIT tests to obtain a large mass of aerosol material. These devices were functional to much higher mass loadings than comparable cascade impactors. For example, the average mass collected by impactors was typically on the order of 15 milligrams or less, while a cascade cyclone obtained well over 150 milligrams without overloading. The cyclones were operated for 30 minutes on both tests, starting at the time of melt ejection. The average value of mass concentration over the fifteen minute sampling period using these
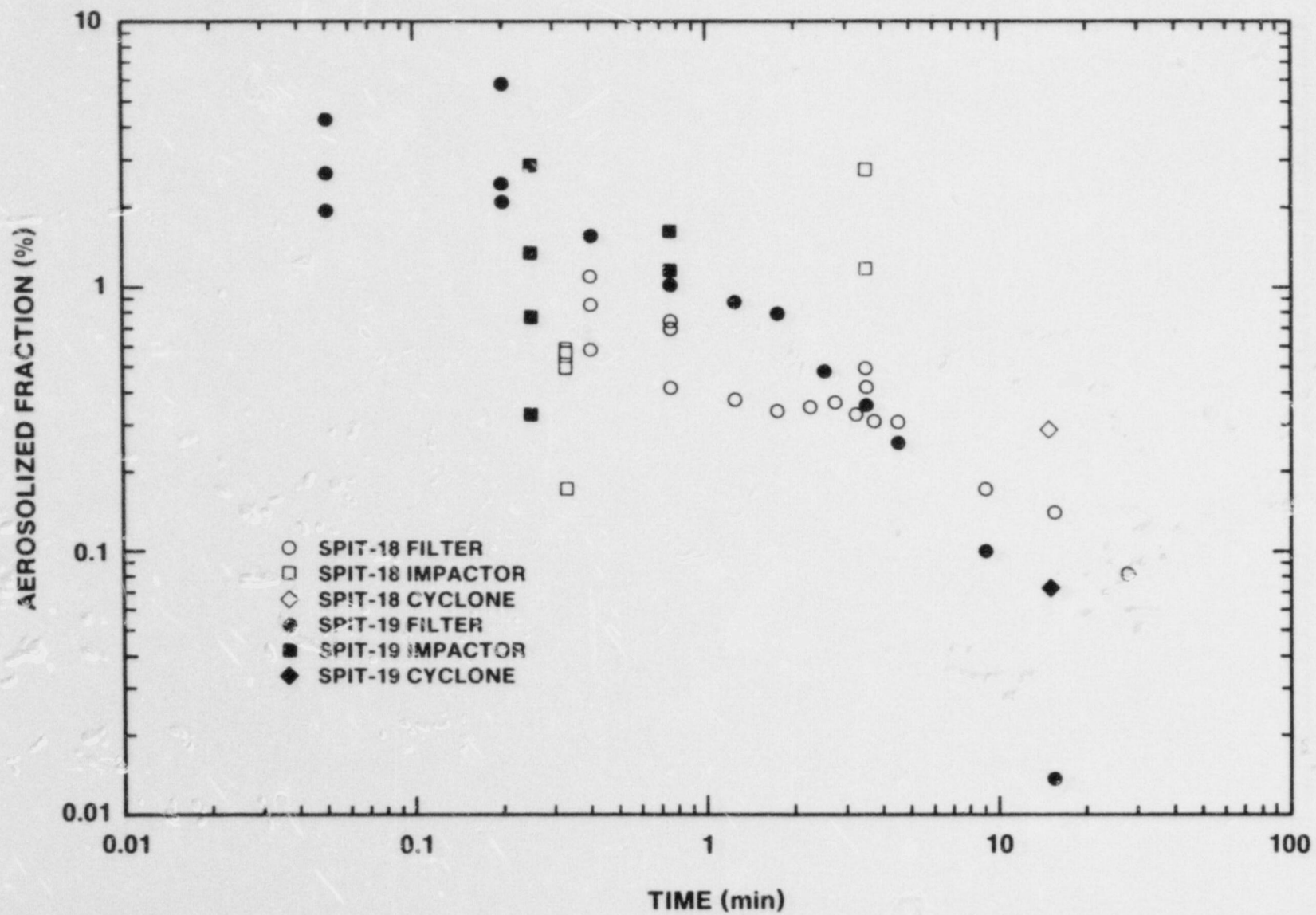
FIGURE 55. FRACTION OF MELT MASS AEROSOLIZED DURING THE SCALED CAVITY EXPERIMENTS

devices was 0.39 and 0.16 g/m^3 for SPIT-18 and SPIT-19, respectively. The results were consistent with the values obtained from the filter samples and impactors. Furthermore, the results provided additional evidence that the concentration in SPIT-19 diminished faster in SPIT-19 than in SPIT-18.

The mass concentration results indicated that the aerosolized fraction in the two SPIT tests at early times was above one percent of the mass of the displaced debris. For samples taken within thirty seconds of discharge, the aerosolized fraction approached five percent or more for SPIT-19. If these indications hold for larger scale events, the amount of airborne material will be significant. The results also indicated that the concentration fell off with time, to approximately one-tenth percent at ten minutes. This behavior was affected by the many leakage paths developed in the interaction chamber during the tests. The surface to volume ratio of the interaction chamber was larger in the experiments than in a reactor configuration, promoting faster deposition.

The cascade impactors were intended to give size distributions of the suspended material. Data presented by Agarwal[23] show that one-hundred micrometer diameter particles were sampled through impactor inlets at slightly better that fifty percent efficiency. Assuming that the efficiency dropped rapidly for particles larger than this size, the upper size range was selected to be one-hundred micrometer equivalent aerodynamic diameter. Each device had eight collection stages followed by a backup filter to retain the smallest particles. A preseparator was used to remove particles larger than ten micrometer aerodynamic equivalent diameter. The cut sizes of the preseparator and each stage for the two flow rates used on the tests are given in Table 3.

The lower bound of the distribution was based on what was considered a reasonable value for the collected materials. Electron photomicrographs of the material in the backup filter and last few stages showed agglomerations of par .cles one-tenth micrometer and smaller. The agglomerates were made up of individual particles that were smaller than would be normally collected in the respective stage where they were found. It was assumed that all small particles collected in these tests were agglomerates that behaved as larger particles. Based on this observation, the lower bound of one-tenth micrometer was selected.

The size distribution data from the impactors used on the two SPIT tests are given in Figures 56 through 67. The plots are a histograms of the mass distribution as a function of aerodynamic equivalent diameter. The vertical axis is a linear scale for the mass fraction in a size interval divided by the log
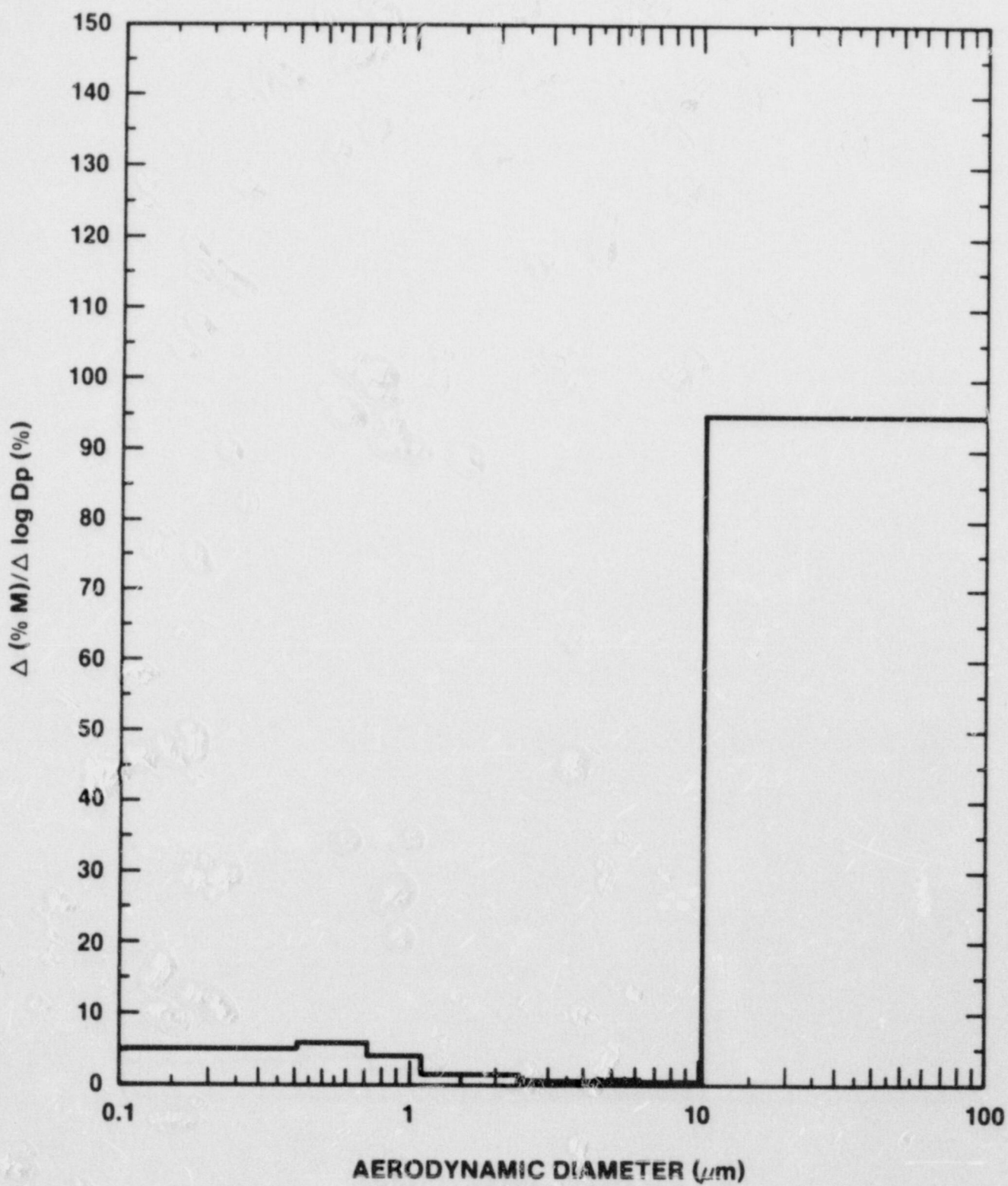
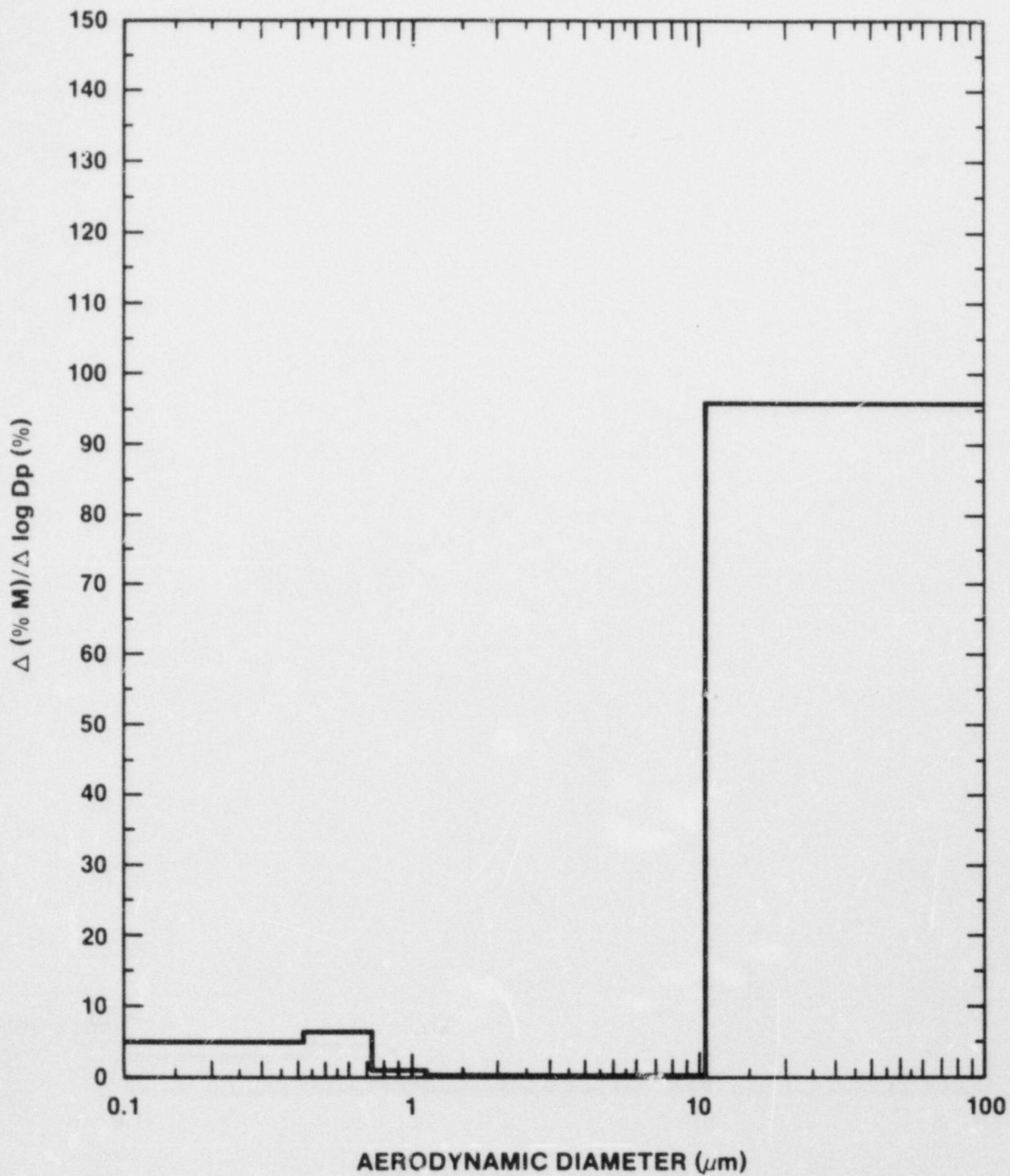FIGURE 56. SPIT-18 AEROSOL SIZE DISTRIBUTION. IMPACTOR A

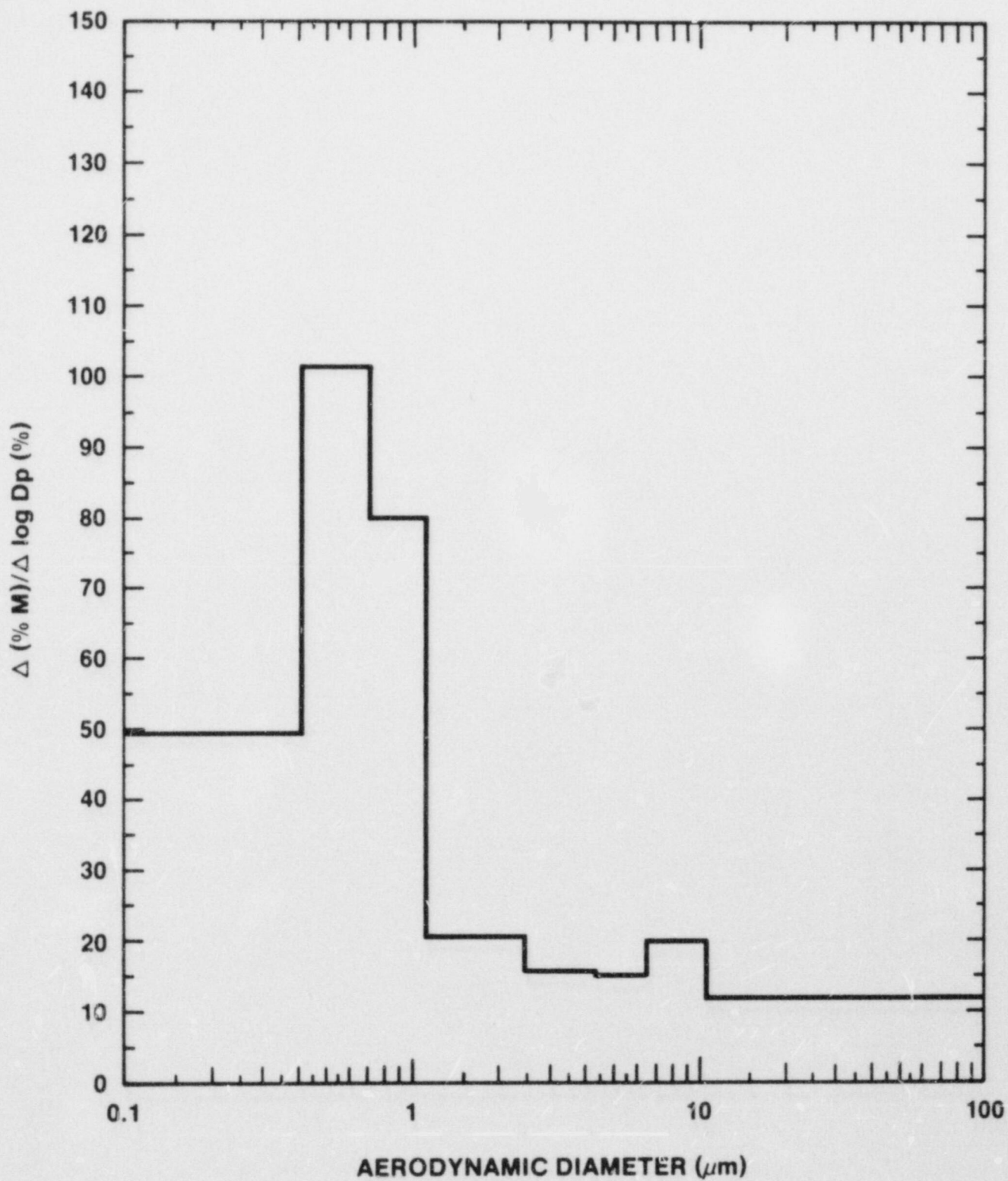FIGURE 57. SPIT-18 AEROSOL SIZE DISTRIBUTION . IMPACTOR B

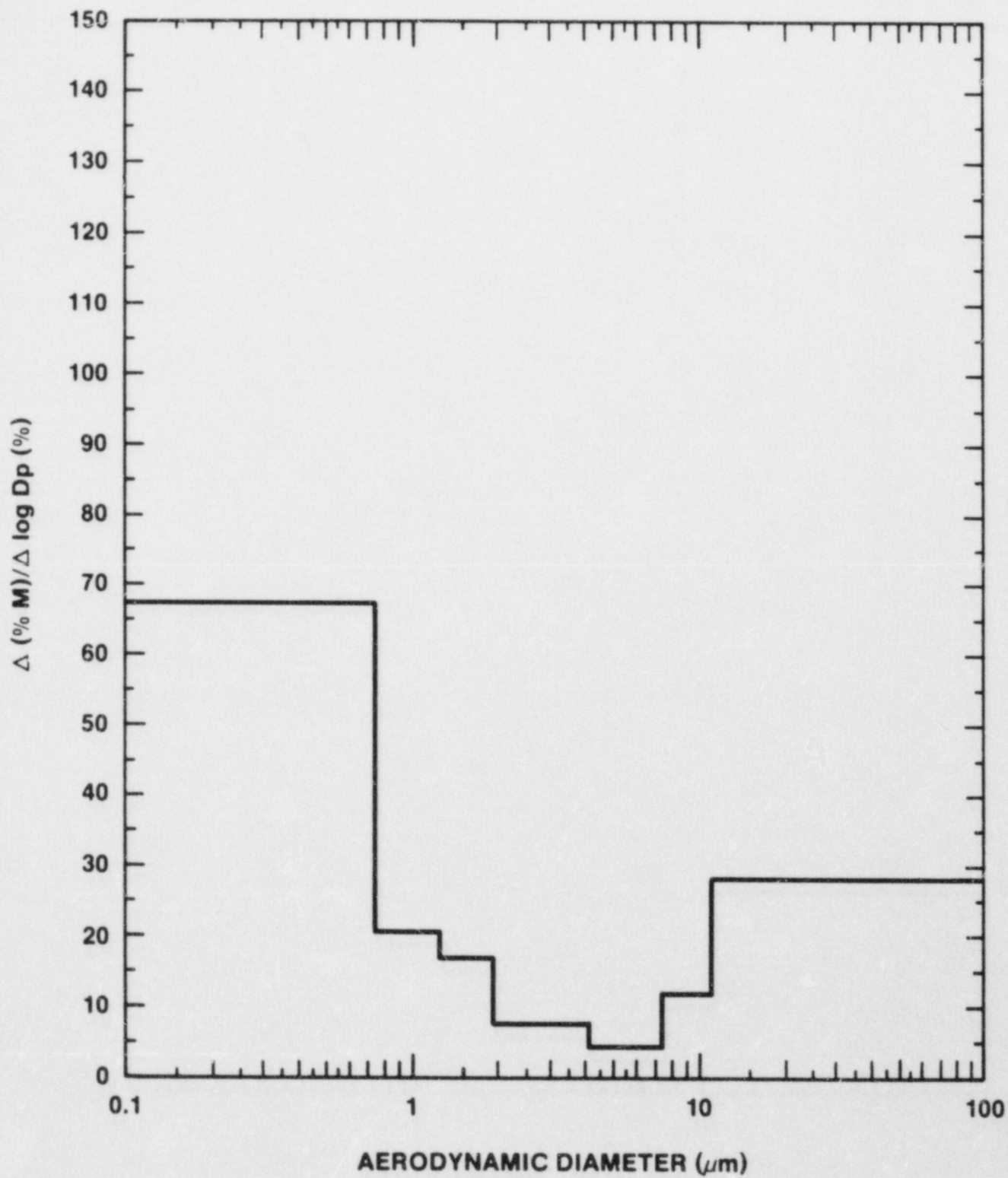FIGURE 58. SPIT-18 AEROSOL SIZE DISTRIBUTION. IMPACTOR C

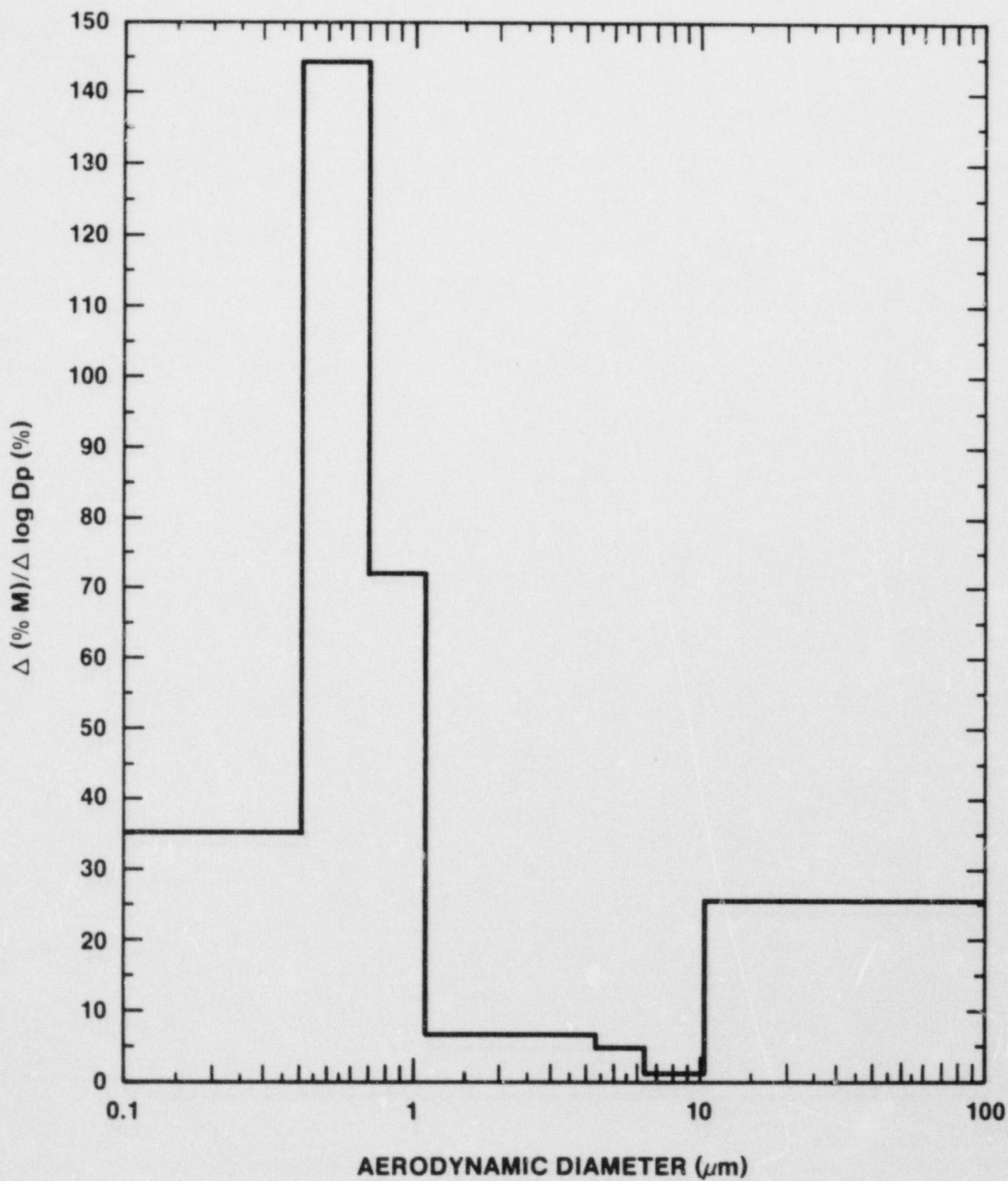FIGURE 59. SPIT-18 AEROSOL SIZE DISTRIBUTION. IMPACTOR D

FIGURE 60.   SPIT-18 AEROSOL SIZE DISTRIBUTION.   IMPACTOR E

FIGURE 61. SPIT-18 AEROSOL SIZE DISTRIBUTION. IMPACTOR F

FIGURE 62. SPIT-19 AEROSOL SIZE DISTRIBUTION. IMPACTOR A

FIGURE 63.   SPIT-19 AEROSOL SIZE DISTRIBUTION, IMPACTOR B

FIGURE 64. SPIT-19 AEROSOL SIZE DISTRIBUTION. IMPACTOR C

FIGURE 65. SPIT-19 AEROSOL SIZE DISTRIBUTION. IMPACTOR D
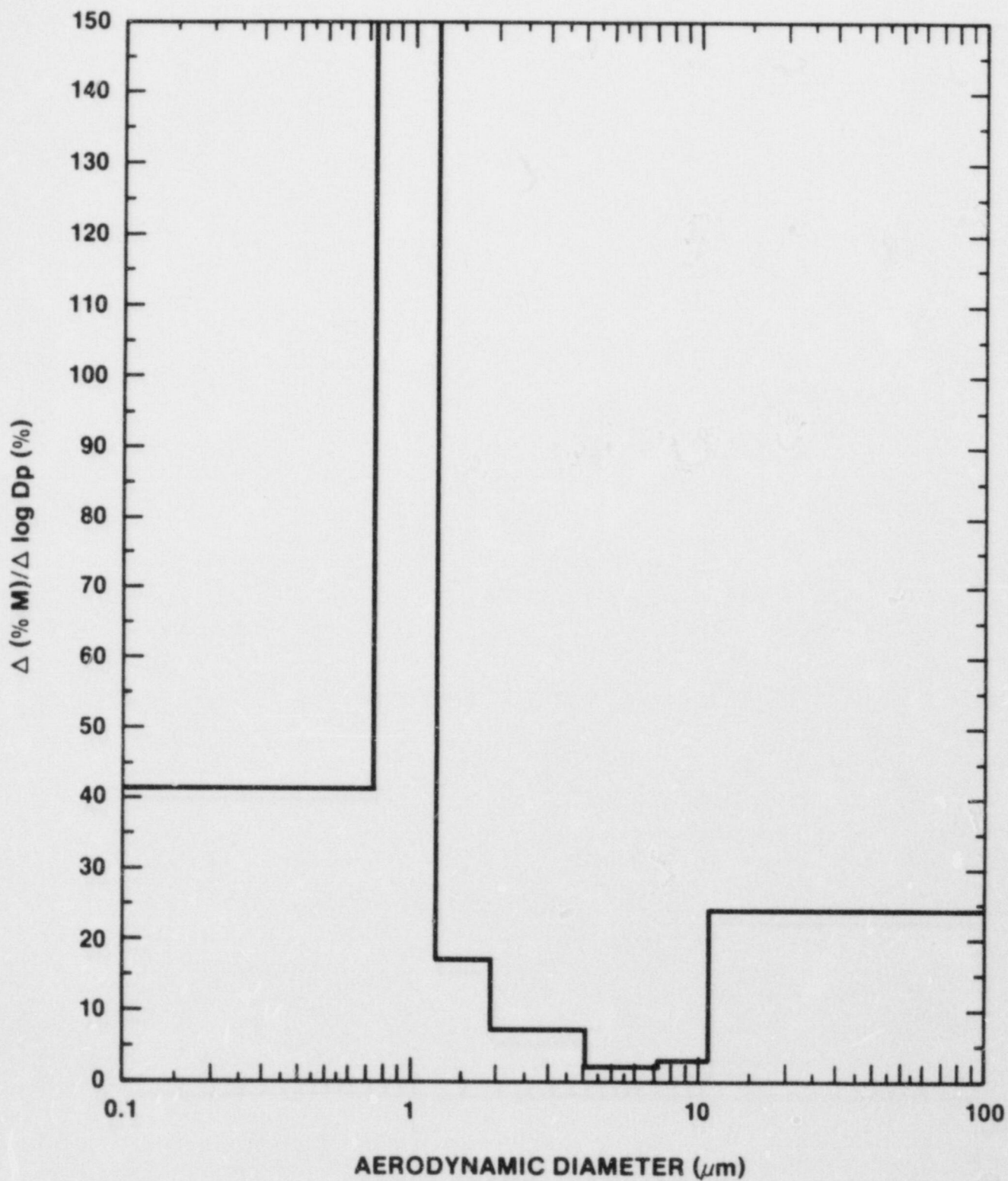
FIGURE 66. SPIT-19 AEROSOL SIZE DISTRIBUTION. IMPACTOR E

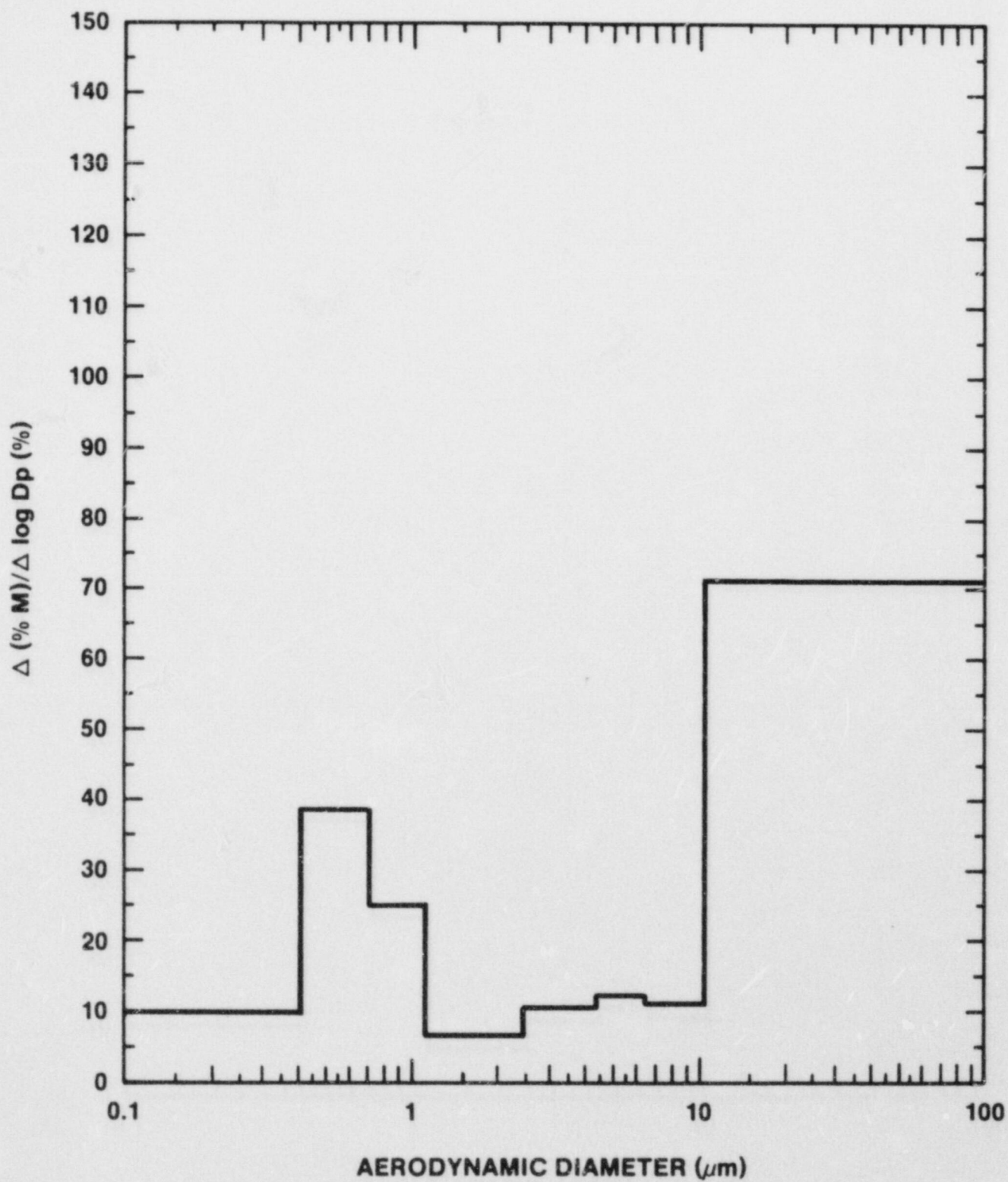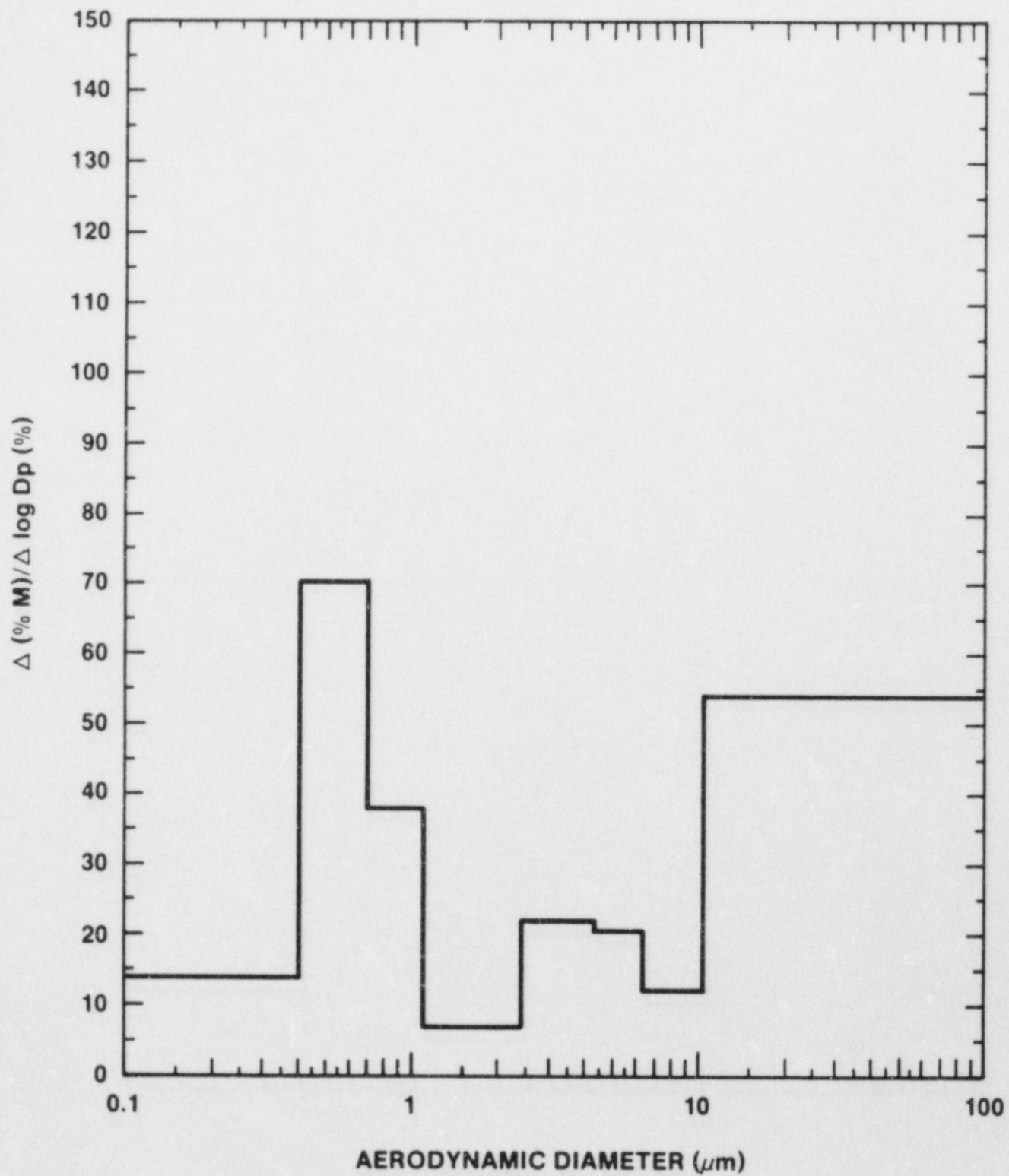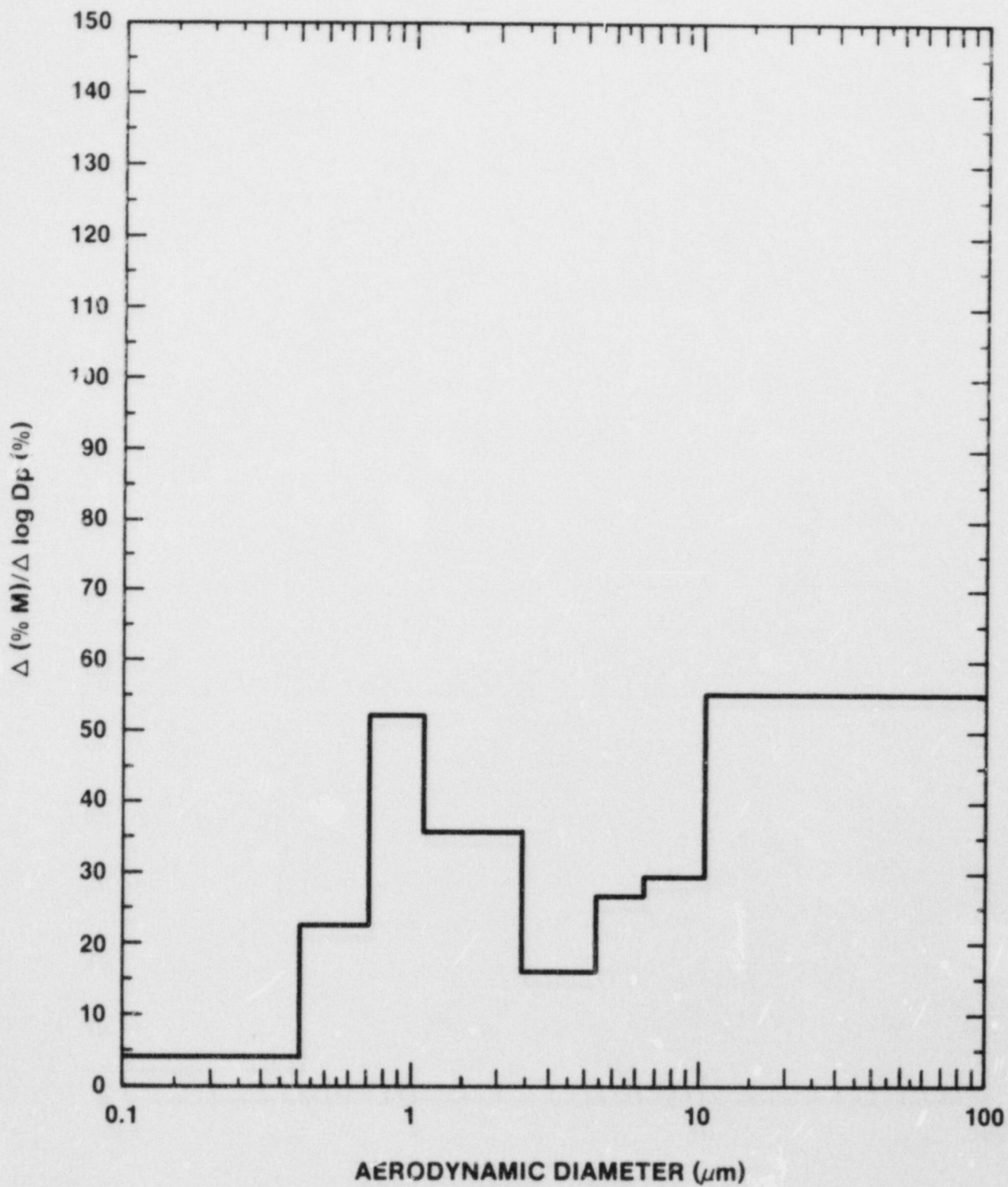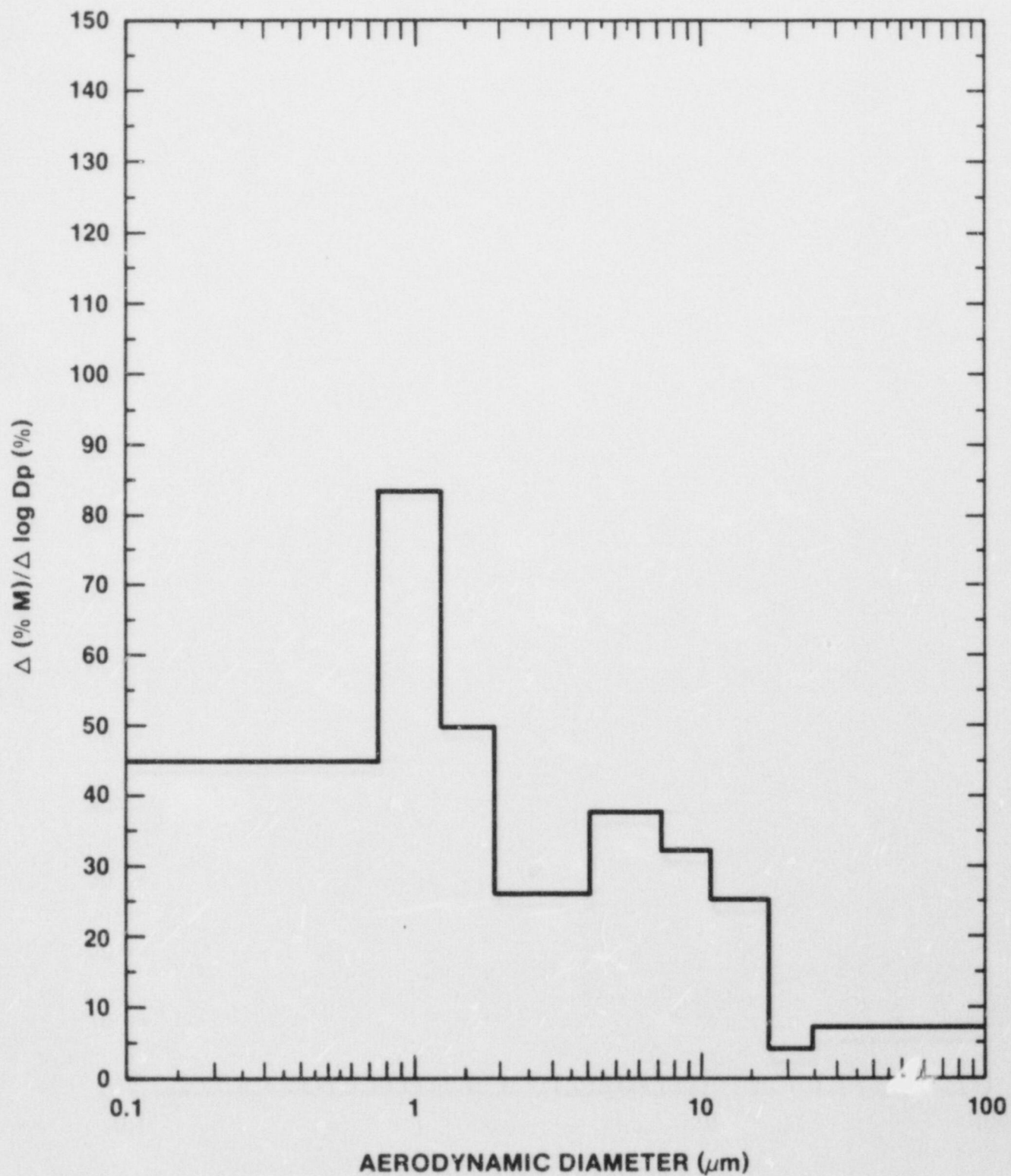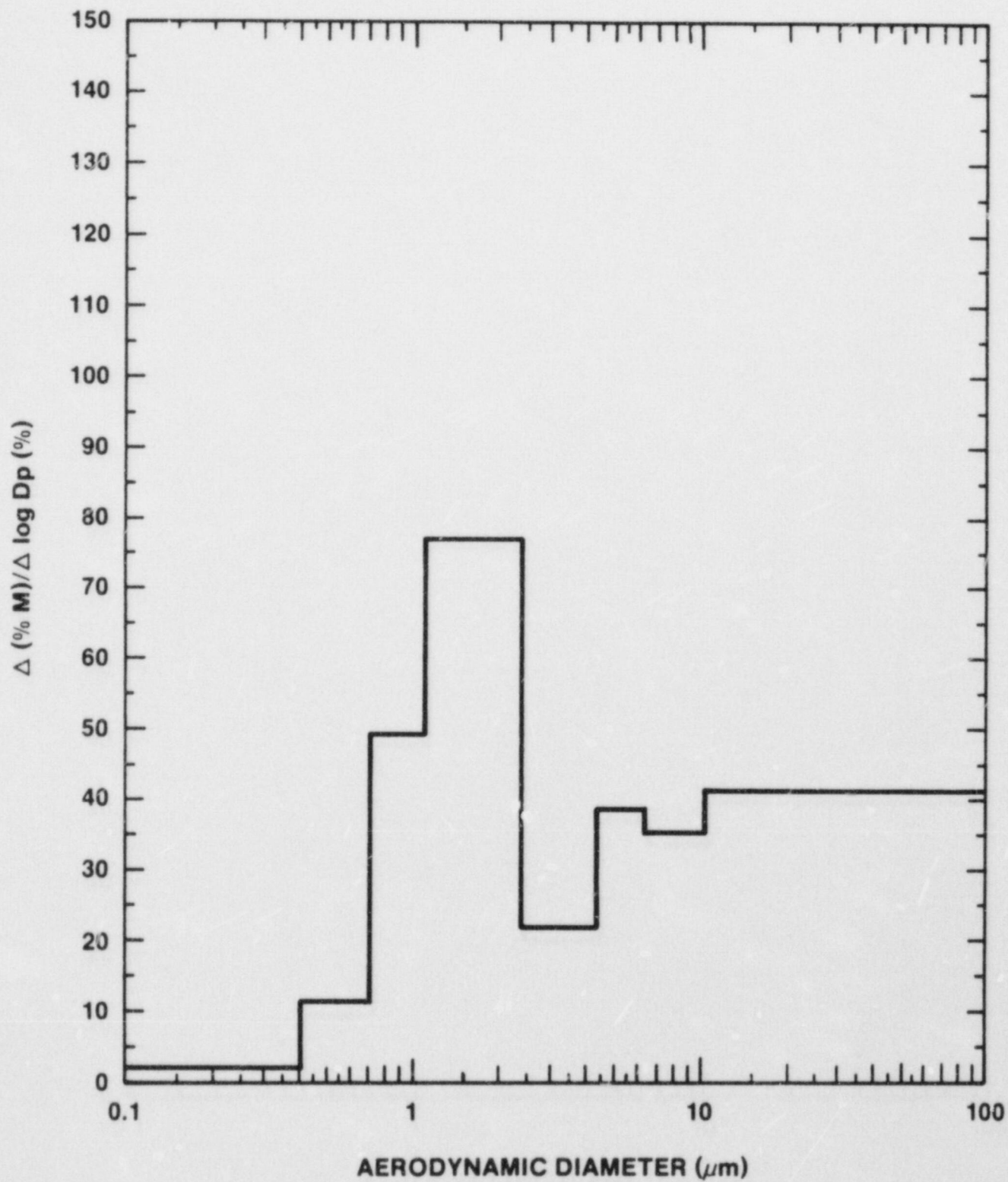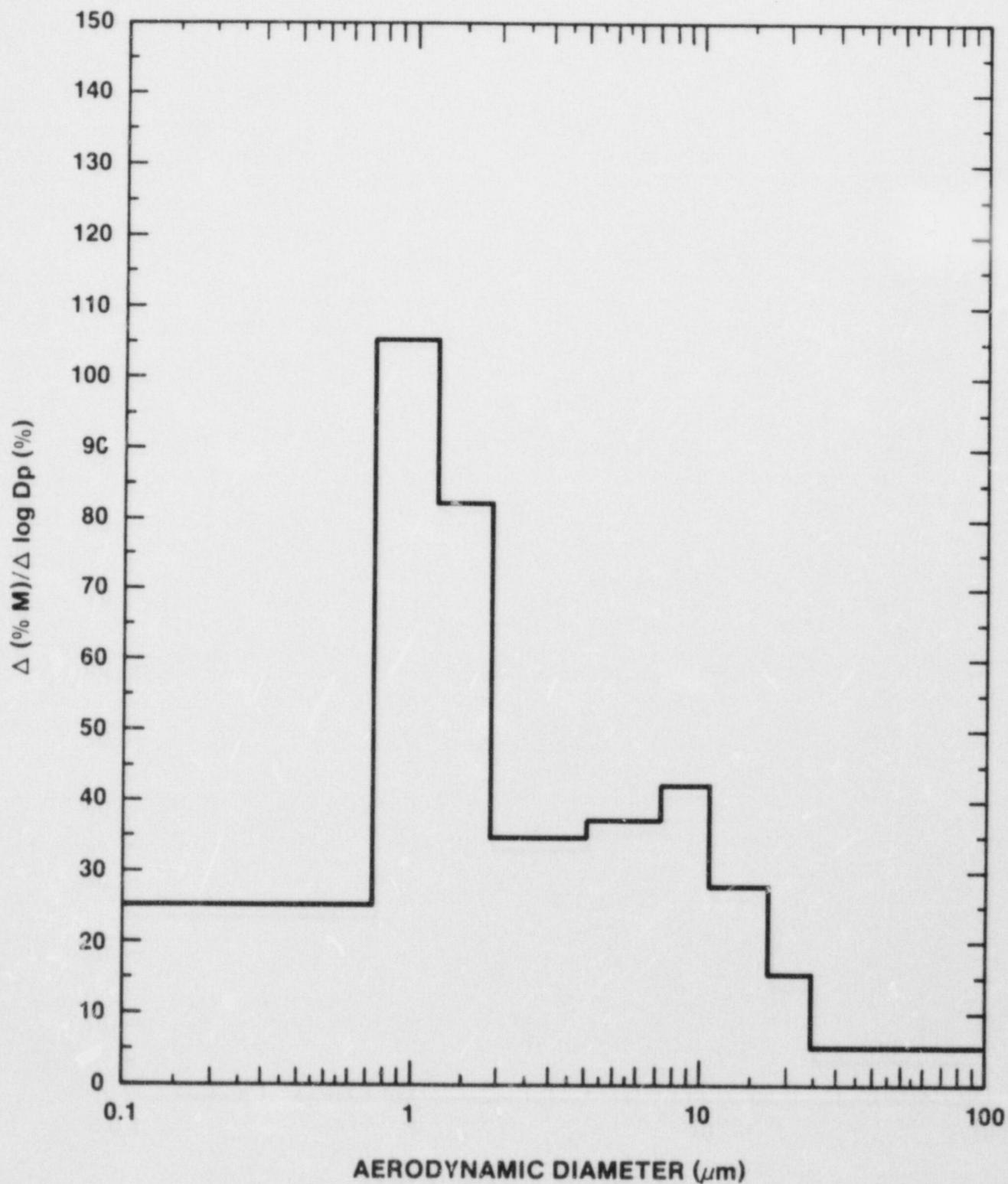FIGURE 67. SPIT-19 AEROSOL SIZE DISTRIBUTION. IMPACTOR F

width of that interval. The horizontal axis is a log scale of the aerodynamic equivalent diameter. This approach caused the area under the curve in any given size interval to be proportional to the mass in that interval, simplifying the interpretation of relative mass contained in different size ranges.

In reviewing the impactor results, the data from impactor A and B on SPIT-18 should be considered with caution. The proximity of the rotating framework to the north wall of the chamber may have caused some spurious debris material to bounce from the back wall and be sampled. This was evident by the significantly larger fraction of the collected mass in the size range greater than ten micrometers. Because the mass collected by the impactor was very small, a single debris particle would be sufficient to cause a substantial shift in the mass distribution. The larger mass concentrations recorded by these two devices were also evidence of the possibility of additional mass in the collection stages. The rotating framework was placed in a different location on the SPIT-19 test to overcome this difficulty. As seen in Figures 62 and 63, there was a relatively smaller fraction of supermicrometer particles in the SPIT-19 results.

Analysis of the SPIT-18 impactor results suggested that the aerosol was principally in two size ranges, below one micrometer and larger than ten micrometers. These results corresponded with those reported from previous SPIT tests in which the jet from the melt generator was allowed to expand freely into the atmosphere.[24] In comparison, the results from the impactors on SPIT-19 indicated the same two ranges in addition to a third mode at nominally five micrometer diameter. Particles in the latter range were thought to have been formed by fragmentation of larger particles caused by the higher gas velocities inherent in SPIT-19. Comparing the results from both tests illustrated the effect of sample flowrate on the size distribution results. In nearly every direct comparison between impactors sampling over the same time interval, the higher flowrate device had substantially more material in the size range greater than ten micrometers.

Electron photomicrographs of the collected aerosol (Figure 68) showed a difference in the character of each size range. The aerosol in the smallest range was an agglomerate of one-tenth micrometer and smaller particles. These were similar to condensation formed particles such as found in steel fumes. The material in the middle and largest sizes were both spherical single particles similar to aerosols formed by freezing of liquid droplets. A higher incidence of nonspherical and broken spheres in the largest range was consistent with the behavior of large drops that crust at the surface and then crack due to internal stress. These were similar in appearance to particles formed by steel droplets ejected from a melt pool by bubble bursting.

-138-
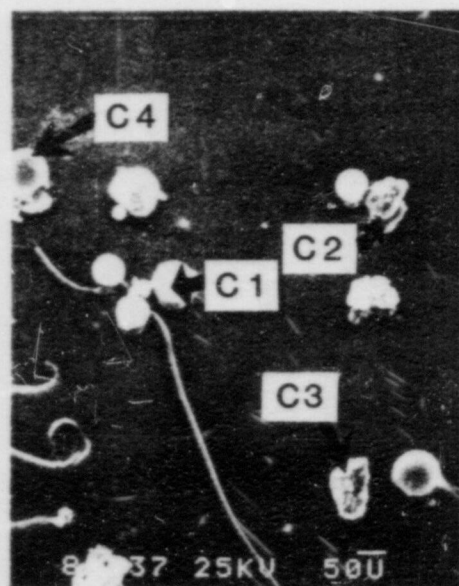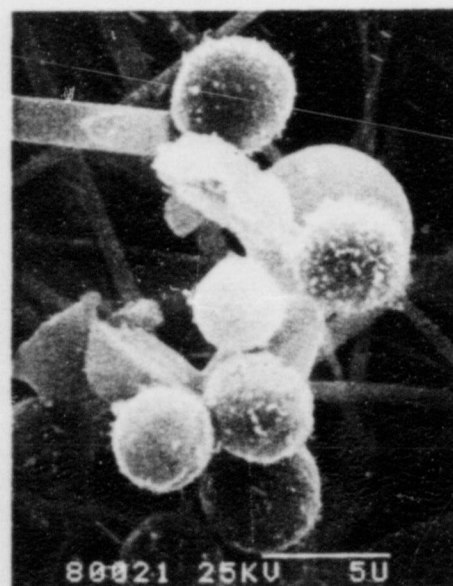
Dp = 65 MICRON   Dp = 5 MICRON   Dp = 0.5 MICRON

FIGURE 68. ELECTRON PHOTOMICROGRAPHS OF COLLECTED AEROSOL PARTICLES

The elemental content of the aerosol was obtained qualitatively by energy dispersive spectroscopy (EDS). The results of this analysis for the smallest particles from each test are given in Figures 69 and 70 for SPIT-18 and SPIT-19, respectively. The particles in this range were homogenous and composed principally of iron. This was expected given that the vapor pressure of the iron was greater than that of alumina. Little or no aluminum was observed in these smallest particles. The largest particles were not homogenous and were principally iron, aluminum, or both as illustrated by Figures 71 through 73, respectively. This characteristic was consistent with the supposition that the larger particles were formed by mechanical means such as bubble bursting or fragmentation.

The sample areas considered by the electron photomicrographs and EDS were not statistically representative of the overall aerosol character. These techniques provided an indication of the formation mechanisms leading to the size and chemical nature of the aerosol. The mechanisms of melt condensation and mechanical breakup[24] should also be active in realistic situations such as severe reactor accidents. Thus the aerosol results obtained from the SPIT and HIPS experiments may be appropriate indications of the mechanics of the source term in such accidents.

H. Interaction Chamber Response

The discharge of the highly fragmented melt particles into the atmosphere of the interaction chamber caused energy to be transferred from the debris to the gas and structure of the chamber. The SPIT tests were instrumented with pressure and temperature transducers to diagnose the direct heating of the chamber atmosphere. The single pressure gauge employed on the SPIT-18 test was mounted on the north wall of the chamber. The four pressure gauges used for the SPIT-19 test were mounted on the ceiling and walls of the chamber (north, west, and south). Thermocouples were placed on the walls and ceiling and also extended into the chamber atmosphere. Detailed descriptions of the devices and their placement are given in Section II.

1. SPIT-18

The chamber pressure history recorded by the gauge on the rear wall of the interaction chamber is shown in Figure 74. The peak pressure recorded was 13.9 kPa, occurring approximately 300 to 400 milliseconds after the start of melt dispersal. The
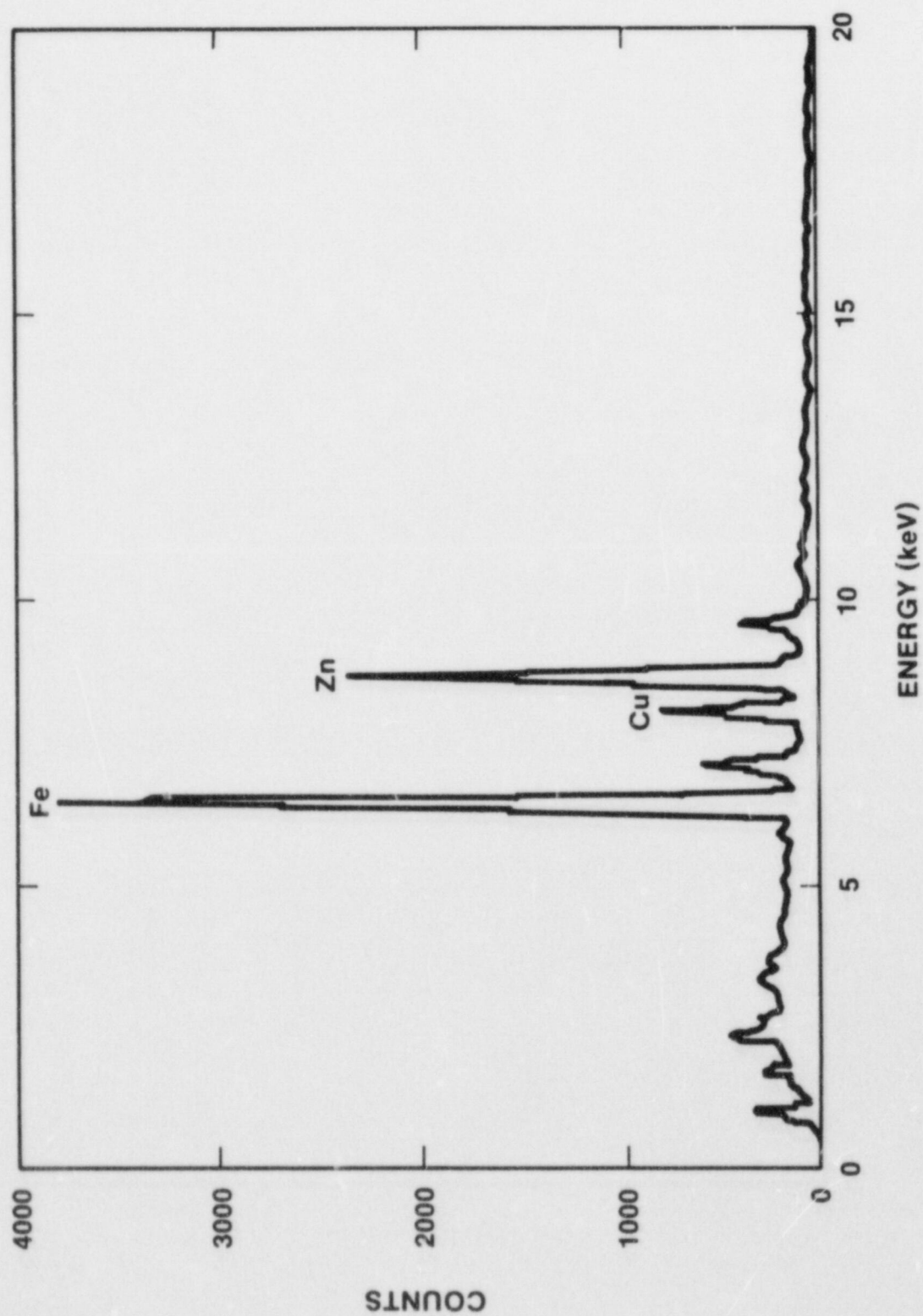
FIGURE 69. ENERGY DISPERSIVE SPECTROSCOPY RESULTS FOR A
SUBMICROMETER PARTICLE FROM THE SPIT–18 TEST
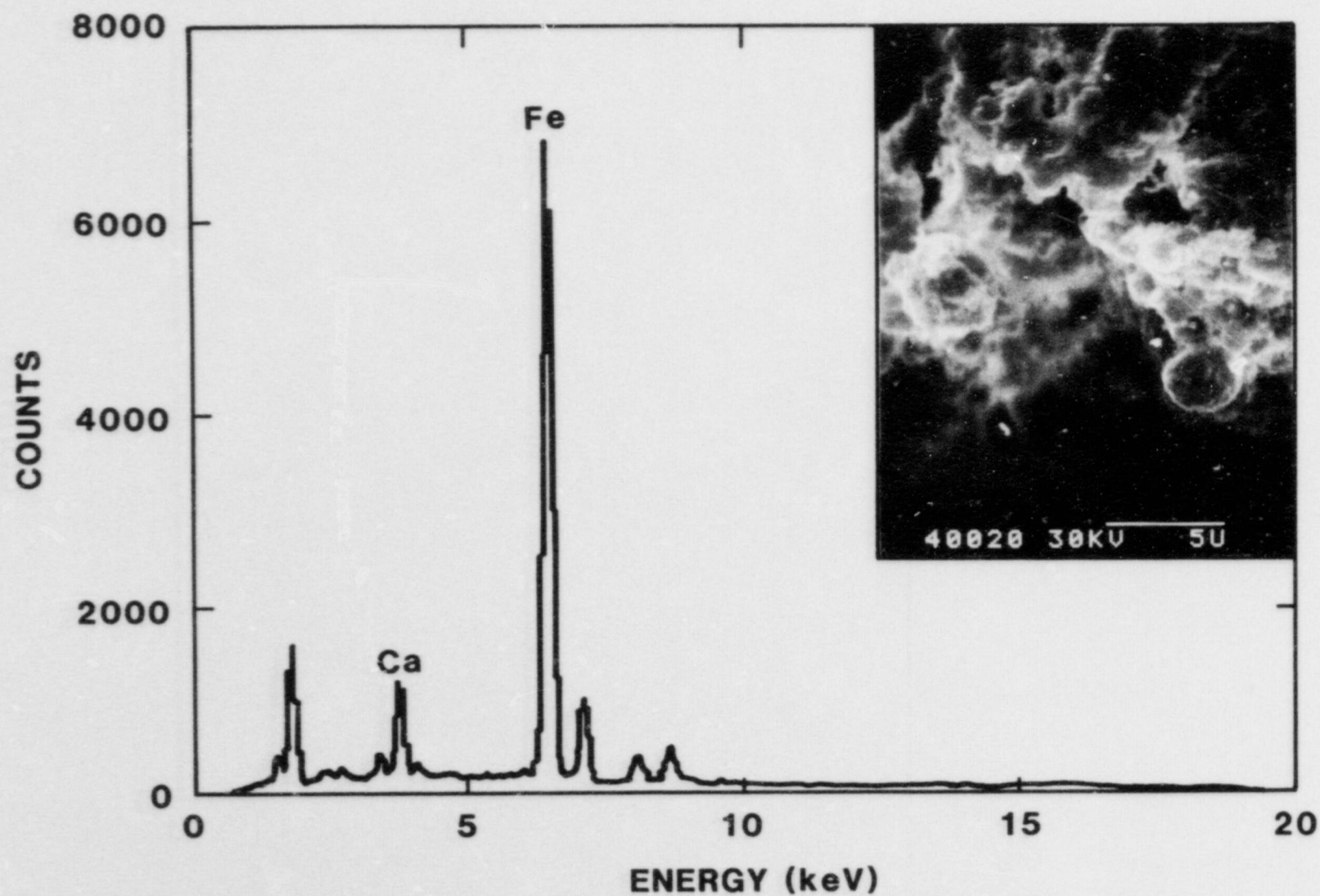
FIGURE 70. ENERGY DISPERSIVE SPECTROSCOPY RESULTS FOR A SUBMICROMETER
PARTICLE FROM THE SPIT-19 TEST

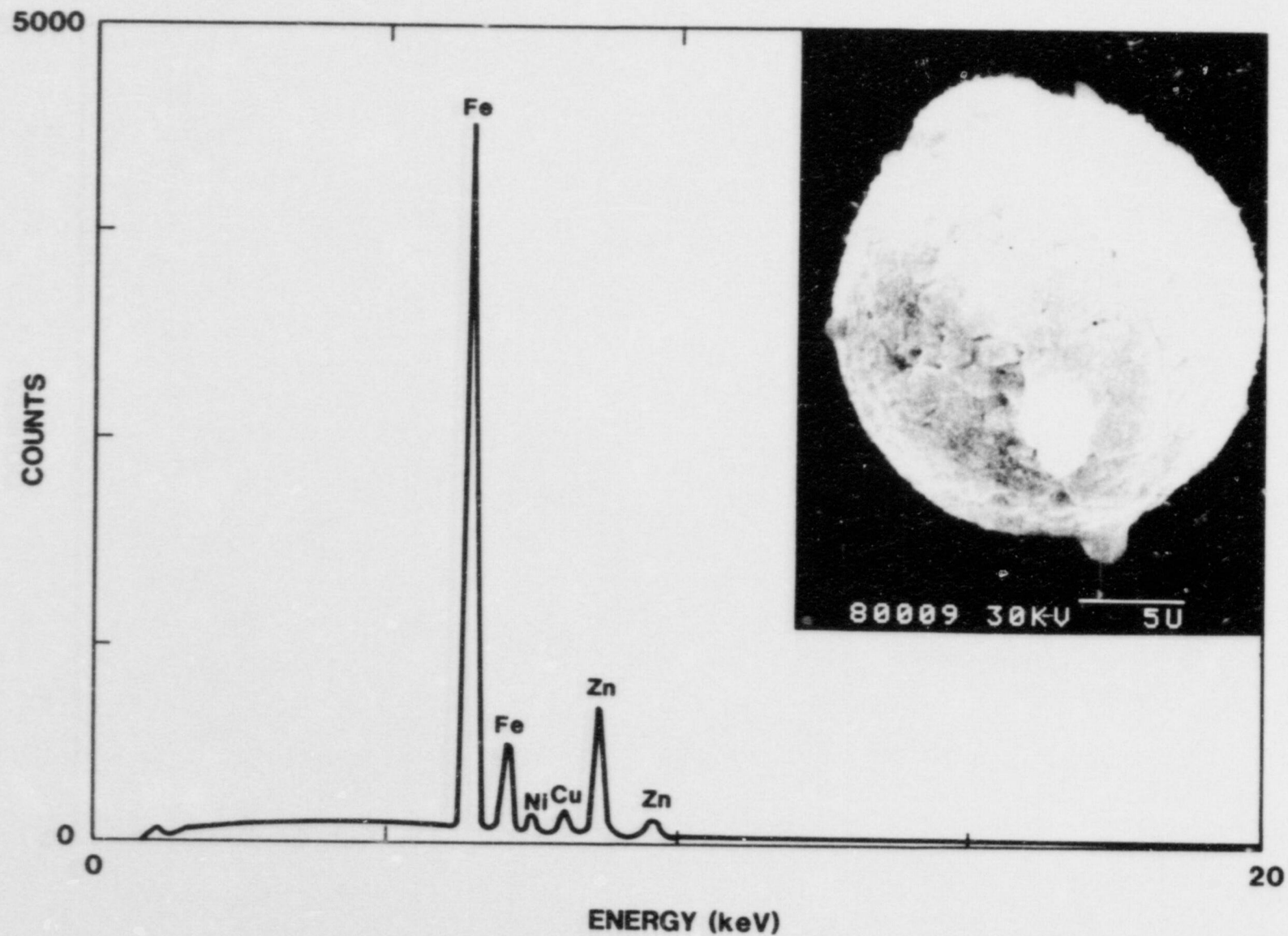FIGURE 71. ENERGY DISPERSIVE SPECTROSCOPY RESULTS FOR A IRON–BEARING
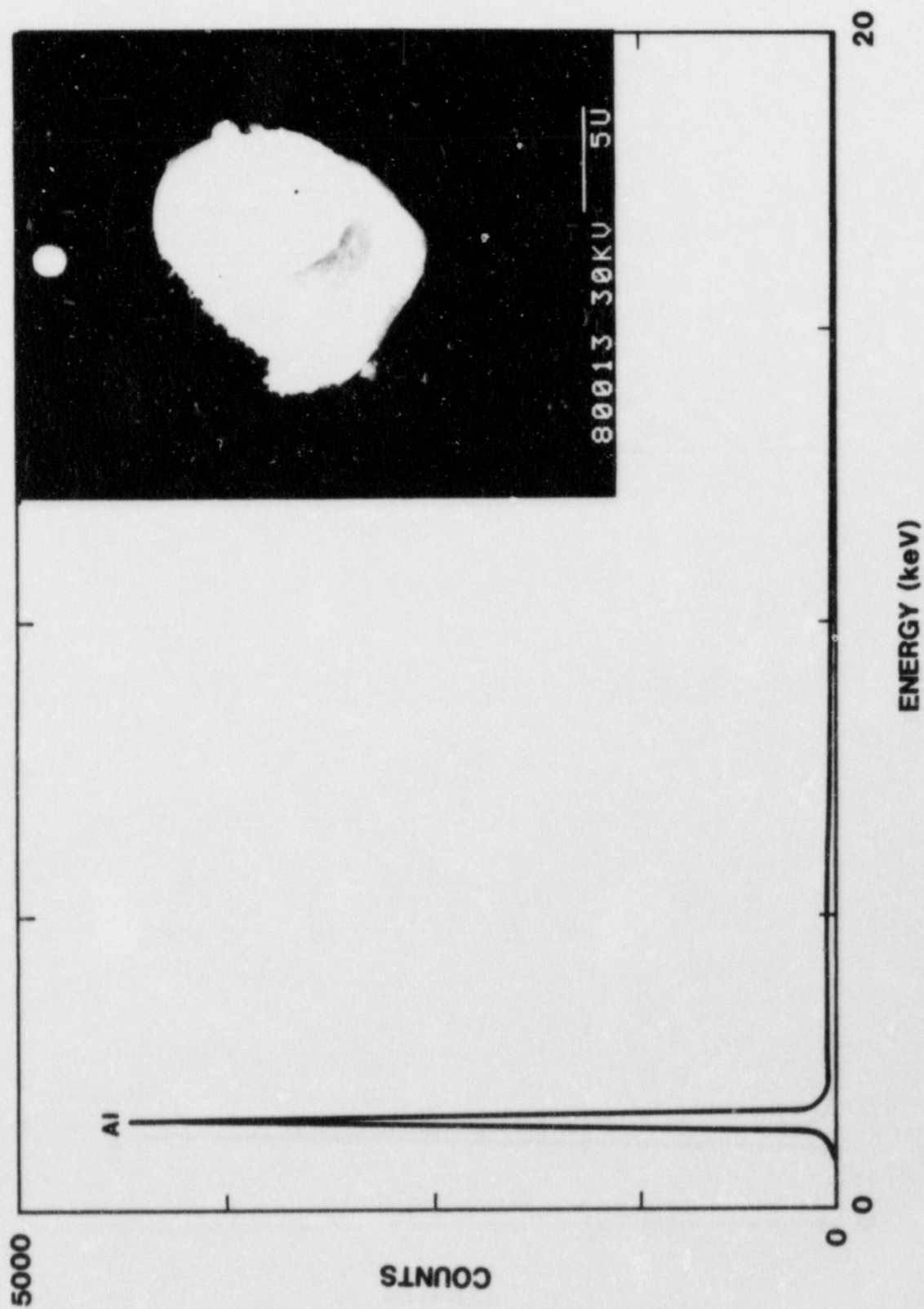SUPERMICROMETER PARTICLE

FIGURE 72. ENERGY DISPERSIVE SPECTROSCOPY RESULTS FOR A ALUMINUM-BEARING SUPERMICROMETER PARTICLE
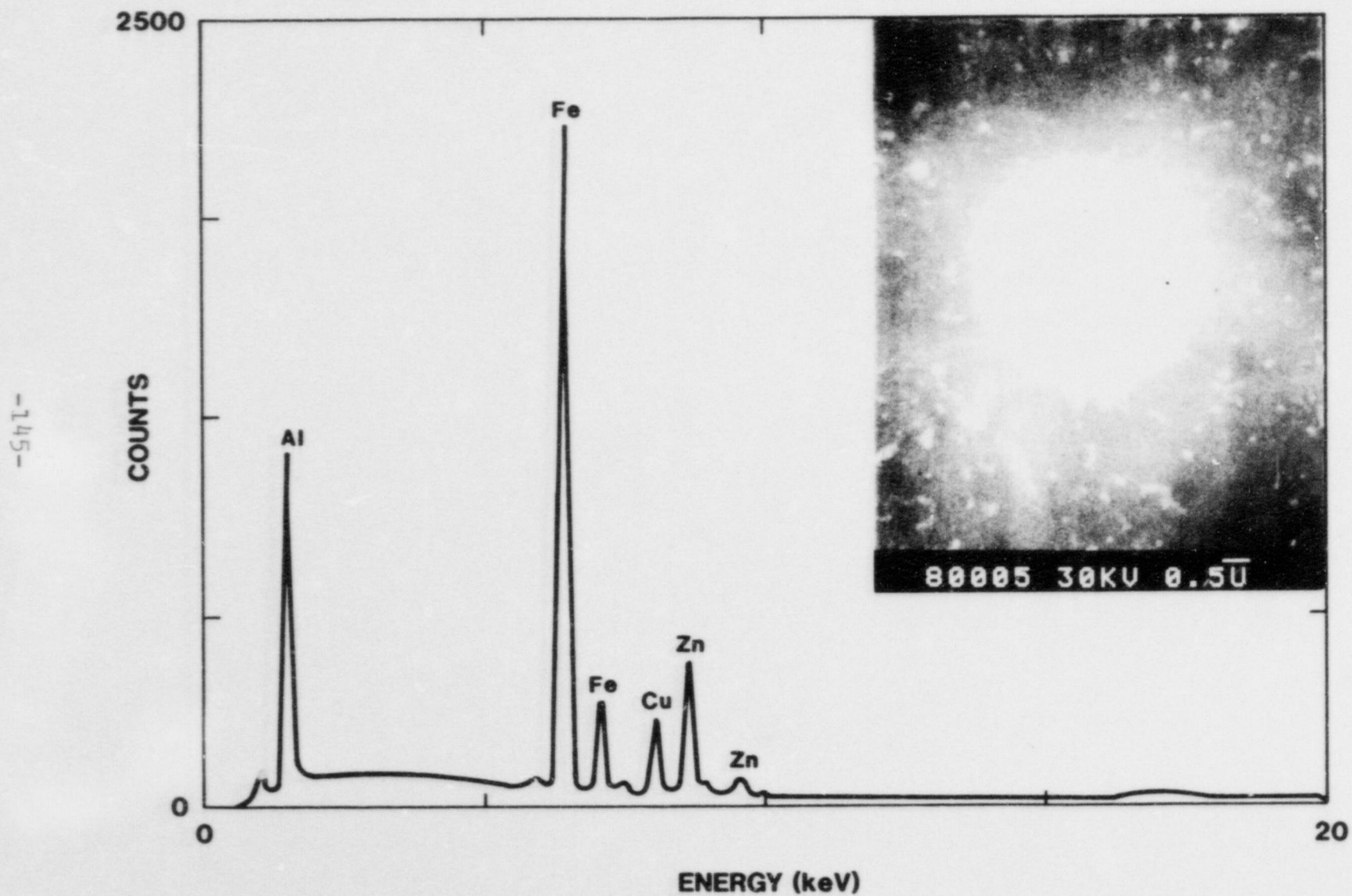
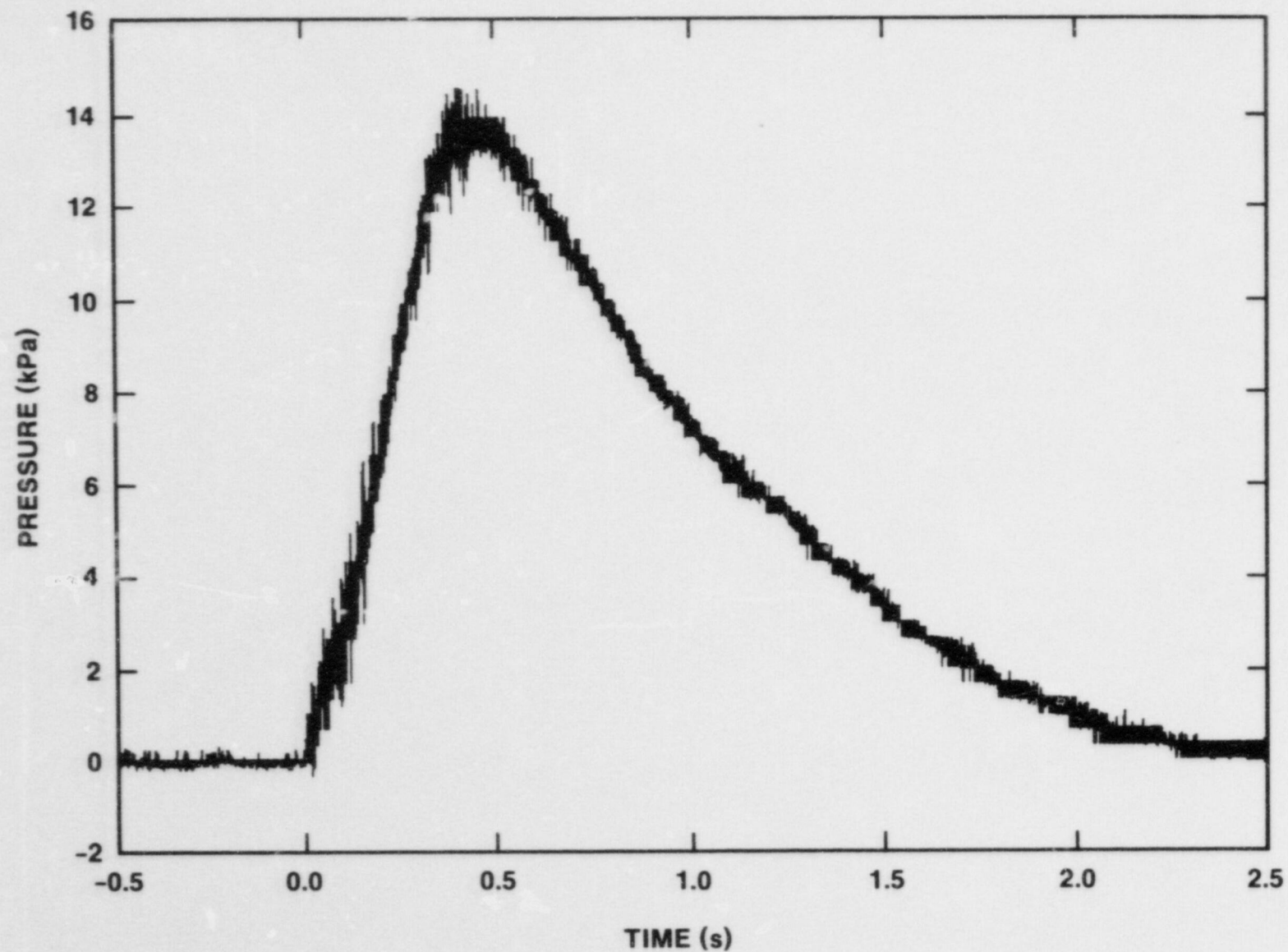FIGURE 73. ENERGY DISPERSIVE SPECTROSCOPY RESULTS FOR A IRON- AND ALUMINUM-BEARING SUPERMICROMETER PARTICLE

FIGURE 74. INTERACTION CHAMBER PRESSURE RECORD FROM THE SPIT-18 TEST

damage to the chamber caused leaks that affected the ultimate pressure level and the pressure decay history. The extent of the influence the leaks had could not be accurately determined. The decrease in pressure to ambient occurred in approximately 650 milliseconds. The rapid fall in pressure relative to what would be expected if only natural cooling were occurring suggested that the leaks were large.

Calculations were performed with a single-particle burning model[25] to determined the maximum overpressure that could be achieved for this experiment. Based on an interaction distance of three meters, the model indicated that the peak overpressure and temperature would be 240 kPa and 838 K, respectively. These values yielded a theoretical energy conversion (the percent of the total energy released to atmosphere) of 52 percent. The model assumed that the displaced mass was in the form of droplets of equivalent to the mass mean diameter. Chemical oxidation and heat transfer were accounted for with the heat of reaction coupled back into the temperature of the particle. The chemical reactions were assumed to be limited by the flow of oxygen to the surface of the drops. The reactions were terminated when the particles become totally oxidized.

The measured pressure increase in the chamber was attributed to both the blowdown of the melt generator and the direct heating of the chamber atmosphere. In order to differentiate between the two effects, the overpressure caused by the blowdown of the melt generator was estimated assuming an isothermal expansion of the gas out of the vessel. This calculation was estimated to develop approximately 8.9 kPa overpressure. If temperature losses were included in the calculation the increase was significantly less, on the order of 2.4 kPa. These two values were then used to define a lower and upper bound for the pressure increase from direct heating of 4.9 to 11.4 kPa, respectively.

Figure 75 shows the recorded behavior from two thermocouples used to measure the temperature of the chamber atmosphere. As indicated above, the theoretical temperature increase for a three meter propagation distance was 838 K. The peak recorded temperatures were also less than expected based on a pressure rise from direct heating of 4.9 to 11.4 kPa. The relatively low measured temperatures suggested that the sensors were not capable of accurately monitoring the fast-rising temperature transient. In addition, the peak recorded temperature of all the thermocouple devices occurred approximately 50 seconds following ejection, well after the chamber pressure had returned to atmospheric level. The recorded rise times of the temperature histories were significantly shorter than specified by the manufacturer, indicating that the temperature change was very nearly a step change compared to the capability of the measuring device. The late time response was attributed to heating of the sensors by debris dispersed on the chamber floor.
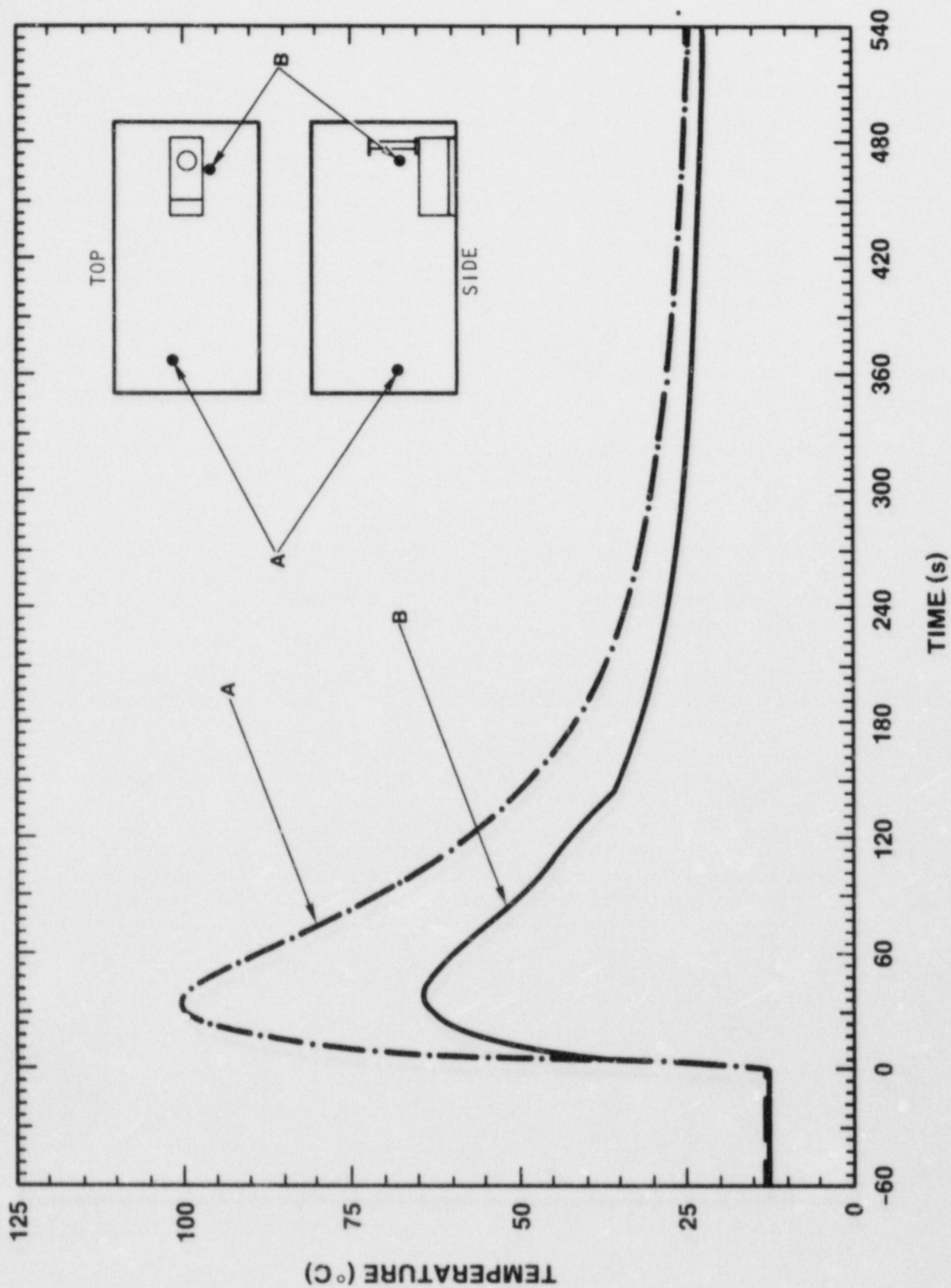
FIGURE 75. SPIT-18 INTERACTION CHAMBER ATMOSPHERE THERMOCOUPLE RECORDS

Direct atmospheric heating involves the exchange of energy between the hot debris and the gas within an enclosure. The energy released is from both thermal energy (latent and sensible heat) and exothermic chemical reactions. For the products of the thermite reaction, the debris energy was estimated to be 3.1 MJ per kilogram of debris for quenching the material from 2800 K to solidification. If all of the iron (100 percent complete reaction) were oxidized, an additional 2.6 MJ per kilogram of debris would be available. Sensible heat would also be available after quenching, but was not included as part of this analysis because the final temperature of the debris was not known.

An estimate of the efficiency of the energy exchange process was made using the assumed energy in the debris and the observed increase in the chamber pressure. Incomplete oxidation of the iron or a different melt temperature would alter the calculated values. It was assumed that only the atmosphere in the chamber interacted with the debris and that it behaved as a perfect gas. Further, only the pressure increase attributed to direct heating (4.9 to 11.4 kPa) was used in the calculations. For these assumptions, it was estimated that the chamber temperature rise corresponding to the measured pressure increase should be 14 K to 40 K. Based on estimated energy available in the 6 kg of melt dispersed, the conversion efficiency range was found to be 1.6 to 4.6 percent. Compared to the theoretical efficiency given above, a relatively small amount of the debris energy went into heating the chamber atmosphere.

The apparent low efficiency of the energy transfer was also supported from posttest observations. The spatial distribution of the debris (Figure 43) and the appearance of the enclosure showed that the debris exiting the cavity had deflected off the ceiling (evidenced by extensive scorch marks) before coming to rest near the north wall. Assuming that the debris was traveling at nominally 45 m/sec, it required 130 milliseconds for the flight from the apparatus to the ceiling and then to the floor. Using a path defined in this manner, calculations with the theoretical single particle model indicated that particles larger than 0.5 millimeter were neither quenched nor completely oxidized. Because virtually all of the particles collected on the pans in the chamber was in the size range greater than 0.42 millimeter (greater than 88 percent), the bulk of the debris mass transferred only a portion of its energy to the atmosphere.

2. SPIT-19

The chamber overpressure observed in the SPIT-18 test prompted the use of several pressure gauges in the SPIT-19 experiment. The recorded pressure histories from these devices are shown in Figures 76 through 79. The pulse arrival time, peak
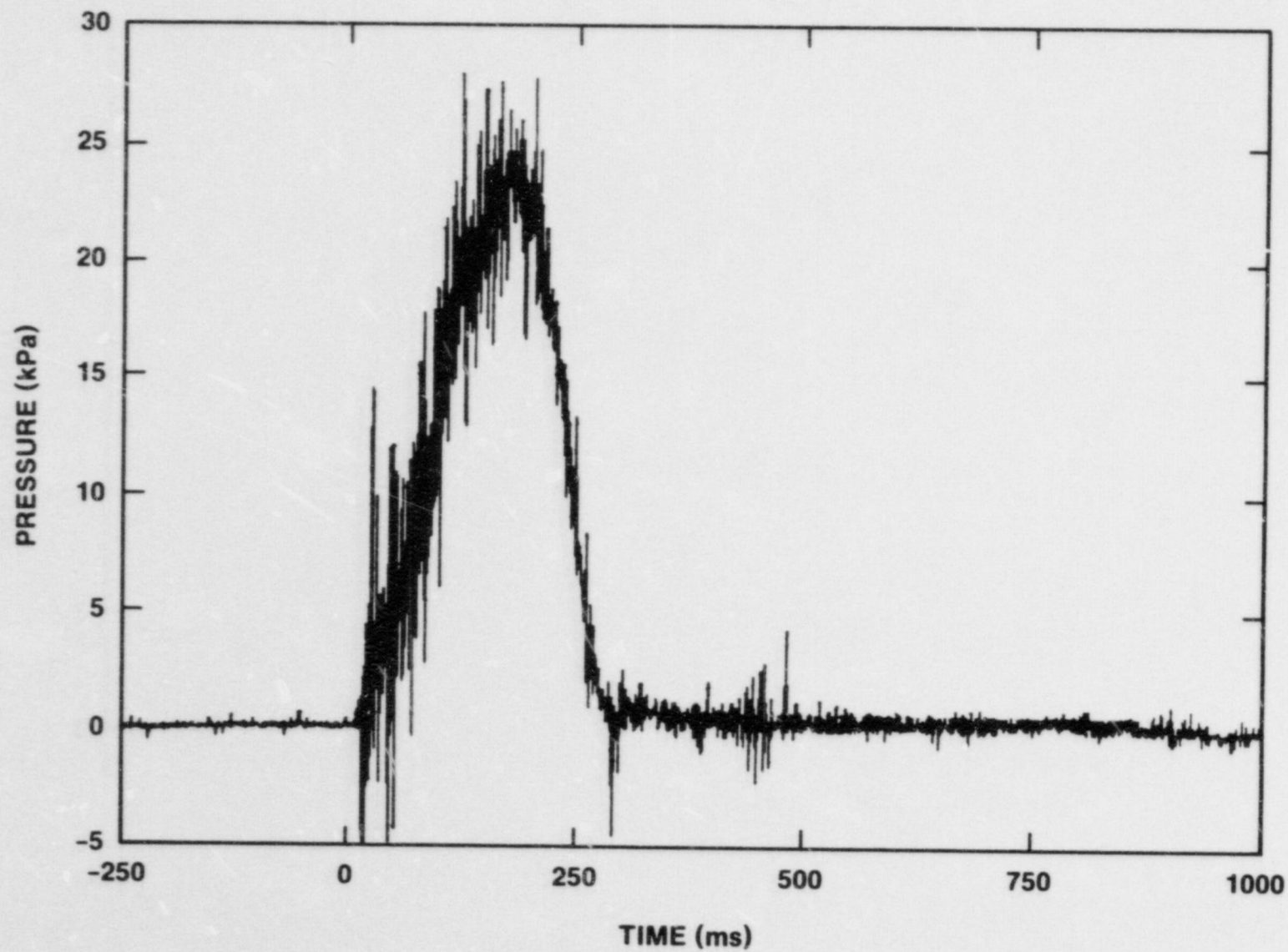
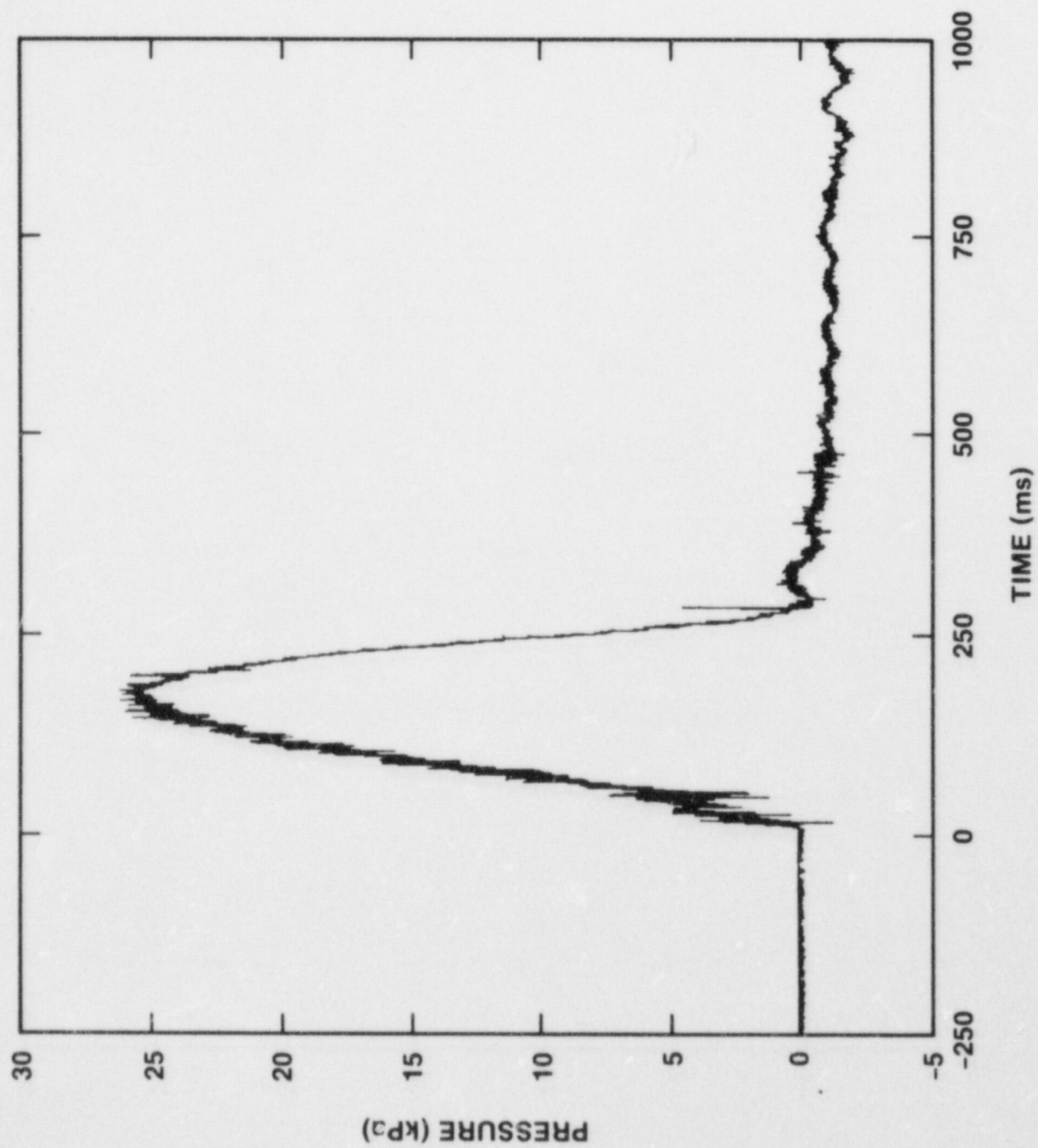FIGURE 76. SPIT-19 INTERACTION CHAMBER PRESSURE RECORD - WEST WALL

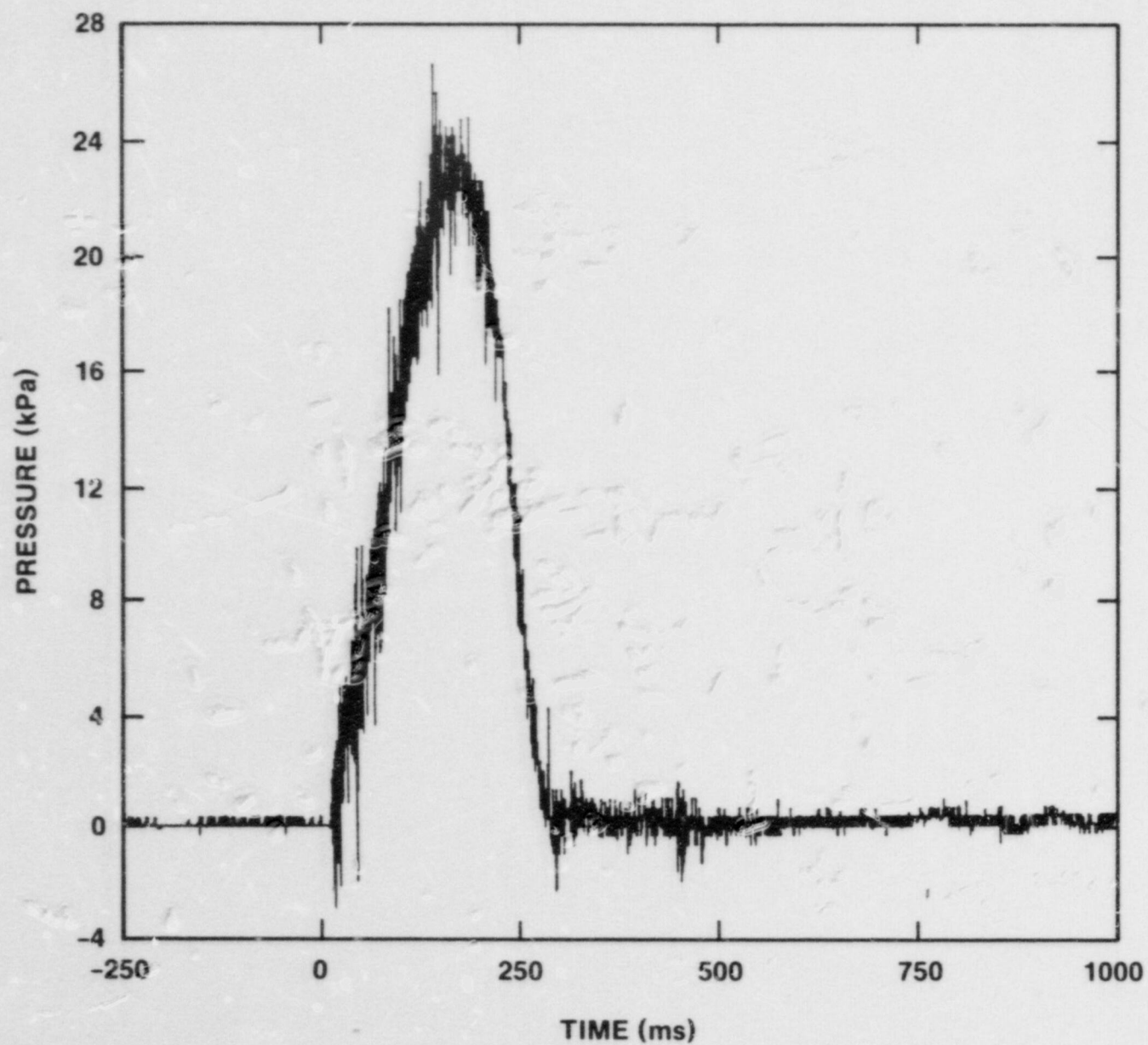FIGURE 77. SPIT-19 IC PRESSURE RECORD – INSERTED INTO CHAMBER

-151-

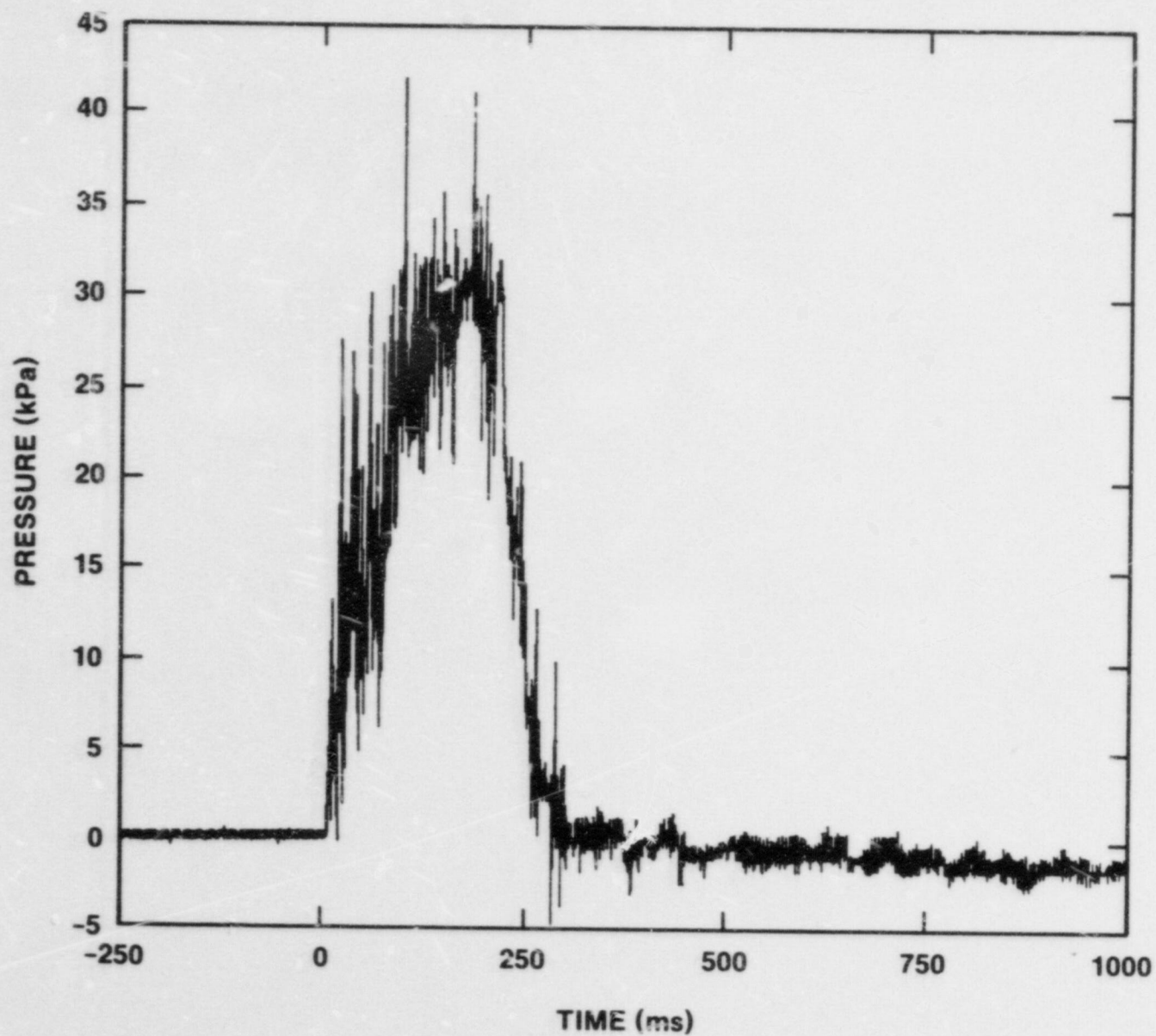FIGURE 78. SPIT-19 IC PRESSURE RECORD – NORTH WALL

FIGURE 79. SPIT–19 IC PRESSURE RECORD – CEILING

pressure magnitude and timing of the pressure peak from each gauge are summarized in Table 20. The times given were referenced to the first appearance of debris from the cavity exit. The expression "Breakaway Time" was determined from extrapolation of the slope of the initial gauge response back to the horizontal baseline. This technique obtained an indication of the velocity of the pressure pulse. As with the SPIT-18 test, the pressure excursion was composed of contributions from the blowdown of the melt generator and from direct heating of the chamber atmosphere. As discussed previously, the pressure increase caused significant damage to the chamber, which allowed an undetermined amount of gas to escape. It was estimated that the expansion of the gas from the melt generator (including the gas dissolved in the melt) caused a 10.3 kPa pressure rise in the chamber. Using this value and the gauge records gave a range of 12.3 to 20.7 kPa for the pressure increase caused by direct heating of the chamber atmosphere.

Table 20
Summary of the SPIT-19
Interaction Chamber Pressure Records

GAUGE LOCATION	BREAKAWAY TIME (ms)	PRESSURE PEAK MAGNITUDE (kPa)	TIME (ms)
South Wall	9.9	31.0	178
West Wall	10.8	22.8	175
In Chamber (Ceiling)	11.9	23.4	185
North Wall	14.5	22.8	173

The range in the pressure levels recorded by the four gauges was large considering that the calculated wave velocities were high enough to cause the chamber to be essentially equilibrated in a time short compared to the pressure generation. Most likely, the temperatures achieved in the chamber were sufficient to cause some perturbation in the response of the gauges. The

gauge on the ceiling and the one on the north wall were probably more susceptible to this effect than the gauges located in the more protected west and south wall areas. Although impossible to quantify, it was estimated that thermal effects could be large enough to cause the observed differences in the recorded behavior.

The data given in Table 20 were used to determine if there was a correlation between the pulse arrival time and the position of the gauge. The velocities were determined using the time interval from initial melt discharge to "breakaway" and a characteristic dimension of the facility. Using the distance from the cavity opening to the gauge locations, the spread in the calculated pressure wave velocities was large. If the position of the pressure source was assumed to be approximately two meters from the cavity exit (coincident with the contact of the debris on the ceiling), then the range of calculated pressure wave velocities (200 to 220 m/sec) was small. The impact of the debris on the ceiling may have caused significant fragmentation or a mechanism for entrainment of the atmosphere in the debris stream. Regardless of the mechanism, the pressure source originated at some distance from the apparatus (i.e. direct atmospheric heating) and was not from the rapid expansion of gas out of the cavity.

Figure 80 gives the response of four thermocouples that were inserted into the interaction chamber atmosphere. The sensors represent several different positions within the chamber to show possible variations in the atmosphere temperature. The records showed significantly higher temperatures (150°C to 250°C) occurring at earlier times than were seen during the previous SPIT-18 test. The peak temperatures were recorded within 20 seconds of the start of melt discharge, which was long compared to the discharge time interval. The peak recorded temperature was less than the actual value because of the slow response of the sensing devices. An estimate of the peak temperature was made by extrapolating the slope of these curves back to zero time. This method indicated that the temperature in the chamber could have been as high as 500°C to 600°C.

The four different locations of the sensors provided an indication of the variation in the temperature in the chamber. The greatest temperature level was recorded by the sensor immediately above and adjacent to the cavity exit, while the lowest values were from a device close to the floor and next to the apparatus. Inspection of the data from all of the thermocouples in the chamber showed no consistent trend except that the devices closer to the floor had somewhat lower peak temperatures.
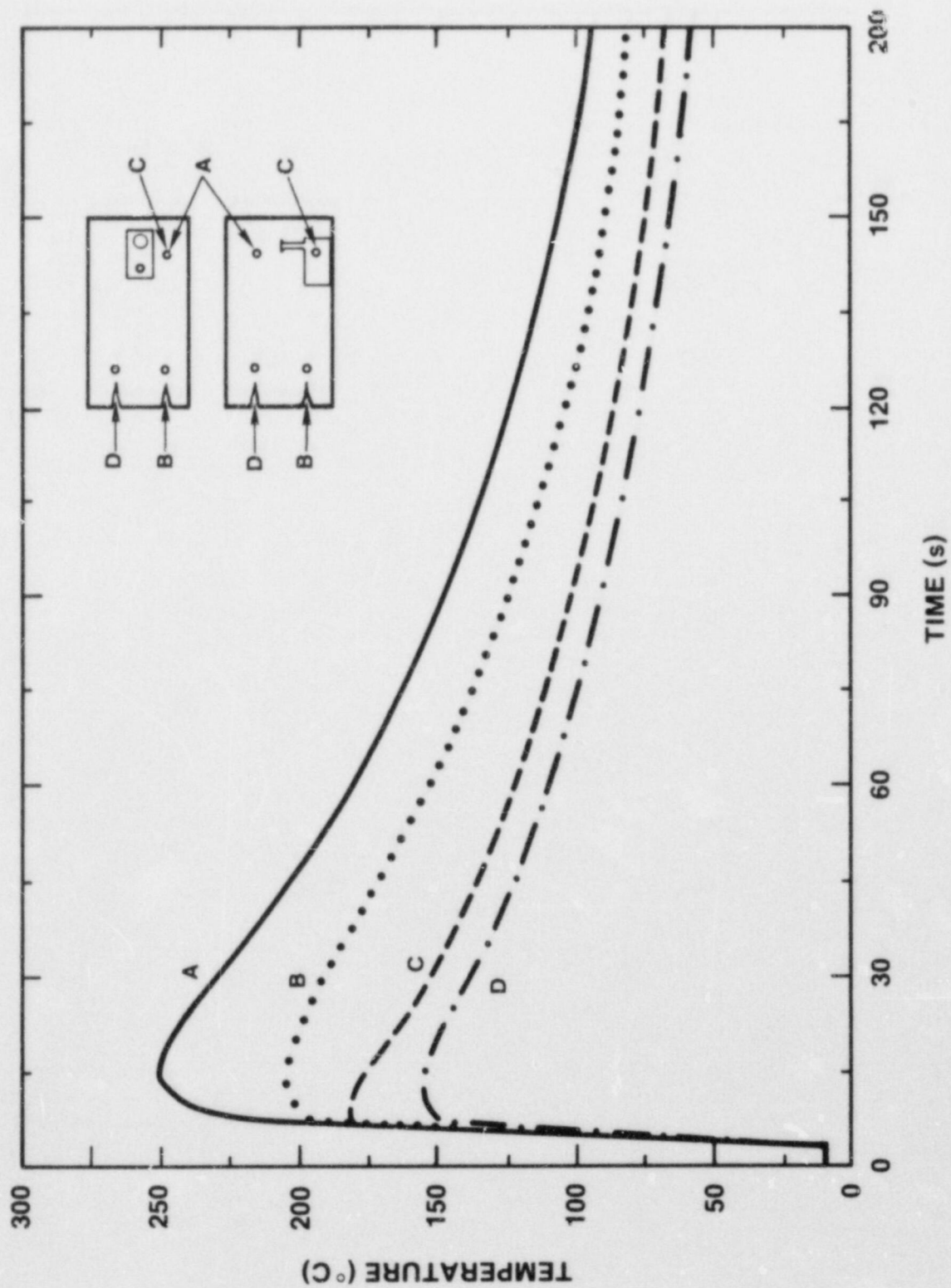
FIGURE 80. SPIT-19 IC ATMOSPHERE TEMPERATURE HISTORY

With a few simplifying assumptions, the exchange of energy between the debris and chamber atmosphere was estimated from the recorded pressure or temperature pulses. As indicated above, the recorded peak temperatures did not concur with the temperature increases calculated from the pressure records. The estimated efficiencies based on the recorded data for the direct atmospheric heating from the SPIT-19 data are given in Table 21. The efficiency was defined as the fraction of the dispersed debris energy (based on a temperature of 2800 K) that was imparted to the atmosphere.

Table 21
Estimated Efficiency of Direct Atmospheric
Heating in the SPIT-19 Experiment

| | Pressure Record | | Temperature Record | |
	12.3 kPa	20.7 kPa	160°C	250°C
Efficiency (%)	2.8	4.8	10.0	1 .4

For comparison, the single particle model[25] was employed to calculate the direct heating in the SPIT-19 experiment. Based on the amount of mass dispersed and a three meter interaction distance, the model predicted a pressure rise of 480 kPa and a temperature increase of 1665 K. Based on these values it was estimated that the energy exchange efficiency was 76%. The efficiency value was significantly greater than determined using the recorded pressure and temperature values from the experiment. The values obtained from the pressure gauge were low because of the losses that occurred when the interaction chamber broke loose from the concrete base. Film records indicated a significant flow area through the damaged regions was available in a time interval comparable to the discharge of debris from the cavity. The results estimated from the thermocouple records were also in error because the sensors were probably directly radiated by the dispersed debris and the peak value was mitigated by the slow response of the gauge.

Although the maximum recorded temperature in the SPIT-19 experiment was approximately 250°C, physical evidence within the chamber indicated the actual temperature was even higher. For example, very little scorching of the painted surfaces was observed in the SPIT-18 test, but virtually all of the paint was

-157-

decomposed in the SPIT-19 event. Further, the polyvinyl-chloride tubing used in the chamber was completely discolored and melted in some areas. The tubing specifications indicated that discoloring initiates at nominally 165°C with the extent of the effect dependent on the time of exposure and the absolute temperature. Considering that the thermocouple records indicated that the chamber was above the initiation point for less than 90 seconds (Figure 80), the maximum temperature must have been well in excess of the recorded value.

3. HIPS-2C and HIPS-5C

The atmospheric pressure by direct heating in the two SPIT experiments indicated that unmanageable levels would be attained if extrapolated to the larger HIPS scale. For example, if 95% of the mass was dispersed (76 kg) and imparted 10% of its energy to the chamber atmosphere, the resulting pressure and temperature would be 1160 K and 411 kPa, respectively. Pressures of this order would clearly fail the interaction chamber, in a manner considerably more dramatic than was observed in either of the SPIT tests. For this reason, the two HIPS experiments were not placed in the chamber.

IV. CONCLUSIONS

The objective of the SPIT and HIPS experiments is to provide data to support modeling of the phenomena involved in high pressure ejection of molten core debris into the cavity beneath the reactor pressure vessel. Such phenomena may accompany reactor accidents that occur at high primary system pressure. Specifically, the experiments investigated the breakup and transport of the core debris out of the cavity and into the containment region. Date were obtained on pressure vessel blowdown history, breach aperture growth, debris discharge history, melt entrainment, particle size distributions, aerosol generation, and energy transfer from the debris to the atmosphere. Based on the results, preliminary models of the governing phenomena were developed.

The four experiments discussed in this report show that high-pressure ejection of molten core debris into a scaled Zion cavity resulted in nearly complete dispersal of debris. Unlike the benign film-flow portrayed in safety studies and analyses, the molten material was highly fragmented into millimeter and smaller particles. These particles resulted from entrainment of the melt by the gas discharged from the simulated reactor pressure vessel. The small size and potentially long propagation of the debris particles made them susceptible to transfer of energy to the atmosphere.

Two 1:20 scale experiments were performed within a steel enclosure to retain the debris and aerosol generated during the melt ejection and debris dispersal processes. Photographic and X-ray observations of the discharged material from the cavity showed it to be composed of highly fragmented debris within a gas stream. The ejected debris caused heating and pressurizing of the enclosure atmosphere that damaged the structure prior to the completion of the test. Direct heating of the enclosure atmosphere occurred in both of the SPIT tests. Estimates of the energy conversion efficiency from the debris to the atmosphere were made based on the recorded temperature and pressure histories and the estimated thermal and chemical energy available in the debris. These calculations resulted in conversion efficiencies from 2.8 to 16.4 percent. The results should not be applied directly to reactor scale because of the limited path lengths involved in the experiments and the uncertainty in the available melt energy. A simple model based on single particle behavior gave a theoretical estimate of efficiency to be 52 to 76percent, with the value highly dependent on the debris length of flight.

Estimated efficiency values obtained from pressure records of transducers placed on the interaction chamber were in the low

end of the stated range because chamber venting occurred during the test and prevented attainment of the actual peak value. The estimates based on the thermocouple data may be higher or lower than actual, depending on the extent of radiation from the debris directly to the sensors or the mitigation of the peak value induced by the slow response of the devices.

The debris collected in the two SPIT tests was in the form of frozen splashes, small spheres, and large agglomerates. The appearance of the splashes suggested that the drops were near freezing when impact occurred. The spheres were created when the molten drop quenched during flight, forming a hard outside surface. Subsequent cooling of the inner core caused shrink holes to develop in many of the recovered particles. The agglomerates were found principally along the wall farthest from the apparatus and were constituted of many small particles firmly adhered together. Mechanical sieving of the spherical debris collected in the two SPIT experiments showed the particle size followed a log-normal distribution with a mass mean size of nominally 0.75 and 0.43 millimeter for SPIT-18 and SPIT-19, respectively. The smaller size of the SPIT-19 debris was a result of the higher gas velocities that existed in the cavity, relative to that used in SPIT-18. The measured debris size agreed with theoretical estimates based on the test conditions.

Electron microprobe analyses of the debris particles indicated the presence of iron, iron oxide, aluminum, and alumina. The composition did not demonstrate extensive separation of the two phases (iron and alumina). Many samples had iron and aluminum coexisting in the same region, suggesting the material was well mixed even at the time of solidification. This behavior indicated that the quenching process probably occurred rapidly, as predicted by the results of particle burning model. The presence of aluminum in the particles suggested that the thermite reaction was not complete. One sample clearly showed the development of the iron oxide layer from the outside surface towards the center of the particle.

Two experiments were performed using 1:10 linear scale models of the Zion cavity (HIPS-2C and HIPS-5C) to study debris dispersal at larger size. In both tests, the quantity of debris dispersed approached 99%. The extent of material that remained in the cavity as a crust layer was less than seen in the smaller scale tests, despite the fact that the driving pressure was lower. Carbon dioxide gas was employed in the HIPS-5C test to determine the influence of gas solubility on the dispersal processes. No measurable difference in debris dispersal could be detected between the carbon dioxide and nitrogen driven tests. Comparison of the results from the four experiments suggests that the extent of debris dispersal will be greater as the scale of the cavity increases.

Excellent aerosol data were obtained in the two SPIT experiments because the suspended material was retained within the chamber. Aerosolized mass fractions were in the range of 1 to 5 percent with the concentration decreasing with time. The bimodal size distributions indicated modes at less than one micrometer and greater than 10 micrometer aerodynamic diameter. A possible third mode was detected at nominally five micrometer diameter. The smallest size range was attributed to condensation of vaporized melt species, while the larger modes were characteristic of mechanical breakup and fragmentation of the melt. Electron photomicrographs of the collected aerosol indicated the one micrometer particles were agglomerates of particles one-tenth micrometer and smaller. The middle and largest modes were spherical particles similar to aerosols formed by freezing of liquid droplets.

The ability of the debris to transfer energy to the atmosphere in conjunction with the extensive dispersal seen in the experiments demonstrated the possibility of heating the containment atmosphere during reactor accident sequences that involve high-pressure melt ejection and transport into the containment volume. The thermal and chemical energy available in but a small fraction of the core inventory is sufficient to cause pressurization to threatening levels. The extensive aerosol that accompanies the dispersal of debris represents a new radionuclide source term not accounted for in present source term evaluations.

The physics of the debris to atmosphere energy transfer and propagation within the containment are not known. Future experimental work will study the behavior of the dispersed debris within a contained volume to permit direct measurement of the atmosphere temperature and pressure. The tests will include those parameters considered to affect debris dispersal and transport such as cavity geometry, containment geometry and structures, the presence of water in the cavity or containment, and the composition of the containment atmosphere. The data from the experiments will be used to develop models to describe the debris and aerosol. The models will then be implemented into larger integral containment response codes to predict severe reactor accidents.

V. REFERENCES

1. USNRC, Reactor Safety Study, <u>An Assessment of Accident Risks in U.S. Commercial Nuclear Power Plants</u>, WASH-1400, USNRC,Wash DC, NUREG/75-014, Oct 1975.

2. <u>Zion Probabilistic Safety Study</u>, Commenwealth Edison Co., Chicago, IL, 1981.

3. <u>Indian Point Probabilistic Safety Study</u>, Power Authority of the State of New York, Consolidated Edison Company of New York, Inc., Buffalo, NY, 1982

4. <u>Sizewell-B Probabilistic Safety Study</u>, Westinghouse Electric Corporation, Pittsburg, PA, WCAP-9991, 1982.

5. <u>Nuclear Power Plant Response to Severe Accidents</u>, IDCOR Technical Summary Report, Technology for Energy Corp., Knoxville, TN, Nov 1984

6. V. E. Denny and B. R. Sehgal, "Analytical Prediction of Core Heatup/Liquefaction/Slumping," Paper 5.4, <u>Proceedings of the International Meeting on Light-Water Reactor Severe Accident Evaluation</u>, Cambridge, MA, Aug 1983.

7. A. T. D. Butland, et al., <u>Report on Phase 1 of the PWR Severe Accident Containment Study</u>, United Kingdom Atomic Energy Authority, AEEW-R1842, Dec 1984.

8. W. W. Tarbell, et al., <u>High-Pressure Melt Streaming (HIPS) Program Plan</u>, Sandia National Laboratories, Albuquerque, NM, NUREG/CR-3025, SAND82-2477, Aug 1984.

9. Powers, D. A., et al., "The Role of Ex-Vessel Interactions in Determining the Severe Reactor Source Term for Fission Products," Paper 11.8, <u>Proceedings of the International Meeting on Light-Water Reactor Severe Accident Evaluation</u>, Cambridge, MA, Aug 1983.

10. Omega Engineering "Temperature Measurement Handbook and Encyclopedia," Stamford, CT, 1986.

11. N. A. Fuchs, <u>The Mechanics of Aerosols</u>, (Pergamon Press, 1964).

12. K. M. Cushing, et al., <u>Particle Sizing Techniques for Control Evaluation: Cascade Impactor Calibrations</u>, Environmental Protection Agency, EPA-600 12-76-280, Oct 1976.

13. A. R. McFarland, et al., "A High Capacity Preseparator for Collecting Large Particles," AIHA Paper #80, American Hygiene Association, Apr 1978.

14. W. Frid, "Behavior of a Corium Jet In High Pressure Melt Ejection from a Reactor Pressure Vessel," Proceedings of the International ANS/ENS Topical Meeting on Thermal Reactor Safety, San Diego, CA, SAND85-1726C, Feb 2-6, 1986.

15. D. A. Powers, The Solubility of Gases in Reactor Core Melts, Sandia National Laboratories Topical Report, Albuquerque, NM, (to be published).

16. Final Safety Analysis Report for the Zion Nuclear Power Station, Commenwealth Edison Co., Chicago, IL, 1972.

17. D. A. Powers and F. E. Arellano, Direct Observation of Melt Behavior During High Temperature Melt/Concrete Interactions, Sandia National Laboratories, Albuquerque, NM, NUREG/CR-2283, SAND81-1754, Jan 1982.

18. J. V. Beck, User's Manual for CONTA-Program for Calculating Surface Heat Flux From Transient Temperatures Inside Solids, Sandia National Laboratories, Albuquerque, NM, SAND83-7134, Dec 1983.

19. S. S. Kutateladze, "Elements of the Hydrodynamics of Gas-Liquid Systems," Fluid Mechanics - Soviet Research, Vol 1, No 4, (1972).

20. M. Pilch and W. W. Tarbell, High Pressure Ejection of Melt from a Reactor Pressure Vessel - the Discharge Phase, Sandia National Laboratories, Albuquerque, NM, NUREG/CR-4383, SAND85-C012, Sept 1985.

21. S. Sitharamayya and K. Subba Raju, Can. J. Chem. Engr., Vol 47, p. 365, (1969).

22. M. Pilch, et al., Acceleration Induced Fragmentation of Liquid Drops, Department of Nuclear Engineering, University of Virginia, Charlottesville, VA, NUREG/CR-2247, Aug 1981.

23. J. K. Agarwal, Aerosol Sampling and Transport, University of Minnesota, Minneapolis, MN, 1975.

24. J. E. Brockmann and W. W. Tarbell, "Aerosol Source Term in High Pressure Melt Ejection," Nuclear Science and Engineering: 88, 342-356 (1984).

25.   M. Pilch and W. W. Tarbell, <u>Preliminary Calculations on Direct Heating of a Containment Atmosphere by Airborne Core Debris</u>, Sandia National Laboratories, Albuquerque, NM, SAND85-2439, NUREG/CR-4455, Sept 1986.

Distribution:

U.S. Government Printing Office
Receiving Branch (Attn: NRC Stock)
8610 Cherry Lane
Laurel, MD 20707
365 copies for R3, R4, R7

U.S. Nuclear Regulatory Commission (18)
Office of Nuclear Regulatory Research
Washington, DC 20555
Attn: B. W. Morris
      C. N. Kelber
      M. Silberberg
      G. Marino
      L. Chan
      C. Ryder
      R. W. Wright
      T. Walker
      R. O. Meyer
      J. Mitchell
      S. B. Burson
      T. Lee (5)
      M. Cunningham
      P. Wood

U.S. Nuclear Regulatory Commission (7)
Office of Nuclear Regulatory Regulation
Washington, DC 20555
Attn: L. G. Hulman
      P. Easky
      J. Rosenthal
      B. Hardin
      Z. Rosztoczy
      R. Barrett
      F. Eltawilla

U.S. Department of Energy (2)
Albuquerque Operations Office
P.O. Box 5400
Albuquerque, NM 87185
Attn: J. R. Roeder, Director
      J. A. Morley, Director
      For: C. B. Quinn
           R. N. Holton

U.S. Department of Energy
Office of Nuclear Safety Coordination
Washington, DC 20545
Attn: R. W. Barber

Electric Power Research Institute (4)
3412 Hillview Avenue
Palo Alto, CA 94303
Attn: R. Vogel
      R. Ritzman
      W. Lowonstein
      R. Sehgal
Brookhaven National Laboratory (5)
Upton, NY 11973
Attn: R. A. Bari
      T. Pratt
      N. Tutu
      G. Greene
      T. Ginsberg

Professor R. Seale
Department of Nuclear Engineering
University of Arizona
Tucson, AZ 85721

Oak Ridge National Laboratory
P.O. Box Y
Oak Ridge, TN 37830
Attn: T. Kress

K. Holtzclaw
General Electric - San Jose
Mail Code 682
175 Kurtner Avenue
San Jose, CA 95125

Argonne National Laboratory (5)
9700 South Cass Avenue
Argonne, IL 60439
Attn: J. Rest
      C. Johnson
      L. Baker, Jr.
      D. Cho
      B. Spencer

Cathy Anderson
Nuclear Safety Oversight Commission
1133 15th St., NW
Room 307
Washington, DC 20005

Battelle Columbus Laboratory (3)
505 King Avenue
Columbus, OH 43201
Attn: P. Cybulskis
      R. Denning
      J. Gieseke

J. E. Antill
Berkeley Nuclear Laboratory
Berkeley GL 139 PB
Gloucestershire
England, U.K.

W. G. Cunliffe
Bldg. 396
British Nuclear Fuels, Ltd.
Springfields Works
Salwick, Preston
Lancashire
England, U.K.

R. Deem
Power Authority State of NY
10 Columbus Circle
New York, NY 10019

Professor Agustin Alonso
E.T.S. Ingenieros Industriales
Jose Gutierrez Abascal, 2
28006 Madrid, Spain

Dr. Alfonso Perez
Department de Seguridad Nuclear
Junta de Energia Nuclear
Avenida Complutense, 22
Madrid - 3
Spain

R. Sherry
JAYCOR
P.O. Box 85154
San Diego, CA 92138

Ktech Corp. (5)
901 Pennsylvania NE
Albuquerque, NM 87110
Attn: D. W. Gilbert (2)
      J. Jackson
      J. W. Ross (2)

Los Alamos National Laboratories
P.O. Box 1663
Los Alamos, NM 87545
Attn: M. Stevenson

UCLA (2)
Nnuclear Energy Laboratory
405 Hilgaard Avenue
Los Angeles, CA 90024
Attn: I. Catton
D. Okrent

University of Wisconsin
Nuclear Engineering Department
1500 Johnson Drive
Madison, WI 53706
Attn: M. L. Corradini

EG&G Idaho
Willow Creek Building, W-3
P.O. Box 1625
Idaho Falls, Idaho 83415
Attn: R. Hobbins

Battelle Pacific Northwest Laboratory
P.O. Box 999
Richland, WA 99352
Attn: M. Freshley

Wiktor Frid
Swedish State Power Board
S-162 FACH 87 VALLINGBY
Sweden

W. Stratton
2 Acoma Lane
Los Alamos, NM 87544

Gesellschaft fur Reaktorsicherheit (GRS)
Postfach 101650
Glockengrasse 2
5000 Koeln 1
Federal Republic of Germany

Kraftwerk Union
Hammerbacher Strasse 1214
Postfach 3220
D-8520 Erlangen 2
Federal Republic of Germany
Attn: Dr. M. Peehs

UKAEA
Reactor Development Division (5)
Winfrith, Dorchester
Dorset DT2 8DH
England, U.K.
Attn: R. Potter
       A. Nichols
       B. Bowsher
       P. Smith
       T. Butland

Nucleare e della Protezione Sanitaria (DISP) (2)
Ente Nazionnle Energie Alternative (ENEA)
Viale Regina Margherita, 125
Casella Postale M. 2358
I-00100 Roma A.D., Italy
Attn: Mr. Manilia
       Mr. G. Petrangeli

Dr. K. J. Brinkman
Reactor Centrum Nederland
1755 ZG Petten
THE NETHERLANDS

Dr. S. J. Niemczyk
1545 18th Street, NW
#112
Washington, DC 20036

Kernforschungszentrum Karlsruhe
Postfach 3640
75 Karlsruhe
Federal Republic of Germany
Attn: H. Rininsland

Mr. H. Bairiot, Chief
Department LWR Fuel
Belgonucleaire
Rue de Champde Mars. 25
B-1050 BRUSSELS, BELGIUM

Japan Atomic Energy Research Institute
Tokai-Mura, Naka-Gun
Ibaraki-Ken 319-11
Japan
Attn: S. Saito

Wang Lu
TVA
400 Commerce, W9C157-CK
Knoxville, TN 37902

M. Fontana
Director, IDCOR Program
ENERGEX
575 Oak Ridge Turnpike
Oak Ridge, TN 37830

Fauske and Associates, Inc. (2)
16W070 West 83rd Street
Burr Ridge, IL 60521
Attn: R. Henry
      M. Plys

Peter Bieniarz
Risk Management Associates
2309 Dietz Farm Road, NW
Albuquerque, NM 87107

Dr. K. Soda
Manager,
Chemical Engineering Safety Laboratory
Department of Nuclear Fuel Safety
Japan Atomic Energy Research Institute
Tokai-Muri, Naku-Gun, Ibaraki-Ken
319-11
Japan

K. Sato, Director
Department of Reactor Safety Research
Japan Atomic Energy Research Institute
Tokai-Mura, Naka-Gun, Ibaraki-Ken
Japan

P. Fehrenbach
Atomic Energy Canada, Ltd.
Chalk River, Ontario
Canada KOJ IJO

M. Hayns
UKAEA
Safety and Reliability Directorate
Wigshaw Lane
Culcheth
Warrington WA3 4NE
Cheshire,
England, U.K.

J. R. Mathews
Aere Harwell
Didcot
Oxfordshire OX11 ORA
England, U.K.

F. Briscoe
UKAEA Culham Laboratory
Abingdon
Oxfordshire OX14 3DB
England, U.K.

H. J. Teague (3)
UKAEA
Safety and Reliability Directorate
Wigshaw Lane
Culcheth
Warrington, WA3 4NE
England, U.K.

M. Jankowski
IAEA
Division of Nuclear Reactor Safety
Wagranerstrasse 5
P.O. Box 100
A/1400 Vienna, Austria

Statens Karnkraftinspektion
L. Hammer
P. O. 27106
S-10252 Stockholm, Sweden

Studsvik Energiteknik AB
K. Johansson
S-611 82 Nykoping, Sweden

Atomic Energy Canada Ltd.
M. Notley
Chalk River, Ontario
Canada K0J 1J0

Atomic Energy Canada Ltd. (2)
Pinawa, Manitoba
Canada R0E 1L0
Attn: H. Rosinger
        D. Wren

Korea Adv Energy Research Inst
H. R. Jun
P.O. Box 7
Daeduk-Danji
Choong-Nam, Korea

Institute of Nuclear Energy Research
Sen-I Chang
P.O. Box 3
Lungtan
Taiwan 325, Republic of China

3141   S. A. Landenberger (5)
3151   W. L. Garner
6400   A. W. Snyder
6410   J. W. Hickman
6411   A. S. Benjamin
6412   A. L. Camp
6414   D. M. Ericson, Jr.
6415   F. E. Haskin
6420   J. V. Walker
6421   P. S. Pickard
6422   D. A. Powers (5)
6422   F. E. Arellano
6422   J. E. Brockmann (4)
6422   E. R. Copus
6422   T. M. Kerley
6422   D. A. Lucero
6422   W. W. Tarbell (5)
6425   W. J. Camp
6425   M. Pilch (4)
6427   M. Berman
6427   B. W. Marshall
6440   D. A. Dahlgren
6442   W. A. Von Riesemann
6449   K. D. Bergeron
6449   D. C. Williams
6449   D. E. Carroll
6454   G. L. Cano
7530   T. B. Lane
7551   R. Berg
7537   N. R. Keltner
8024   P. W. Dean

2. TITLE AND SUBTITLE	3 LEAVE BLANK

PRESSURIZED MELT EJECTION INTO SCALED
REACTOR CAVITIES

5. AUTHOR(S)

William W. Tarbell   James W. Ross
Marty Pilch   Don W. Gilbert
John E. Brockmann

7. PERFORMING ORGANIZATION NAME AND MAILING ADDRESS (Include Zip Code)

Sandia National Laboratories
Division 6422
Albuquerque, NM 87185-5800

13. ABSTRACT (200 words or less)

This report describes four tests performed in the High-Pressure Melt
Streaming Program (HIPS) using linear-scaled cavities of the Zion Nuclear Power
Plant. These experiments were conducted to study the phenomena involved in
high-pressure ejection of core debris into the cavity beneath the reactor
pressure vessel. One-tenth and one-twentieth linear scale models of reactor
cavities were constructed and instrumented. The first test used an apparatus
constructed of alumina firebrick to minimize the potential interaction beween
the ejected melt and cavity maerial. The remaining three experiments used
scaled representations of the Zion nuclear plant geometry, constructed of
prototypic concrete composition.

Calculations were also performed to compare with experimental data and to
provide information regarding the relevant physical processes. Estimates of the
pressure vessel blowdown history, breach aperture growth, melt entrainment and
particle size, debris discharge history, and energy transfer from the debris to
the atmospere were completed and presented along with the experimental data.